UNIVERSITEIT VAN PRETORIA
UNIVERSITY OF PRETORIA
YUNIBESITHI YA PRETORIA

Selective Feature Preserved Elastic Surface Registration in Complex Geometric Morphology

Gerhardus J. Jansen van Rensburg

29th June 2011

UNIVERSITEIT VAN PRETORIA
UNIVERSITY OF PRETORIA
YUNIBESITHI YA PRETORIA

Selective Feature Preserved Elastic Surface Registration in Complex Geometric Morphology

by

Gerhardus J. Jansen van Rensburg

A dissertation submitted in partial fulfillment of the requirements for the degree

Master of Engineering

in the

Faculty of Engineering, the Built Environment and Information Technology

University of Pretoria

Pretoria

South Africa

2010

Abstract

Title: Selective Feature Preserved Elastic Surface Registration in Complex Geometric Morphology

Author: Gerhardus Jacobus Jansen van Rensburg

Supervisors: Dr. S. Kok
Dr. D.N. Wilke

Deforming a complex generic shape into a representation of another complex shape is investigated. An initial study is done on the effect of cranial shape variation on masticatory induced stress. A finite element analysis is performed on two different skull geometries. One skull geometry has a prognathic shape, characterised by jaws protruding forward, while the other has a non-prognathic form.

Comparing the results of the initial finite element analyses, the effect of an undesired variation in shape and topology on the resulting stress field is observed. This variation in shape and topology can not be attributed to the cranial shape variation that is investigated. This means that the variation in the masticatory induced stress field that is due to the relative degree in prognathism can not be quantified effectively.

To best compare results, it would be beneficial to have a computational domain for the different skull geometries that have one-to-one correspondence. An approach to obtain a computational domain that represents various geometries with the exact same mesh size and connectivity between them does exist. This approach involves deforming a generic mesh to represent different target shapes.

This report covers an introductory study to register and deform a generic mesh to approximately represent a complex target geometry. Various procedures are investigated, implemented and combined to specifically accommodate complex geometries like that of the human skull.

A surface registration procedure is implemented and combined with a feature registration procedure. Feature lines are extracted from the surface representation of each skull as well as the generic shape. These features are compared and an initial deformation is applied to the generic shape to better represent the corresponding features on the target.

Selective feature preserved elastic surface registration is performed after the initial feature based registration. Only the registration to surfaces of featureless areas and matched feature areas are allowed along with user selected areas during surface registration.

The implemented procedures have various aspects that still require improvement before the desired study regarding prognathism's effect on masticatory induced stress could truly be approached pragmatically. Focus is only given to the use of existing procedures while the additional required improvements could be addressed in future work. It is however required that the resulting discretised domain obtained in this initial study be of sufficient quality to be used in a finite element analysis (FEA).

The implemented procedure is illustrated using the two original skull geometries. Symmetric versions of these geometries are generated with a one-to-one correspondence map between them. The skull representations are then used in a finite element analysis to illustrate the appeal of having computational domains with a consistent mapping between them. The variation in the masticatory induced stress field due to the variation in cranial shape is illustrated using the consistent mapping between the geometries as part of this example.

Acknowledgements

I would like to thank and acknowledge the following persons and entities:

- D.N. Wilke and S. Kok for their supervision.
- The Advanced Mathematical Modelling division of Modelling and Digital Science at the CSIR for funding the research.
- M.L. Mac Kay and Prof. M. Steyn from the Anthropology Department at the University of Pretoria.
- The University of Pretoria for the use of skulls in their collection.
- Labuschagne and Partners at the Little Company of Mary Hospital for producing the CT scans used in reconstructing digital surface representations of the skulls.

Contents

1 Introduction **1**
1.1 Background . . . 1
1.2 Outline of Thesis . . . 3
1.2.1 Chapter 2: Background Work and Problem Statement . . . 3
1.2.2 Chapter 3: Elastic Surface Registration . . . 4
1.2.3 Chapter 4: Geometric Features . . . 4
1.2.4 Chapter 5: Feature Registration . . . 4
Landmark Nodes . . . 5
Feature lines . . . 5
1.2.5 Chapter 6: Proposed Registration Procedure . . . 6
1.2.6 Chapter 7: Conclusions . . . 8

2 Background Work and Problem Statement **9**
2.1 Introduction . . . 9
2.2 Prognathism in the human skull . . . 10
2.3 Mastication . . . 11
2.3.1 Teeth . . . 11
2.3.2 Bone . . . 11
2.3.3 Muscles . . . 12
2.4 Finite Element Model . . . 13
2.4.1 Geometries . . . 14
2.4.2 Material Properties . . . 14
2.4.3 Boundary Conditions . . . 14
2.5 Results . . . 16
2.6 Problem Statement . . . 22

3 Surface Registration **25**
3.1 Point Set Registration . . . 26
3.1.1 The Iterative Closest Point Algorithm . . . 26
Application . . . 28
3.2 Elastic Surface Registration . . . 31
3.2.1 Registration Procedure . . . 31
3.2.2 Application . . . 35
Registration on Femur Geometries . . . 35
Registration on Skull Geometries . . . 40
3.3 Remarks and Conclusions . . . 43

4 Geometric Features **44**
4.1 Introduction . . . 44
4.2 Local Structure Tensor . . . 45
4.2.1 Feature Classification . . . 46
4.2.2 Spatial Search Speed-up . . . 48
4.3 Differential Geometry Surface Information . . . 49
4.3.1 Application to a Discretised Surface . . . 50
4.3.2 Enhanced Moving Least Squares Approximation . . . 51
Generating a smooth local surface approximation . . . 51
Estimating curvatures and their derivatives . . . 53
4.3.3 Shape Index Feature Points . . . 54
4.3.4 Ridges and Valleys . . . 56
Determining ridge nodes: . . . 56
Determining valley nodes: . . . 58
Connecting nodes into lines . . . 62
Thresholding . . . 63
4.4 The Selection of Matching Features . . . 65

5 Feature Registration **68**
5.1 Feature Point Registration . . . 69
5.1.1 Radial Basis Function Interpolation . . . 69
5.2 Feature Line Registration . . . 74
5.2.1 Registration Procedure . . . 74
Point Matching . . . 75

Line Matching 76
Transformation Computation 77
Implementation 80
Application 80
5.3 Surface registration 81
5.3.1 Orthognathic Representation 83

6 Proposed Registration Procedure 91
6.1 Step 1: Rotate, Scale and Translate 93
6.2 Step 2: Use Lines of Curvature 94
6.2.1 Feature Surfaces 94
6.3 Step 3: Register Allowable Surface 99
6.4 Step 5: Mesh Quality 102
6.4.1 Quality Metric 104
6.4.2 Usable Skull Mesh Generation 106
6.5 Analysis on Registered Skull Geometries 109
6.5.1 The effect of non-unique registration on FEA result 111
6.5.2 Linearity and constructing an approximate result from principal shape components 118

7 Conclusions 122
7.1 Remarks and Possible Future Work 122

A FEA on Skull Geometries 133
A.1 Introduction 133
A.2 Geometries 134
A.2.1 Model Creation 134
A.3 Material Properties 135
A.4 Boundary Conditions 135
A.4.1 Muscle Forces 136
A.4.2 Reaction Forces 138
A.5 Analysis 141
A.6 Results 149

B Affine Iterative Closest Point Problem 155
B.1 Reformulating the ICP problem 155

B.2 Lie group and lie algebra 156
B.3 Performing an Affine ICP transformation 157

C Shape Context Correspondence **160**
C.1 Shape Context 160
C.2 Point Matching 163

D Dolphin Feature Example **164**

Nomenclature

a	-	Lower scale bound in the reformulated ICP.
b	-	Upper scale bound in the reformulated ICP.
c	-	Counter, indicating the c^{th} triangle patch on the target shape surface mesh.
c_k	-	Correspondence between a generic and data shape.
$\mathbf{c}$	-	Vector containing the rotation, reflection and scale variables used in the reformulated ICP.
d	-	Counter, indicating the d^{th} triangle patch on the generic shape surface mesh.
$\mathbf{d}$	-	Distance from a point to it's registered location.
D	-	Distance.
$\mathbf{D}_j$	-	Set of linear bases of a diagonal matrix. The only non-zero entry is $D_{jj} = 1$.
E	-	Young's modulus.
$\mathbf{E}_j$	-	Linearised bases of the special orthogonal group representation of an invertible matrix.
f	-	Smoothing parameter in the elastic surface registration procedure.
f_i	-	Function evaluation at location i.
F	-	Force.
$\mathcal{F}$	-	Implicit surface $\mathcal{F}(\mathbf{x}) = 0$.
h	-	Positive increasing function for determining element quality.
H	-	Reference plane.
i	-	Counter. $i = 1, 2, .., k_{\max}$ where $k_{\max}$ is the maximum number of iterations for example.

$\mathbf{I}$	-	Identity matrix.
$\mathbf{J}$	-	Jacobian matrix.
k	-	Iteration.
L	-	A line.
$\mathbf{m}$	-	The points on the generic shape.
$\mathbf{m_t}$	-	Point correspondence of the target on the generic shape translated so it's centroid is at the origin of the Cartesian coordinate axis.
M	-	Moment.
$\mathbf{M}_{b,b}$	-	Matrix containing evaluations of a radial basis function.
$\mathcal{M}$	-	Model or generic shape.
n	-	Number of neighbours used in the elastic registration procedure.
$\mathbf{n}$	-	Unit normal.
N	-	Indicates size. N_p is the number of points in the target shape and N_m the number of points in the model shape for example.
p	-	Linear polynomial.
p_i^j	-	Portion of points on one line L_i registered to line L'_j
$\mathbf{p}$	-	The points on the target shape.
$\mathbf{p}_i$	-	A specific point.
$\mathbf{p_t}$		Target shape $\mathbf{p}$ after it is translated so the centroid is at the origin of the Cartesian coordinate axis
$\mathbf{P}_b$	-	Matrix containing boundary coordinates.
$\mathcal{P}$	-	Data or target shape.
q_m	-	Element quality of tetrahedron m.
$\mathbf{Q}$	-	Matrix. $\mathbf{Q} = \mathbf{JW}^{-1}$ when determining element quality.
r	-	Radius.
r_j	-	Rotation variables in the reformulated ICP.
$\mathbf{r}$	-	The registration location. $\mathbf{r}_{w_j}$ is the possible registered location of point $\mathbf{w}_j$ onto a target shape for example.
$\mathbf{R}$	-	Rotation Matrix.
$\mathbb{R}$	-	Real number indicator. $\mathbb{R}^3$ indicates a tensor consisting of three real numbers.
s_j	-	Scale variables in the reformulated ICP.

S^{k-1}	-	Deformation applied to $\mathcal{W}^{k-1}$ to better approximate the target.
S_i	-	Shape index.
$\mathbf{S}$	-	Scale Matrix.
$\mathbf{t}$	-	Translation vector.
T	-	Transformation.
T_h	-	Threshold, used when pruning false lines.
T_m	-	Indicates size. T_m is the number of triangles in the model shape
T_p	-	Indicates size. T_p is the number of triangles in the target shape.
$\mathcal{T}$	-	A tetrahedron.
u_j	-	Reflection variables in the reformulated ICP.
$\mathbf{U}$	-	Reflection matrix.
$\mathbf{w}$	-	The points on the deformable surface.
$\mathbf{W}$	-	Jacobian matrix that maps the tetrahedron $\mathcal{T}_R$ to tetrahedron $\mathcal{T}_I$
$\mathcal{W}$	-	Deformable surface in the elastic registration procedure.
$\mathbf{x}$	-	Nodal coordinates

Greek Symbols

α	-	Coefficients used in radial basis function interpolation
$\boldsymbol{\beta}$	-	Coefficients of the linear polynomial when using RBF interpolation.
γ	-	Smoothing parameter in the elastic registration procedure
δ	-	Shift variable used in positive increasing function.
ε	-	The average distance of point set correspondence in the ICP procedure.
	OR	The average total deformation applied to the deformable surface during elastic registration.
ε_T	-	Tolerance.
ζ	-	Machine epsilon or tolerance ($0 < \zeta \ll 1$).
κ	-	Principal curvature.
λ	-	Eigenvalue.
μ	-	Average shape index.
ν	-	Poisson's ratio.
ξ	-	Compact radial basis function scaling factor.
$\boldsymbol{\varpi}$	-	Principal curvature direction.
σ_0	-	Smoothing parameter in the elastic registration procedure
σ_m	-	Determinant of the matrix $\mathbf{S}_m$.
τ	-	Curvature derivative or extremality coefficient.
ϕ	-	Radial basis function.

Superscripts

-1	-	Inversion.
k	-	Iteration counter. $k-1$ indicates the previous iteration.
T	-	Tensor transpose.

Subscripts

$0, 1, 2, ...$	-	Used where the number represents the index within a list or set.
i	-	Quantity in list defining the target shape. $i \in \{1, 2, ..., N_p\}$
$i, j, k, ...$	-	Used where indicial notation is used and summation is implied.
j	-	Quantity in list defining the generic shape. $j \in \{1, 2, ..., N_m\}$
k	-	Iteration counter. $k-1$ indicates the previous iteration.
m	-	Indicates a value related to the generic shape $\mathcal{M}$.
p	-	Indicates a value related to the target shape $\mathcal{P}$.
x, y, z	-	Indicates coordinates in the x -, y - and z- axis.

Mathematical Symbols and Operators

$\in$	-	Indicates membership of a set.
Σ	-	Summation.
$\|.\|$	-	Frobenius norm.
$\|\|.\|\|$	-	Euclidean distance.
$\det(.)$	-	Determinant of a matrix.
$\mathrm{tr}(.)$	-	Trace of a matrix.
∂	-	Partial derivative.
∇	-	Gradient.

Acronyms and Abbreviations

ba	-	Basion - Landmark position on the human skull.
CT	-	Computed Tomography.
FEA	-	Finite Element Analysis.
FEM	-	Finite Element Model.
FSI	-	Fluid Structure Interaction.
GI	-	Gnathic index - The distance ratio of the lines connecting the basion landmark to the prostion and nasion landmarks on the human skull. This ratio is expressed as a percentage quantity.
ICP	-	Iterative Closest Point - Procedure used in rigid registration.
LST	-	Local Structure Tensor.
MLS	-	Moving Least Squares.
MRI	-	Magnetic Resonance Imaging.
n	-	Nasion - Landmark position on the human skull.
OC	-	Occipital condyles - Condyles at the foramen magnum where the skull articulates with the spinal column.
PCA	-	Principal Component Analysis - Statistical analysis to determine the principal modes of variation within sample data.
pr	-	Prostion - Landmark position on the human skull.
RBF	-	Radial Basis Function - Interpolation function used to interpolate a scalar quantity known at select positions within spatial data.
TMJ	-	Temporomandibular joint - Joint connecting the mandible to the skull.
TPS	-	Thin Plate Spline - A type of radial basis function.

List of Figures

1.1 Landmarks on the (a) front, (b) side and (c) bottom of the human skull [43]. 2
1.2 Flow diagram illustrating the basic idea of combining feature and surface registration. In the implemented procedure, the result of the feature based registration is used as input and also dictates allowable surfaces used during surface registration. 7

2.1 Masticatory muscles [12]. (a) Masseter, (b) Temporalis and (c) the lateral and medial Pterygoid. 13
2.2 Boundary condition positions on the skull. (a) Lateral view of the prognathic skull indicating the Temporal fossa and zygomatic arch (cheek bone). The jaw hinge or temporomandibular joint is indicated by TMJ and the seven sections of the temporalis muscle attachment positions are indicated by numbers 1 through 7. (b) Inferior view of the prognathic skull. The location of boundary constraints are the occipital condyles (OC) on the foramen magnum. Reaction forces are determined at the left and right temporomandibular joints (TMJL and TMJR) and either the first molar (M1) or first incisor (I1) for the applied muscle forces when balancing the system. 15
2.3 Muscles and reaction forces on (a) the prognathic skull form and (b) orthognathic skull form for a vertical molar bite. 17
2.4 Lateral view of the working side Von Mises stress for a molar bite on the (a) prognathic and (b) orthognathic skull form as well as for an incisor bite on the (c) prognathic and (d) orthognathic FEA. The units of the stress contours are in N/cm^2. 18
2.5 Semi-transparent view of the (a) prognathic and (b) orthognathic skull form. 19

2.6 Lateral cut views through the two skulls to illustrate the difference between their boundary surfaces. (a) Location of the cut planes in (b) and (c). (d) Location of the cut planes (e) and (f). 20
2.7 Frontal cut views through the two skulls to illustrate the difference between their boundary surfaces. (a) Location of the cut planes in (b) and (c). (d) Location of the cut planes (e) and (f). 21
2.8 First three modes of a principal component analysis done on the human femur varied between ±3 standard deviations. This is done after 46 different femur geometries are represented using the same mesh with only updated nodal coordinates [19]. (a) Frontal and (b) lateral view. 23

3.1 Lateral view of rigid registration results on two femur geometries obtained from the INRIA shape repository [4]. (a) Initial relative position and alignment of the two femurs. From this starting position, the rigid registration result is obtained by ICP for (b) rotation and translation only and (c) allowing isotropic scaling in addition to rotation and translation. 29
3.2 Isometric view of rigid registration results on two femur geometries obtained from the INRIA shape repository [4]. (a) Initial relative position and alignment of the two femurs. From this starting position, the rigid registration result is obtained by ICP for (b) rotation and translation only and (c) allowing isotropic scaling in addition to rotation and translation. 30
3.3 Convergence rate of the ICP. The blue line is obtained when only allowing rotation and translation while the red line is the convergence rate when rotation, translation and isotropic scale is allowed. At each iteration, ε is the function value after performing the least squares optimisation in Equation (3.5). 30
3.4 Determining the registration of a point $\mathbf{w}_j$ onto one of the n closest triangles with (a) the registered point inside and (b) outside of the triangle boundary. 33

3.5 Elastic registration on the isotropic scale ICP result. (a) Lateral view of the rigid registration result on the two femur geometries. (b) Lateral view of the elastic surface registration result to deform the black wire-frame mesh into the target geometry at iteration 100. . . 35
3.6 Elastic registration on the isotropic scale ICP result. (a) Isometric view of the rigid registration result on the two femur geometries. (b) Isometric view of the elastic surface registration result to deform the black wire-frame mesh into the target geometry at iteration 100. . . 36
3.7 Improvement on the average deformation similarity criteria in Equation (3.11) subject to varying user controlled parameters. (a) $\sigma_0 = 10$ and $f = 1.0715$ while varying γ. (b) $f = 1.0715$ and $\gamma = 2$ while varying σ_0. (c) $\sigma_0 = 10$ and $\gamma = 2$ while varying f. 37
3.8 Various deformed generic surface target representations obtained with different user controlled parameters. Mesh **A** is the registration result with the parameters set to $\gamma = 2$, $\sigma_0 = 0.5$ and $f = 1.0715$ at 10 registration iterations. Mesh **B** is the registration result with the parameters set to $\gamma = 2$, $\sigma_0 = 50$ and $f = 1.0715$ at 75 registration iterations. Mesh **C** is the registration result with the parameters set to $\gamma = 2$, $\sigma_0 = 10$ and $f = 1.3$ at 20 registration iterations. Mesh **D** is the registration result with the parameters set to $\gamma = 2$, $\sigma_0 = 10$ and $f = 1.1$ at 40 registration iterations. The average total deformation plots in Figure 3.7 also indicate where meshes **A** - **D** are chosen. . . 38
3.9 Initial position of the smoothed skull mesh and it's reflection. . . . 41
3.10 Initial position of the smoothed skull mesh and it's reflection. . . . 41
3.11 Problems with the sinus in elastically registering the smooth skull mesh into its reflection. (a) Position of cut plane (c) and (e). (b) Position of cut plane (d) and (f). (c), (d) Initial position of deformable mesh in relation to the target (The blue mesh in Figure 3.10 is set as the deformable mesh and is registered onto it's reflection). (e), (f) Elastic registration result at iteration 100. The red line represents the position of the target surface in that plane and the black line the deformable mesh surface. 42

4.1 Points on skull geometry where $\lambda_1 < 5 \times \lambda_2$. This condition represents spheres, saddles, ridges and valleys within a certain degree. (a) Frontal, (b) side and (c) bottom view. 46
4.2 Points on skull geometry where $\lambda_1 < 100 \times \lambda_2$. This condition represents spheres, saddles, ridges and valleys within a certain degree. (a) Frontal, (b) side and (c) bottom view. 46
4.3 Points on skull geometry where $\lambda_1 > 2'000 \times \lambda_2$. This condition represents planes to a certain degree. (a) Frontal, (b) side and (c) bottom view. 47
4.4 Points on skull geometry where $\lambda_1 > 20'000 \times \lambda_2$. This condition represents planes to a certain degree. (a) Frontal, (b) side and (c) bottom view. 47
4.5 Points for $\lambda_1 < 50 \times \lambda_2$ on a refined dolphin model using (a) 3-ring neighbourhood (b) 15 nearest neighbours 49
4.6 (a) The MLS projection. Given a point $\mathbf{p}_j$, the local reference plane H and a point $\mathbf{q}$ on H is first determined. An MLS surface is then defined implicitly by the MLS projection as the set of points that project on to themselves [37]. (b) The estimation of a modified MLS approximation to the mesh [37]. 51
4.7 Points on skull geometry where $\kappa_{\max} > |\kappa_{\min}|$. (a) Frontal, (b) side and (c) bottom view. 54
4.8 Points on skull geometry where $\kappa_{\min} < -|\kappa_{\max}|$. (a) Frontal, (b) side and (c) bottom view. 54
4.9 Frontal view highlighting points on skull geometry where $\kappa_{\max} > 5 \times \text{average}(\kappa_{\max})$ in blue and $\kappa_{\min} < 5 \times \text{average}(\kappa_{\min})$ in red. (a) Ridges and valleys split up in (b) to show only ridges and (c) only valleys. 55
4.10 Side view highlighting points on skull geometry where $\kappa_{\max} > 5 \times \text{average}(\kappa_{\max})$ in blue and $\kappa_{\min} < 5 \times \text{average}(\kappa_{\min})$ in red. (a) Ridges and valleys split up in (b) to show only ridges and (c) only valleys. 55
4.11 Lower view highlighting points on skull geometry where $\kappa_{\max} > 5 \times \text{average}(\kappa_{\max})$ in blue and $\kappa_{\min} < 5 \times \text{average}(\kappa_{\min})$ in red. (a) Ridges and valleys split up in (b) to show only ridges and (c) only valleys. 55
4.12 Shape index of a dolphin geometry after using a 5-ring neighbourhood for MLS surface fitting. (a) Isometric (b) top and (c) side view. . . 57

4.13 Shape index of the skull geometry after using a 3-ring neighbourhood for MLS surface fitting. (a) Frontal, (b) side and (c) bottom view. 57
4.14 Feature points automatically extracted from skull geometry for radius $r_i = 10$ and $\alpha = 0.1, \beta = 0.1$. (a) Frontal, (b) side and (c) bottom view. 58
4.15 Crest nodes and lines on a hand geometry. (a) Possible ridge (blue) and valley (red) points obtained by using only principal curvatures and derivatives along with (b) the lines after connecting points in the relevant principal direction. (c) The equivalent ridge and valley lines obtained by using curvature derivative zero crossing procedure. For visual clarity only lines with more than 8 segments are displayed. . 60
4.16 Crest lines on a refined and smoothed bishop geometry. (a) Ridge (blue) and valley (red) lines obtained by using only principal curvatures and directions. (b) The equivalent ridge and valley lines obtained by using curvature derivative zero crossing procedure. . . . 60
4.17 Crest nodes on the refined version of a dolphin geometry. (a) and (c) Ridge (blue) and valley (red) nodes obtained by using only principal curvatures and directions. (b) and (d) The equivalent ridge and valley nodes obtained by using curvature derivative zero crossing procedure. 61
4.18 Crest lines on the refined version of a dolphin geometry. (a) Ridge (blue) and valley (red) lines obtained by using only principal curvatures and directions. (b) The equivalent ridge and valley lines obtained by using curvature derivative zero crossing procedure. Lines have been pruned and line width scaled according to threshold calculated with Equation (4.11) and a minimum threshold value of $T_h = 10$. 61

4.19 Extracted ridge (blue) and valley (red) lines on the refined trim-star geometry. (a) Extracted crest nodes with presence of false edges already evident on the smoother areas of the geometry. (b) Allowable crest nodes after filtering out those that don't satisfy the local structure tensor condition $\lambda_1 < 10 \times \lambda_2$. (c) The extracted crest nodes that satisfy the local structure tensor filtering condition in (b). (d) The ridge and valley lines constructed using only the filtered crest nodes. In this figure some spurious or false lines are still present indicating that thresholding might still be required. These false lines are likely picked up due to the local discretisation. 62
4.20 Filtering crest nodes on the refined version of a dolphin geometry. (a) Ridge (blue) and valley (red) nodes extracted using 100 nearest neighbour search with extremality zero crossing procedure. (b) Points for feature areas satisfying $\lambda_1 < 100 \times \lambda_2$ resulting from 3-ring neighbourhood local structure evaluation. (c) Ridge and valley nodes remaining after the filter procedure. 63
4.21 Frontal view of the skull geometry with extracted ridge nodes in blue and valley nodes in red. (a) and (b) show all of the crest nodes on the geometry and (c) contains only nodes that satisfy the local structure tensor condition $\lambda_1 < 50 \times \lambda_2$. 64
4.22 Side view of the skull geometry with extracted ridge nodes in blue and valley nodes in red. (a) and (b) show all of the crest nodes on the geometry and (c) contains only nodes that satisfy the local structure tensor condition $\lambda_1 < 50 \times \lambda_2$. 65
4.23 Lower view of the skull geometry with extracted ridge nodes in blue and valley nodes in red. (a) and (b) show all of the crest nodes on the geometry and (c) contains only nodes that satisfy the local structure tensor condition $\lambda_1 < 50 \times \lambda_2$. 65
4.24 Thresholded ridge lines on the skull geometry after first applying the filter $\lambda_1 < 50 \times \lambda_2$ and then thresholding lines to $T_h = 200$. (a) Frontal and (b) lateral view. Only lines with more than 4 line segments are displayed. 66

4.25 Thresholded valley lines on the skull geometry after first applying the filter $\lambda_1 < 50 \times \lambda_2$ and then thresholding lines to $T_h = 200$. (a) Frontal and (b) lateral view. Only lines with more than 4 line segments are displayed. 66

5.1 Geometric dissimilarity illustrating the average shape of the scapula of male ($n_m = 52$, *open symbols*) and female ($n_f = 42$, *closed symbols*) western African lowland Gorillas. (a) Recorded coordinates of homologous points on each specimen. (b) The varying coordinates due to difference in shape as well as location and orientation with respect to axes during landmark digitisation. (c) Superimposed landmark coordinates after applying the Procrustes method. The common coordinate system allows for further statistical analysis. (d) Visualising statistical results, the average male-female variation is shown using both difference vectors and a thin plate spline deformation grid magnified by a scale factor of two [54]. 72

5.2 Radial Basis Function Performance. (a) Original Configuration (b) MQB, (c) IMQB, (d) Gauss, (e) Linear, (f) Cubic, (g) TPS. The deformable mesh is displayed as a black wire-frame and the target as the semi-opaque pink surface. The blue dots indicate deformable landmark positions and the red dots the target positions. In (b) through (g) these landmark coordinates coincide exactly. 73

5.3 Two sets of lines to be registered [59]. (a) The target skull $\mathcal{P}$ on the left is composed of 591 lines and 19'302 points. (b) Reference skull $\mathcal{M}$ on the right is composed of 583 lines and 19'368 points. These subjects have a variation in shape as well as differences in the number and topology of the lines. 75

5.4 Registering two lines [59]. (a) Illustration revealing that computing registration parameters is not obvious due to the non-bijectivity of matched points. (b) After discarding non-consistent matched points, line registration parameters are computed consistently. 76

5.5 Registration of $\mathcal{M}$ towards $\mathcal{P}$ [59]. (a) The deformed set $\mathcal{M}$ with $\mathcal{P}$. Matched points are linked with the two sets reasonably superimposed. In (b) $\mathcal{M}$ is in it's original position, allowing an estimated extent of the deformation between the two sets. 78

5.6 Building and using a topological registration map [59]. (a) The registration graph: each node is a line of a set and an oriented link represents the relation "is registered with". (b) Extracted subsets of corresponding lines of different data sets. If a sub-graph contains at least one line of each data set, it defines a subset of common lines found on all geometries in the sample. 79
5.7 Common lines to all six skulls used by Subsol *et al.* [59]. The thin lines show the lines of the different geometries used and the thicker lines the average common lines constituting the atlas. 79
5.8 Feature line registration on dolphin geometries. (a) Original position of a target and base dolphin geometry. (b) Updated position of the target dolphin geometry relative to the base shape after isotropic scale ICP registration. (c) Feature registration of the base dolphin to the aligned target configuration at iteration 100. The target geometry is illustrated in its aligned position with the target features in red and the deformed base geometry features in blue. 82
5.9 Frontal view of feature registration on the smooth skull and its reflection. (a) Feature lines of the smoothed skull and its reflection. (b) Feature registration result and (c) the average of the initial and registered positions to create a symmetric model. Blue lines indicate the features of the deformable surface with red lines indicating the target features. 83
5.10 Lower view of feature registration on the smooth skull and its reflection. (a) Feature lines of the smoothed skull and its reflection. (b) Feature registration result and (c) the average of the initial and registered positions to create a symmetric model. Blue lines indicate the features of the deformable surface with red lines indicating the target features. 83

5.11 Elastic surface registration of the smooth skull onto its reflection. The blue mesh in Figure 3.10 is set as the deformable mesh and is registered onto it's reflection. (a) Reflected smooth skull geometry. (b) Reflected smooth skull geometry set as the target with the original smooth skull shown as the black wire-frame. (c) Elastic surface registration results after first applying the feature registration of Figures 5.9 and 5.10. (d) The average of the smooth skull and registered nodal coordinates resulting in a symmetric skull surface. 84

5.12 Asymmetry in the original smooth skull geometry. (a) Displacement from the symmetric skull mesh coordinates back to the original scaled by a factor of 3. (b) The absolute distance (norm of the distance vector) from the original to symmetric nodal coordinates illustrated as scalars on the symmetric skull representation. The color bar values are in millimeters. 84

5.13 Reflected registration incorporating an initial feature match. Simply registering the smooth skull geometry onto it's reflection in Chapter 3 created problems with especially the sinuses. The same cut planes of Figure 3.11 are presented here compared to the registration result after an initial feature match. (a), (c) The initial registration and (b), (d) result after initial feature registration at iteration 100. Recall that the red line indicates the target geometry in the plane with black the surface deformed during registration. 85

5.14 Elastic registration on the orthognathic skull. (a) The initial deformable mesh. (b) The rigid registration result to align the orthognathic skull to the deformable mesh with (c) the registration result at iteration 60. (d) The smoothed deformed mesh at iteration 60. . 87

5.15 Frontal view of elastic registration on the orthognathic skull. (a) The cut plane illustrating the position of the subsequent figures taken for the registration result. (b) The target and deformable geometry after isotropic scale ICP registration. (c) The result of an initial surface feature registration. Elastic surface registration is performed after an initial feature registration resulting in base mesh deformation at iteration (d) 10, (e) 20, (f) 30, (g) 40, (h) 50 and (i) 60. The red line represents the position of the target surface in that plane and the black line the deformable mesh surface. Note that the topology doesn't change although it might appear that way. This appearance is due to the registered feature coming in and out of the plane where these figures are generated. 88

5.16 Lateral view of elastic registration on the orthognathic skull. (a) The cut plane illustrating the position of the subsequent figures taken for the registration result. (b) The target and deformable geometry after isotropic scale ICP registration. (c) The result of an initial surface feature registration. Elastic surface registration is performed after an initial feature registration resulting in base mesh deformation at iteration (d) 10, (e) 20, (f) 30, (g) 40, (h) 50 and (i) 60. The red line represents the position of the target surface in that plane and the black line the deformable mesh surface. 89

5.17 Difference between the original and smoothed registration result at iteration 60. (a) Result of the elastic surface registration at iteration 60. This is the same cut as visible in Figure 5.15 (i). (b) The result showed in (a) after 10 Taubin [61] smoothing iterations. The red line represents the position of the target surface in the cut plane and the black line the deformable mesh surface. 90

6.1 Flow diagram illustrating the various components of the registration procedure proposed and implemented. 92

6.2 (a) Original position of the orthognathic skull geometry relative to the smoothed base skull. (b) Frontal and (c) lateral view of the orthognathic skull and base skull represented by the black wire-frame mesh. 93

6.3 (a) Rigid registration position of the orthognathic skull geometry relative to the smoothed base skull after an isotropic ICP registration. (b) Frontal and (c) lateral view of the orthognathic skull and base skull represented by the black wire-frame mesh. 93
6.4 (a) User selected allowable features on the symmetric base skull geometry. (b) Frontal, (c) lateral and (d) lower view. 95
6.5 Registration of allowable base geometry features to the orthognathic skull. (a) Frontal, (b) lateral and (c) lower view of the base geometry features relative to the orthognathic skull. (d) Frontal, (e) lateral and (f) lower view of the base geometry features registered and deformed to the corresponding features on the orthognathic skull. 96
6.6 Registration of allowable base geometry features to the orthognathic skull. (a) The registration result on an opaque target skull and (b) semi-transparent target surface. Blue lines indicate the features of the deformable surface with red lines indicating the target features. 96
6.7 All feature points on the symmetric base skull for $\kappa_{\max} > 0.2$ and $\kappa_{\min} < -0.2$. (a) Frontal, (b) lateral and (c) lower view. 98
6.8 All feature points on the orthognathic target skull for $\kappa_{\max} > 0.18$ and $\kappa_{\min} < -0.18$. (a) Frontal, (b) lateral and (c) lower view. 98
6.9 Feature points on the symmetric base skull for $\kappa_{\max} > 0.2$ and $\kappa_{\min} < -0.2$ corresponding to the user specified allowable feature lines in Figure 6.4. (a) Frontal, (b) lateral and (c) lower view. 98
6.10 Feature points on the orthognathic target skull for $\kappa_{\max} > 0.18$ and $\kappa_{\min} < -0.18$ corresponding to the user specified allowable feature lines in Figure 6.6. (a) Frontal, (b) lateral and (c) lower view. . . . 99
6.11 Elastic registration on the orthognathic skull. (a) The rigid registration result to align the orthognathic skull to the deformable mesh with (b) the registration result at iteration 60. This registration result is obtained after an initial allowable feature registration and filtering for allowable surfaces. The compared result of Figure 5.14 employed full feature and subsequent full elastic surface registration. 100

6.12 Frontal view of elastic registration on the orthognathic skull for automatically selected allowable features. (a) The target and deformable geometry after isotropic scale ICP registration. After the initial registration of selected features in Figure 6.6, elastic surface registration is performed and smoothed resulting in (b) the smoothed registration result at iteration 60. The gray and red line sections represent the target surface. Grey represents the automatically discarded areas while the red lines represent the allowable and featureless target surface in the same plane as Figure 5.15. The black line represents the deformable mesh surface. 101

6.13 Lateral view of elastic registration on the orthognathic skull for automatically selected allowable features. (a) The target and deformable geometry after isotropic scale ICP registration. After the initial registration of selected features in Figure 6.6, elastic surface registration is performed and smoothed resulting in (b) the registration result at iteration 60. The gray and red line sections represent the target surface. Grey represents the automatically discarded areas while the red lines represent the allowable and featureless target surface in the same plane as Figure 5.16. The black line represents the deformable mesh surface. 101

6.14 (a) Orthognathic target skull geometry with (b) the registration result and (c) the symmetric version on the registration result. (d) Prognathic target skull geometry with (e) the registration result and (f) the symmetric version on the registration result. 103

6.15 Inverted elements retained after mesh improvement in the orthognathic skull representation. (a) Global position of inverted elements. (b) Detail showing the four inverted surface elements. 108

6.16 Mesh quality evaluated using Equation (6.4). (a) Symmetric prognathic skull representation. (b) Original mesh generated on the average surface using TetGen [9]. (c) Symmetric orthognathic skull representation. 108

6.17 Histogram illustrating the element quality of the optimised prognathic and orthognathic mesh representations as well as the element quality of the original mesh generated on the average skull surface. 109

6.18 Von Mises stress contours for a molar bite scaled to show a maximum of 8 MPa. (a) Prognathic, (b) Average and (c) Orthognathic skull shape. 110
6.19 (a) The Von Mises stress in the prognathic skull shape plotted on the mesh representing the average shape. (b) The Von Mises stress in the orthognathic skull shape plotted on the mesh representing the average shape. (c) The difference in Von Mises stress between the prognathic and orthognathic finite element results $\sigma^{\mathrm{vM}}_{\mathrm{prognathic}} - \sigma^{\mathrm{vM}}_{\mathrm{orthognathic}}$ shown for the range $[-8, 8]$ MPa. All of the contours are plotted on the mesh representing the average skull shape. (a)-(b)=(c) 111
6.20 (a) Three different meshes representing the orthognathic skull shape. (b) Detail of the meshes in (a) illustrating a difference in nodal coordinate positions. This is done for both prognathic and orthognathic skull shape. Three meshes representing each shape is used to quantify the influence the uniqueness of a registration result obtained by this method has on the final FEA result. 112
6.21 The difference in Von Mises stress between the results obtained using different prognathic and orthognathic skull shape mesh representation. Three mesh versions of the prognathic and of the orthognathic skull shape are used. An FEA is done on the molar bite load case using all six meshes. The FEA result on the prognathic meshes is compared to the result on the orthognathic meshes in the same way as Figure 6.19 (c). In each row the same prognathic mesh is compared to a different orthognathic mesh while each column shows the result of the same orthognathic mesh compared to a different prognathic mesh. Contours are given for the range $[-2, 2]$ MPa. 113
6.22 Histogram illustrating the distribution of stress variation. The results given in Figure 6.21 is categorised to show the small percentage of elements where a significant variation occur. The absolute value of these results are used and normalised to illustrate them on the same histogram. The majority of elements are seen to fall below 5% of the maximum absolute difference in Von Mises stress. 114

6.23 The variation of the difference in Von Mises stress using the original results compared to the difference in Von Mises stress when one of the original results is compared with the result on a new mesh representation. (a) Figure 6.21 (a) - Figure 6.21 (b). (b) Figure 6.21 (a) - Figure 6.21 (c). (c) Figure 6.21 (a) - Figure 6.21 (d). (d) Figure 6.21 (a) - Figure 6.21 (g). 116

6.24 The Von Mises stress result for a molar bite analysis using the same nodes to apply boundary conditions on the three different orthognathic skull shape mesh representations. 117

6.25 (a) The difference in Von Mises stress for the original prognathic and orthognathic skull analyses also displayed in Figure 6.19 (c). (b) The variation noticed when comparing the Von Mises stress for the original prognathic and second orthognathic skull analyses to the original also displayed in Figure 6.23 (a). Contours are given for the range $[-2, 2]$ MPa. 118

6.26 (a) The FEA resulting Von Mises stress on the average skull shape. (b) The average Von Mises result of the prognathic and orthognathic stresses plotted on the average skull mesh. (c) The difference in Von Mises stress $\sigma^{\text{vM}}_{\text{average}} - \left(\sigma^{\text{vM}}_{\text{prognathic}} + \sigma^{\text{vM}}_{\text{orthognathic}}\right)/2$. This falls in the range $[-2.699, 3.247]$ MPa. 120

6.27 Histogram illustrating the distribution of stress variation. The absolute value of the results given in Figure 6.26 (c) is categorised to show the small percentage of elements where a significant variation occur. The majority of elements are seen to fall below 0.162 MPa, which is 5% of the maximum difference in Von Mises stress 3.247 MPa. 121

A.1 Free body diagram of the skull in the yz-plane. Muscle force components are visible in their approximate locations (red) as well the reaction forces (blue) for the working side of both the crania and mandible 139

A.2 Results of sensitivity analysis done on the orthognathic skull for a molar bite. This analysis was chosen because F_{LRx} is the largest in comparison to other resultant forces when an incisor bite or prognathic skull shape is considered. Working:balancing ratio of F_{LRx} left 1:$\frac{7}{3}$ and right $\frac{7}{3}$:1 for Von Mises stress set to a maximum of (a), (b) 300 N/cm^2 and (c), (d) 50 N/cm^2. Slight variation in stress field is only visible for stresses far below the range of stresses used in drawing conclusions from FEA results. 142
A.3 Muscle contribution and reaction forces on the prognathic skull for a vertical molar bite. 145
A.4 Muscle contribution and reaction forces on the orthognathic skull for a vertical molar bite. 146
A.5 Muscle contribution and reaction forces on the prognathic skull for a vertical incisor bite. 147
A.6 Muscle contribution and reaction forces on the orthognathic skull for a vertical incisor bite. 148
A.7 Lateral view of the working side stresses for a molar bite on full prognathic and orthognathic FEA results in N/cm^2. (a), (b) 1st principal stress (c), (d) 2nd principal stress (e), (f) 3rd principal stress and (g), (h) Von Mises stress. 150
A.8 Lateral view of the working side stresses for incisor bite on full prognathic and orthognathic FEA results in N/cm^2. (a), (b) 1st principal stress (c), (d) 2nd principal stress (e), (f) 3rd principal stress and (g), (h) Von Mises stress. 151
A.9 Lateral view of the working side muscle contribution to Von Mises stress. The molar bite for prognathic and orthognathic FEA results are given in N/cm^2. (a), (b) Temporalis (c), (d) superficial masseter (e), (f) deep head masseter and (g), (h) medial pterygoid contributions. 152
A.10 Von Mises stress concentrations. (a) Lower view of the incisal bite analysis on the orthognathic skull geometry with detail in (c). (b) Lower view of the molar bite analysis on the prognathic skull geometry with detail in (d). Stress concentrations in these two analyses are shown with reference to Table A.6. Maximum Von Mises stress occurs at stress concentrations and can not be compared. 154

C.1 a) 2D log-polar histogram bins for 2D shape context. b) 3D spherical coordinates for use in setting up 3D shape context histogram. [68] . 162
C.2 Shape context after first creating skeletal lines. This is done here by Xie *et al.* [69] for two different elephant outlines. The images illustrate the image position for setting up a shape context histogram for points A in (a) and C in (b). 162
C.3 Shape context histograms of the four points a) A, b) B, c) C and d) D marked in Figure C.2 [69]. Here the corresponding points are seen to have similar histograms if (a) and (c) are compared for example. 162

D.1 Original position of a target and base dolphin geometry. The target geometry is illustrated in its original position with the target features in red and the base geometry features in blue. (a) Isometric, (b) lateral and (c) lower view. 165
D.2 Position of a target dolphin geometry relative to the base shape after isotropic scale ICP registration. The target geometry is illustrated in its registered position with the target features in red and the base geometry features in blue. (a) Isometric, (b) lateral and (c) lower view. 166
D.3 Feature registration of a base dolphin to the aligned target configuration. The target geometry is illustrated in its aligned position with the target features in red and the deformed base geometry features in blue. Only the registered feature lines on both geometries are shown. (a) Isometric, (b) lateral and (c) lower view. 167

List of Tables

5.1 Some radial basis functions with compact support $f(\xi)$ and global support $f(x)$ 71

6.1 Mesh Quality compared to original mesh generated from the symmetric skull surface. The tetrahedral mesh representations representing the prognathic and orthognathic skull shapes are then improved using MESQUITE [5] with boundary nodes constrained. 107
6.2 Range values for difference in Von Mises Stress. In each case the Von Mises stress result of the analysis of a molar bite on a orthognathic skull representation is subtracted from the same analysis done on a prognathic skull representation per element. 115
6.3 Distances from the nodal coordinates on each mesh representation to (a) the position on the generic surface mesh for surface points and (b) the tetrahedral mesh representing the average skull shape. . . . 117

A.1 Initial muscle forces. (a) Working side force values used and (b) balancing side as a percentage of working side force derived from [57] with equivalent force value. 136
A.2 Temporalis muscle section force distribution. (a) Activity of muscle sections approximated from [15] for a vertical bite force. (b) Nodes in each section and (c) weighted resultant force value. 136
A.3 Prognathic force values and directions. 143
A.4 Orthognathic force values and directions. 144
A.5 Minimum and maximum displacements obtained from finite element analysis for all mastication forces. 153
A.6 Maximum Von Mises stress obtained from finite element analysis for individual mastication forces and full analysis. 153

Chapter 1

Introduction

1.1 Background

The need to find the deformation required to morph one complex geometry into another arose from a study done on the effect of prognathism on masticatory induced stress in the human skull.

Maxillary alveolar prognathism is defined as the percentage relationship between two lines, both with origin at the cranial base (ba) and through the cranial landmark positions of nasion (n) and prosthion (pr). This attribute is characterised by either one or both jaws projecting forward, clearly influencing the general shape of the maxillofacial region of the skeleton. For the location of these landmarks see Figure 1.1.

In the initial study, a comparison is made on results obtained from a finite element analysis on two different skull geometries.

To best compare results, it would be beneficial to have a computational domain for the different skulls that have one-to-one correspondence. If this is possible, even more patient specific geometries could be analysed as part of a complete study on prognathism's effect on masticatory induced stress using domains with one-to-one correspondence.

The principal shape components within a class of geometries, or even the deformation and stress components could be extracted if the same analysis is done using a larger statistical sample with a consistent mapping between them. The difference in stress or displacement from the mean stress and deformation due to prognathism or some other mode of variation could then be compared or calculated due to the

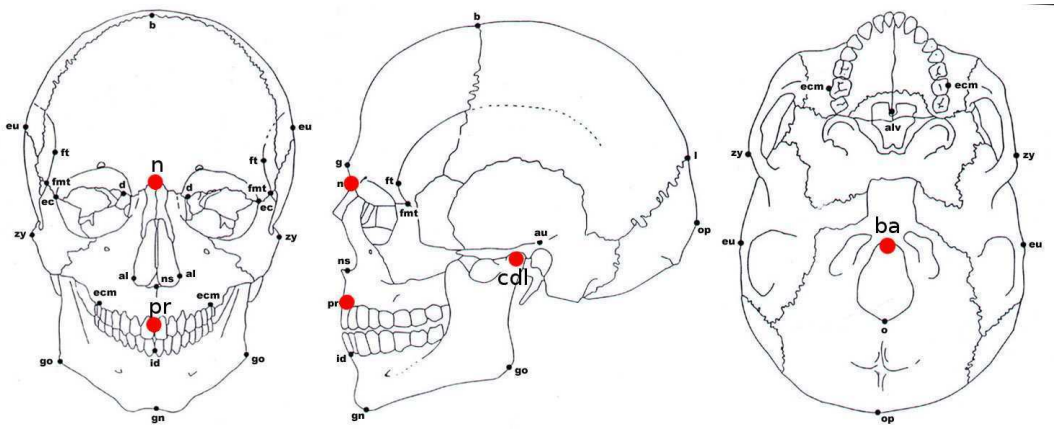

(a) (b) (c)

Figure 1.1: Landmarks on the (a) front, (b) side and (c) bottom of the human skull [43].

existence of this consistent mapping.

Unfortunately one-to-one correspondence of the computational domain generated from extracted geometries, or even alternative designs in the engineering industry, is highly unlikely. An approach to obtain a computational domain that represents various geometries with the exact same mesh size and connectivity between the nodes does however exist. This could be achieved by deforming a generic mesh into that resembling all different geometries in the sample.

This report covers an introductory study to register and deform a generic mesh (also called the base mesh, deformable mesh or model shape) into a representation of a complex target geometry or data shape. Various procedures are investigated, implemented and combined to specifically accommodate complex geometries like that of the human skull.

The procedures implemented have various aspects that still require improvement before the desired study regarding prognathism's effect on masticatory induced stress, could truly be approached pragmatically. Focus is only given to the use of existing procedures while the additional required improvements could be addressed in future work. It is however required that the resulting discretised domain obtained in this initial study be of sufficient quality to use in a finite element analysis (FEA) [24].

UNIVERSITEIT VAN PRETORIA
UNIVERSITY OF PRETORIA
YUNIBESITHI YA PRETORIA

1.2 Outline of Thesis

1.2.1 Chapter 2: Background Work and Problem Statement

The background work involves performing a finite element analysis (FEA) on two skulls. A prognathic and non-prognathic skull form is selected from the University of Pretoria's skull collection. Computed tomography (CT) scans of these geometries are used to construct surface mesh representations. The surfaces are then edited and smoothed before creating tetrahedral meshes for use in the aforementioned FEA. Masticatory induced stress is determined for a bite force on the first molar and first incisor. Resulting stress fields on the different geometries analysed are then compared.

Problems are discussed in drawing conclusions on the resulting stress field due to differences in the analysed geometries. The geometries analysed seem to differ in more ways than prognathism alone. Differences in these geometries are especially visible when comparing the sinuses and internal features. The latter could be as a result of decay.

Suggestions are made on how prognathism's effect on masticatory induced stress could be inspected better. The variation in stress due to prognathism alone would probably require the use of a larger sample of geometries. If it is then possible that a single mesh can be used to appropriately represent the different skull geometries by only updating nodal coordinates, a more rigorous analysis on the variation in stress field due to prognathism can be performed.

Principal modes of variation in human skull geometry can be obtained from a principal component analysis (PCA) [36] on the large data set. Each data shape is represented with different nodal coordinates only. If one of these modes is to represent prognathism, this mode could be identified with the help of medical experts and isolated. The deviation from the stress in the mean skull shape due to this mode can then be determined to better support or contradict the hypothesis.

This hypothesis states that a different stress field is expected in the crania of a human with prognathic[1] facial form when compared to that of a human with orthognathic[2] facial form during a similar cycle of mastication. Bone adapts to mechanical needs and different skull geometries are therefore expected to undergo thickening in different locations.

[1] One or both jaws projecting forward.
[2] Jaws don't project forward giving a flatter facial profile.

UNIVERSITEIT VAN PRETORIA
UNIVERSITY OF PRETORIA
YUNIBESITHI YA PRETORIA

The remainder of the project is focused on investigating the possible registration and deformation of a generic skull geometry to better represent a new target data shape.

1.2.2 Chapter 3: Elastic Surface Registration

Deforming a generic surface into a target configuration is done using elastic surface registration. In the procedure implemented for this report, this involves finding and reducing the difference between two surfaces.

The closest distance form every point on one surface to that on the opposite surface may be used as a similarity measure. Firstly, issues related to a difference in the target and generic shape orientation and scale is addressed. It is then possible to deform the generic surface into a representation of the target shape.

The generic to target closest distance directions and inverse of the target to generic closest distances are used. A deformation field is determined with Gaussian weighted smoothing and applied to the generic mesh. This process is performed iteratively until some requirement on the similarity between the deformed and target mesh is satisfied or no further improvement is possible.

Full registration with the implemented procedure could have undesired results when applying it to a geometry as complex as the skull. The use of feature based registration as an initial deformation before elastic surface registration is mentioned and investigated.

1.2.3 Chapter 4: Geometric Features

Extracting curvature information from a discretised surface representation is investigated and discussed. Areas of the surface can be classified as possible feature rich areas or flat surfaces using this local curvature variation.

Feature points, ridges and valley lines on the surface mesh are automatically extracted. The use of these features in the implemented feature based registration is discussed in Chapter 5.

1.2.4 Chapter 5: Feature Registration

There are different methods that could be used to deform a generic mesh into that closely resembling a target geometry. Varying methods differ in complexity and the

UNIVERSITEIT VAN PRETORIA
UNIVERSITY OF PRETORIA
YUNIBESITHI YA PRETORIA

final accuracy with which they resemble the target. Some of these feature based methods and their usual applications are investigated. The use of landmark points as well as feature lines are discussed.

Landmark Nodes

The simplest method involves manually defining landmark nodes on the generic mesh. The landmarks on other geometries can be obtained by either marking it on the digital geometry or by using a digitising stylus. Alternatively, methods exist to extract and classify landmarks by using differential geometry and shape context histograms.

If a relationship between target and generic landmark coordinates is found, the target coordinates can be scaled, translated and rotated so that the distance between corresponding landmarks are minimised in a least squares sense. The displacement required to deform the generic landmark coordinates into the target configuration is then determined. This displacement is applied using radial basis functions or another mesh movement method to deform the rest of the mesh into an approximate target configuration.

Feature lines

Feature lines can be extracted from surface meshes by applying differential geometry principles. Feature lines or parts thereof on a target shape can be compared with those on a generic surface mesh in order to find possible equivalents. Rigid body movement and a scale factor is applied to the target feature lines. This is done so that the generic features are matched in a least squares sense.

Various techniques can be used in determining the deformation required from the generic to target feature lines. The displacement from an original generic line to the deformed state can be determined. With nodal displacements known, a mesh movement method can be applied to the generic mesh to deform it into an approximate target configuration.

The use of feature lines as an initial coarse registration is implemented and investigated before applying the elastic surface registration procedure. Improved results are obtained for the creation of a symmetric skull from an edited and smoothed mesh compared to the original attempt where feature lines weren't used. Figure 1.2 illustrates the basic concept of combining feature based registration with elastic

UNIVERSITEIT VAN PRETORIA
UNIVERSITY OF PRETORIA
YUNIBESITHI YA PRETORIA

surface registration to deform a generic mesh into a target representation.

Registering a new complex target shape could still present a few problems. This is addressed in the proposed registration procedure. In the proposed combination of procedures, unmatched feature surfaces are automatically discarded prior to surface registration. Higher confidence areas are used in combination with user-selected allowable regions of the surface in an attempt to improve the registration result.

1.2.5 Chapter 6: Proposed Registration Procedure

The proposed registration procedure is a combination of an implemented elastic surface registration and feature line registration procedures. The feature registration is done before surface registration to find matching features. Unmatched features are seen as a possible difference in topology between the generic and target geometry. The reason for this is that an unmatched feature line could possibly be due to a hole in one volume with no equivalent hole in the other.

Features are expanded to contain not only the thresholded lines of curvature, but entire feature surfaces. Registration to an unmatched surface is simply ignored during elastic surface registration. As an example, feature registration is done using only user selected features on the assumed generic skull surface. The unmatched features and associated feature areas on the target can be automatically discarded to reduce the amount of editing needed before registration. This procedure in conjunction with additional user constraints on allowable surfaces are inspected. The procedure still requires further attention on the uniqueness of a registration result for use in eventually registering a larger set of skull geometries.

The Department of Anatomy at the University of Pretoria is in the process of creating a digital database from the skulls in their possession. In future, the registration could be performed on a statistical sample of these geometries. The variation in stress field attributed to individual modes of geometric variation can then be analysed.

The benefits of having meshes with one-to-one correspondence is illustrated in a few examples. This is done with registered representations of the two human skull geometries used in the initial analysis. An FEA is done on symmetric versions of these skulls. By deforming a skull mesh into that of it's mirror image, a symmetrical skull is simply obtained from the average between the original and deformed configuration. The deviation from symmetry in the skull is then removed and the

UNIVERSITEIT VAN PRETORIA
UNIVERSITY OF PRETORIA
YUNIBESITHI YA PRETORIA

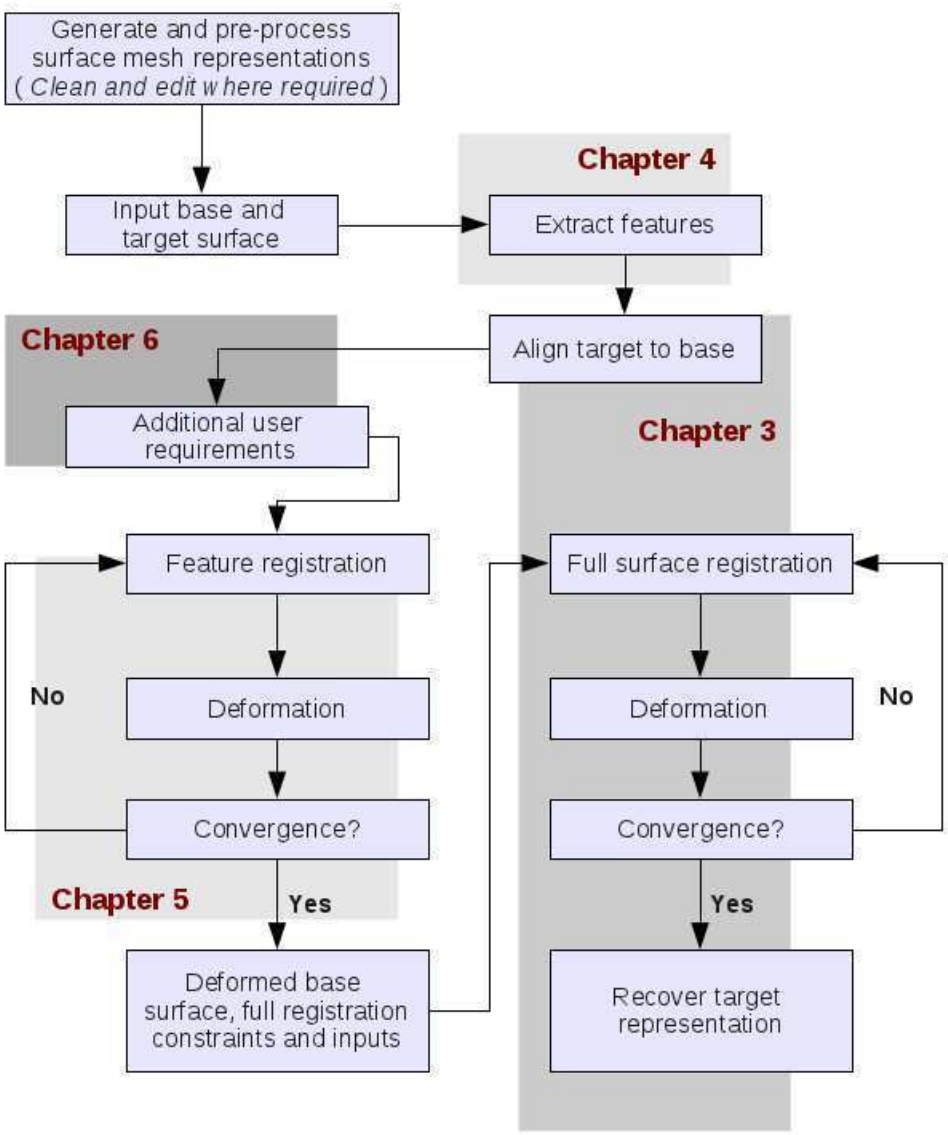

Figure 1.2: Flow diagram illustrating the basic idea of combining feature and surface registration. In the implemented procedure, the result of the feature based registration is used as input and also dictates allowable surfaces used during surface registration.

UNIVERSITEIT VAN PRETORIA
UNIVERSITY OF PRETORIA
YUNIBESITHI YA PRETORIA

stress variation due to this asymmetry can be neglected. By analysing symmetric geometries, the variation in stress is more likely due to the relative degree of prognathism than due to the relative degree of asymmetry.

1.2.6 Chapter 7: Conclusions

Remarks, possible future work and the possible use and application of a reliable registration procedure are discussed in Chapter 7.

Chapter 2

Background Work and Problem Statement

2.1 Introduction

The forces applied through the cycles of mastication are influenced by a variety of factors. The size and strength of masticatory muscles and their attachment to structures within the crania are of importance. The size and form of cranial structures and the location of healthy teeth and gums also have major influence.

To simulate mastication and determine the corresponding stress field, a finite element model can be created and analysed from a digital patient's cranial geometry. This includes decisions made on the appropriate material properties, boundary conditions and imposed loads.

The background work aims to apply the general rules of bone behavior and muscle activity in order to test a hypothesis about a single facial characteristic and is done in collaboration with a Ph.D. student in Anthropology.

The hypothesis of the Ph.D. work states that the location of bone stress in the crania of a prognathic facial form will vary from that in the orthognathic facial form. An attempt to test the hypothesis with the aid of a finite element tool is done with this in mind.

An account of how material properties and boundary conditions are set up in the finite element model for each skull is covered in Appendix A along with some results on the finite element analysis. A broad overview of the initial work done for this study is given in this chapter. This is accompanied by conclusions on how elastic

UNIVERSITEIT VAN PRETORIA
UNIVERSITY OF PRETORIA
YUNIBESITHI YA PRETORIA

registration could help in finding the change in a masticatory induced stress field due to a change in prognathism. If a large enough statistical sample of geometries can be represented with the same mesh, a principal component analysis (PCA) [36] could recover the mode of variation closely linked to prognathism. The variation in stress field due to this mode could be quantified once it is isolated.

2.2 Prognathism in the human skull

Evolutionary biologists and dental practitioners are interested in the history and study of sub-nasal maxillary alveolar prognathism. This attribute is characterised by either one or both jaws projecting froward, influencing the general shape of the maxillofacial region of the skeleton. Upon visual inspection, this is one of the most noticeable morphological characteristics of the human skull.

Maxillary alveolar prognathism is defined as the distance ratio between two lines. These lines both have their origin at the cranial base (ba) and connect this point to the cranial landmarks of nasion (n) and prosthion (pr) positions [14]. The location of these landmarks are highlighted in red on Figure 1.1.

Expressed as a percentage quantity, the distance ratio is termed the gnathic index (GI) and is defined as

$$\mathrm{GI} = \frac{\|\mathrm{pr} - \mathrm{ba}\|}{\|\mathrm{n} - \mathrm{ba}\|} \times 100. \tag{2.1}$$

This index is also termed the alveolar index. Skulls with a gnathic index below 97.9 are orthognathous. Mesognathous skulls have an index between 98 and 102.9 while prognathous skulls have a GI value above 103 [53].

In the study of geometric morphology[1], statistical correlations have been found between various cranial characteristics in modern human skulls. Research has found that prognathic individuals have longer jaws in relation to their cranial base length along with other geometric characteristic [18, 63]. The crania itself is flatter and the foramen magnum[2] is positioned further back. With a decrease in the degree of prognathism, the jaws shorten accompanied by a forward movement of the posterior region of the cranial base. The prognathic facial form can also be linked to a short and lower face height, longer posterior upper, an increase in orbit height and

[1] Statistical analysis of form based on Cartesian landmark coordinates.
[2] Where the spine articulates with the cranial base.

UNIVERSITEIT VAN PRETORIA
UNIVERSITY OF PRETORIA
YUNIBESITHI YA PRETORIA

decrease in orbital breadth [18, 63].

2.3 Mastication

If a prognathic and non-prognathic skull were scaled so that the distance from the jaw hinge to the site of effective muscle attachment is the same, these muscle forces in the prognathic form would have to be larger than that of the non-prognathic form to exert the same incisal bite force. This is due to the relative distance from the jaw hinge and muscle attachments to the position of the applied bite force.

The masticatory system is made up of various bone structures, muscle fibres and other tissue types with a wide range of differing properties and effects. When using an FEA toolkit to simulate mastication, the detail with which these material properties and boundary conditions are modelled could dramatically affect the accuracy.

Attention is given to previous studies where mastication is simulated using primate skull geometries. The mandible, which is attached to the skull itself through the temporomandibular joint (TMJ), acts as a lever during mastication. The distance from the bite force on the tooth to the TMJ (approximately at the (cdl) landmark in Figure 1.1) and the relative muscle attachments result in a different applied force for the prognathic and orthognathic skull form.

2.3.1 Teeth

The forces of mastication change in magnitude throughout the dental arcade. Posterior teeth where the larger possible bite force occurs have a greater occlusal surface area. The location of the molars in closer proximity to the masseter and medial pterygoid muscles create a greater force at this location [48].

The periodontal ligament and alveolar bone surrounding the teeth at the load bearing point also dictate what force is exerted. Using a feedback loop from receptors that monitor stress, teeth are protected from potentially damaging forces [46].

2.3.2 Bone

Like other tissues, bone has the ability to change and repair. It functions as the framework for mobility and also acts as support, protection and the body's calcium

UNIVERSITEIT VAN PRETORIA
UNIVERSITY OF PRETORIA
YUNIBESITHI YA PRETORIA

reserve. Bones contain the cells responsible for bone formation (osteoblasts) and bone resorption (osteoclasts). During remodelling, osteoblasts deposit bone as a result of high strain while osteoclasts reabsorb bone due to decreased strain signals [66].

Specific adaptations in bone morphology vary throughout the skeleton. This depends on the composition of compact and cancellous bone, anatomical location and the specific function of a particular bone. Cancellous bone is first to react to the change in mechanical needs and undergoes a greater change in density while cortical bone experiences prolonged change [56].

Bone structures in the craniofacial area serve in part to accommodate and support the stresses created during the cycles of mastication [67]. A particular study [55] focused on temporal bone variation subject to climate changes. In this study Smith *et al.* noted that neural evolution and mechanical stresses caused by the availability of certain foods also played a role in the observed variation.

Some researchers have claimed that the roll of mastication forces acting on the skull dictates skull shape more than any other external force [49]. The muscles of mastication change with force and intensity and the skull is thought to be optimised to meet the mechanical needs during feeding. The skull is presumably thicker in certain areas to accommodate masticatory induced stress.

The variation in stress due to prognathism in the facial form is therefore assumed to result in a difference in bone mass within certain areas of the facial structure.

2.3.3 Muscles

Masticatory muscles have corresponding skeletal attachments on the skull, maxilla, and mandible. Each of these muscles act on the underlying bone to create a required bite force.

The strength with which muscle forces are applied is dictated by several factors. Some of these factors include muscle fibre length, sacromere length and the directional orientation of the fibres themselves [16]. The temporalis muscle, masseter muscle and medial pterygoid are used in the elevation of the mandible [30]. These muscles act on the mandible during the cycles of mastication and are modelled in this report. The masseter muscle is divided into the deep and superficial portions. The approximate position of the muscles modelled are described below with reference to Figure 2.1:

UNIVERSITEIT VAN PRETORIA
UNIVERSITY OF PRETORIA
YUNIBESITHI YA PRETORIA

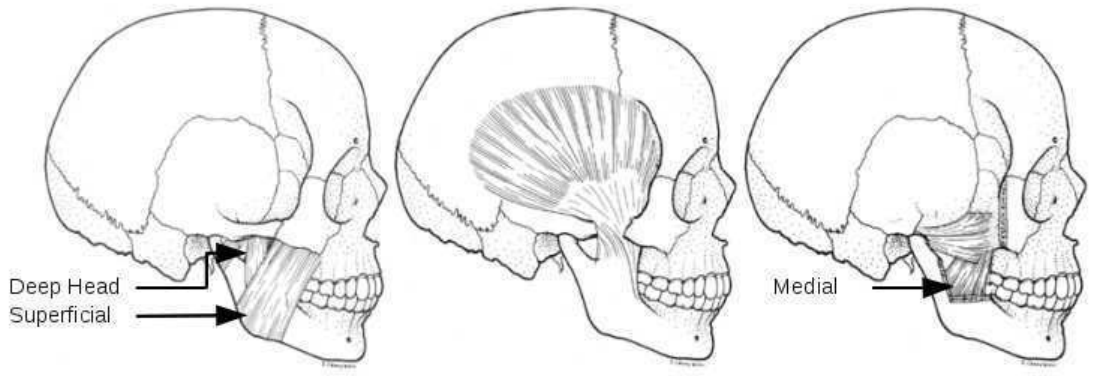

(a) (b) (c)

Figure 2.1: Masticatory muscles [12]. (a) Masseter, (b) Temporalis and (c) the lateral and medial Pterygoid.

- The superficial masseter originates at the anterior and inferior $^2/_3$ margin of the zygomatic arch and inserts at the angle of the mandible. This muscle is the front most muscle visible in Figure 2.1 (a)
- The deep head masseter originates on the posterior $^1/_3$ of the medial surface of the zygomatic arch and inserts at the ramus of the mandible [30]. This muscle is illustrated as the two sections of the inner muscles visible in Figure 2.1 (a)
- The temporalis muscle characterised by its fan shape encompasses the temporal fossa on the lateral sides of the skull and inserts on the coronoid process of mandible. It is divided into an anterior portion and shallower posterior region [16, 30]. This muscle and it's attachment to the mandible is visible in Figure 2.1 (b)
- The medial pterygoid muscle used in jaw elevation has an origin at the pterygoid fossa of the sphenoid bone and inserts at the angle of the mandible on the medial side [30]. The lateral pterygoid is the muscle that attaches at the TMJ position in Figure 2.1 (c) with the medial pterygoid attached lower on the mandible.

2.4 Finite Element Model

A brief overview of the finite element model used in analysing the two skull forms for masticatory induced stress field is given in this chapter while the reader is referred

UNIVERSITEIT VAN PRETORIA
UNIVERSITY OF PRETORIA
YUNIBESITHI YA PRETORIA

to Appendix A for additional detail.

2.4.1 Geometries

Considering that the reason for this study is a validation on the adaptation of skull form to minimise internal stress due to mastication, two skulls were selected for analysis based on gnathic index and sufficient dentition from the University of Pretoria skull collection [39]. A skull with a gnathic index of 106.9 is used to represent a prognathic facial form and a skull with a gnathic index of 91.5 represents the orthognathic facial form in the work done.

Taking into account that exact stress values aren't required and that this study is mainly concerned with the variation in stress pattern, a four noded tetrahedral finite element mesh was created from the digital surface representation of these skull forms using TetGen [9].

2.4.2 Material Properties

Significant variation in material properties have been documented for a range of different bones and within different areas of the same bone structure [47]. The anisotropic nature of bone and how to model it however is not the focus of this research.

Tetrahedral finite element meshes were imported into PreView [7] to set up the model. This is done by defining material properties and boundary conditions. For similar analyses done in literature, isotropic bone material properties have been reported to produce realistic stress patterns [17, 20, 32, 35, 38, 60].

The Young's modulus and Poisson's ratio used in this study was taken from literature to be 16 GPa and 0.3 [17, 20, 32, 35, 38, 50, 60].

2.4.3 Boundary Conditions

FEBio [3], a solver developed specifically for biomechanic finite element applications is used in performing this study. Although this allowed for muscles and tendons to be modelled using an array of element types, it was decided that the forces of mastication would be modelled as external forces on the available skull geometries. These forces are applied to nodes in the region representing the approximate sites of muscle attachment described previously with the help of Figures 2.1 and 2.2.

UNIVERSITEIT VAN PRETORIA
UNIVERSITY OF PRETORIA
YUNIBESITHI YA PRETORIA

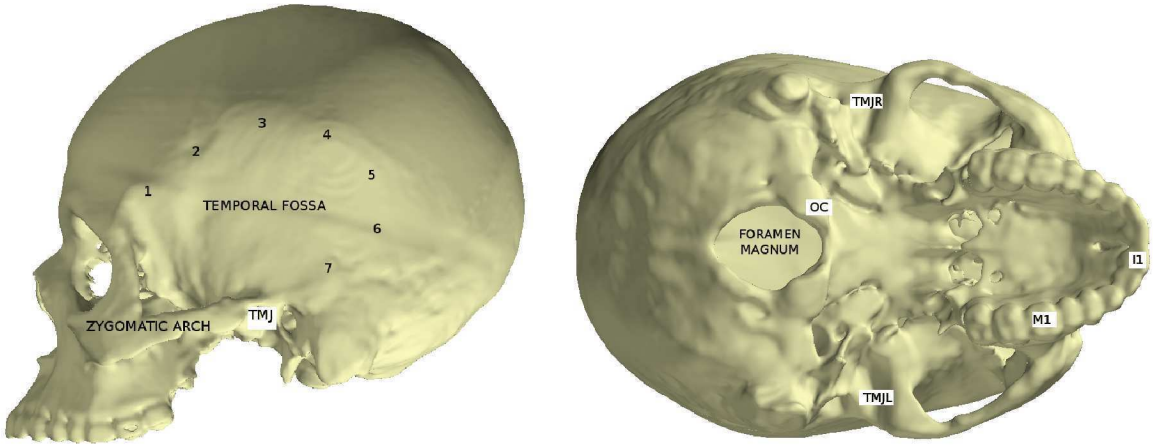

(a) (b)

Figure 2.2: Boundary condition positions on the skull. (a) Lateral view of the prognathic skull indicating the Temporal fossa and zygomatic arch (cheek bone). The jaw hinge or temporomandibular joint is indicated by TMJ and the seven sections of the temporalis muscle attachment positions are indicated by numbers 1 through 7. (b) Inferior view of the prognathic skull. The location of boundary constraints are the occipital condyles (OC) on the foramen magnum. Reaction forces are determined at the left and right temporomandibular joints (TMJL and TMJR) and either the first molar (M1) or first incisor (I1) for the applied muscle forces when balancing the system.

UNIVERSITEIT VAN PRETORIA
UNIVERSITY OF PRETORIA
YUNIBESITHI YA PRETORIA

Muscle force values are first approximated for a vertical bite force on the first incisor and first molar. These teeth are visible as I1 and M1 in Figure 2.2. Muscle action during the cycles of mastication are different for working and balancing sides. For this stress simulation the left side of the skull is chosen as the working side of the dental arcade where bite force is applied. Here force values used are determined from literature [64] while force scaling factors on the right side are obtained from a study on muscle activity during mastication [57].

Mastication is an internally balanced system. Keeping this in mind, a system of equations is set up and solved to obtain the bite force at the tooth and reaction forces at the temporomandibular joint (TMJ) for each skull model. In doing so a number of assumptions are made and the problem is considered as a rigid body under static loading. The model was constrained in the region of the foramen magnum at the occipital condyles in all six degrees of freedom to prevent rigid body movement. These locations on the skull and an accompanying short description is also visible in Figure 2.2.

For further information on setting up and solving the system of equations, as well as a free body diagram, the reader is referred to Appendix A and Figure A.1 in particular.

Both skulls are treated similarly and several finite element analyses were run for both incisal and molar bite using FEBio [3]. Muscle forces with their balancing reaction forces are applied as boundary conditions with the nodal coordinates of the occipital condyles at the foramen magnum constrained. Figure 2.3 shows the applied muscle forces and reaction forces obtained for a full molar bite in such a way that the system is balanced for both prognathic and orthognathic skull form.

Post processing and visualisation is done using PostView [6]. Using the boundary conditions obtained from the static analysis displayed in Figure 2.3, the results of a linear elastic finite element analysis on these skull forms for a molar bite can be seen in Figure 2.4 (a) and (b). The full incisor bite resultant Von Mises stress field is also visible in Figure 2.4 (c) and (d) with further examples in Appendix A.

2.5 Results

Comparing the results of the finite element analyses on the two skull forms present a few problems. These skull forms could have other differences in form not correlated to only the gnathic index. This is undesired when drawing conclusions on the effect

UNIVERSITEIT VAN PRETORIA
UNIVERSITY OF PRETORIA
YUNIBESITHI YA PRETORIA

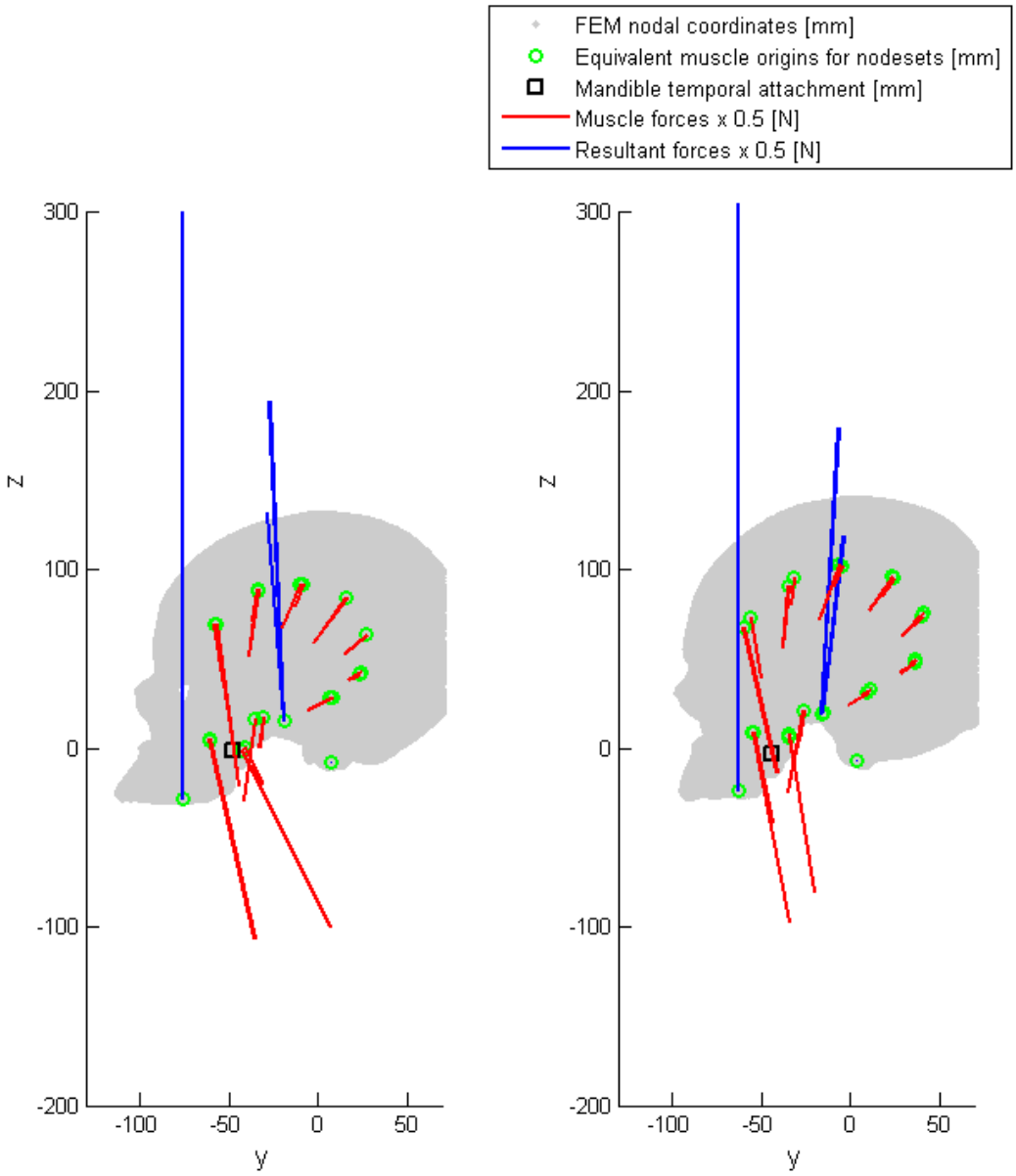

Figure 2.3: Muscles and reaction forces on (a) the prognathic skull form and (b) orthognathic skull form for a vertical molar bite.

UNIVERSITEIT VAN PRETORIA
UNIVERSITY OF PRETORIA
YUNIBESITHI YA PRETORIA

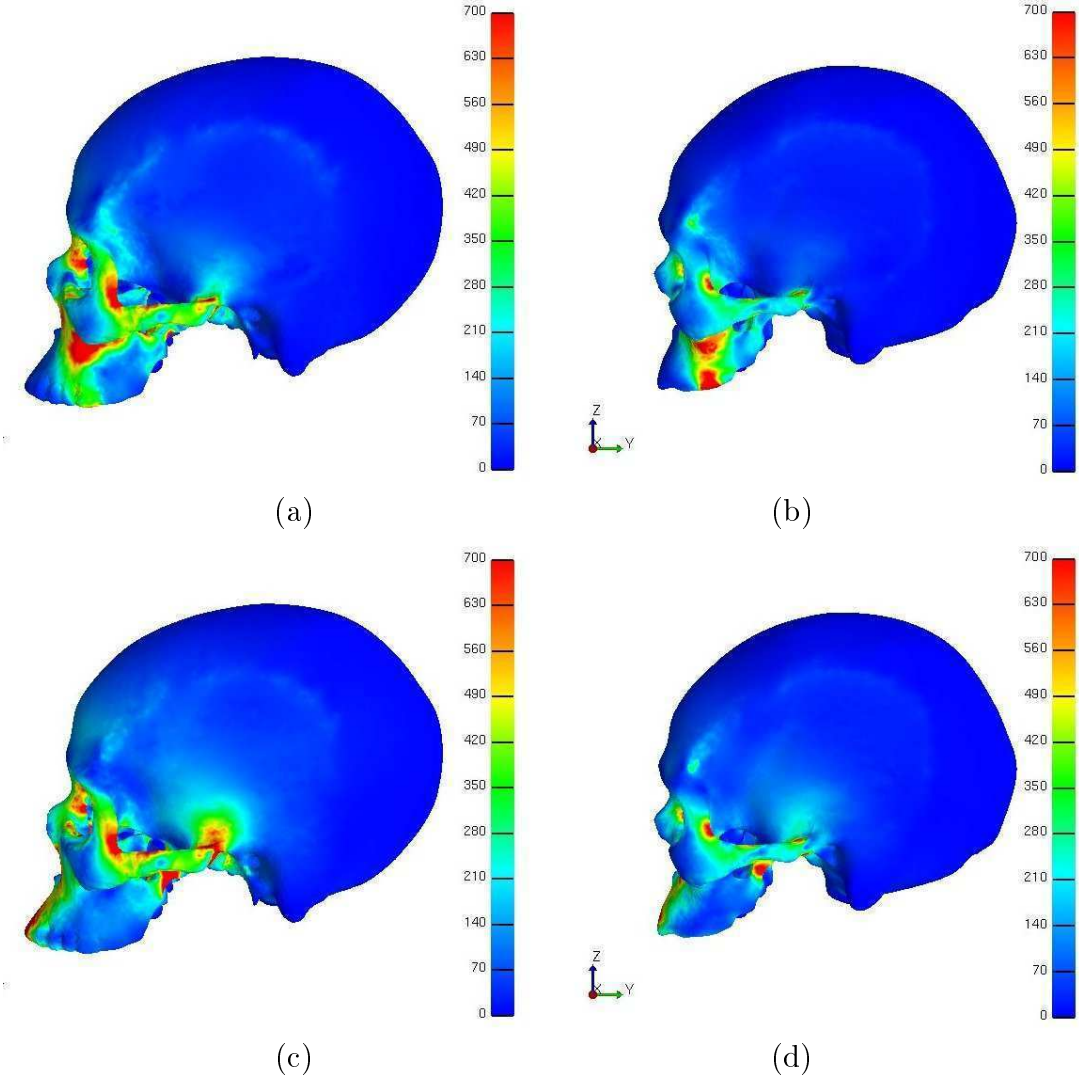

Figure 2.4: Lateral view of the working side Von Mises stress for a molar bite on the (a) prognathic and (b) orthognathic skull form as well as for an incisor bite on the (c) prognathic and (d) orthognathic FEA. The units of the stress contours are in N/cm^2.

UNIVERSITEIT VAN PRETORIA
UNIVERSITY OF PRETORIA
YUNIBESITHI YA PRETORIA

(a) (b)

Figure 2.5: Semi-transparent view of the (a) prognathic and (b) orthognathic skull form.

of only prognathism on the resultant masticatory stress.

The skull geometries used vary in more ways than is desired. Due to decay and the presence of features or bone volume in one skull that is not present in the other, an unbiased comparison can't be ensured. Some of these differences in the original geometries are illustrated in Figures 2.5 through 2.7.

In Figure 2.5, the skull forms are displayed with semi-transparency. Despite the difference in the presence of teeth, the sinuses are seen to have vastly different form and volume. Figures 2.6 and 2.7 show cuts made through the geometry to view the boundary surfaces. From these cuts it is visible that although these skull forms are shaped differently in areas as expected, they seem to have endured varying bone loss in different areas.

To do the finite element analyses in this chapter, the skull geometries have been processed, cleaned and smoothed manually and independent of one another. For this reason it is possible that additional variation between the geometries could also be present due to slightly different fixing and smoothing strategies. In addition, the current results can only be compared visually, which is an unfortunate problem. A more rigorous comparison could be obtained if it is possible to have the same mesh

UNIVERSITEIT VAN PRETORIA
UNIVERSITY OF PRETORIA
YUNIBESITHI YA PRETORIA

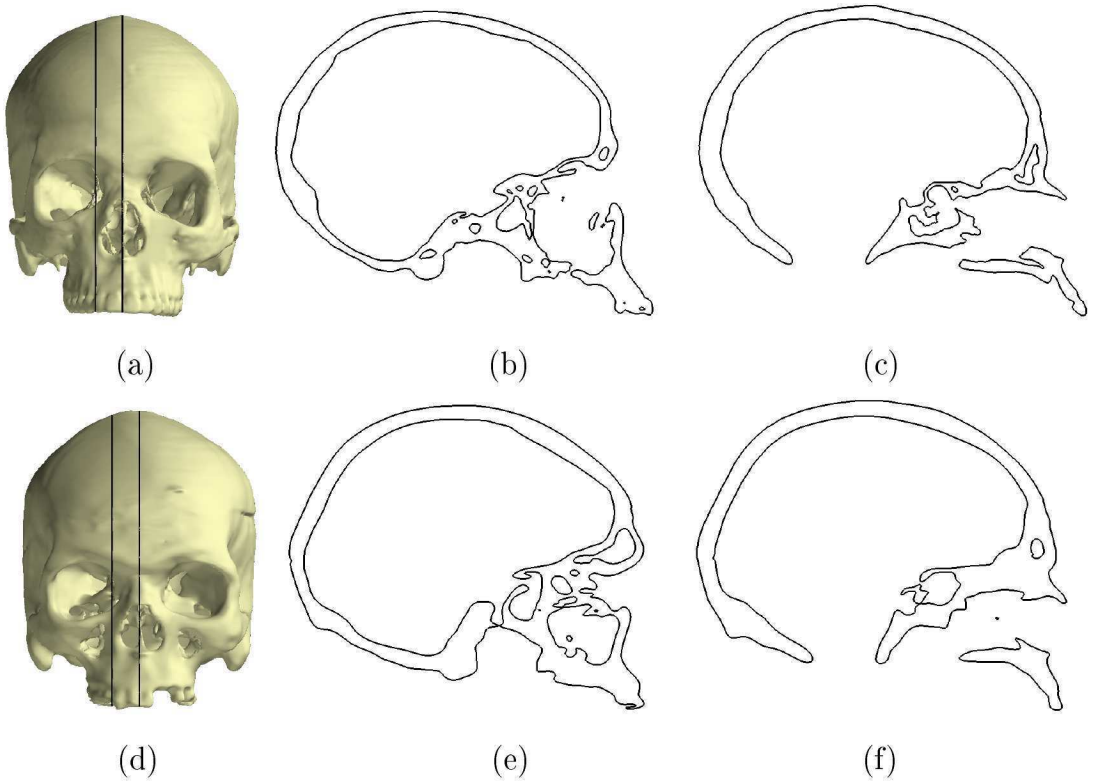

Figure 2.6: Lateral cut views through the two skulls to illustrate the difference between their boundary surfaces. (a) Location of the cut planes in (b) and (c). (d) Location of the cut planes (e) and (f).

UNIVERSITEIT VAN PRETORIA
UNIVERSITY OF PRETORIA
YUNIBESITHI YA PRETORIA

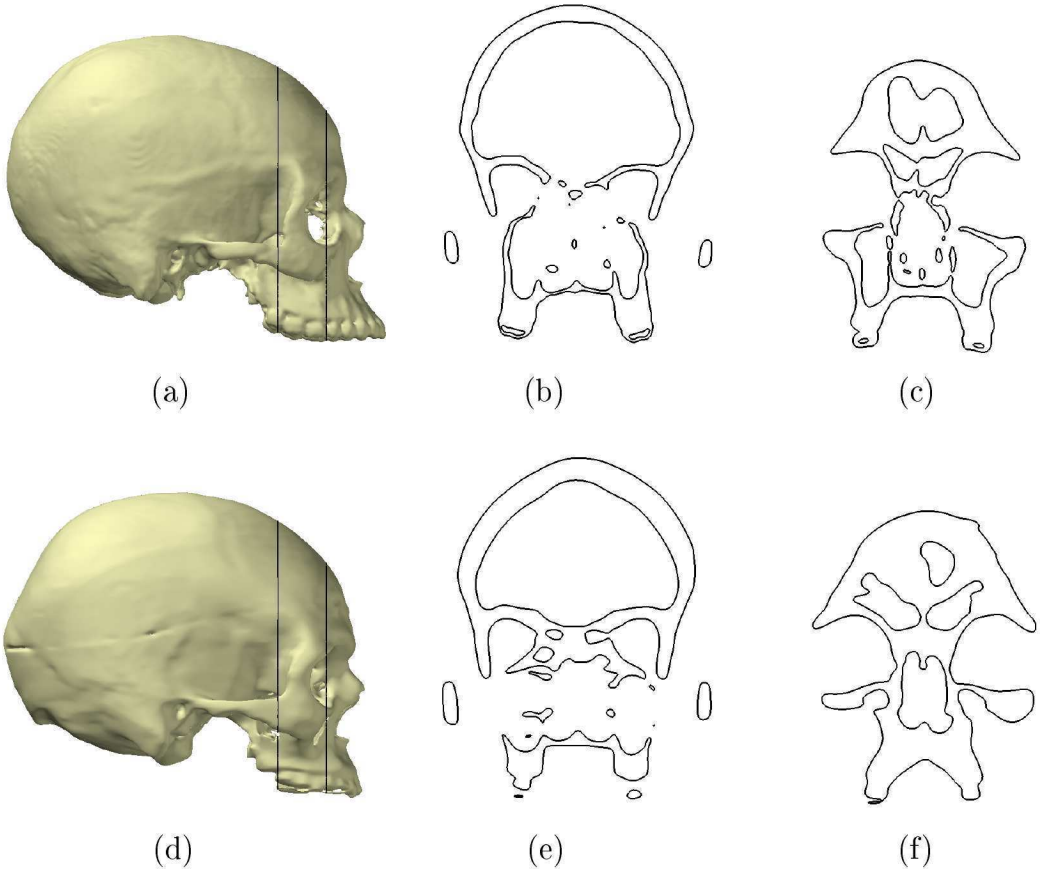

Figure 2.7: Frontal cut views through the two skulls to illustrate the difference between their boundary surfaces. (a) Location of the cut planes in (b) and (c). (d) Location of the cut planes (e) and (f).

UNIVERSITEIT VAN PRETORIA
UNIVERSITY OF PRETORIA
YUNIBESITHI YA PRETORIA

analysed with only updated nodal coordinates to represent the difference in form.

Similar work on comparing different geometries have been performed. In Bryan *et al.* [19] for example, 46 femur geometries were modelled using the same updated mesh. From these 46 training geometries, a statistical model ready for use in a finite element analysis was created. Inter-patient variability was illustrated as the principal components of shape and variable material property. The first three modes of variation obtained in their experiments in form and material property are illustrated in Figure 2.8.

Stress and strain fields resulting from finite element analyses on such registered geometries or variation in stress due to a specific principal mode of variation could also be done. Based on the problems and shortcomings in comparing the finite element results in the initial work, it was decided that the rest of the work for the author's masters degree be approached as an introduction into elastic registration.

Again referring to Figures 2.6 and 2.7, it appears that the prognathic skull has lost more internal detail than the orthognathic skull while other features present in the prognathic skull have no equivalent in the orthognathic skull. This vast difference restricts the accuracy with which one skull could be deformed to represent the other geometry.

2.6 Problem Statement

The development of a tool for use in obtaining a better result to conclude or inspect the validity of the hypothesis stating prognathism's effect on masticatory induced stress is sought. Adequately deforming a generic skull shape into that of a different patient geometry should allow the registration of a statistical sample of skulls.

The use of a single finite element mesh with different nodal coordinates to represent each data shape in the statistical sample would be of great use. If this is achievable, all shapes in the sample set can be represented by simply updating the nodal coordinates of the generic mesh. The baseline mesh could then be created using the mean nodal coordinates and an analysis on the mean skull form could be used as the baseline stress field.

Doing a principal component analysis[3] (PCA) on the registered coordinates of the statistical sample would produce the principal modes of variation in this set. If

[3]Statistical analysis to determine the principal modes of variation in a data sample [36].

UNIVERSITEIT VAN PRETORIA
UNIVERSITY OF PRETORIA
YUNIBESITHI YA PRETORIA

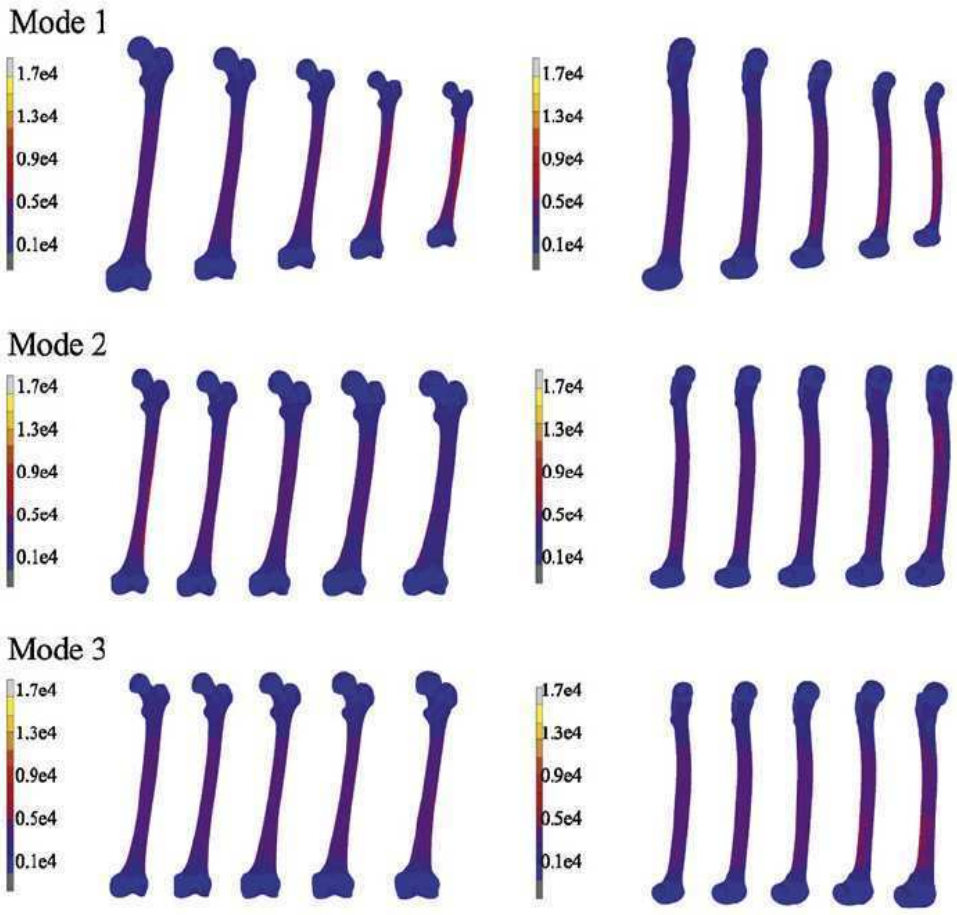

(a) (b)

Figure 2.8: First three modes of a principal component analysis done on the human femur varied between ±3 standard deviations. This is done after 46 different femur geometries are represented using the same mesh with only updated nodal coordinates [19]. (a) Frontal and (b) lateral view.

UNIVERSITEIT VAN PRETORIA
UNIVERSITY OF PRETORIA
YUNIBESITHI YA PRETORIA

a principal mode of variation in the group of skulls is linked to prognathism, the affect of this mode on the baseline stress field can be obtained to either support or disprove the hypothesis.

The aim of the work done in the development of a tool for elastic surface registration on skull geometries are outlined:

- A deformed version of the chosen generic skull mesh should adequately represent the target geometry for use in a finite element analysis.
- Different form representations should be obtained with as little user input as possible.
- Scale effects should be taken care of as far as possible if only a few skulls are available. When comparing the stress variation between two skulls for example, it is undesired that the variation be attributed to a difference in scale. If many skulls are available this would not be a problem. Performing PCA on a larger statistical set of related geometries should isolate scale as one of the principal modes of variation. Scale is visible as the first mode of variation in the sample of femur geometries in Figure 2.8.

Chapter 3

Surface Registration

When matching a reference geometry onto a target geometry it is important to firstly take into account their difference in scale and orientation. After a rigid registration is performed, a consistent deformation of the generic geometry is required to best represent that of the target.

A selected registration technique is discussed in this chapter. This is done aimed at deforming an unstructured mesh of complex geometry into a target configuration by only updating nodal coordinates. The final goal of the registration procedure is to deform a generic digital patient geometry or atlas into that of others in a statistical set. With this in mind the difficult subject of closely similar geometries with slightly different topology is also addressed and investigated in subsequent chapters.

Rigid registration is first discussed using a modified iterative closest point (ICP) procedure reformulated from the original method proposed by Besl and McKay [13]. After aligning the target geometry with a generic mesh, elastic surface registration is addressed as used by Bryan *et al.* [19]. In [19], 46 femur geometries were registered in an attempt to create a statistical model ready for use in finite element analysis. After successful registration, inter-patient variability was illustrated as the principal components of shape and material property.

The selected elastic surface registration procedure is applied to a few sample problems. A test case is done on two femur geometries to first inspect how one geometry can be aligned to the other using the reformulated ICP procedure. The elastic registration procedure is then applied to deform one femur mesh to represent the other by updating nodal coordinates only. The femur registration is also used

UNIVERSITEIT VAN PRETORIA
UNIVERSITY OF PRETORIA
YUNIBESITHI YA PRETORIA

to perform an analysis on the sensitivity to user controlled parameters.

Another test case is performed aimed at creating a symmetric skull surface. This symmetric mesh is created from a cleaned skull mesh with all of the teeth present and is intended for use as the generic shape in the final registration example of this project. Problems in performing this registration procedure to obtain the symmetric smooth skull is discussed briefly. In addition, the effect of user inputs on the registration result is inspected and assumptions made on what is needed to perform elastic registration on the skull geometries.

Considering the inadequate registration on geometries of this complexity and the non-unique results produced using only the selected procedure, conclusions are drawn to investigate other registration techniques. These techniques could then be applied in conjunction with the implemented elastic surface registration procedure. The possibility is discussed to improve the surface registration by including a more formal process for feature matching and registration. The issue of obtaining a unique registration result is discussed briefly and it is decided to retain the implemented registration procedure with the same parameters as used by Bryan *et al.* [19]. Further improvement to the registration procedure to obtain optimum results could be inspected in future work and is not addressed in this report.

3.1 Point Set Registration

The registration of point sets is an important issue in pattern recognition and computer vision. One of the most common methods for rigid registration is the Iterative Closest Point (ICP) algorithm [13]. This algorithm is widely used in some form or other and has been studied and improved by many researchers.

Modified versions of the ICP algorithm attempt anisotropic scaling in addition to rotation and translation. One such method [28] is discussed in this section and implemented.

3.1.1 The Iterative Closest Point Algorithm

The problem of obtaining a rigid transformation in point set registration is approached by Besl and McKay [13] as a least squares problem. For two overlapping point sets in $\mathbb{R}^m$, a rigid registration between two $m-D$ point sets aims to find the translation and rotation required to best align a data shape to the base or generic

UNIVERSITEIT VAN PRETORIA
UNIVERSITY OF PRETORIA
YUNIBESITHI YA PRETORIA

shape.

Suppose the data and generic shape point sets are given as $\mathcal{P} \triangleq \{\mathbf{p}_i\}_{i=1}^{N_p}$ and $\mathcal{M} \triangleq \{\mathbf{m}_j\}_{j=1}^{N_m}$. The ICP algorithm involves performing a least squares optimisation problem where an applied transformation T is sought to best align $\mathcal{P}$ to $\mathcal{M}$:

$$\min_{T, j \in \{1,2,\ldots,N_m\}} \left(\sum_{i=1}^{N_p} \|T(\mathbf{p}_i) - \mathbf{m}_j\|_2^2 \right). \tag{3.1}$$

In the original ICP procedure, this transformation is made up of a rotation matrix and translation vector so that the least squares optimisation problem becomes:

$$\min_{\mathbf{R}, \mathbf{t}, j \in \{1,2,\ldots,N_m\}} \left(\sum_{i=1}^{N_p} \|(\mathbf{R}\mathbf{p}_i + \mathbf{t}) - \mathbf{m}_j\|_2^2 \right), \tag{3.2}$$

such that:

$$\mathbf{R}^T\mathbf{R} = \mathbf{I}_m, \quad \det(\mathbf{R}) = 1,$$

where $\mathbf{R} \in \mathbb{R}^{m \times m}$ is a rotation matrix and $\mathbf{t} \in \mathbb{R}^m$ a translation vector. In performing the registration, the ICP method involves iteratively performing two steps. For a k^{th} iteration:

- A correspondence is first built up between the two point sets. The correspondence for point $\mathbf{p}_i$ in the data set is given by

$$c_k(i) = \underset{j \in \{1,2,\ldots,N_m\}}{\arg\min} \left(\|(\mathbf{R}_{k-1}\mathbf{p}_i + \mathbf{t}_{k-1}) - \mathbf{m}_j\|_2^2 \right), \quad i = 1, 2, \ldots, N_p. \tag{3.3}$$

This could be done by using a $k-d$ tree nearest neighbour search algorithm to determine the closest point on the model shape.

- A rotation and translation is then determined from

$$(\mathbf{R}_k, \mathbf{t}_k) = \underset{\mathbf{R}^T\mathbf{R} = \mathbf{I}_m, \det(\mathbf{R}) = 1, \mathbf{t}}{\arg\min} \left(\sum_{i=1}^{N_p} \left\|(\mathbf{R}\mathbf{p}_i + \mathbf{t}) - \mathbf{m}_{c_k(i)}\right\|_2^2 \right), \tag{3.4}$$

  and applied to $\mathcal{P}$ before performing another iteration.

The ICP procedure was modified by Du *et al.* [28] to perform affine iterative transformations. The transformation, T, in Equation (3.1) now consists of reflection, rotation and anisotropic scale matrices as well as a translation vector. With the translation vector easily determined and the use of lie groups and lie algebra, the

ICP problem is reformulated as in Appendix B in such a way that the optimisation problem is iteratively performed subject to 9 variables. This results in the k^{th} iteration constrained optimisation problem written in the form

$$\varepsilon = \min_{\mathbf{c}} \quad \sum_{i=1}^{N_p} \left\| \mathbf{U}_{k-1} \left(\mathbf{I} + \sum_{j=1}^{N_r} u_j \mathbf{E}_j \right) \mathbf{S}_{k-1} \left(\mathbf{I} + \sum_{j=1}^{N_s} s_j \mathbf{D}_j \right) \times \mathbf{R}_{k-1} \left(\mathbf{I} + \sum_{j=1}^{N_r} r_j \mathbf{E}_j \right) \mathbf{p}_{\mathbf{t}i} - \mathbf{m}_{\mathbf{t}i} \right\|_2^2 \tag{3.5}$$

with $\mathbf{c} \triangleq \{u_1, ..., u_{N_r}, s_1, ..., s_{N_s}, r_1, ..., r_{N_r}\}^T$ consisting of N_r reflection, N_s scale and N_r rotation variables. $\mathbf{U}_{k-1}$, $\mathbf{S}_{k-1}$ and $\mathbf{R}_{k-1}$ are the reflection, rotation and anisotropic scale matrices applied at the previous iteration of the procedure. Only an update to these matrices is found iteratively to better align the data set to the generic shape. This is done using the linearised basis $\mathbf{E}_j$ of the special orthogonal group representation discussed in Section B.2. $\mathbf{D}_j$ is the set of bases of a diagonal matrix with the only non-zero entries at $D_{jj} = 1$.

Application

The affine iterative closest point procedure as outlined in this chapter was implemented in Python [8]. The elastic surface registration procedure used by Bryan *et al.* [19] is applied to the registration of femur geometries in their article. For this reason, two femur surface meshes are obtained from the INRIA model shape repository [4] to illustrate the accurate implementation of this procedure.

One of the femur geometries obtained is from a right and the other from a left femur. The one femur is first reflected so that both represent the same side. The one model's axis is then transformed so both femur shapes are approximately aligned.

Before performing the rigid registration on the femur geometries, both models were translated so their nodal center lay on the origin of the Cartesian coordinate axis. This position is then used as the starting position for registration, as seen in Figure 3.1 (a) and 3.2 (a). From this starting position, the following two rigid registrations are performed:

- The first registration is applied only allowing rotation and translation. For this procedure, all three scale variables are constrained at a value of 1.

UNIVERSITEIT VAN PRETORIA
UNIVERSITY OF PRETORIA
YUNIBESITHI YA PRETORIA

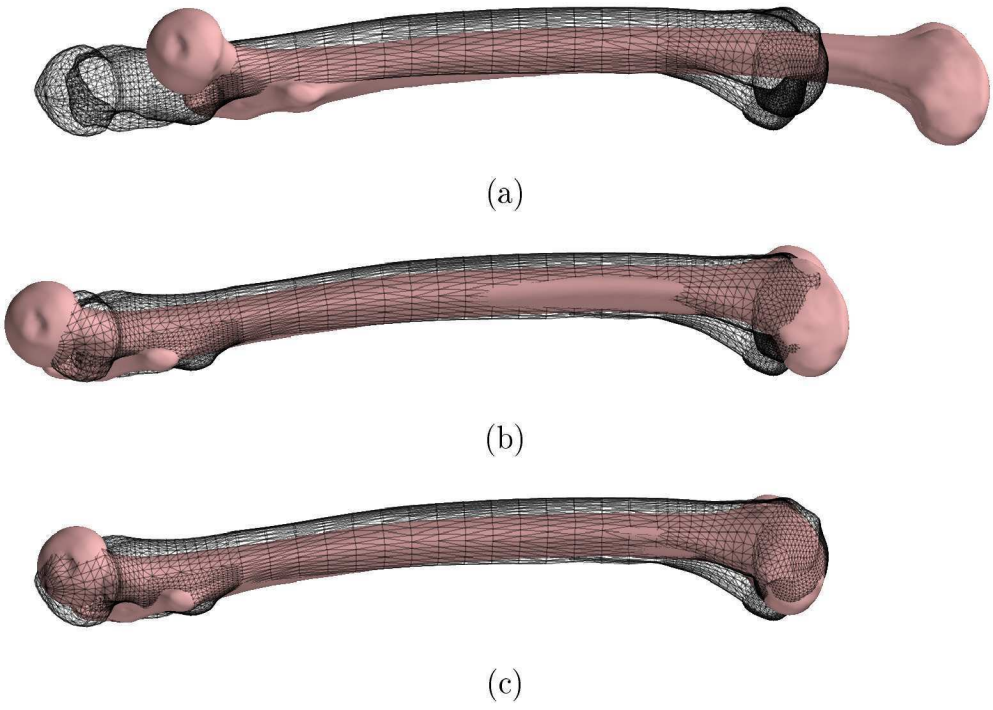

(a)

(b)

(c)

Figure 3.1: Lateral view of rigid registration results on two femur geometries obtained from the INRIA shape repository [4]. (a) Initial relative position and alignment of the two femurs. From this starting position, the rigid registration result is obtained by ICP for (b) rotation and translation only and (c) allowing isotropic scaling in addition to rotation and translation.

UNIVERSITEIT VAN PRETORIA
UNIVERSITY OF PRETORIA
YUNIBESITHI YA PRETORIA

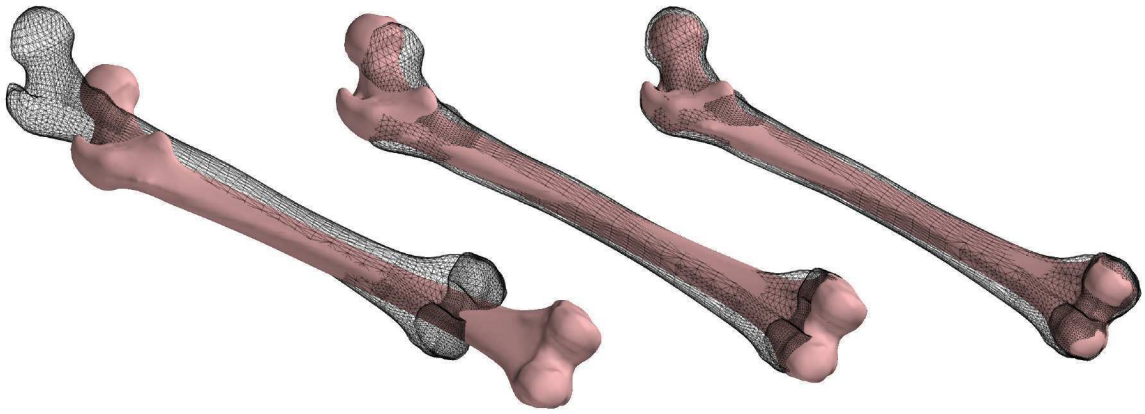

(a) (b) (c)

Figure 3.2: Isometric view of rigid registration results on two femur geometries obtained from the INRIA shape repository [4]. (a) Initial relative position and alignment of the two femurs. From this starting position, the rigid registration result is obtained by ICP for (b) rotation and translation only and (c) allowing isotropic scaling in addition to rotation and translation.

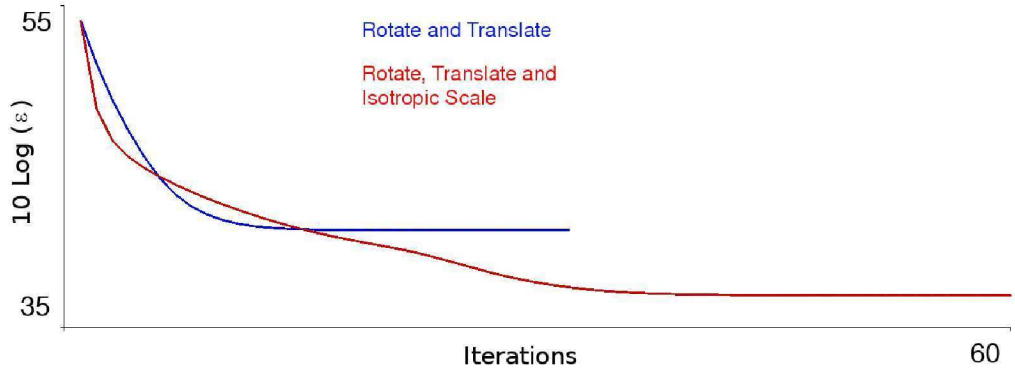

Figure 3.3: Convergence rate of the ICP. The blue line is obtained when only allowing rotation and translation while the red line is the convergence rate when rotation, translation and isotropic scale is allowed. At each iteration, ε is the function value after performing the least squares optimisation in Equation (3.5).

UNIVERSITEIT VAN PRETORIA
UNIVERSITY OF PRETORIA
YUNIBESITHI YA PRETORIA

- The second registration is performed using an isotropic scale affine ICP with scale variables constrained to be within the bounds $[0.7, 1.2]$. These bounds were selected arbitrarily for this example and the optimisation is done with the additional requirement that all scale variables be equal.

The results of these rigid registrations on the femur geometries are visible in Figures 3.1 and 3.2. Anisotropic scaling is not considered in this report as the actual shape of the target should remain unchanged. The convergence rates of the affine ICP and isotropic scale affine ICP results of Figures 3.1 and 3.2 are visible in Figure 3.3.

3.2 Elastic Surface Registration

The elastic surface registration procedure of Moshfeghi *et al.* [44] as implemented and improved by Bryan *et al.* [19] is discussed in this section. They used this registration procedure to analyse the performance of orthopaedic implants while accounting for inter-patient variability in bone quality and geometry.

The creation of a three dimensional, statistical, finite element analysis ready model of a femur was achieved by Bryan *et al.* [19] via a registration scheme based on elastic surface matching and mesh morphing.

Establishing a correspondence between each member of the training set requires initially registering a common baseline mesh to each femur model surface. To do this, the target geometries are first aligned to the generic model using an ICP procedure [13]. After rigid registration is performed, surface matching iteratively deforms the baseline mesh vertices to better match the target surface.

In the registration procedure used by Bryan *et al.* [19], a smooth and accurate final mesh is obtained through user defined inputs that control the magnitude and speed of deformation. The registration is refined at each iteration through these user specified parameters. Initially the deformations have greater support, roughly aligning the surfaces before decreasing the support radius for finer local mesh deformations.

3.2.1 Registration Procedure

The elastic surface registration as used by Bryan *et al.* [19] is outlined in this subsection. Two meshes are taken as an input with $\mathcal{M}$ the generic surface and

UNIVERSITEIT VAN PRETORIA
UNIVERSITY OF PRETORIA
YUNIBESITHI YA PRETORIA

$\mathcal{P}$ the target surface. These two meshes don't have to have the same number of degrees of freedom or connectivity. The generic surface is deformed iteratively to better represent the target geometry without its connectivity being affected.

The data and generic surface mesh is represented as

$$\mathcal{P} \triangleq \left\{ \left\{ \begin{array}{ccc} x_{p_i} & y_{p_i} & z_{p_i} \end{array} \right\}_{i=1}^{N_p}, \{\triangle_c\}_{c=1}^{T_p} \right\} \tag{3.6}$$

and

$$\mathcal{M} \triangleq \left\{ \left\{ \begin{array}{ccc} x_{m_j} & y_{m_j} & z_{m_j} \end{array} \right\}_{j=1}^{N_m}, \{\triangle_d\}_{d=1}^{T_m} \right\}. \tag{3.7}$$

In this representation, $\left\{ \begin{array}{ccc} x_{p_i} & y_{p_i} & z_{p_i} \end{array} \right\}$ is the i^{th} vertex of the target surface with N_p vertices. $\triangle_c$ refers to triangle patch c of which there is a total of T_p representing the target surface for example. Key steps to deform $\mathcal{M}$ into $\mathcal{P}$ are as follows:

- Registration inputs are specified. These include the target mesh $\mathcal{P}$ and base mesh $\mathcal{M}$. Other user specified parameters are a nearest neighbour parameter n, smoothing parameters γ, σ_0 and f, maximum number of iterations k_{max} and stopping criterion tolerance ε_T.

- Coarse registration with ICP is performed to align the target geometry to the generic mesh.

- The iteration counter and deformable surface is initialised so that $k = 1$ and $\mathcal{W}^{k-1} = \left\{ \begin{array}{ccc} x_{m_j} & y_{m_j} & z_{m_j} \end{array} \right\}_{j=1}^{N_m}$. Registration is performed while $k \leq k_{max}$:

  - Four $k-d$ tree representations are constructed. This is done for the centroids of surface triangulations and nodal coordinates of both $\mathcal{W}^{k-1}$ and $\mathcal{P}$.

  - For each node $\mathbf{w}_j$ in $\mathcal{W}^{k-1}$, $j \in \{1, 2, ..., N_m\}$, a registration to the target surface is determined. This can be better understood by also consulting Figure 3.4.

    * Using the $k-d$ tree representation of the target surface triangle centroids, the n nearest target triangles to $\mathbf{w}_j$ are determined.
    * The location of a registration point on these closest triangles are determined. This point $\mathbf{r}_{w_j}$, is produced by drawing a line from the point $\mathbf{w}_j$ perpendicular to the plane of each registered triangle. A

UNIVERSITEIT VAN PRETORIA
UNIVERSITY OF PRETORIA
YUNIBESITHI YA PRETORIA

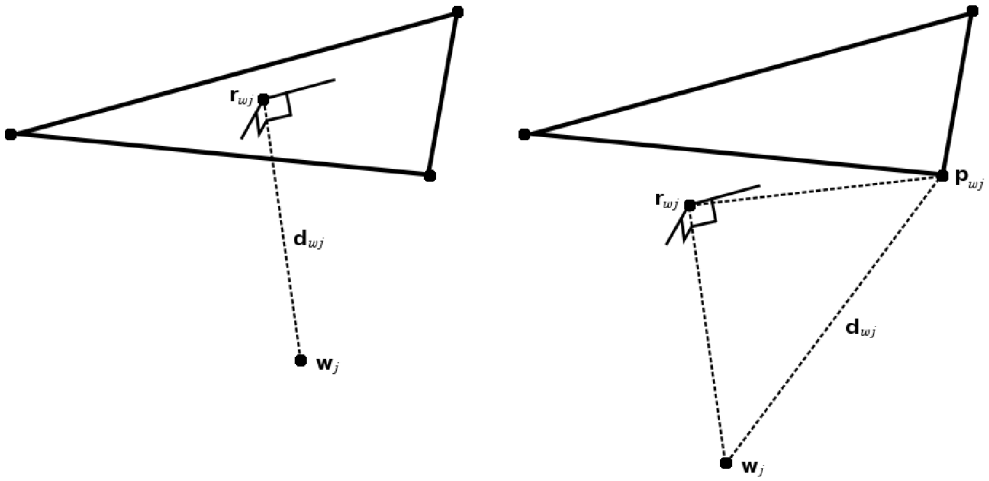

(a) (b)

Figure 3.4: Determining the registration of a point $\mathbf{w}_j$ onto one of the n closest triangles with (a) the registered point inside and (b) outside of the triangle boundary.

distance measure is then assigned to these triangles. If the point $\mathbf{r}_{w_j}$ lies inside a triangle, the distance measure is computed as $\left|\mathbf{r}_{w_j} - \mathbf{w}_j\right|$. Alternatively, if the point lies outside the triangle the distance measure is computed as $\left|\mathbf{r}_{w_j} - \mathbf{w}_j\right| + \left|\mathbf{p}_{w_j} - \mathbf{r}_{w_j}\right|$, where $\mathbf{p}_{w_j}$ is the closest vertex of that triangle to point $\mathbf{w}_j$.

* Inspecting all these distance measures for all n closest triangles, the closest triangle to point $\mathbf{w}_j$ is obtained. Using only this closest triangle, the required displacement to the target surface is determined. If the point $\mathbf{r}_{w_j}$ lies inside the closest triangle, the displacement is calculated as $\mathbf{d}_{w_j} = \mathbf{r}_{w_j} - \mathbf{w}_j$. Alternatively, if the point lies outside the triangle the displacement is calculated as $\mathbf{d}_{w_j} = \mathbf{p}_{w_j} - \mathbf{w}_j$.

– This registration procedure is then done again for the $\mathcal{P}$ onto $\mathcal{W}^{k-1}$. For each node $\mathbf{p}_i$ in $\mathcal{P}$, $i \in \{1, 2, ..., N_p\}$, a displacement to the deformable surface is determined as $\mathbf{d}_{p_i} = \mathbf{r}_{p_i} - \mathbf{p}_i$ if the point $\mathbf{r}_{p_i}$ lies inside the closest triangle or $\mathbf{d}_{p_i} = \mathbf{m}_{p_i} - \mathbf{p}_i$ if the point $\mathbf{r}_{p_i}$ lies outside the closest triangle.

– Having registered $\mathcal{W}^{k-1}$ onto $\mathcal{P}$ and $\mathcal{P}$ onto $\mathcal{W}^{k-1}$, a smooth displacement

UNIVERSITEIT VAN PRETORIA
UNIVERSITY OF PRETORIA
YUNIBESITHI YA PRETORIA

field is computed for a point $\mathbf{x}$ as

$$S^{k-1}(\mathbf{x}) = \frac{1}{\gamma}\left[\frac{\sum_{j=1}^{N_m} G\left(\|\mathbf{x}-\mathbf{w}_j\|\right)\mathbf{d}_{w_j}}{\sum_{j=1}^{N_m} G\left(\|\mathbf{x}-\mathbf{w}_j\|\right)} - \frac{\sum_{j=1}^{N_m} G\left(\|\mathbf{x}-\mathbf{r}_{p_i}\|\right)\mathbf{d}_{p_i}}{\sum_{j=1}^{N_m} G\left(\|\mathbf{x}-\mathbf{r}_{p_i}\|\right)}\right]. \quad (3.8)$$

In Equation (3.8), $G(d)$ is the Gaussian weighting function suggested by Moshfeghi [44]:

$$G(d) = e^{-d/\sigma_k^2}, \quad (3.9)$$

where d is a positive scalar distance measure. The smoothing parameter σ_k is decreased at each iteration allowing for more compact support using the update $\sigma_k = \sigma_0 f^{-k}$ with $1 \leq f \leq 2$.

- The deformable surface is updated as

$$\mathcal{W}_j^k = \mathcal{W}_j^{k-1} + S^{k-1}(\mathbf{w}_j). \quad (3.10)$$

- To prevent mesh folding, Bryan *et al.* [19] preformed a set number of improved Laplacian smoothing iterations to the deformable mesh $\mathcal{W}_j^k$ before performing another registration iteration.
- Convergence is determined on the average total deformation applied for the current iteration and the solution is terminated if

$$\varepsilon = \frac{1}{N_m}\sum_{j=1}^{N_m}\left|S^{k-1}(\mathbf{w}_j)\right| \leq \varepsilon_T. \quad (3.11)$$

In their study, Bryan *et al.* [19] used a nearest neighbour parameter $n = 50$, the smoothing parameters $\gamma = 2$, $\sigma_0 = 10$ and $f = 1.0715$ and the maximum iterations k_{max} set to 100 when registering the femur geometries. Bryan *et al.* [19] report that setting up a greater similarity measure in registration could result in mesh folding.

The updated nodal coordinates of the generic mesh is returned after reaching a stopping criterion. This stopping criterion could either be the satisfaction of Equation (3.11) or that the maximum number of iterations is reached.

UNIVERSITEIT VAN PRETORIA
UNIVERSITY OF PRETORIA
YUNIBESITHI YA PRETORIA

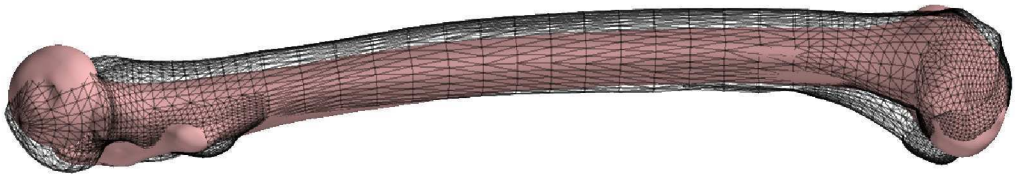

(a)

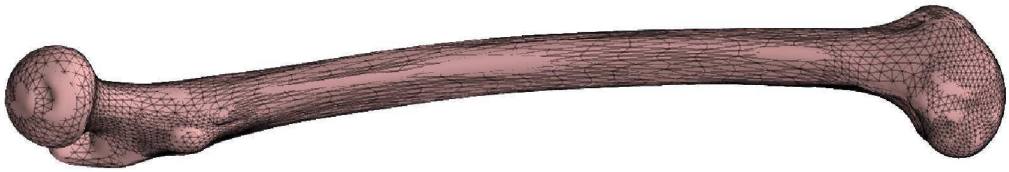

(b)

Figure 3.5: Elastic registration on the isotropic scale ICP result. (a) Lateral view of the rigid registration result on the two femur geometries. (b) Lateral view of the elastic surface registration result to deform the black wire-frame mesh into the target geometry at iteration 100.

3.2.2 Application

Registration on Femur Geometries

The elastic surface registration is implemented in Python. The performance of this registration procedure with the same parameter values as used by Bryan *et al.* [19] on the two femur surface meshes is visible in Figures 3.5 and 3.6.

The isotropic scale rigid registration result is used as the starting position of the elastic surface registration procedure. The chosen generic surface model is deformed to best fit the other geometry. From the figures illustrating this result, no real problem in registering these geometries are noticed.

The effect of selecting various registration parameters on the obtained result is visible in Figures 3.7 and 3.8. This analysis is done to determine the sensitivity of the registration result to user controlled inputs. To obtain the convergence plot in Figure 3.7 (a), the smoothing parameter γ is varied while the other parameters are kept as used by Bryan *et al.* [19]. This is then done again for a varying σ_0

UNIVERSITEIT VAN PRETORIA
UNIVERSITY OF PRETORIA
YUNIBESITHI YA PRETORIA

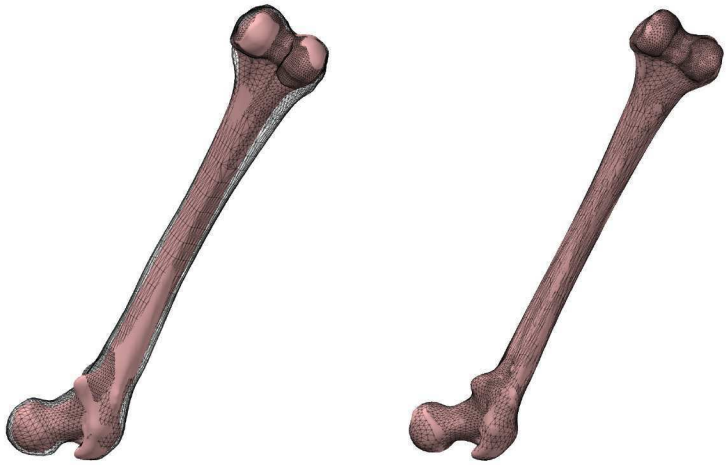

(a) (b)

Figure 3.6: Elastic registration on the isotropic scale ICP result. (a) Isometric view of the rigid registration result on the two femur geometries. (b) Isometric view of the elastic surface registration result to deform the black wire-frame mesh into the target geometry at iteration 100.

and varying f in Figures 3.7 (b) and (c). These figures show the convergence of ε in Equation (3.11) subject to these varying parameters for the femur registration problem.

The effect of performing 10 Taubin [61] smoothing iterations after every 5 elastic registration iterations is visible as the jumps in these figures. The smoothing done in the implemented procedure is chosen for it's ability to reduce high frequency surface noise without compromising subject volume. It is an enhanced version of Laplacian type smoothing.

Bryan *et al.* [19] mention the need for smoothing to prevent mesh folding and maintain a good quality mesh. Unfortunately the smoothing type and frequency of application is not mentioned. The spikes visible in Figure 3.7 seem to happen at a stage in the procedure where very localised deformations are applied. These very localised deformations likely resemble high frequency surface noise and can be largely undone by applying a few smoothing iterations.

Using the convergence plots of Figure 3.7, four of the deformed meshes are selected and shown in Figure 3.8 to inspect how close the registration came to represent the target femur geometry. The four meshes are obtained as follow:

UNIVERSITEIT VAN PRETORIA
UNIVERSITY OF PRETORIA
YUNIBESITHI YA PRETORIA

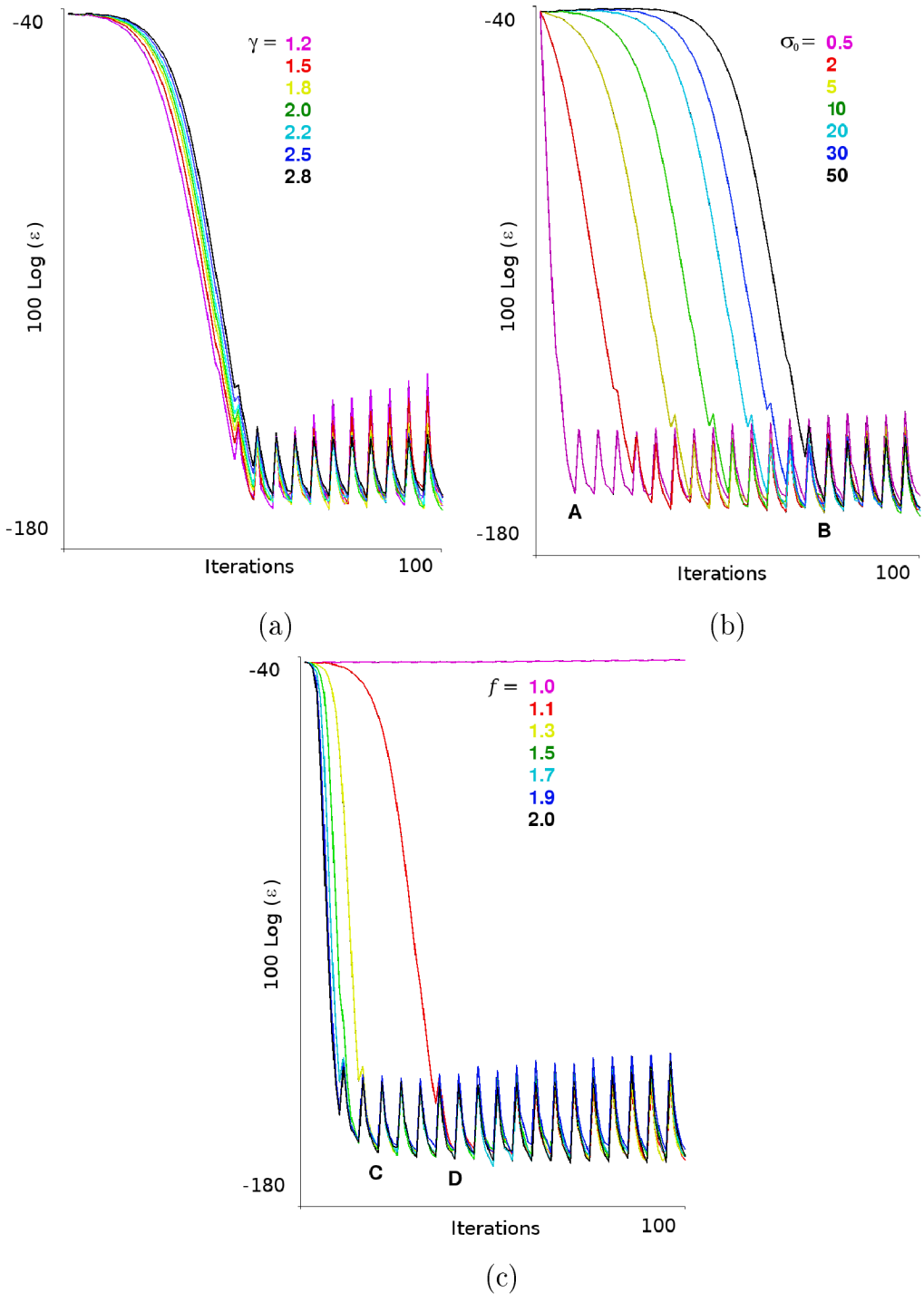

Figure 3.7: Improvement on the average deformation similarity criteria in Equation (3.11) subject to varying user controlled parameters. (a) $\sigma_0 = 10$ and $f = 1.0715$ while varying γ. (b) $f = 1.0715$ and $\gamma = 2$ while varying σ_0. (c) $\sigma_0 = 10$ and $\gamma = 2$ while varying f.

UNIVERSITEIT VAN PRETORIA
UNIVERSITY OF PRETORIA
YUNIBESITHI YA PRETORIA

(a)

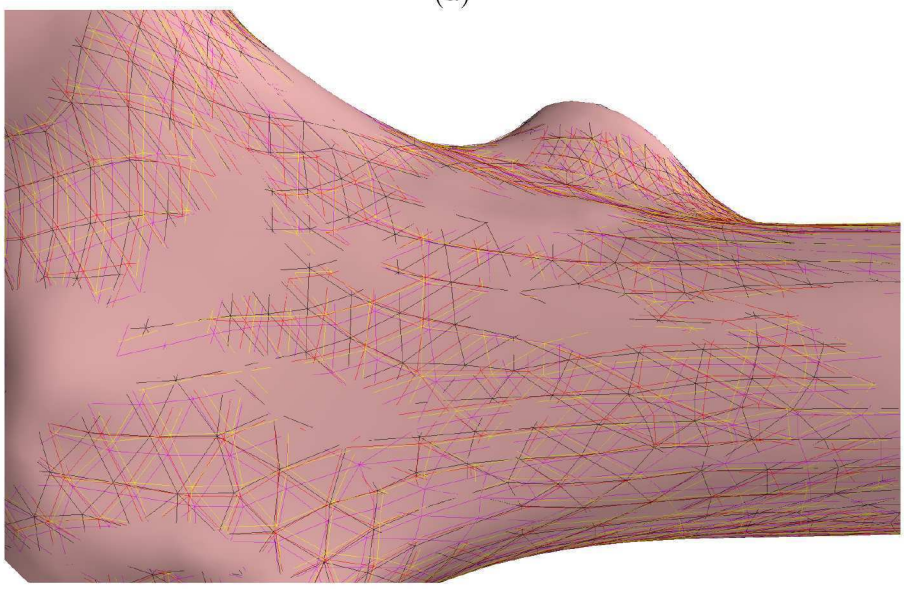

(b)

Figure 3.8: Various deformed generic surface target representations obtained with different user controlled parameters. Mesh **A** is the registration result with the parameters set to $\gamma = 2$, $\sigma_0 = 0.5$ and $f = 1.0715$ at 10 registration iterations. Mesh **B** is the registration result with the parameters set to $\gamma = 2$, $\sigma_0 = 50$ and $f = 1.0715$ at 75 registration iterations. Mesh **C** is the registration result with the parameters set to $\gamma = 2$, $\sigma_0 = 10$ and $f = 1.3$ at 20 registration iterations. Mesh **D** is the registration result with the parameters set to $\gamma = 2$, $\sigma_0 = 10$ and $f = 1.1$ at 40 registration iterations. The average total deformation plots in Figure 3.7 also indicate where meshes **A** - **D** are chosen.

UNIVERSITEIT VAN PRETORIA
UNIVERSITY OF PRETORIA
YUNIBESITHI YA PRETORIA

- Mesh **A** is the registration result with the parameters set to $\gamma = 2$, $\sigma_0 = 0.5$ and $f = 1.0715$ at 10 registration iterations.
- Mesh **B** is the registration result with the parameters set to $\gamma = 2$, $\sigma_0 = 50$ and $f = 1.0715$ at 75 registration iterations.
- Mesh **C** is the registration result with the parameters set to $\gamma = 2$, $\sigma_0 = 10$ and $f = 1.3$ at 20 registration iterations.
- Mesh **D** is the registration result with the parameters set to $\gamma = 2$, $\sigma_0 = 10$ and $f = 1.1$ at 40 registration iterations.

Out of this analysis done on the sensitivity of the registration result to user selected registration parameters, it is apparent that a target representation result obtained with this method is not unique. The four deformed femur meshes all seem to adequately represent the target surface with a wide range of different final nodal coordinates as visible in Figure 3.8 (b).

The parameters σ_0 and f influence the effective radius of the Gaussian smoothing function given in Equation (3.9). The smoothing parameter σ_0 is the initial support radius and therefore a smaller value would allow local deformations faster while a larger initial value would help account for initial global misalignment. This is visible as the small gradient in the first few iterations of the convergence plots. The effect of choosing the initial support radius $\sigma_0 = 10$ depends on the overall scale of the deformable and target mesh. If the meshes were now scaled with a factor of 10 before repeating the analysis, the effect of $\sigma_0 = 10$ would be the same as using $\sigma_0 = 1$ in the original analysis.

The parameter f in addition affects the rate at which the effective Gaussian support radius decays. A larger parameter forces localised deformation at an earlier stage where the choice of parameter $f = 1$ may be understood as a constant Gaussian support radius for all iterations. The deformation applied at each iteration with $f = 1$ is repeatedly determined using the initial support radius σ_0 .

The parameter γ in Equation (3.8) simply has an effect on the amount of smooth deformation field calculated that is applied to the deformable mesh. Using the suggestion of the paper by Bryan *et al.* [19], this parameter set to $\gamma = 2$ simply implies that half of the computed deformation at each iteration is applied to the deformable mesh.

UNIVERSITEIT VAN PRETORIA
UNIVERSITY OF PRETORIA
YUNIBESITHI YA PRETORIA

Registration on Skull Geometries

The implemented procedure is applied to the creation of a symmetric skull representation. This symmetric skull will be used as the generic mesh and deformed into representations of the two skull geometries used in the initial FEA.

To create a symmetric generic skull form, a cleaned and smoothed version of the prognathic skull form is used as the basis on which this generic form is built. The orientation of this smoothed skull is first updated so that it best matches it's reflected mesh. The original position of the smooth skull surface in relation to it's reflection is given in Figure 3.9. The position of the smoothed skull is then updated using the ICP procedure in the following way:

- An iteration of the ICP procedure is performed allowing only rotation and translation.
- The average of the nodal coordinates in their previous and current position is determined and set as the new skull position.
- The target is updated as the reflected skull surface of the new skull position before another iteration is performed.

The result after rotating and translating the smoothed skull surface to best fit it's reflection is visible in Figure 3.10. To then create a symmetric version of the cleaned and smoothed skull, an elastic registration from the skull to it's reflection is first required. If the registration is adequate, the average between the undeformed and deformed mesh should result in a symmetric version. This symmetric skull shape could then be used as the generic mesh in subsequent registrations to geometries in the statistical sample of skull shapes.

While deforming the smooth skull into it's reflection, a few problems appear in the result obtained with the original procedure. One such problem is highlighted in the cut planes depicted in Figure 3.11. The overlapping sinuses create a problem in elastic registration where a closest point on the opposite mesh is used to determine a registered position. To solve this problem, Chapter 4 focuses on the extraction of features on a surface mesh. These features are extracted with the aim of using an additional feature based registration.

UNIVERSITEIT VAN PRETORIA
UNIVERSITY OF PRETORIA
YUNIBESITHI YA PRETORIA

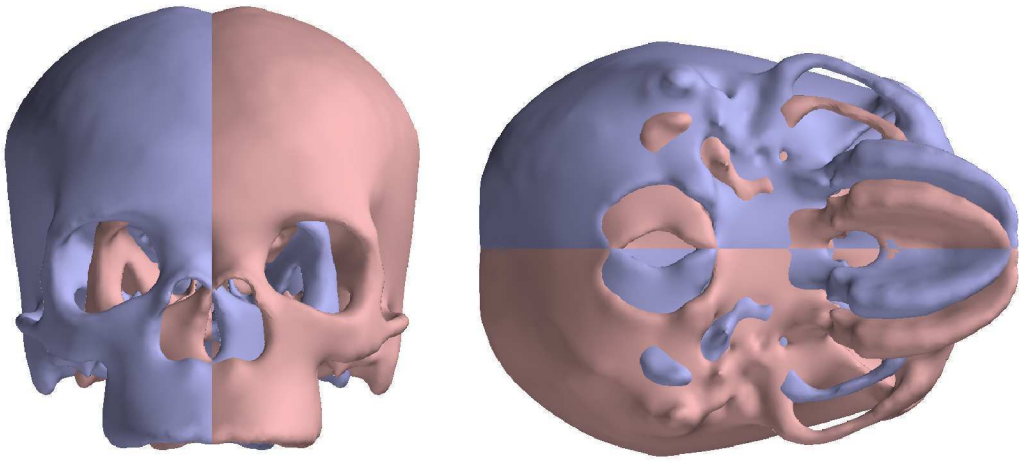

(a) (b)

Figure 3.9: Initial position of the smoothed skull mesh and it's reflection.

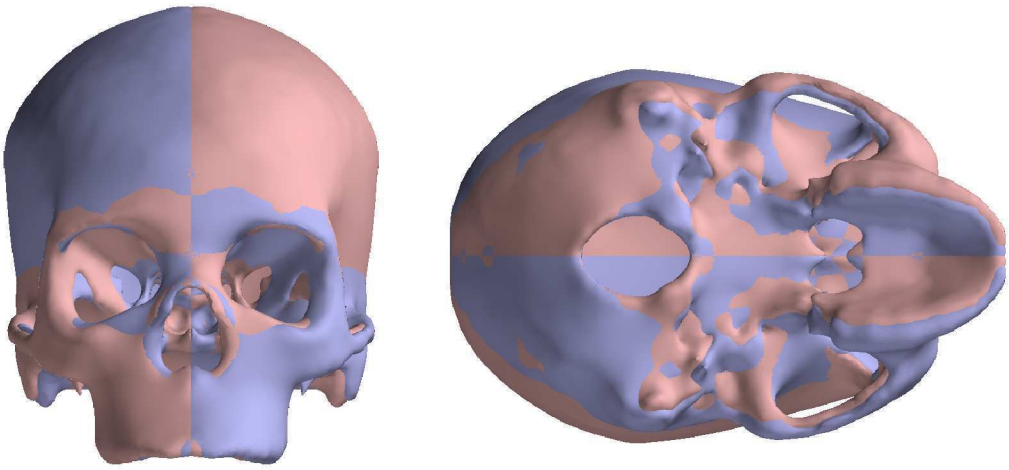

(a) (b)

Figure 3.10: Initial position of the smoothed skull mesh and it's reflection.

UNIVERSITEIT VAN PRETORIA
UNIVERSITY OF PRETORIA
YUNIBESITHI YA PRETORIA

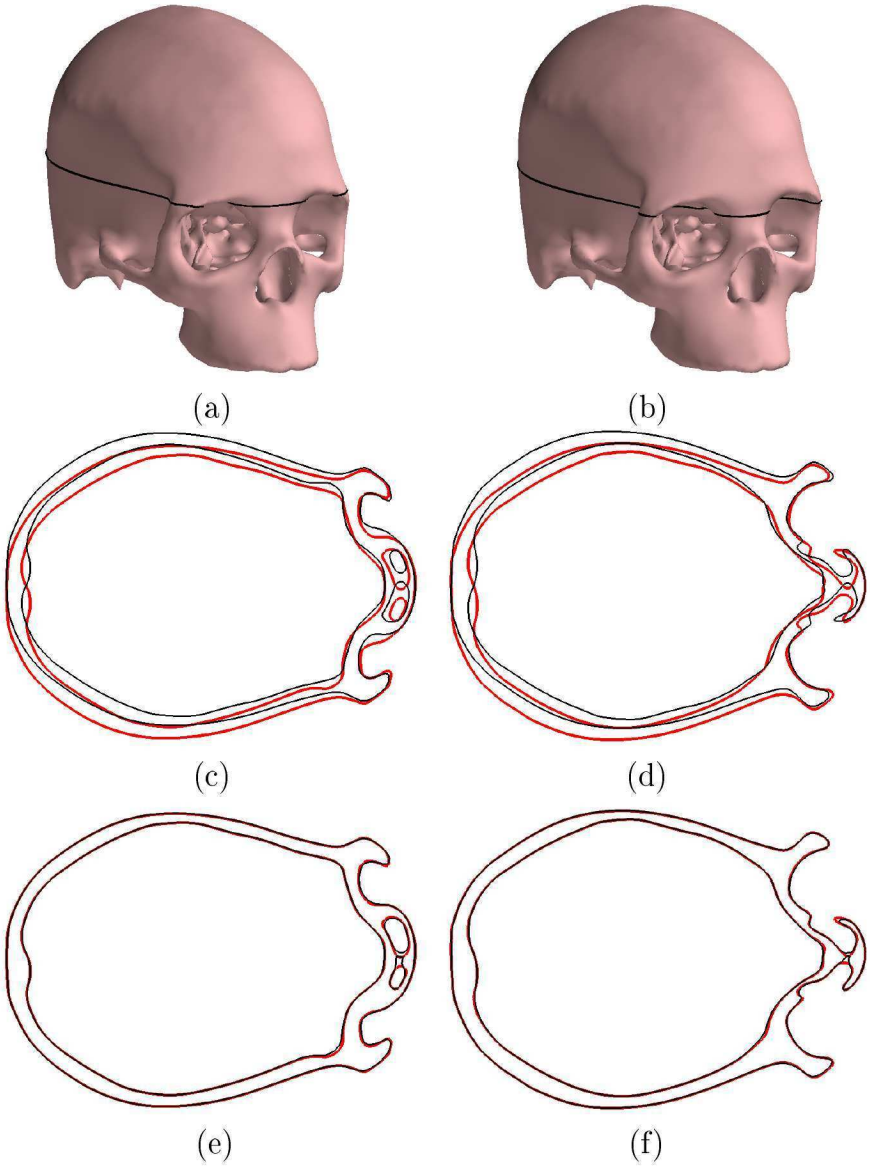

Figure 3.11: Problems with the sinus in elastically registering the smooth skull mesh into its reflection. (a) Position of cut plane (c) and (e). (b) Position of cut plane (d) and (f). (c), (d) Initial position of deformable mesh in relation to the target (The blue mesh in Figure 3.10 is set as the deformable mesh and is registered onto it's reflection). (e), (f) Elastic registration result at iteration 100. The red line represents the position of the target surface in that plane and the black line the deformable mesh surface.

UNIVERSITEIT VAN PRETORIA
UNIVERSITY OF PRETORIA
YUNIBESITHI YA PRETORIA

3.3 Remarks and Conclusions

Apart from the questionable uniqueness of a registration result, additional alterations to the procedure are also required in order to compare the masticatory induced stresses in various skull forms. Where surfaces overlap, it is possible to obtain a registration of the deformable surface to sections on the target surface that are visibly invalid.

The possibility of this invalid registration is visible in the initial attempt to create a symmetric skull mesh for use as a generic mesh surface. This generic surface will be deformed into representations of the two skull geometries used in the initial FEA.

If a more rigorous approach is followed to first ensure corresponding feature registration, this could be done in conjunction with the elastic surface registration procedure implemented to possibly obtain better registration results. Again referring to Figure 3.11, it is decided that at least some kind of usable representation is required for this initial work into elastic registration using the implemented procedure. It was decided that the remainder of the work done for this report would be focused on incorporating feature based registration along with the implemented surface registration. This would be done in a way that complements the surface registration procedure and wouldn't necessarily improve on the uniqueness of the registration result.

The uniqueness of the registration result would necessarily affect the accuracy with which the modes of variation are represented using the implemented procedure. It also implies an uncertainty in claiming one-to-one correspondence between various shapes and the accurate mapping of one surface onto another which is not ideal. The final results obtained on the difference in stress field for the varying skull geometries would therefore simply be considered the maximum possible difference due to the inherent uncertainty.

The accuracy with which the registration is performed could form the basis of subsequent research. A unique and path independent registration result could perhaps be achieved through a better defined optimisation procedure, but this would not be addressed in the current work.

Chapter 4

Geometric Features

4.1 Introduction

Features in a sample of subjects are frequently required. This could be for statistical analysis or simply to classify and process a geometry. Although this project is aimed at performing elastic surface registration to deform a generic shape into a target geometry, a better result is expected if a more rigorous approach is implemented for common feature registration. For that reason, the extraction of surface and feature information on a computational domain is investigated in this chapter.

Focus is first given to the local structure tensor. This is mainly used in inhomogeneous mesh coarsening and smoothing. This is done to best preserve the features in a given mesh during this operation. The detection of feature points and crest lines on a surface mesh is then investigated from methods that employ differential geometry concepts. Thresholding is also discussed. This is done after feature extraction to filter out insignificant feature lines.

Likely feature surfaces can be extracted from the local structure tensor analysis. If a local smooth surface approximation or discrete differential geometry operators are applied to extract feature lines, focus could be given to only these areas. In doing so far less false crest lines are already noticeable, reducing the need for additional thresholding and also speeding up computation if the local structure tensor result is already available.

After focusing on feature extraction in this chapter, later chapters will use the extracted features to determine feature correspondence during registration. Feature recognition could aid in matching selected features while disregarding others. Fea-

UNIVERSITEIT VAN PRETORIA
UNIVERSITY OF PRETORIA
YUNIBESITHI YA PRETORIA

tures that can't be matched due to possible topological[1] inconsistencies could also be automatically disregarded.

4.2 Local Structure Tensor

Given a tessellated surface mesh, the unit normal of each triangle can be obtained with very little effort. The accepted standard dictates triangle connectivity defined in an anti-clockwise manner for positive normal direction, often referred to as the right hand rule. Keeping this standard in mind, a triangle's unit normal vector may be calculated.

Two vectors are first obtained using the three vertices that make up the triangle. Both vectors have their origin at one of the triangle vertices and are in the direction of the other two respectively. The normalised result of the cross product between these vectors is the triangle unit normal.

When aimed at recognising localised surface features, the change in surface gradient in a specific area is inspected. Surface gradient information can be captured by the local structure tensor [71]. In order to determine the local structure tensor at a specific vertex $\mathbf{p}$, given by

$$LST(\mathbf{p}) = \sum_{i \in N-\text{neighbours}} \begin{bmatrix} n_x n_x & n_x n_y & n_x n_z \\ n_y n_x & n_y n_y & n_y n_z \\ n_z n_x & n_z n_y & n_z n_z \end{bmatrix}_i , \tag{4.1}$$

the normal of each i^{th} neighbouring vertex, $\begin{pmatrix} n_x & n_y & n_z \end{pmatrix}_i$ also needs calculation. This is done by defining the vertex unit normal vector as the weighted average of the normals of all its incident triangles. The weight attributed to each triangle is determined using the distance from the vertex to the triangle centroid and triangle area. The unit normal of each triangle is multiplied with the area of the triangle and divided by the distance to the triangle centroid. The result obtained after adding all weighted triangle normals incident to the vertex is normalised to approximate the vertex unit normal.

The local structure tensor is defined as the summation of the matrices corresponding to the neighbours of a local vertex. This simple summation allows for

[1] Two structures are topologically similar if one can be completely morphed into the other and one-to-one correspondence remains continuous.

UNIVERSITEIT VAN PRETORIA
UNIVERSITY OF PRETORIA
YUNIBESITHI YA PRETORIA

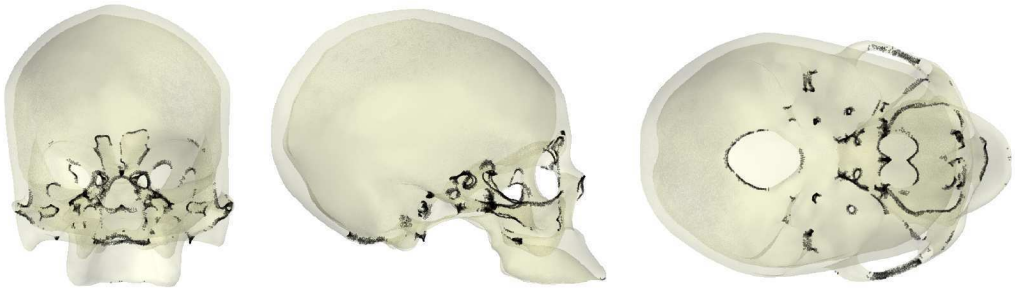

(a) (b) (c)

Figure 4.1: Points on skull geometry where $\lambda_1 < 5 \times \lambda_2$. This condition represents spheres, saddles, ridges and valleys within a certain degree. (a) Frontal, (b) side and (c) bottom view.

(a) (b) (c)

Figure 4.2: Points on skull geometry where $\lambda_1 < 100 \times \lambda_2$. This condition represents spheres, saddles, ridges and valleys within a certain degree. (a) Frontal, (b) side and (c) bottom view.

neighbour contributions to be evaluated in arbitrary order. It is also worth noting that the neighbours considered may be more than only those incident to the local vertex. Additional layers of neighbouring nodes may also be included depending on the size of local features compared to the size of the elements of the tessellated surface mesh. Filtering out the effect of surface noise by using additional layers of neighbouring vertices also proves helpful.

4.2.1 Feature Classification

The eigenvalues and eigenvectors of the local structure tensor indicates the overall distribution of vectors in a local vertex neighbourhood [71]. The features are categorised locally into different types namely spheres and saddles, lines and planes.

Considering the evaluation of features within a surface mesh, let the eigenvalues

UNIVERSITEIT VAN PRETORIA
UNIVERSITY OF PRETORIA
YUNIBESITHI YA PRETORIA

(a) (b) (c)

Figure 4.3: Points on skull geometry where $\lambda_1 > 2'000 \times \lambda_2$. This condition represents planes to a certain degree. (a) Frontal, (b) side and (c) bottom view.

(a) (b) (c)

Figure 4.4: Points on skull geometry where $\lambda_1 > 20'000 \times \lambda_2$. This condition represents planes to a certain degree. (a) Frontal, (b) side and (c) bottom view.

of the local structure tensor be λ_1, λ_2 and λ_3 with $\lambda_1 \geq \lambda_2 \geq \lambda_3$. The following cases may be considered:

- Spheres and saddles: $\lambda_1 \approx \lambda_2 \approx \lambda_3 > 0$.
- Ridges and valleys: $\lambda_1 \approx \lambda_2 \gg \lambda_3 \approx 0$.
- Planes: $\lambda_1 \gg \lambda_2 \approx \lambda_3 \approx 0$.

Figures 4.1 through 4.4 show results that could be extracted after performing a local structure tensor analysis on the unstructured surface mesh representation of a human skull. For the intended study the intricate details and structures within the nasal cavity and sinuses aren't of statistical importance. In these areas unwanted detail was removed. After then simplifying and smoothing the mesh, vertex normals were determined and 3 layers of neighbouring nodes were used to extract local feature information.

UNIVERSITEIT VAN PRETORIA
UNIVERSITY OF PRETORIA
YUNIBESITHI YA PRETORIA

Figures 4.1 and 4.2 show various thresholds of areas that could be considered feature rich. These areas could be included into the classification for spheres, saddles, ridges and valleys. Vertices are displayed here where the eigenvalues satisfy the conditions $\lambda_1 < 5 \times \lambda_2$ and $\lambda_1 < 100 \times \lambda_2$ respectively.

The third eigenvalue $\lambda_3 \leq \lambda_2$ is only required to differentiate spheres and saddles from ridges and valleys. Very few of the features in a human skull geometry can be classified as spherical or saddle points compared to the quantity of ridges and valleys. The intended use of the local structure tensor is to simply classify areas as feature rich or flat. Because of this, no distinction is made between spheres, saddles, ridges and valleys in Figures 4.1 and 4.2.

All nodes satisfying the conditions $\lambda_1 > 2'000 \times \lambda_2$ and $\lambda_1 > 20'000 \times \lambda_2$ are shown in Figures 4.3 and 4.4. Here, areas are highlighted to illustrate what could be considered flat or featureless, showing the third case mentioned above for planes.

4.2.2 Spatial Search Speed-up

Because evaluating mesh connectivity is imperative when using N-ring neighbours, it is often possible and beneficial to rather use a user specified amount of nearest neighbouring points. For each mesh node, the spatial domain could simply be evaluated with a nearest neighbour search algorithm for the specified number of closest neighbours. This eliminates the need for mesh connectivity information beyond determining unit normal orientation, producing a significant speed-up in local structure calculation.

A drawback to this proposed method is that it is possible to pick up nodes on opposing surfaces when only the spatial node distribution is evaluated. This happens when different surfaces or parts of a surface are close to one another, preventing successful use of this procedure. The intricate details of a human brain geometry with all it's folds for example could pose a problem in certain areas. This could therefore result in describing areas as feature rich that are in actual fact smooth but simply close to opposing surfaces. Depending on the intended use of the local structure tensor analysis, it is up to the user's discretion to determine the required accuracy.

In case these problems occur in the geometry, only the neighbouring unit normals that correlate to a certain degree could be used in evaluating the local structure tensor. Alternatively, the N-ring procedure should be employed when significant

UNIVERSITEIT VAN PRETORIA
UNIVERSITY OF PRETORIA
YUNIBESITHI YA PRETORIA

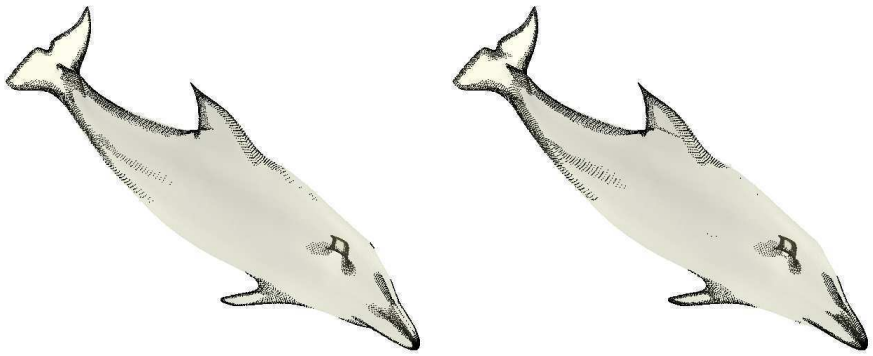

(a) (b)

Figure 4.5: Points for $\lambda_1 < 50 \times \lambda_2$ on a refined dolphin model using (a) 3-ring neighbourhood (b) 15 nearest neighbours

differences between the local and nearest neighbour unit normals are a possibility.

In Figure 4.5, the points satisfying $\lambda_1 < 50 \times \lambda_2$ is shown on a dolphin geometry. This condition combines the points that are closely related to spheres, saddles, ridges and valleys. The local structure tensor procedure is first done using a 3-ring neighbourhood and then a 15 nearest neighbour search using the k-d tree spatial search algorithm. Significant speed-up is obtained with very little difference in the final reported areas of interest.

The obtained area of interest depends on the support used. If a 5-ring neighbourhood is used, or 20 nearest neighbours for example, the reported area would be larger while smaller support would result in picking up very localised feature areas.

4.3 Differential Geometry Surface Information

For a smooth oriented surface $\mathcal{S}$, the maximal and minimal curvatures are such that $\kappa_{\max} \geq \kappa_{\min}$ with corresponding principal directions $\boldsymbol{\varpi}_{\max}$ and $\boldsymbol{\varpi}_{\min}$. The curvature derivatives along these directions are then $\tau = \partial\kappa/\partial\boldsymbol{\varpi}$, defined locally in the neighbourhood of non-umbilical points [45].

Points on a surface where $\kappa_{\max} = \kappa_{\min}$ are called umbilical points. Principal directions are not defined at these points, making it impossible to determine curvature derivatives. Closure of these points where either one of the curvature derivatives vanishes are however required to form ridges and valleys.

Concave and convex crest lines on a smooth surface are dual with respect to surface normal orientation. With a normal defined consistently, these lines could

UNIVERSITEIT VAN PRETORIA
UNIVERSITY OF PRETORIA
YUNIBESITHI YA PRETORIA

be extracted and classified as ridges and valleys on the surface. Concave crest lines are expected where points on the line satisfy the conditions: [45]

$$\tau_{\max} = 0 \qquad \partial\tau_{\max}/\partial\boldsymbol{\varpi}_{\max} < 0 \qquad \kappa_{\max} > |\kappa_{\min}|\,, \tag{4.2}$$

while points on a convex crest line satisfy the following conditions:

$$\tau_{\min} = 0 \qquad \partial\tau_{\min}/\partial\boldsymbol{\varpi}_{\min} < 0 \qquad \kappa_{\min} < -|\kappa_{\max}|\,. \tag{4.3}$$

4.3.1 Application to a Discretised Surface

Numerous techniques have been proposed to extract curvature information from a discretised surface representation. Some techniques approximate an implicit smooth surface either globally [21, 45] or locally [21, 37, 70]. Other techniques approximate surface information through the application of discrete curvature operators [33, 40]. For the purpose of this report, focus is given to the application of an approximate smooth local implicit surface.

Given a surface in the implicit form $\mathcal{F}(\mathbf{x}) = 0$, $\mathbf{x} = \begin{pmatrix} x_1 & x_2 & x_3 \end{pmatrix}$, the principal curvatures and associated curvature directions can be obtained at a specific point on the surface from an eigen-analysis on $\nabla\mathbf{n}$. The unit normal $\mathbf{n}$ at this point on surface $\mathcal{F}$ is taken as $\nabla\mathcal{F}/|\nabla\mathcal{F}|$ [21, 37, 40, 45, 70]. This means that the eigenvalues of matrix $\nabla^2\mathcal{F}/|\nabla\mathcal{F}|$ would be the principal curvatures while the associated eigenvectors are the principal curvature directions.

The curvature derivative or extremality coefficient for a given principal curvature and associated curvature direction is given by [70]

$$\tau = \frac{\partial\kappa}{\partial\boldsymbol{\varpi}} = \frac{\mathcal{F}_{ijk}\varpi_i\varpi_j\varpi_k + 3\kappa\mathcal{F}_{ij}\varpi_i n_j}{|\nabla\mathcal{F}|}. \tag{4.4}$$

In this equation, summation over repeated indices are implied with $\mathcal{F}_{ij}$ and $\mathcal{F}_{ijk}$ indicating the second and third partial derivatives of $\mathcal{F}(\mathbf{x})$. Choosing a local coordinate frame $\mathbf{u} \times \mathbf{v} = \mathbf{w}$ in such a way that the origin is situated on the surface and $\mathbf{w} = \mathbf{n}$, the surface approximation could be given in the form of a bi-variate polynomial

$$p(u,v) = \frac{1}{2}\left(b_0u^2 + 2b_1uv + b_2v^2\right) + \frac{1}{6}\left(c_0u^3 + 3c_1u^2v + 3c_2uv^2 + c_3v^3\right) + \ldots \tag{4.5}$$

UNIVERSITEIT VAN PRETORIA
UNIVERSITY OF PRETORIA
YUNIBESITHI YA PRETORIA

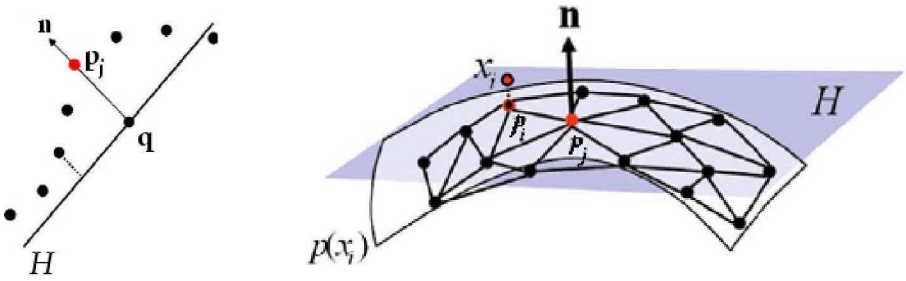

(a) (b)

Figure 4.6: (a) The MLS projection. Given a point $\mathbf{p}_j$, the local reference plane H and a point $\mathbf{q}$ on H is first determined. An MLS surface is then defined implicitly by the MLS projection as the set of points that project on to themselves [37]. (b) The estimation of a modified MLS approximation to the mesh [37].

In this local coordinate frame, Equation (4.4) is simplified to become [70]

$$\tau = \frac{\partial \kappa}{\partial \varpi} = \mathcal{F}_{ijk}\varpi_i\varpi_j\varpi_k. \tag{4.6}$$

A moving least squares approximation is chosen to construct a local smooth surface approximation. The required surface information is approximated and then applied to the original mesh nodes. This is discussed in the following subsection while procedures followed to extract feature points using shape index and extracting ridge and valley lines are discussed thereafter.

4.3.2 Enhanced Moving Least Squares Approximation

A moving least squares (MLS) surface is implicitly defined as the set of points that project on to themselves under the MLS projection. The procedure to approximate this surface involves first determining an appropriate local reference plane and then fitting a bi-variate polynomial to points projected on this reference plane in a least squares manner [37, 70].

Generating a smooth local surface approximation

Given an unstructured surface mesh $\mathcal{M}$ approximating the smooth surface $\mathcal{S}$ in $\mathbb{R}^3$, let $\mathbf{p}_j$ be a point on the mesh with $\{\mathbf{p}_i\}_{i\in N-\text{neighbours}}$ the set of points in its N-ring neighbourhood. Only the neighbours whose normals don't make obtuse

UNIVERSITEIT VAN PRETORIA
UNIVERSITY OF PRETORIA
YUNIBESITHI YA PRETORIA

angles with that of the center node are selected and kept in the $N-$neighbours set [70]. Alternatively, S. Kim and C. Kim [37] suggest fitting a weighted least squares approximation with a Gaussian weighting function that lends higher support to point within in the 1-ring neighbourhood of $\mathbf{p}_j$.

The following general procedure is followed to approximate a bi-variate polynomial surface for curvature, curvature derivatives and principal curvature direction estimation [37, 70]:

- The vertex unit normal $\mathbf{n}_j$ for each point $\mathbf{p}_j$ in the mesh is determined as the weighted average of the neighbouring face normals. The weighting is done in the same way explained under the local structure tensor section, using triangle areas and the distance from the point to the incident triangle centroids.

- A local reference plane $H = \{\mathbf{p}_j | \langle \mathbf{n}, \mathbf{p}_j \rangle = 0, \mathbf{p}_j \in \mathbb{R}^3\}$ is determined through the point $\mathbf{p}_j$ with the same unit normal $\mathbf{n} = \mathbf{n}_j$. In Figure 4.6 (a) this is illustrated should point $\mathbf{q}$ be moved to be exactly point $\mathbf{p}_j$.

- The orthogonal projections $\{\mathbf{x}_i\}_{i \in N-\text{neighbours}}$ and $\{f_i\}_{i \in N-\text{neighbours}}$ perpendicular distance of the neighbouring points onto and from the reference plane are determined.

- A local orthonormal coordinate system is set up with origin at $\mathbf{p}_j$. Using the plane normal direction as $\mathbf{w}$, the local reference coordinate directions are determined. The rotation required from global direction $\mathbf{z}$ to $\mathbf{w}$ is first determined and then applied to the global coordinate system. This is done in such a way that the local coordinate system is consistently defined for all points on the mesh.

- Orthogonal projections of the N-ring neighbours, $\mathbf{x}_i$ can then be rewritten in terms of its components in the two directions $\mathbf{u}$ and $\mathbf{v}$ in the plane.

- A local smooth surface approximation is finally made as a third degree polynomial $p(\mathbf{x}_i)$ that minimises the least squares error

$$\sum_{i \in N-\text{neighbours}} (p(\mathbf{x}_i) - f_i)^2 . \tag{4.7}$$

An example of an estimated MLS surface constructed by fitting a polynomial through neighbouring points in a least squares manner is visible in Figure 4.6 (b).

UNIVERSITEIT VAN PRETORIA
UNIVERSITY OF PRETORIA
YUNIBESITHI YA PRETORIA

The same speed up can be obtained as in subsection 4.2.2 by applying a spatial nearest neighbour search algorithm. Without the need to evaluate mesh connectivity, a simple search for N nearest neighbours is applied. Again only those neighbours with sufficient similarity between unit normals are used in fitting the local least squares approximation. This step is already a requirement in doing the enhanced least squares fit.

Estimating curvatures and their derivatives

After fitting a local bi-variate third degree polynomial approximated surface $z = p(\mathbf{x}_i)$, the principal curvatures, curvature derivatives and principal curvature directions in the local coordinate frame can be obtained. This is done by applying the principles of differential geometry to the resulting implicit surface.

The principal curvatures and associated curvature directions can be obtained from an eigen-analysis on $\nabla\mathbf{n}$ at point $\mathbf{p}_i$ of a surface in the form of Equation (4.5). Noting that in this particular case point $\mathbf{p}_i$ is at the local origin, the solution to the eigenvalue problem

$$\begin{bmatrix} b_0 & b_1 \\ b_1 & b_2 \end{bmatrix} \begin{bmatrix} \varpi_1 \\ \varpi_2 \end{bmatrix} = \kappa \begin{bmatrix} \varpi_1 \\ \varpi_2 \end{bmatrix}, \tag{4.8}$$

produces the principal curvatures $\kappa_{\max}$ and $\kappa_{\min}$ with associated principal curvature directions $\boldsymbol{\varpi}_{\max}$ and $\boldsymbol{\varpi}_{\min}$ in the local coordinate frame. The curvature derivatives can then be calculated from Equation (4.6) as [70]

$$\tau = \begin{bmatrix} \varpi_1^2 \\ \varpi_2^2 \end{bmatrix}^T \begin{bmatrix} c_0 & c_1 \\ c_2 & c_3 \end{bmatrix} \begin{bmatrix} \varpi_1 \\ \varpi_2 \end{bmatrix}. \tag{4.9}$$

Converting the principal curvature directions into the global coordinate frame is also done. This is required to help determine the presence of ridge and valley nodes as well as to connect these nodes into lines.

The principal curvatures determined at each point may be used to classify areas and points on the geometry. The MLS procedure is performed on the skull geometry used to generate Figures 4.1 through 4.4. Curvature information is extracted and used to display areas on the geometry that are concave and convex. Figure 4.7 represents the concave areas and Figure 4.8 the convex areas of the skull geometry.

Figures 4.9 through 4.11 illustrate ridge and valley areas on the skull geometry. Only points within some degree of the average curvature evaluated is displayed.

UNIVERSITEIT VAN PRETORIA
UNIVERSITY OF PRETORIA
YUNIBESITHI YA PRETORIA

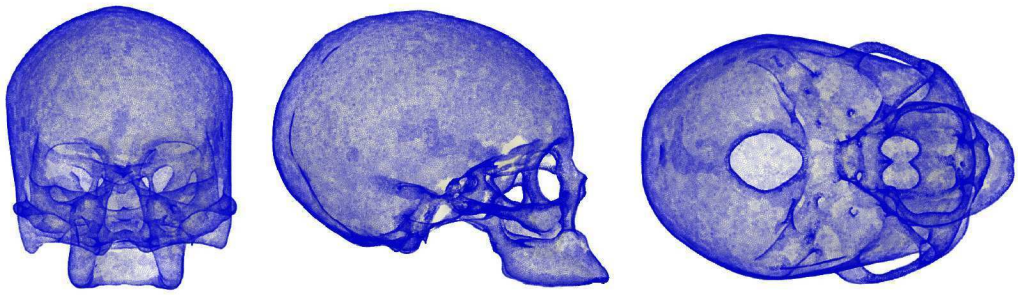

(a) (b) (c)

Figure 4.7: Points on skull geometry where $\kappa_{\max} > |\kappa_{\min}|$. (a) Frontal, (b) side and (c) bottom view.

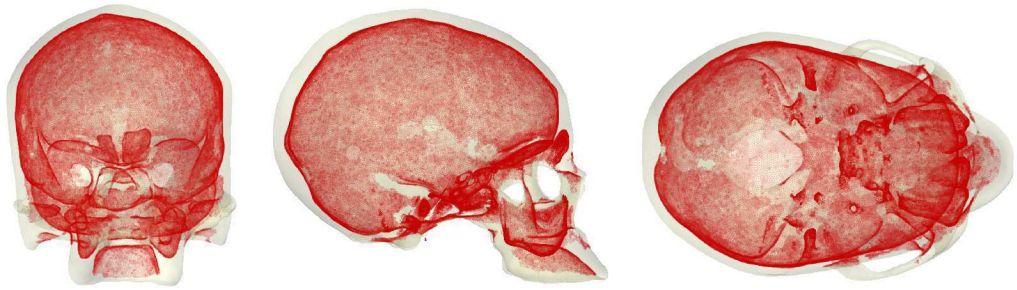

(a) (b) (c)

Figure 4.8: Points on skull geometry where $\kappa_{\min} < -|\kappa_{\max}|$. (a) Frontal, (b) side and (c) bottom view.

When using the local structure tensor to evaluate and find feature rich areas on a geometry it is impossible to differentiate between ridges and valleys. Obtaining differential geometry information on the other hand allows one to make this distinction.

4.3.3 Shape Index Feature Points

Feature points can be automatically extracted from differential geometry information such as that obtained after performing the MLS procedure. These feature points are defined in areas where large shape variation can be obtained by a calculated shape index.

The shape index S_i is a quantitative measure of the shape of a surface point $\mathbf{p}_i$

UNIVERSITEIT VAN PRETORIA
UNIVERSITY OF PRETORIA
YUNIBESITHI YA PRETORIA

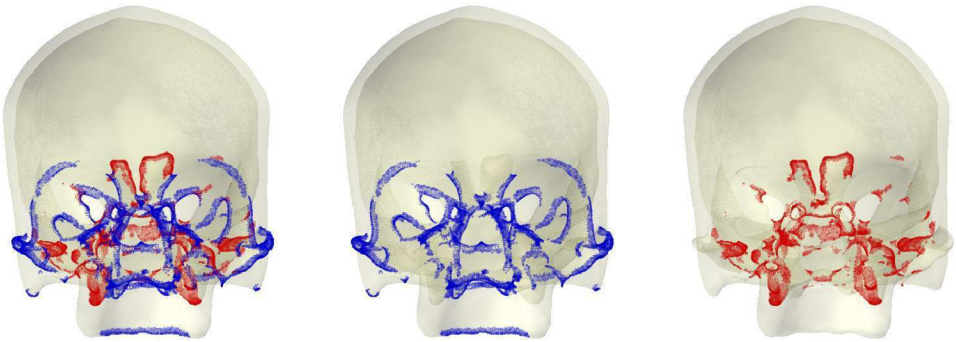

(a) (b) (c)

Figure 4.9: Frontal view highlighting points on skull geometry where $\kappa_{\max} > 5 \times$ average($\kappa_{\max}$) in blue and $\kappa_{\min} < 5 \times$ average($\kappa_{\min}$) in red. (a) Ridges and valleys split up in (b) to show only ridges and (c) only valleys.

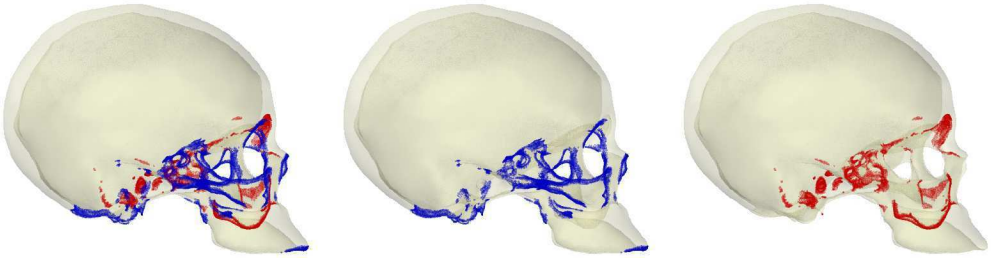

(a) (b) (c)

Figure 4.10: Side view highlighting points on skull geometry where $\kappa_{\max} > 5 \times$ average($\kappa_{\max}$) in blue and $\kappa_{\min} < 5 \times$ average($\kappa_{\min}$) in red. (a) Ridges and valleys split up in (b) to show only ridges and (c) only valleys.

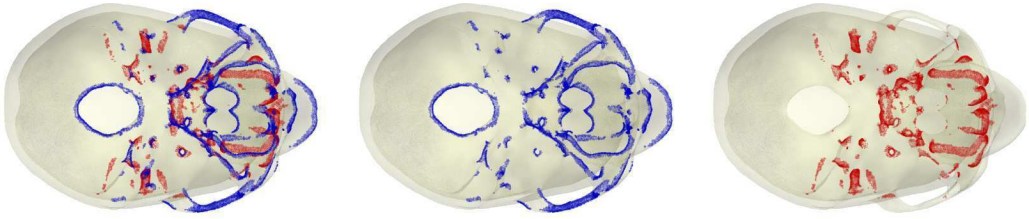

(a) (b) (c)

Figure 4.11: Lower view highlighting points on skull geometry where $\kappa_{\max} > 5 \times$ average($\kappa_{\max}$) in blue and $\kappa_{\min} < 5 \times$ average($\kappa_{\min}$) in red. (a) Ridges and valleys split up in (b) to show only ridges and (c) only valleys.

UNIVERSITEIT VAN PRETORIA
UNIVERSITY OF PRETORIA
YUNIBESITHI YA PRETORIA

determined by [22]

$$S_i(\mathbf{p}_i) = \frac{1}{2} - \frac{1}{\pi}\tan^{-1}\left(\frac{\kappa_{\max}(\mathbf{p}_i) + \kappa_{\min}(\mathbf{p}_i)}{\kappa_{\max}(\mathbf{p}_i) - \kappa_{\min}(\mathbf{p}_i)}\right). \tag{4.10}$$

All shapes are mapped into the interval $[0, 1]$ with this definition. Larger shape index values represent convex surfaces while smaller values represent concave surfaces. These shape index values capture the characteristics of shape objects and can be used for feature point extraction. Following the work done by Chen *et al.* [22], a window is drawn on the surface around a candidate feature point $\mathbf{p}_i$ by including points in a sphere of radius r_i. This point is then marked as a feature point if the shape index $S_i(\mathbf{p}_i)$ satisfies:

- $S_i(\mathbf{p}_i)$ =max of shape indexes and $S_i(\mathbf{p}_i) \geq (1+\alpha) \times \mu$ or
- $S_i(\mathbf{p}_i)$ =min of shape indexes and $S_i(\mathbf{p}_i) \leq (1-\beta) \times \mu$

where $\mu = \frac{1}{N_r}\sum_{j=1}^{N_r} S_i(\mathbf{p}_j)$ and $0 \leq \alpha, \beta \leq 1$. The parameters α and β control the selection of feature points and N_r is the number of points in the local window.

The shape index of a dolphin geometry is given in Figure 4.12. The shape index of the skull geometry is then given in Figure 4.13 with the corresponding feature points automatically extracted for a radius $r_i = 10$, $\alpha = 0.1$ and $\beta = 0.1$ in Figure 4.14.

4.3.4 Ridges and Valleys

The ridge and valley nodes are found after obtaining curvature information at each mesh vertex. The mesh vertices that approximate ridge and valley nodes can be found by either finding the zero crossing of extremality coefficients or using only principal curvatures and directions. The nodes are then connected into lines following the directions of principal curvature.

An outline of how to obtain and differentiate between crest nodes is derived from the requirements on concave and convex crest lines presented in Equations (4.2) and (4.3).

Determining ridge nodes:

- For each node $\mathbf{p}_j$ satisfying $\kappa_{\max} > |\kappa_{\min}|$ the immediate neighbours are inspected.

UNIVERSITEIT VAN PRETORIA
UNIVERSITY OF PRETORIA
YUNIBESITHI YA PRETORIA

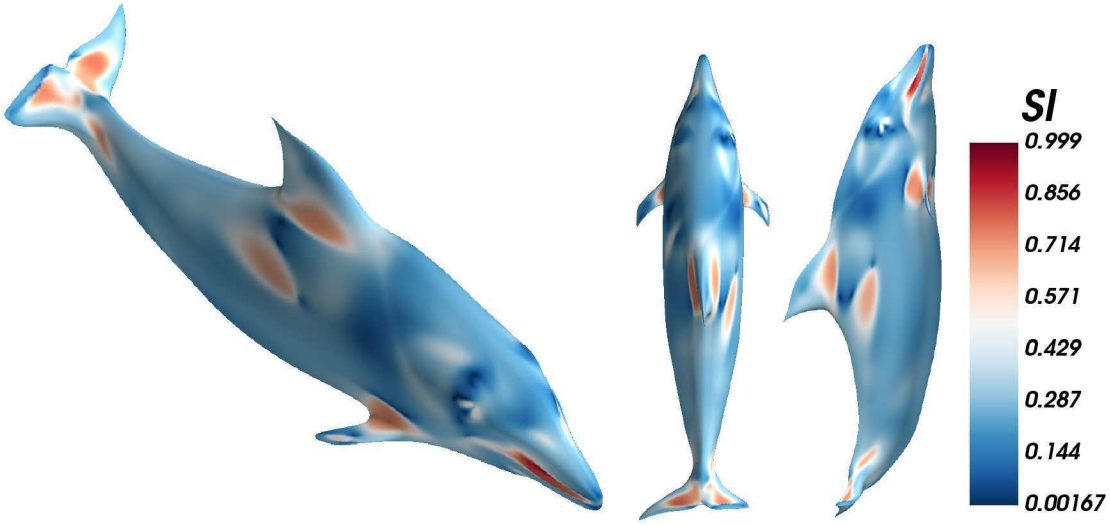

(a) (b) (c)

Figure 4.12: Shape index of a dolphin geometry after using a 5-ring neighbourhood for MLS surface fitting. (a) Isometric (b) top and (c) side view.

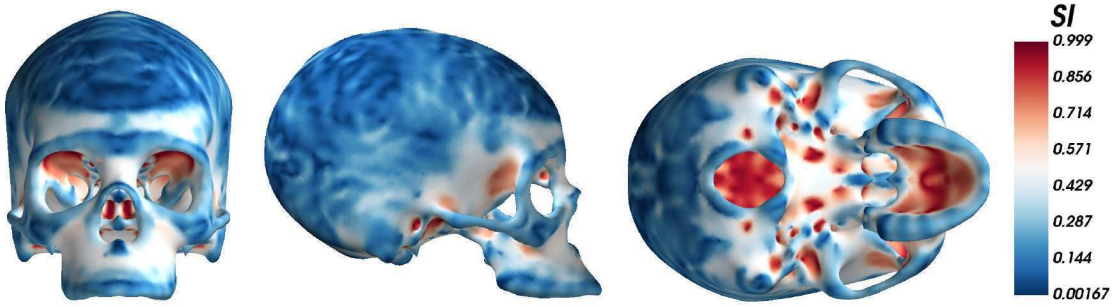

(a) (b) (c)

Figure 4.13: Shape index of the skull geometry after using a 3-ring neighbourhood for MLS surface fitting. (a) Frontal, (b) side and (c) bottom view.

UNIVERSITEIT VAN PRETORIA
UNIVERSITY OF PRETORIA
YUNIBESITHI YA PRETORIA

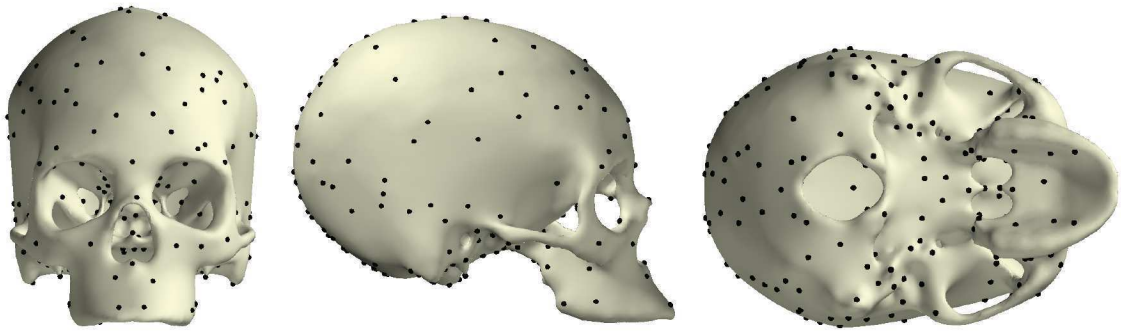

(a) (b) (c)

Figure 4.14: Feature points automatically extracted from skull geometry for radius $r_i = 10$ and $\alpha = 0.1, \beta = 0.1$. (a) Frontal, (b) side and (c) bottom view.

- The vector distance to the neighbours are determined.
- Only the neighbours who lie more in direction $\boldsymbol{\varpi}_{\max}$ than $\boldsymbol{\varpi}_{\min}$ are added to the neighbour set I.
- If only principal curvatures and directions are used:
  - $\mathbf{p}_j$ is considered a possible ridge node if for all $i \in I : \kappa^j_{\max} > \kappa^i_{\max}$ is satisfied.
- If the zero crossing of extremality coefficients is required:
  - $\forall i \in I$: If $\boldsymbol{\varpi}^j_{\min} \bullet \boldsymbol{\varpi}^i_{\min} < 0$, the sign of the relevant extremality coefficient is reversed so $\tau^i_{\max} = -\tau^i_{\max}$.
  - $\mathbf{p}_j$ is considered a possible ridge node if for any $i \in I : \tau^j_{\max} \times \tau^i_{\max} < 0$ and $\kappa^j_{\max} > \kappa^i_{\max}$ is satisfied.

Determining valley nodes:

- For each node $\mathbf{p}_j$ satisfying $\kappa_{\min} < -|\kappa_{\max}|$ the immediate neighbours are inspected.
- The vector distance to the neighbours are determined.
- Only the neighbours who lie more in direction $\boldsymbol{\varpi}_{\min}$ than $\boldsymbol{\varpi}_{\max}$ are added to the neighbour set I.

UNIVERSITEIT VAN PRETORIA
UNIVERSITY OF PRETORIA
YUNIBESITHI YA PRETORIA

- If only principal curvatures and directions are used:
  - $\mathbf{p}_j$ is considered a possible valley node if for all $i \in I : \kappa^j_{\min} < \kappa^i_{\min}$ is satisfied.
- If the zero crossing of extremality coefficients is required:
  - $\forall i \in I$: If $\varpi^j_{\max} \bullet \varpi^i_{\max} < 0$, the sign of the relevant extremality coefficient is reversed so $\tau^i_{\min} = -\tau^i_{\min}$.
  - $\mathbf{p}_j$ is considered a possible valley node if for any $i \in I : \tau^j_{\min} \times \tau^i_{\min} < 0$ and $\kappa^j_{\min} < \kappa^i_{\min}$ is satisfied.

The procedure of finding the zero crossing of curvature derivatives is more mathematically sound when determining crest nodes. This being the case, it would be the preferred method in determining whether a mesh node is likely to be part of a feature line. As in the smooth surface case, the sign of principal curvature directions are not uniquely defined. This is because curvature lines follow line fields and not vector fields [33].

From Equations (4.2) and (4.3) the zero crossing of extremality coefficients are required. These zero crossings of τ depend on a consistent choice for the sign of the principal directions between neighbours. Should the orientation of a neighbouring principal direction be reversed, the sign of the corresponding τ as determined from Equation (4.9) also needs changing.

Due to higher order terms present in the polynomial surface approximation, the resulting curvature derivatives are very sensitive to surface discretisation. The different approaches possible to extract curvature lines by either principal curvatures or the zero crossing of extremality coefficients is visible in the results of Figures 4.15 through 4.18. Although using principal curvatures seem to detect less false crest lines, it is still somewhat prone to report these. Both methods however recover the main lines of interest in a similar fashion and after appropriate thresholding should result in approximately the same reported features .

As the detection of crest lines is sensitive to surface discretisation, subdivided faces without sufficient smoothing could for example recover the original mesh edges as features. This can be seen in the seemingly repeated lines or parts thereof on the refined dolphin geometry of Figure 4.18 and false crest nodes on the refined trim-star geometry of Figure 4.19 (a). As with other spurious or false lines, most

UNIVERSITEIT VAN PRETORIA
UNIVERSITY OF PRETORIA
YUNIBESITHI YA PRETORIA

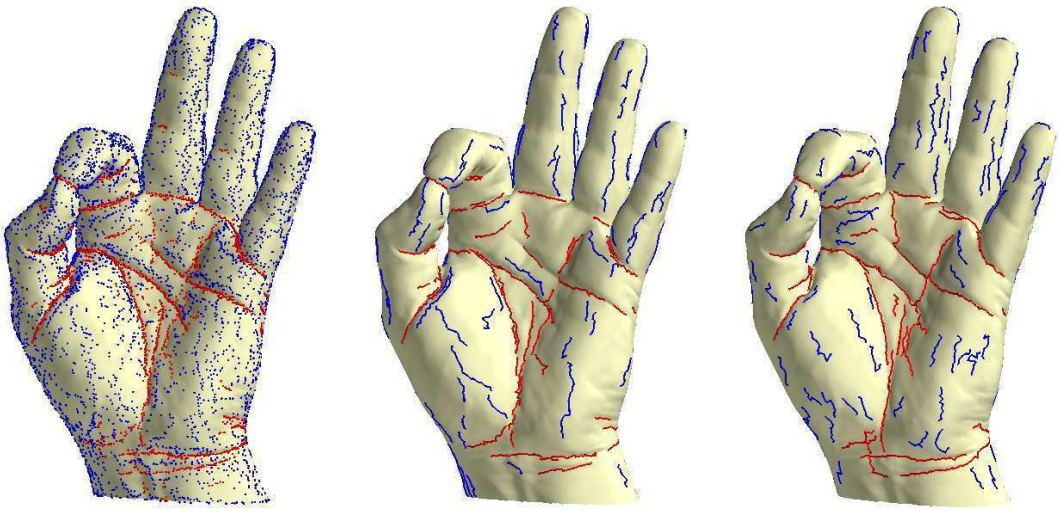

(a) (b) (c)

Figure 4.15: Crest nodes and lines on a hand geometry. (a) Possible ridge (blue) and valley (red) points obtained by using only principal curvatures and derivatives along with (b) the lines after connecting points in the relevant principal direction. (c) The equivalent ridge and valley lines obtained by using curvature derivative zero crossing procedure. For visual clarity only lines with more than 8 segments are displayed.

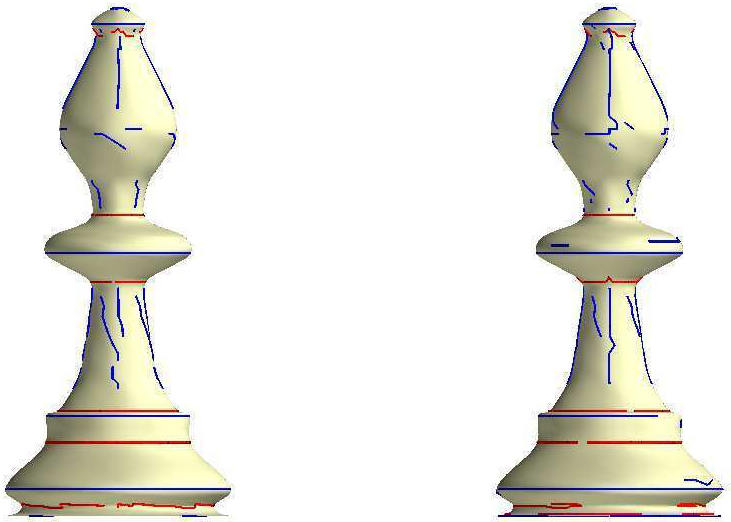

(a) (b)

Figure 4.16: Crest lines on a refined and smoothed bishop geometry. (a) Ridge (blue) and valley (red) lines obtained by using only principal curvatures and directions. (b) The equivalent ridge and valley lines obtained by using curvature derivative zero crossing procedure.

UNIVERSITEIT VAN PRETORIA
UNIVERSITY OF PRETORIA
YUNIBESITHI YA PRETORIA

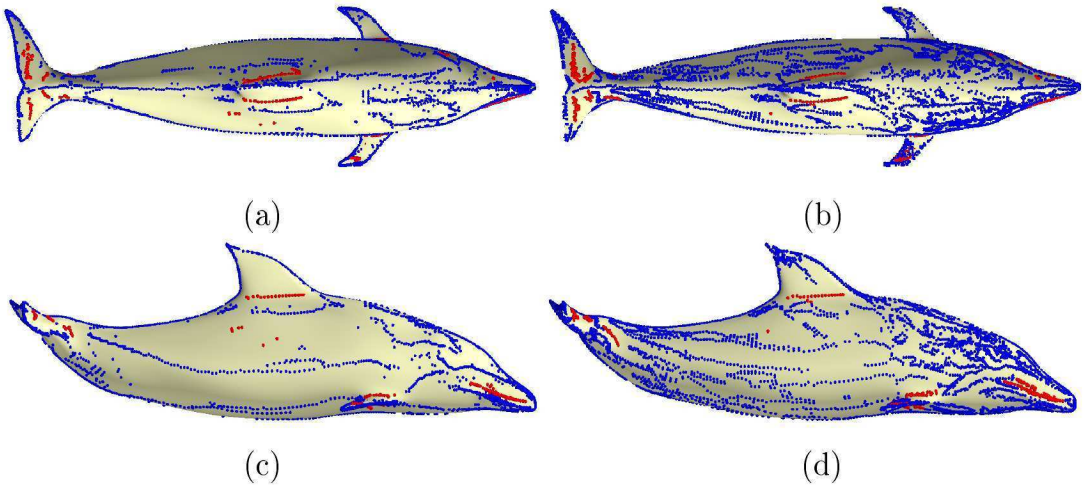

(a) (b)

(c) (d)

Figure 4.17: Crest nodes on the refined version of a dolphin geometry. (a) and (c) Ridge (blue) and valley (red) nodes obtained by using only principal curvatures and directions. (b) and (d) The equivalent ridge and valley nodes obtained by using curvature derivative zero crossing procedure.

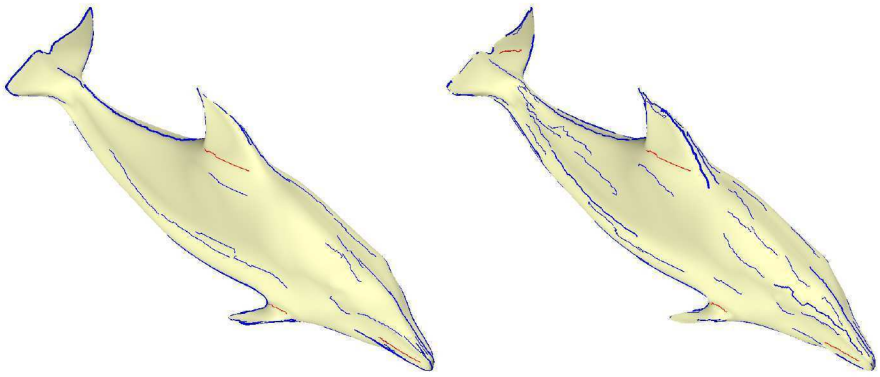

(a) (b)

Figure 4.18: Crest lines on the refined version of a dolphin geometry. (a) Ridge (blue) and valley (red) lines obtained by using only principal curvatures and directions. (b) The equivalent ridge and valley lines obtained by using curvature derivative zero crossing procedure. Lines have been pruned and line width scaled according to threshold calculated with Equation (4.11) and a minimum threshold value of $T_h = 10$.

UNIVERSITEIT VAN PRETORIA
UNIVERSITY OF PRETORIA
YUNIBESITHI YA PRETORIA

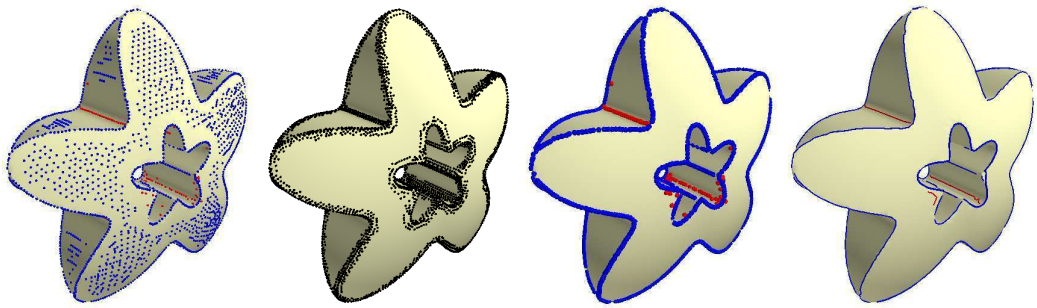

(a) (b) (c) (d)

Figure 4.19: Extracted ridge (blue) and valley (red) lines on the refined trim-star geometry. (a) Extracted crest nodes with presence of false edges already evident on the smoother areas of the geometry. (b) Allowable crest nodes after filtering out those that don't satisfy the local structure tensor condition $\lambda_1 < 10 \times \lambda_2$. (c) The extracted crest nodes that satisfy the local structure tensor filtering condition in (b). (d) The ridge and valley lines constructed using only the filtered crest nodes. In this figure some spurious or false lines are still present indicating that thresholding might still be required. These false lines are likely picked up due to the local discretisation.

of these lines on the dolphin geometry could be pruned. Unfortunately those with sufficient curvature or those that form part of a line with sufficient threshold are still reported when using the implemented method.

Figures 4.19 and 4.20 illustrate the use of the local structure tensor information to filter ridge and valley nodes.

Connecting nodes into lines

To obtain ridge and valley lines the extracted crest nodes are connected in the direction of principal curvature. Ridges follow the direction of minimum curvature while valleys follow the maximum curvature directions. When connecting the ridge and valley lines, it is again important to note that the orientation of the principal direction is irrelevant. Starting at nodes with maximum curvature:

- For each extracted crest node, a search is performed in both positive and negative orientation of the principal curvature direction.
- Neighbouring crest nodes found in these directions are then considered possible line segment partners.
- A connection is made to these neighbouring nodes.

UNIVERSITEIT VAN PRETORIA
UNIVERSITY OF PRETORIA
YUNIBESITHI YA PRETORIA

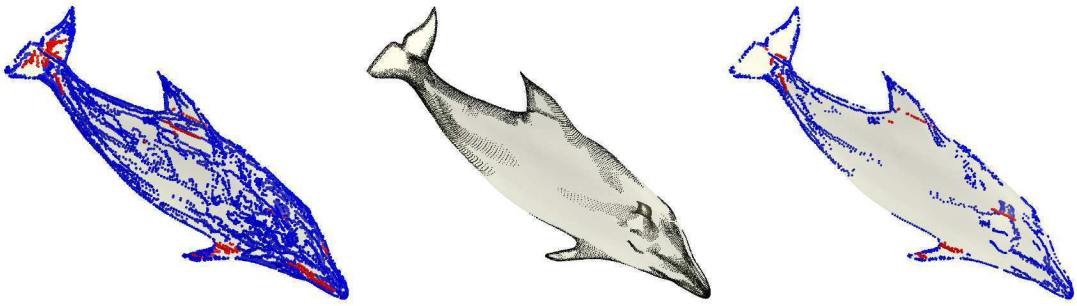

(a) (b) (c)

Figure 4.20: Filtering crest nodes on the refined version of a dolphin geometry. (a) Ridge (blue) and valley (red) nodes extracted using 100 nearest neighbour search with extremality zero crossing procedure. (b) Points for feature areas satisfying $\lambda_1 < 100 \times \lambda_2$ resulting from 3-ring neighbourhood local structure evaluation. (c) Ridge and valley nodes remaining after the filter procedure.

  - If more than one possible neighbour is detected in a given principal direction orientation, a connection is made to the neighbour who lies more in this direction.

- If any remaining neighbours have been detected as possible crest nodes, these are pruned.

Thresholding

Thresholding is used to get rid of insignificant or false reported ridge and valley lines. The criterion selected and implemented in this report first assigns a single value to every line. This value could be obtained by integrating a curvature or extremality dependent function along the line.

The chosen method implemented involves determining a line threshold as [45]

$$T_h = \int \kappa ds \approx \frac{1}{2} \sum_{i=1}^{n} \|\mathbf{p}_{i+1} - \mathbf{p}_i\| \left(\kappa_{i+1} + \kappa_i\right). \tag{4.11}$$

This calculation uses the trapezoid approximation of the integral. Here, the length of each line segment is multiplied with the average line curvature. For ridges, the κ value is taken as $\kappa_{\max}$ while $-\kappa_{\min}$ is used when determining valley line threshold values.

All of the lines with a threshold value below a user specified scalar value are pruned. In addition, the use of the local structure tensor is also seen as an easy

UNIVERSITEIT VAN PRETORIA
UNIVERSITY OF PRETORIA
YUNIBESITHI YA PRETORIA

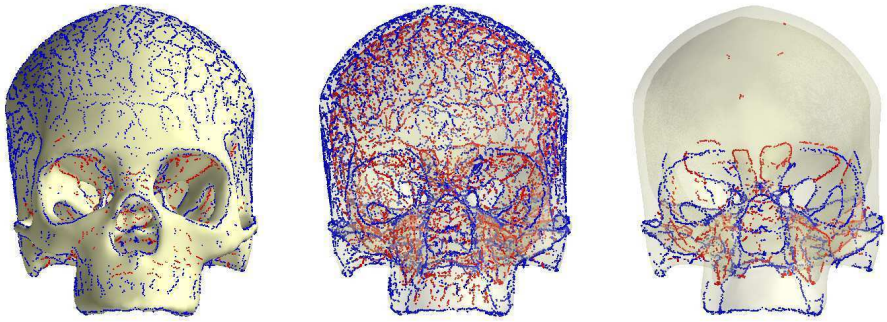

(a) (b) (c)

Figure 4.21: Frontal view of the skull geometry with extracted ridge nodes in blue and valley nodes in red. (a) and (b) show all of the crest nodes on the geometry and (c) contains only nodes that satisfy the local structure tensor condition $\lambda_1 < 50 \times \lambda_2$.

method to avoid unnecessary computation. If the results of a local structure tensor analysis is available or easily determined, the areas containing possible feature curves could first be extracted. Fitting a local smooth surface approximation and determining curvatures, curvature directions and derivatives can then be done on only the filtered areas. Alternatively it could be applied to only preserve crest nodes within a user specified feature rich area.

In Figure 4.19 the effect of local structure tensor filtering is visible. Here the entire method of approximating a local smooth surface and extracting feature lines was first applied. It was then filtered to only keep nodes where $\lambda_1 < 10 \times \lambda_2$. The resulting feature lines require less effort to determine an appropriate threshold value.

The possibility of using the local structure tensor result as a pre-curvature estimation step is also considered. Figures 4.21 through 4.23 show crest nodes extracted from a skull geometry. The first case was run on the entire skull model, finding 10'977 ridge and 8'170 valley nodes. A local structure tensor filter was then applied to find nodes where $\lambda_1 < 50 \times \lambda_2$. This is implemented using a nearest neighbour search for 30 of the closest nodes. The MLS approximated implicit surface and crest node extraction procedure was then done on only the 36'617 nodes satisfying the local structure filter instead of the 191'957 nodes of the original model geometry. The resulting 2'936 ridge and 1'708 valley nodes are connected into lines without the need for much additional thresholding. The final thresholded lines with more than 4 line segments are displayed in Figures 4.24 and 4.25.

UNIVERSITEIT VAN PRETORIA
UNIVERSITY OF PRETORIA
YUNIBESITHI YA PRETORIA

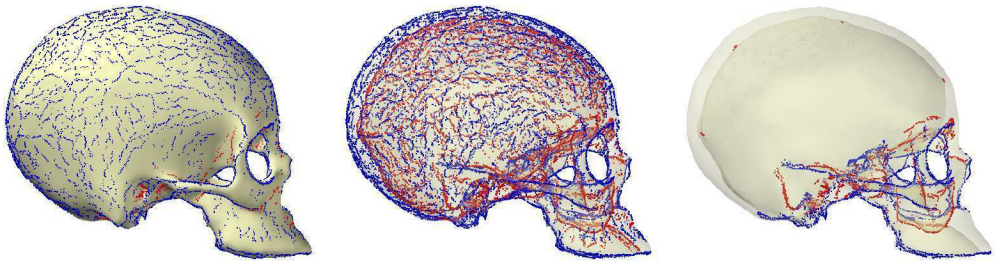

(a) (b) (c)

Figure 4.22: Side view of the skull geometry with extracted ridge nodes in blue and valley nodes in red. (a) and (b) show all of the crest nodes on the geometry and (c) contains only nodes that satisfy the local structure tensor condition $\lambda_1 < 50 \times \lambda_2$.

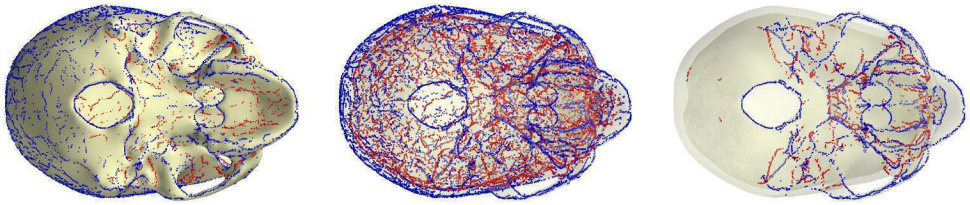

(a) (b) (c)

Figure 4.23: Lower view of the skull geometry with extracted ridge nodes in blue and valley nodes in red. (a) and (b) show all of the crest nodes on the geometry and (c) contains only nodes that satisfy the local structure tensor condition $\lambda_1 < 50 \times \lambda_2$.

4.4 The Selection of Matching Features

The information obtained from a local structure tensor analysis can be used to first evaluate the existence of specific features in a given geometry. This would be the first step to determine something akin to feature covariance between like geometries.

Where closely similar geometries need registering, problems would occur for instances where there is a difference in the topology or if the features overlap as in the case with creating a symmetric smoothed skull geometry in Figure 3.11.

Differences in topology can arise from the geometry itself such as a bullet wound in one skull and no equivalent trauma on the other or even skull degradation. It could also arise as a result of post-processing when surface representations are constructed from MRI or Computed Tomography (CT) scan data. A requirement to completely register a reference skull onto the target geometry would therefore almost certainly develop the need to alter the connectivity of the reference mesh. This would then destroy the required one-to-one consistent mapping between all

UNIVERSITEIT VAN PRETORIA
UNIVERSITY OF PRETORIA
YUNIBESITHI YA PRETORIA

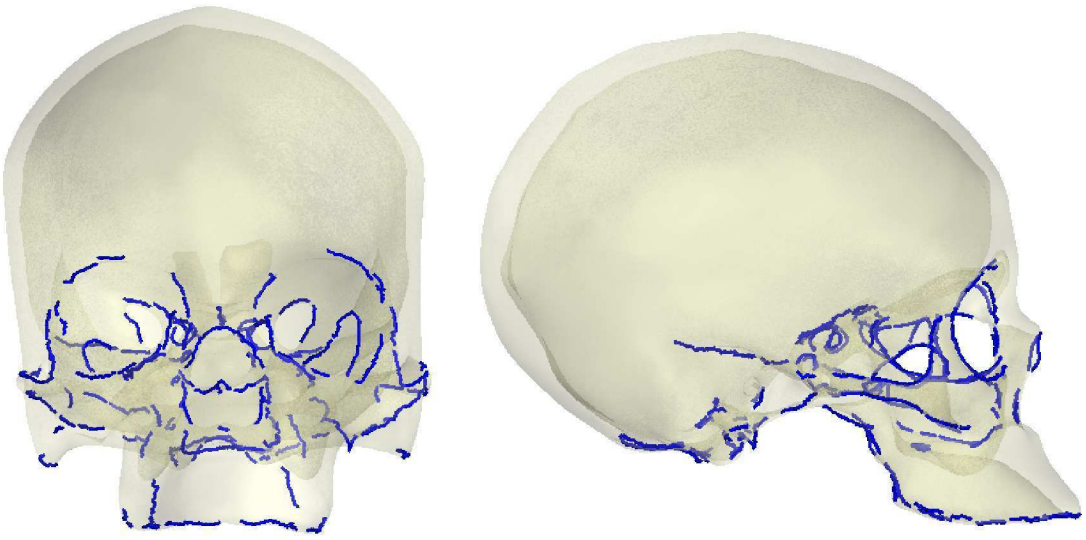

(a) (b)

Figure 4.24: Thresholded ridge lines on the skull geometry after first applying the filter $\lambda_1 < 50 \times \lambda_2$ and then thresholding lines to $T_h = 200$. (a) Frontal and (b) lateral view. Only lines with more than 4 line segments are displayed.

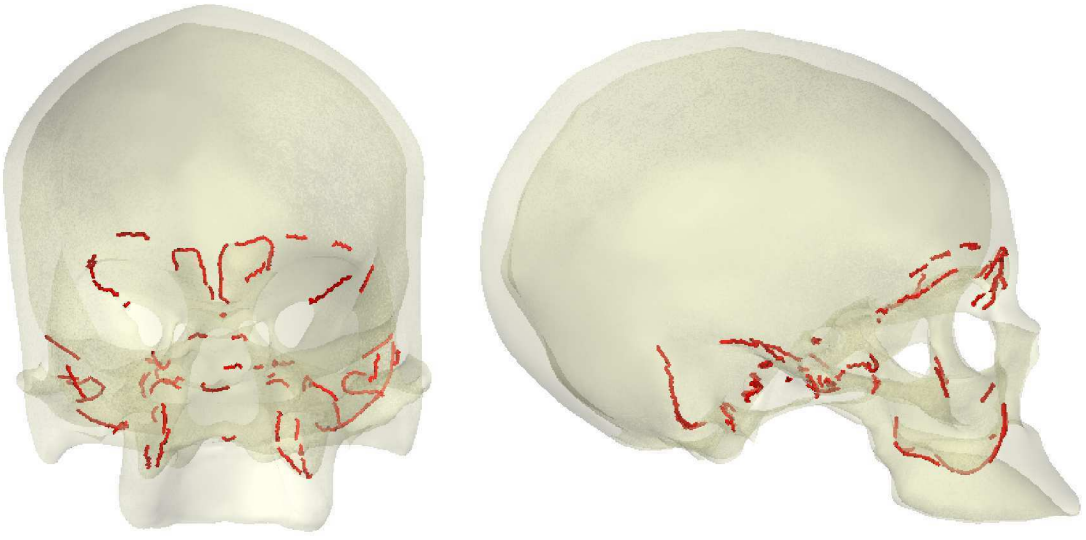

(a) (b)

Figure 4.25: Thresholded valley lines on the skull geometry after first applying the filter $\lambda_1 < 50 \times \lambda_2$ and then thresholding lines to $T_h = 200$. (a) Frontal and (b) lateral view. Only lines with more than 4 line segments are displayed.

UNIVERSITEIT VAN PRETORIA
UNIVERSITY OF PRETORIA
YUNIBESITHI YA PRETORIA

registered geometries in the sample.

To overcome this problem, a registration routine is required where only selected features are matched. The extraction of feature lines makes it possible to better quantify and describe features within a given geometry. These lines could be used to determine similarities between objects.

If a line or line segment has no equivalent in another geometry of interest, it could be discarded after registration. In this way only matched features would be used in eventually determining the deformation required to morph one geometry into another.

Chapter 5

Feature Registration

With features extracted from both a base and target surface, feature registration can be performed before elastic surface registration in an attempt to improve the registration result. The use of feature points in mesh deformation is discussed using radial basis function interpolation (RBF) in this chapter.

The registration of feature lines is implemented with the help of literature resources and applied as an adaptation of the elastic surface registration procedure previously implemented. Registering feature lines as a step before elastic surface registration is then applied and illustrated. In creating the symmetric smooth skull, this step greatly improves the final registered result.

It is then applied to the registration of the orthognathic skull geometry with less success. Here the vast difference in topology and non-corresponding features are seen to cause undesired results. This is due to the way in which the registration is performed. All nodes and all surfaces are used in the original elastic registration procedure. This presents a few issues where points or surfaces on the target geometry have no equivalent on the generic mesh for example.

Because of the difficulty in registering the generic shape to the orthognathic skull form, it is suggested that only user selected features be registered along with featureless surfaces. The feature areas associated with unregistered features are then classified as forbidden and ignored during elastic surface registration. The generic mesh is deformed using only the registration on allowable surfaces. This suggestion greatly reduces the amount of user interference required in registering these complex geometries, as will be seen in Chapter 6.

UNIVERSITEIT VAN PRETORIA
UNIVERSITY OF PRETORIA
YUNIBESITHI YA PRETORIA

5.1 Feature Point Registration

Feature points are classically marked manually in the study of geometric morphology. The landmark positions in Figure 1.1 for example could be obtained by marking these points on a skull with a digital stylus. The digitised landmark coordinates of a statistical sample of skulls can then be used in a statistical analysis where certain shape characteristics and their relationships are investigated.

Landmark coordinates could also be obtained manually or automatically from digital surface representations. Matched points on a surface mesh could be marked and the difference and similarity between shapes could be studied in the same way.

In this subsection, a short overview of Radial Basis Function (RBF) interpolation is discussed with particular detail given to the Thin Plate Spline (TPS) basis function. RBFs and specifically the TPS is most commonly used in geometric morphology to graphically represent the deformation or difference between generic and target landmark coordinates within a statistical sample [42, 54]. Deforming a base mesh to a target configuration may also be done using radial basis function interpolation as it is inexpensive. This is because connectivity is not required in deforming a mesh.

Shape context feature points are also commonly used in registration and is briefly mentioned in Appendix C. This is an automatic method for finding correspondences between all the points in a shape or feature points extracted after applying differential geometry for example. These points are classified using histograms within a greater shape context.

5.1.1 Radial Basis Function Interpolation

Radial Basis Function Interpolation can be applied to scattered data. If a spatial distribution of points exist with displacements or field values known at a select few locations for example, an interpolated field can be approximated.

In [26], RBF interpolation is used to update the mesh used in a Fluid Structure Interaction (FSI) simulation. The displacement of the internal nodes to a fluid mesh are derived from the given displacement of the structural nodes on the interface.

The interpolation function describing a displacement field for example is ap-

UNIVERSITEIT VAN PRETORIA
UNIVERSITY OF PRETORIA
YUNIBESITHI YA PRETORIA

proximated by the sum of basis functions

$$S(\mathbf{x}) = \sum_{i=1}^{N_b} \alpha_i \phi\left(\|\mathbf{x} - \mathbf{x}_{b_i}\|\right) + p(\mathbf{x}) \tag{5.1}$$

where $\mathbf{x}_{b_i}$ are the coordinates with known displacement values, $p(\mathbf{x})$ is a polynomial and N_b the number of coordinates with known displacement. The function $\phi(d)$ is a basis function with respect to the euclidean distance d.

The minimal degree of polynomial $p(\mathbf{x})$ depends on the choice of basis function. Choosing to use conditionally positive definite basis functions of order $m \leq 2$ allows the use of a linear polynomial. This has the added advantage that rigid body translations are exactly recovered [26].

The coefficients α_i and polynomial are determined from interpolation conditions. This is done by solving the system

$$\begin{Bmatrix} \mathbf{d}_b \\ \mathbf{0} \end{Bmatrix} = \begin{bmatrix} \mathbf{M}_{b,b} & \mathbf{P}_b \\ \mathbf{P}_b^T & \mathbf{0} \end{bmatrix} \begin{Bmatrix} \boldsymbol{\alpha} \\ \boldsymbol{\beta} \end{Bmatrix} \tag{5.2}$$

with $\mathbf{d}_b$ the known displacements. $\mathbf{M}_{b,b}$ is an $n_b \times n_b$ matrix containing the evaluation of the basis function

$$\phi_{b_i b_j} = \phi\left(\left\|\mathbf{x}_{b_i} - \mathbf{x}_{b_j}\right\|\right). \tag{5.3}$$

$\mathbf{P}_b$ is an $n_b \times 4$ matrix with $\mathbf{P}_{b_i} = \begin{Bmatrix} 1 & x_{b_i} & y_{b_i} & z_{b_i} \end{Bmatrix}$. The coefficients α_i are contained in $\boldsymbol{\alpha}$ and $\boldsymbol{\beta}$ contains the coefficients of the linear polynomial. With the system solved, finding the displacement at an unprescribed coordinate in the field simply requires the evaluation of the interpolation function in Equation (5.1).

Various radial basis functions are available, many of them finding application within specific fields of research. In geometric morphology for instance, the thin plate spline (TPS) is commonly used to visualise modes of variation between subjects in a statistical sample or to visualise the difference between subjects [42, 54]. An example of one of these studies on the geometric morphology of African lowland Gorilla scapulae is illustrated in Figure 5.1. Here the landmarks are visible in (a) with the measurements in (b) and the transformed coordinates after applying the Procrustes[1] method in (c). The TPS radial basis function is finally used to illustrate

[1] Translation, reflection, orthogonal rotation and scaling of a set of points to best conform them to a set of reference points. The fit is evaluated using the sum of squared errors between corresponding points [42].

UNIVERSITEIT VAN PRETORIA
UNIVERSITY OF PRETORIA
YUNIBESITHI YA PRETORIA

Name	Function
CP C^0	$(1-\xi)^2$
CP C^2	$(1-\xi)^4(4\xi+1)$
CTPS C^0	$(1-\xi)^5$
CTPS C^1	$1+\frac{80}{3}\xi^2-40\xi^3+15\xi^4-\frac{8}{3}\xi^5+20\xi^2 log(\xi)$
Linear	x
Cubic	x^3
Thin plate spline (TPS)	$x^2 log(x)$
Multi-quadratic bi-harmonic (MQB)	$\sqrt{a^2+x^2}$
Inverse multi-quadratic bi-harmonic (IMQB)	$(a^2+x^2)^{\frac{-1}{2}}$
Gaussian (G)	$exp(-x^2)$

Table 5.1: Some radial basis functions with compact support $f(\xi)$ and global support $f(x)$

the variation between male and female Gorilla scapulae.

Radial basis functions can be divided into two groups: functions with global support and functions with local support [26]. Local or compact support functions are generally scaled with a support radius r such that $\xi = x/r$. The basis function $\phi_r = \phi(\xi)$ is then used instead of the original $\phi(x)$.

Using compact support mainly moves the nodes within a circle or sphere of radius r around the nodes with known displacement. Large support radii result in greater support and so involves solving denser matrices. This is also always the case when dealing with functions with global support.

A list of RBFs are documented in Table 5.1. The MQB and IMQB methods have an additional parameter a that controls the shape of the function. Larger a values result in functions that are flatter with smaller values resulting in narrow cone-like functions.

Applying a few radial basis functions to the deformation of a base dolphin geometry is illustrated in Figure 5.2. For the two different dolphin geometries 14 landmark positions were marked manually. RBF interpolation is then used to deform the mesh if these points on the one dolphin is required to match the landmark positions on the target dolphin exactly.

Different functions have a totally different effect on the deformed mesh. From this simple example it seems that more landmarks are required to better deform the one geometry into an approximate representation of the other.

If a feature point registration procedure like shape context correspondence briefly

UNIVERSITEIT VAN PRETORIA
UNIVERSITY OF PRETORIA
YUNIBESITHI YA PRETORIA

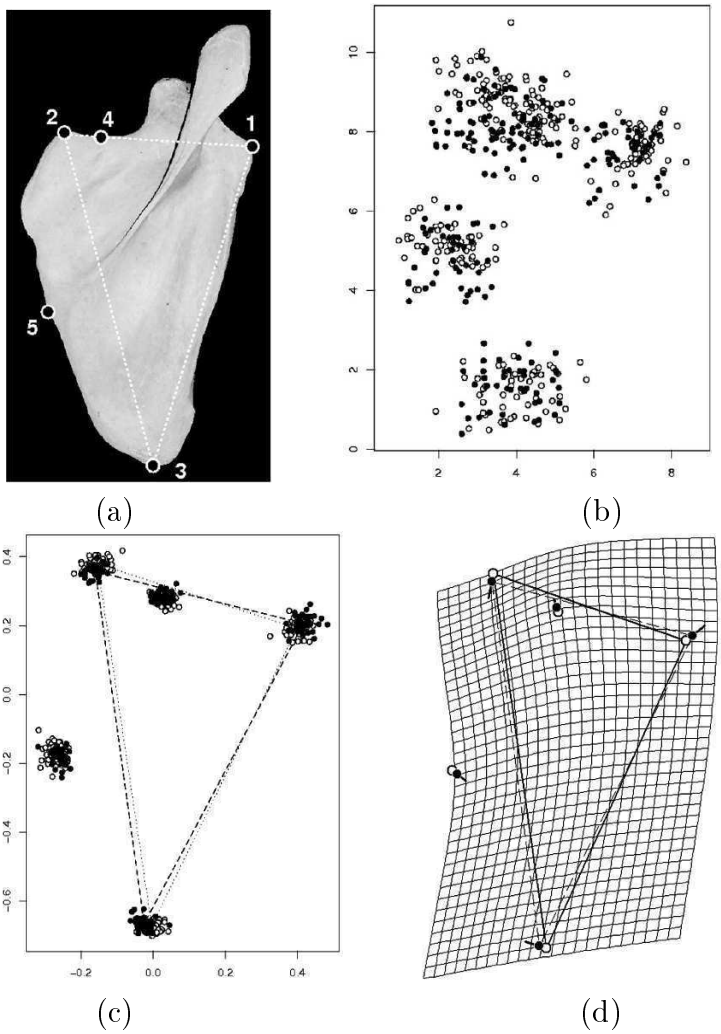

Figure 5.1: Geometric dissimilarity illustrating the average shape of the scapula of male ($n_m = 52$, *open symbols*) and female ($n_f = 42$, *closed symbols*) western African lowland Gorillas. (a) Recorded coordinates of homologous points on each specimen. (b) The varying coordinates due to difference in shape as well as location and orientation with respect to axes during landmark digitisation. (c) Superimposed landmark coordinates after applying the Procrustes method. The common coordinate system allows for further statistical analysis. (d) Visualising statistical results, the average male-female variation is shown using both difference vectors and a thin plate spline deformation grid magnified by a scale factor of two [54].

UNIVERSITEIT VAN PRETORIA
UNIVERSITY OF PRETORIA
YUNIBESITHI YA PRETORIA

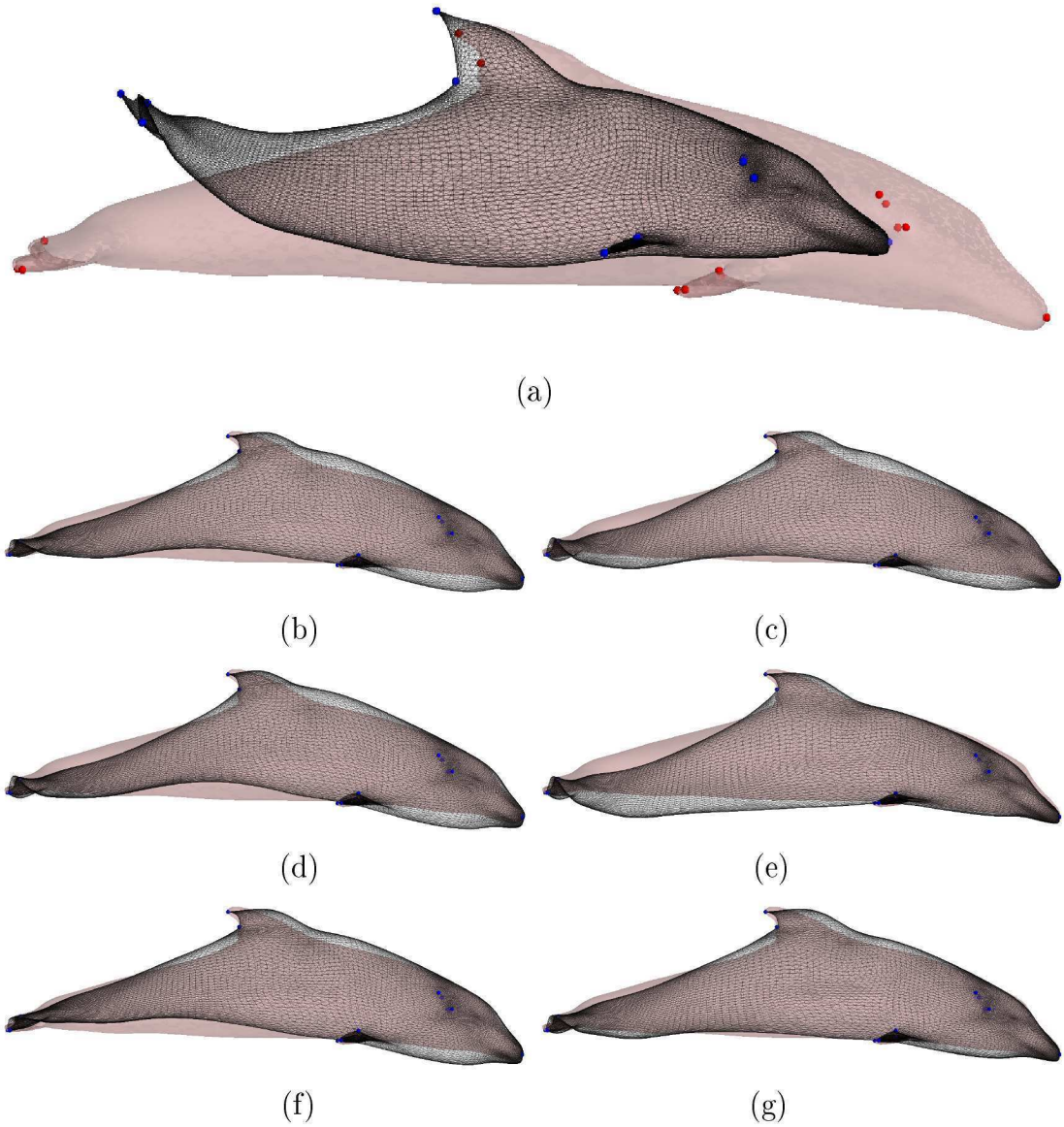

Figure 5.2: Radial Basis Function Performance. (a) Original Configuration (b) MQB, (c) IMQB, (d) Gauss, (e) Linear, (f) Cubic, (g) TPS. The deformable mesh is displayed as a black wire-frame and the target as the semi-opaque pink surface. The blue dots indicate deformable landmark positions and the red dots the target positions. In (b) through (g) these landmark coordinates coincide exactly.

UNIVERSITEIT VAN PRETORIA
UNIVERSITY OF PRETORIA
YUNIBESITHI YA PRETORIA

discussed in Appendix C is used, deformation could be determined by radial basis function interpolation. It is decided that the scope of work covered by this report would not include additional surface registration procedures but only work with the original elastic surface registration procedure implemented. If landmark coordinates or landmark coordinate displacement is available, radial basis function interpolation could be used before performing full surface registration. This step would result in a preferred initial condition when performing elastic surface registration.

5.2 Feature Line Registration

Crest lines like those extracted from a surface mesh in subsection 4.3.4 of this report, or even those obtained from something like voxel density data, can be compared and registered. The methodology and approach of Subsol *et al.* [59] is explained in this section for matching sets of feature lines in a generic and target geometry.

In their work, correspondences are found between sets of features by using a non-rigid registration algorithm. Common features are identified and common feature subsets are used in creating an automatic anatomical atlas of the human skull. This is all done to finally average the features in the creation of the atlas from where a variability analysis is done on common feature positions. Their registration procedure is outlined in subsection 5.2.1 and the procedure implemented for this report is also detailed along with experimental results.

5.2.1 Registration Procedure

Given two sets of feature lines on two different geometries like that of Figure 5.3, the aim of Subsol *et al.* is to match and extract common features. A twofold result is sought [59] :

- Line correspondence: which line L_i on the target geometry $\mathcal{P}$ corresponds to a line L_j of geometry $\mathcal{M}$. This allows extracting the common lines to all models in the statistical set used in creating the atlas.

- Point correspondence: the points of each skull that correspond to the points on the skulls over the different sets are required. This is needed to finally do the averaging of the lines and also study inter-patient variability.

UNIVERSITEIT VAN PRETORIA
UNIVERSITY OF PRETORIA
YUNIBESITHI YA PRETORIA

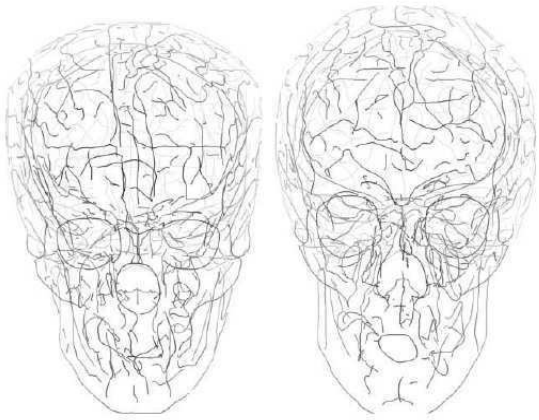

(a) (b)

Figure 5.3: Two sets of lines to be registered [59]. (a) The target skull $\mathcal{P}$ on the left is composed of 591 lines and 19'302 points. (b) Reference skull $\mathcal{M}$ on the right is composed of 583 lines and 19'368 points. These subjects have a variation in shape as well as differences in the number and topology of the lines.

The registration procedure proposed in their work uses a heuristic algorithm based on an iterative scheme, gradually updating the local registration. In implementing this, each feature location influences matching decisions made at other locations. This is done as an adaptation of the ICP [13] where the deformations between anatomical structures are modelled by affine, polynomial and spline functions.

Point Matching

At each iteration the points of the lines of $\mathcal{M}$ are linked with their closest neighbour in the lines of $\mathcal{P}$ with respect to the Euclidean distance. This preliminary simple matching gives an initial list of point pairs. From Figure 5.4, it is seen that this simple closest point match is not bijective[2]. Here each point on the reference geometry feature set only has a single match whereas points on the target could have no correspondent or even more than one.

[2] A bijective match means that two conditions are satisfied: (1) Every one point in the model point set $\mathcal{M}$ is registered to at most one point in the data point set $\mathcal{P}$ (Injective / one-to-one). (2) Every point in the data point set $\mathcal{P}$ has at least one point match on the model set $\mathcal{M}$ (surjective / onto).

UNIVERSITEIT VAN PRETORIA
UNIVERSITY OF PRETORIA
YUNIBESITHI YA PRETORIA

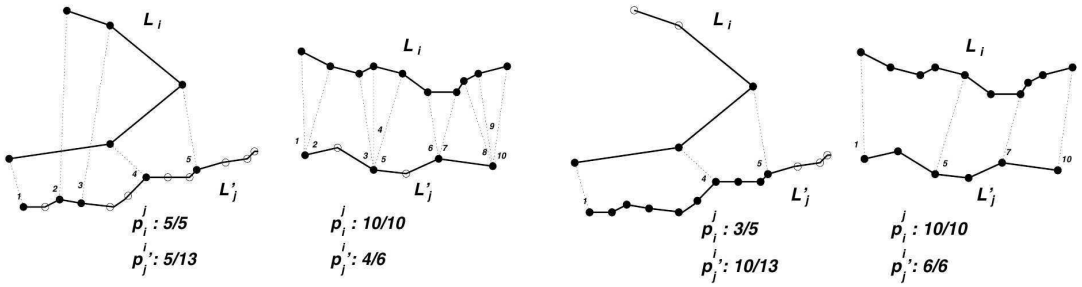

(a) (b)

Figure 5.4: Registering two lines [59]. (a) Illustration revealing that computing registration parameters is not obvious due to the non-bijectivity of matched points. (b) After discarding non-consistent matched points, line registration parameters are computed consistently.

Line Matching

In estimating whether two lines $L_i \in \mathcal{M}$ and $L'_j \in \mathcal{P}$ are registered, the portion of points of one line registered to the points of another line is needed.

The portion p_i^j of points on line L_i registered to L'_j and the portion p'^i_j of points on line L'_j registered to L_i are used. If p_i^j or p'^i_j is larger than a given threshold, it can be seen as a positive registration. Due to the non-bijectivity of the matched points, computing these registered portions is not simply done with the initial closest point registrations.

In Figure 5.4, this non-bijectivity is visible. In the example of a registration obtained in Figure 5.4 (a), 100% of line L_i is registered to 40% of L'_j. The points at 2 and 3 are joined to a portion of L_i that is invalid. This causes a cross match, resulting in non-physical deformation. In the example of a registration in Figure 5.4 (a), the multiple matching scenario is visible. These problems are addressed by introducing two additional constraints:

- An injectivity[3] constraint allows at most one link made between a point on L'_j and a point on L_i.
- The ordering of corresponding points are checked. This implies that the same portion of L'_j can not be matched to different portions of L_i.

[3] A one-to-one match for at least each point in the model shape $\mathcal{M}$ is injective. Every point in the model point set is registered to at most one point in the data point set $\mathcal{P}$

UNIVERSITEIT VAN PRETORIA
UNIVERSITY OF PRETORIA
YUNIBESITHI YA PRETORIA

The additional constraints are imposed by sorting the matched points according to their distance. This is because closer corresponding pairs are more likely to be a correct match. The most likely matched point p_0 of L_i is chosen as a starting point. The line is then followed in both directions. Each correspondence along a direction is inspected and treated accordingly:

- If the correspondence is made to a point on another line than that of p_0, the search propagation along that direction of the line is discontinued.
- If the corresponding point has already been marked, a cross or multiple matching could be present and the current matching is discarded. Further propagation along that direction of the line is again discontinued.
- If the correspondence has not been marked, the matching is kept. All points between the previous and the current matched point on L'_j are marked as also being matched to the line segment connecting the two matched points on L_i.
- Once the process has terminated, it is repeated using the next most likely match.

Treating initial matched points in this way, Subsol *et al.* [59] obtain a consistent point correspondence. Although points marked between positive matched points on the same line segment of L'_j aren't explicitly matched, their matches are used in determining the matched point portions p_i^j and p'^i_j. This procedure does not suddenly make the match bijective but at least allows for a consistent mapping from $\mathcal{M}$ to $\mathcal{P}$. Multiple matches onto the same point and cross matches are removed.

Registration portions are checked when applying the registration. Only the registration to lines above a user specified registration threshold is applied. If a threshold of 50% is chosen for example p_i^j, p'^i_j or both need to be above the required threshold for it to qualify as a positive registration.

Transformation Computation

Based on the matched points, Subsol *et al.* [59] compute a transformation T by minimising the least squares criterion:

$$\sum_{k \in \mathcal{M}^j} \left\| T\left(p_k^j\right) - p'^k_j \right\|_2^2 . \tag{5.4}$$

UNIVERSITEIT VAN PRETORIA
UNIVERSITY OF PRETORIA
YUNIBESITHI YA PRETORIA

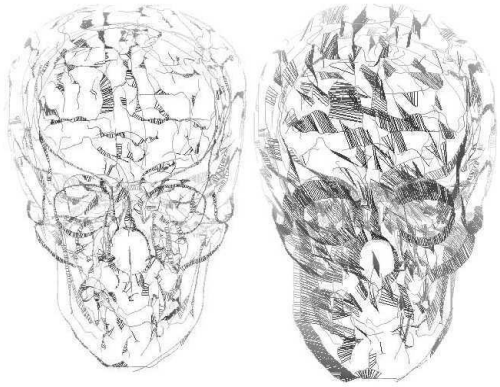

(a) (b)

Figure 5.5: Registration of $\mathcal{M}$ towards $\mathcal{P}$ [59]. (a) The deformed set $\mathcal{M}$ with $\mathcal{P}$. Matched points are linked with the two sets reasonably superimposed. In (b) $\mathcal{M}$ is in it's original position, allowing an estimated extent of the deformation between the two sets.

Here k resembles a matched point out of the total point correspondence list $\mathcal{M}^j$. This point of $\mathcal{M}$ and it's corresponding point in $\mathcal{P}$ are given as p_k^j and p'^k_j.

In their procedure Subsol *et al.* [59] used a constant iteration scheme. 30 iterations are performed with the required registration threshold incremented from 0% to 50%. In the first 10 iterations rigid transformation is applied. 10 iterations of affine transformation[4] is followed and the final 10 iterations are used to apply spline transformations.

The registration of one skull's feature lines to another in Figure 5.3 as done by Subsol *et al.* is seen in Figure 5.5. To build the anatomical atlas, six skulls were registered to one another and the registration used in setting up a registration map. This registration map is used as a consistency check and an example of one of these maps is displayed in Figure 5.6.

The registration map is used to extract features common to all subjects in the sample. These common features and their positive registrations are used to build the final skull atlas shown in Figure 5.7.

[4]An affine transformation between two vector spaces comprises a linear transformation and translation. Mapping $\mathbf{x}$ to a different vector space with an affine transformation: $\mathbf{x} \mapsto \mathbf{A}\mathbf{x} + \mathbf{b}$.

UNIVERSITEIT VAN PRETORIA
UNIVERSITY OF PRETORIA
YUNIBESITHI YA PRETORIA

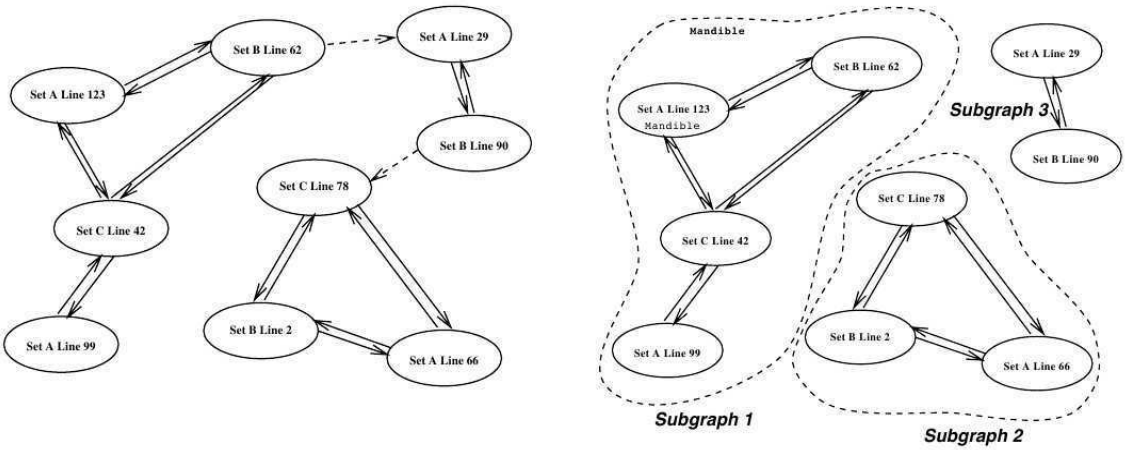

(a) (b)

Figure 5.6: Building and using a topological registration map [59]. (a) The registration graph: each node is a line of a set and an oriented link represents the relation "is registered with". (b) Extracted subsets of corresponding lines of different data sets. If a sub-graph contains at least one line of each data set, it defines a subset of common lines found on all geometries in the sample.

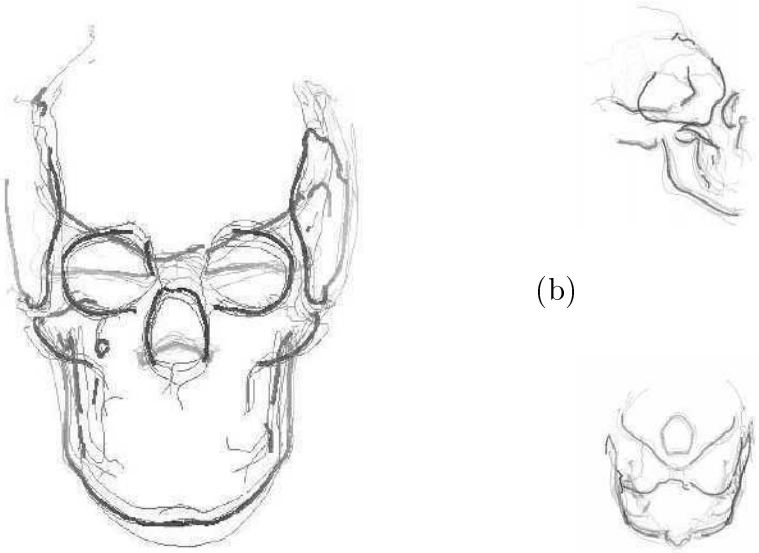

(a) (b) (c)

Figure 5.7: Common lines to all six skulls used by Subsol *et al.* [59]. The thin lines show the lines of the different geometries used and the thicker lines the average common lines constituting the atlas.

UNIVERSITEIT VAN PRETORIA
UNIVERSITY OF PRETORIA
YUNIBESITHI YA PRETORIA

Implementation

In this report a slightly different procedure was implemented. The same ideas presented in [59] are used but combined with work done on the full surface registration implemented earlier in this study. After obtaining the feature lines:

- The target object $\mathcal{P}$ is first oriented to best fit the generic shape $\mathcal{M}$ using the iterative closest point procedure described in subsection 3.1.1.
- Point correspondences are obtained in the same way as done by Subsol *et al.* [59]. This is however not only done for $\mathcal{M}$ onto $\mathcal{P}$ but also for $\mathcal{P}$ onto $\mathcal{M}$. An additional requirement is also added that the dot product of matched point unit normals be greater than zero.
- Correspondences with a distance greater than a user specified value is discarded.
- Correspondences are filtered for both sets in the same way as Subsol *et al.* [59] to get rid of inconsistent point matches.
- The closest line segment to each inexact matched point is inspected. The closest point on that line segment is determined as a possible final matched coordinate.
- Using the matched points and their registered positions, a smooth deformation field is applied. This is done as in the elastic surface registration algorithm of Bryan *et al.* [19] with the use of Equation (3.8).
- Registration and deformation is applied iteratively using the same parameters as in the original elastic registration procedure of subsection 3.2.1.

Application

The performance of the implemented feature registration procedure is illustrated using two dolphin geometries. The two original geometries is obtained from the INRIA model shape repository [4]. The one geometry is then refined, manipulated and smoothed to generate the target geometry in the feature registration example. The other geometry is only refined and smoothed. Registration of the features on the dolphin geometries is presented in Appendix D of this report with only the lateral views of Figures D.1 through D.3 reproduced in Figure 5.8 for visual clarity.

UNIVERSITEIT VAN PRETORIA
UNIVERSITY OF PRETORIA
YUNIBESITHI YA PRETORIA

Crest lines on the two geometries are extracted and thresholded to get rid of less significant lines. The target geometry and it's crest lines are displayed in Figure 5.8 (a) and D.1. In this figure the lines on the generic dolphin shape is also displayed in it's original position.

A rigid registration is performed on the target geometry allowing isotropic scale with upper and lower constraints set as 0.5 and 1.5. The results of the isotropic scale ICP registration is displayed in Figures 5.8 (b) and D.2. After rigid registration, the feature line registration procedure is implemented to deform the lines on the generic dolphin geometry to better represent that of the target. Registered and deformed lines are visible in Figures 5.8 (c) and D.3. Only registered lines with a matched point portion of at least 50% are used and displayed.

5.3 Surface registration

Creating a symmetric smoothed skull with elastic surface registration is again performed. The smooth skull and it's reflection is taken in their position relative to one another following the rigid registration procedure discussed in section 3.3.

Registration of the ridge and valley lines of the skull onto the lines of its mirrored projection is performed before the elastic registration procedure. Lines on the smooth skull and it's reflection are visible in Figures 5.9 and 5.10. These figures demonstrate the registration of the one set of lines onto the other. After feature registration the average nodal coordinates before and after is obtained and also displayed. These average feature lines are noticeably more symmetric than the lines on the original smoothed skull geometry.

The deformed skull after feature registration is used as the initialised deformable surface when performing the elastic registration procedure. The final registration and the averaged symmetric skull representation are visible in Figures 5.11 (c) and (d).

To view the asymmetry of the original skull shape, the displacements back to the original skull form is used and applied with a factor of three. This asymmetry is displayed in Figure 5.12 (a). The distance from the averaged symmetric shape to the equivalent nodal coordinate on the original surface is also displayed in Figure 5.12 (b). In Figure 5.12 (b) the non-uniqueness of the registration procedure as inspected in subsection 3.2.2 is again visible. This is noticed when considering that the absolute distance value from the original mesh nodes to the symmetric

UNIVERSITEIT VAN PRETORIA
UNIVERSITY OF PRETORIA
YUNIBESITHI YA PRETORIA

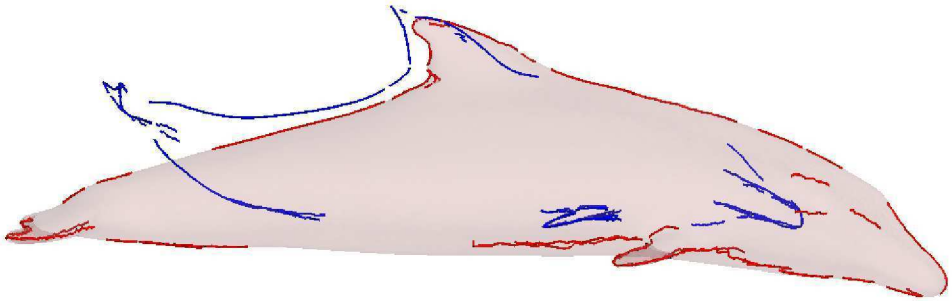

(a)

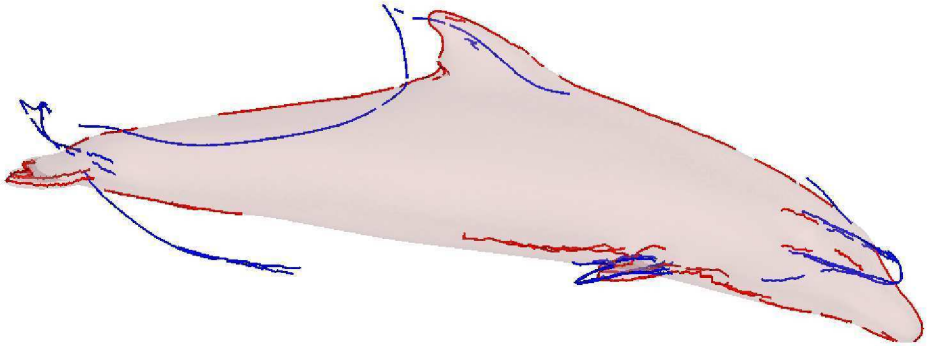

(b)

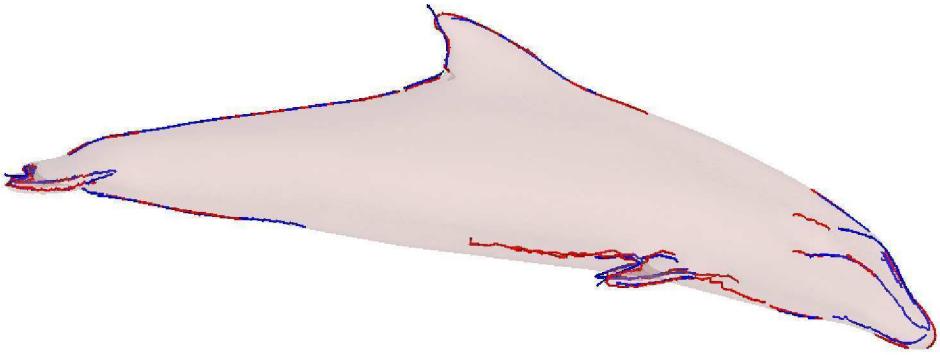

(c)

Figure 5.8: Feature line registration on dolphin geometries. (a) Original position of a target and base dolphin geometry. (b) Updated position of the target dolphin geometry relative to the base shape after isotropic scale ICP registration. (c) Feature registration of the base dolphin to the aligned target configuration at iteration 100. The target geometry is illustrated in its aligned position with the target features in red and the deformed base geometry features in blue.

UNIVERSITEIT VAN PRETORIA
UNIVERSITY OF PRETORIA
YUNIBESITHI YA PRETORIA

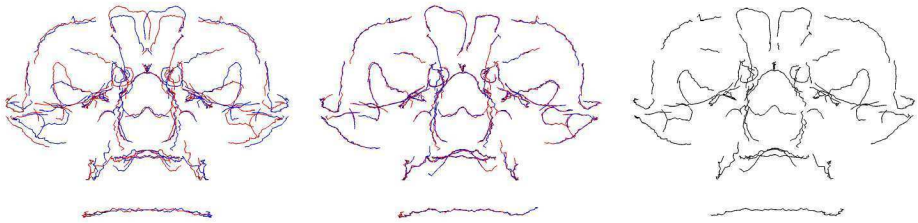

(a) (b) (c)

Figure 5.9: Frontal view of feature registration on the smooth skull and its reflection. (a) Feature lines of the smoothed skull and its reflection. (b) Feature registration result and (c) the average of the initial and registered positions to create a symmetric model. Blue lines indicate the features of the deformable surface with red lines indicating the target features.

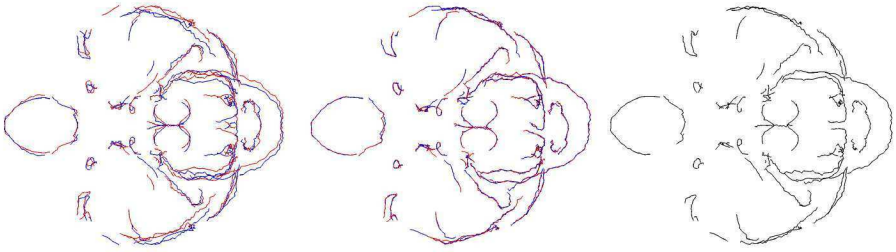

(a) (b) (c)

Figure 5.10: Lower view of feature registration on the smooth skull and its reflection. (a) Feature lines of the smoothed skull and its reflection. (b) Feature registration result and (c) the average of the initial and registered positions to create a symmetric model. Blue lines indicate the features of the deformable surface with red lines indicating the target features.

version is not in itself symmetric. It would seem that one side of the skull mesh has to deform more than the other side in order for a symmetric version to appear. The overall appearance of the color contours in Figure 5.12 (b) however is mainly symmetric in the facial region.

The results obtained in this chapter is compared to the initial registration results of Figure 3.11. Comparing these results in Figure 5.13, there is an improvement in the registered generic mesh when first applying feature registration.

5.3.1 Orthognathic Representation

The symmetric version of the smoothed skull is done to create an example generic skull surface for use in subsequent registrations. To test the registration of this

UNIVERSITEIT VAN PRETORIA
UNIVERSITY OF PRETORIA
YUNIBESITHI YA PRETORIA

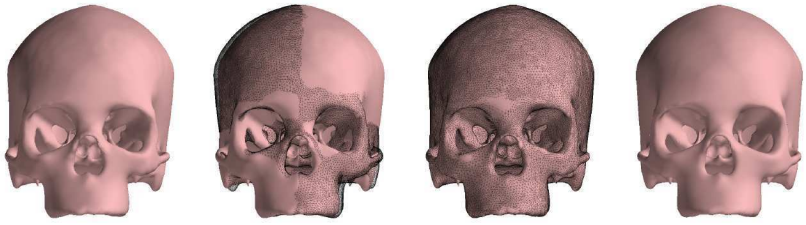

(a) (b) (c) (d)

Figure 5.11: Elastic surface registration of the smooth skull onto its reflection. The blue mesh in Figure 3.10 is set as the deformable mesh and is registered onto it's reflection. (a) Reflected smooth skull geometry. (b) Reflected smooth skull geometry set as the target with the original smooth skull shown as the black wire-frame. (c) Elastic surface registration results after first applying the feature registration of Figures 5.9 and 5.10. (d) The average of the smooth skull and registered nodal coordinates resulting in a symmetric skull surface.

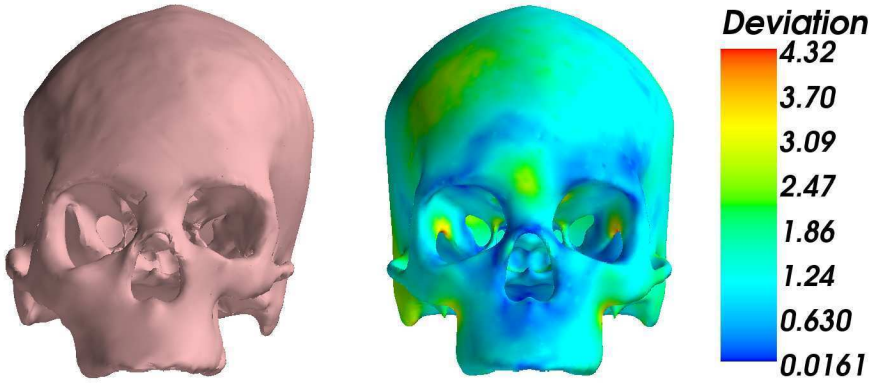

(a) (b)

Figure 5.12: Asymmetry in the original smooth skull geometry. (a) Displacement from the symmetric skull mesh coordinates back to the original scaled by a factor of 3. (b) The absolute distance (norm of the distance vector) from the original to symmetric nodal coordinates illustrated as scalars on the symmetric skull representation. The color bar values are in millimeters.

UNIVERSITEIT VAN PRETORIA
UNIVERSITY OF PRETORIA
YUNIBESITHI YA PRETORIA

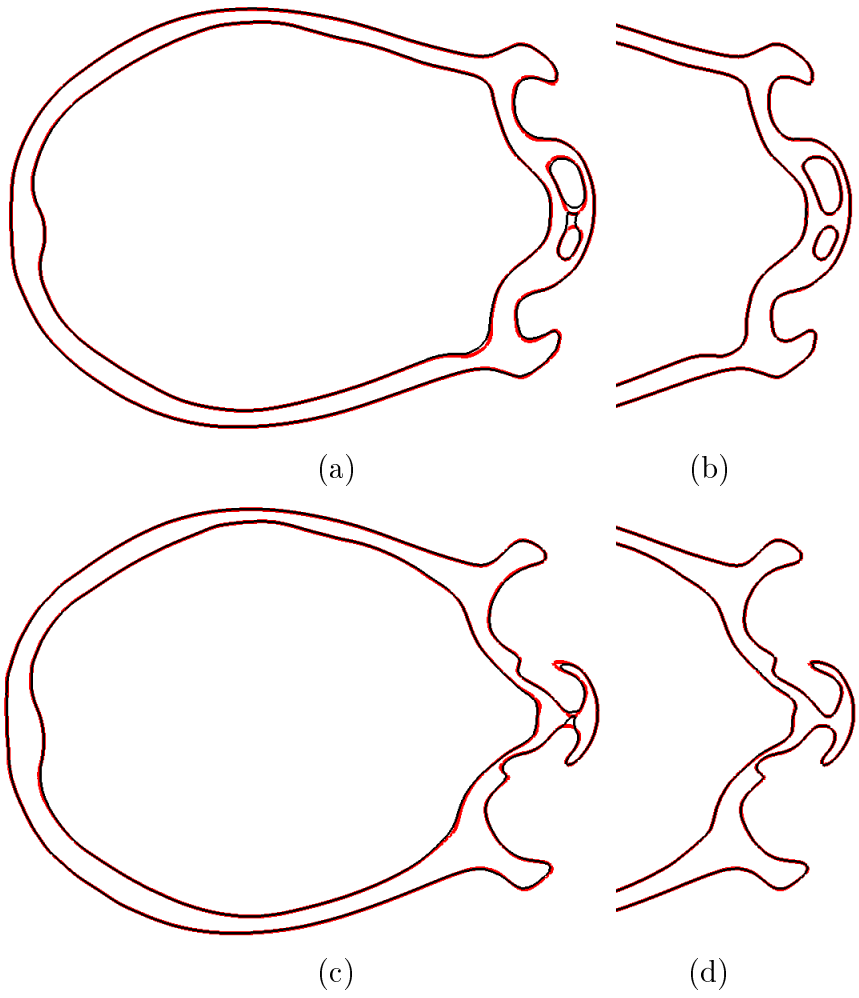

Figure 5.13: Reflected registration incorporating an initial feature match. Simply registering the smooth skull geometry onto it's reflection in Chapter 3 created problems with especially the sinuses. The same cut planes of Figure 3.11 are presented here compared to the registration result after an initial feature match. (a), (c) The initial registration and (b), (d) result after initial feature registration at iteration 100. Recall that the red line indicates the target geometry in the plane with black the surface deformed during registration.

UNIVERSITEIT VAN PRETORIA
UNIVERSITY OF PRETORIA
YUNIBESITHI YA PRETORIA

generic shape to a new skull geometry elastic surface registration is performed on the original orthognathic skull.

After a rigid registration, the orthognathic skull is aligned to the generic shape and the generic shape is deformed to represent the target. The registration of the generic shape to the orthognathic skull is done by first performing a feature registration and then a surface fitting. Feature lines on the generic shape and orthognathic surface are registered and the deformed generic surface is used as an input to the elastic surface registration procedure. The resultant registration and deformed generic shape is visible in Figure 5.14.

From the registration results visible in Figures 5.14 through 5.17, a full registration seems undesirable. Unmatched features are not used in the feature registration but the surfaces associated with these still affect the elastic surface registration. For this reason it would be beneficial to describe a registration to unmatched feature areas of the target and generic surface as unallowable.

The effect of unmatched features on the registration could be automatically reduced by restricting registration to areas of the surface mesh associated with these unmatched features. Registration restriction is explained and implemented in the proposed combination of procedures, presented in the next chapter. This reduces the amount of user interference required in adequately deforming the generic shape into a representation of the orthognathic skull form for example.

In Figure 5.17 significant deformation is seen to occur in the noisy internal areas during smoothing, indicating that the problem has reached the final stage. An example of what happens at this stage is visible on the femur problem convergence plots in Figure 3.7. In the smoothing stages of the procedure, the smoothing done to improve element quality removes the inconsistent localised deformation and high frequency surface noise applied during registration. This manifests as peaks in the convergence plots.

UNIVERSITEIT VAN PRETORIA
UNIVERSITY OF PRETORIA
YUNIBESITHI YA PRETORIA

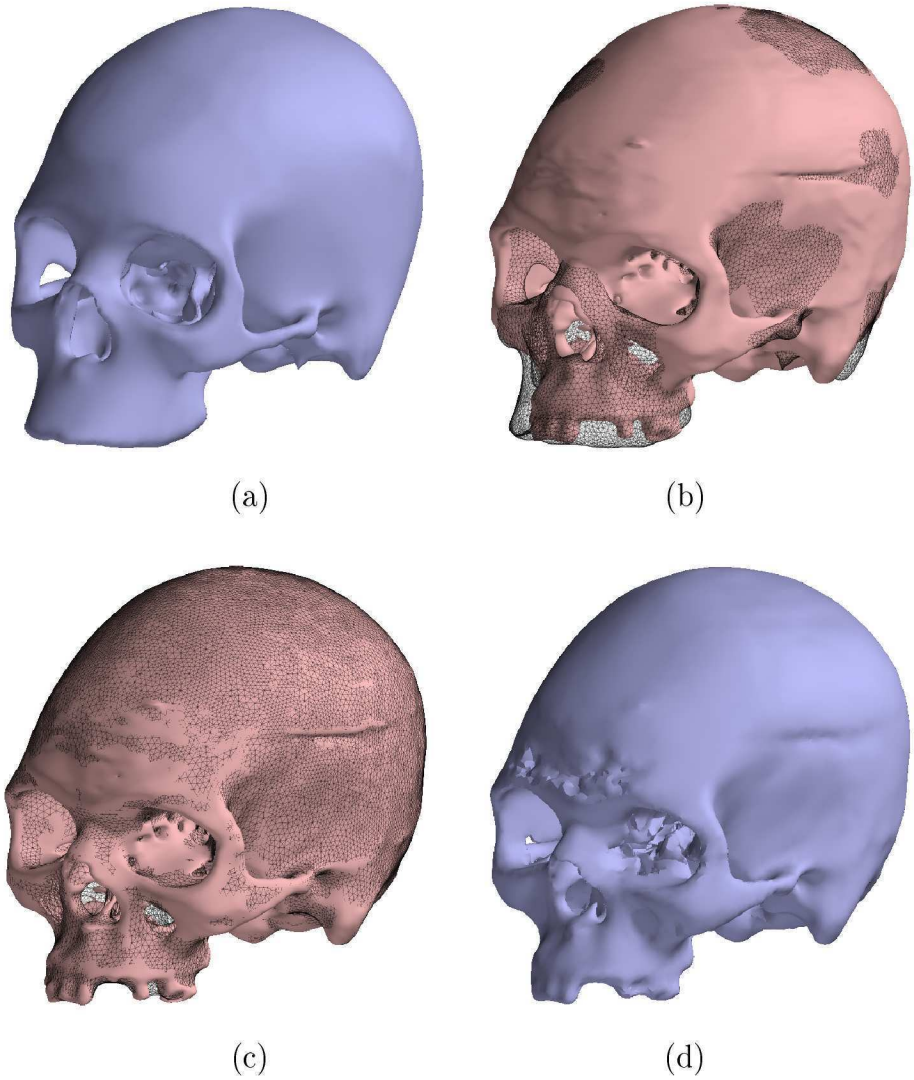

(a) (b)

(c) (d)

Figure 5.14: Elastic registration on the orthognathic skull. (a) The initial deformable mesh. (b) The rigid registration result to align the orthognathic skull to the deformable mesh with (c) the registration result at iteration 60. (d) The smoothed deformed mesh at iteration 60.

UNIVERSITEIT VAN PRETORIA
UNIVERSITY OF PRETORIA
YUNIBESITHI YA PRETORIA

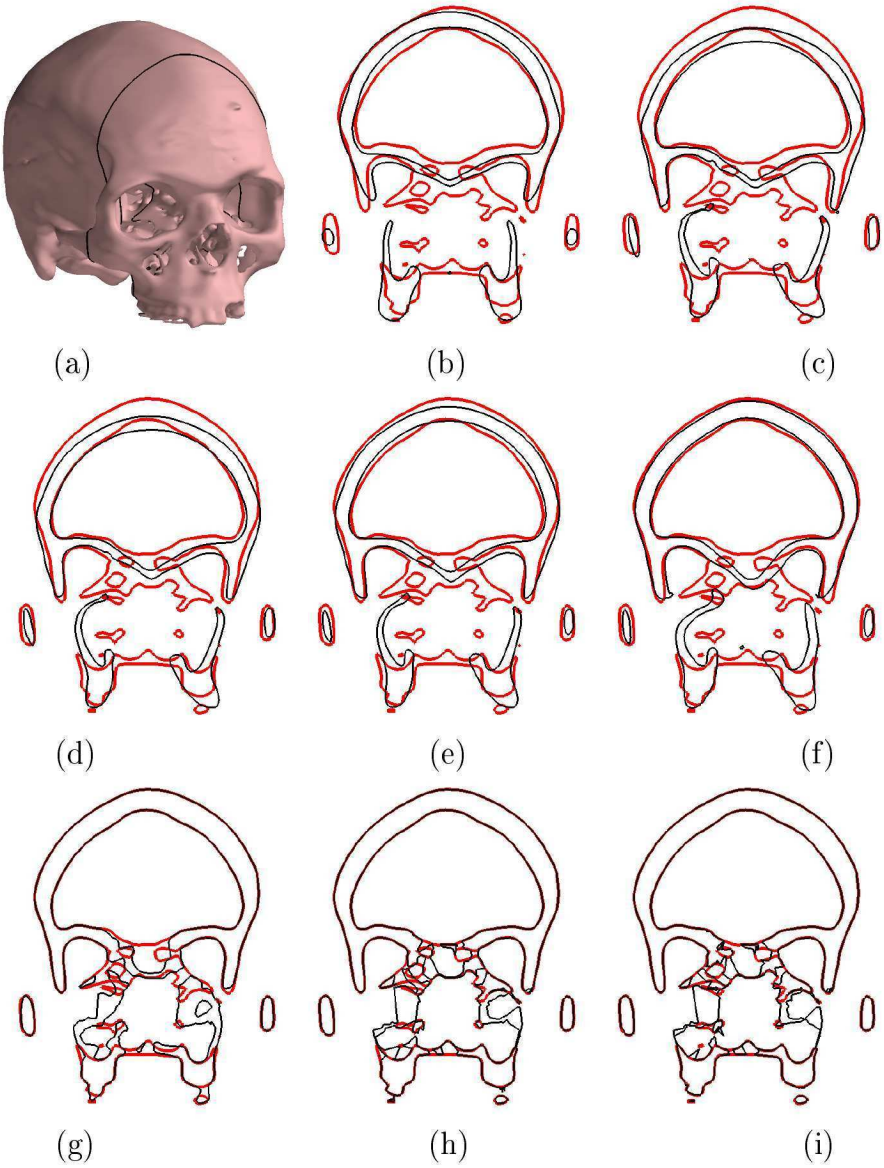

Figure 5.15: Frontal view of elastic registration on the orthognathic skull. (a) The cut plane illustrating the position of the subsequent figures taken for the registration result. (b) The target and deformable geometry after isotropic scale ICP registration. (c) The result of an initial surface feature registration. Elastic surface registration is performed after an initial feature registration resulting in base mesh deformation at iteration (d) 10, (e) 20, (f) 30, (g) 40, (h) 50 and (i) 60. The red line represents the position of the target surface in that plane and the black line the deformable mesh surface. Note that the topology doesn't change although it might appear that way. This appearance is due to the registered feature coming in and out of the plane where these figures are generated.

UNIVERSITEIT VAN PRETORIA
UNIVERSITY OF PRETORIA
YUNIBESITHI YA PRETORIA

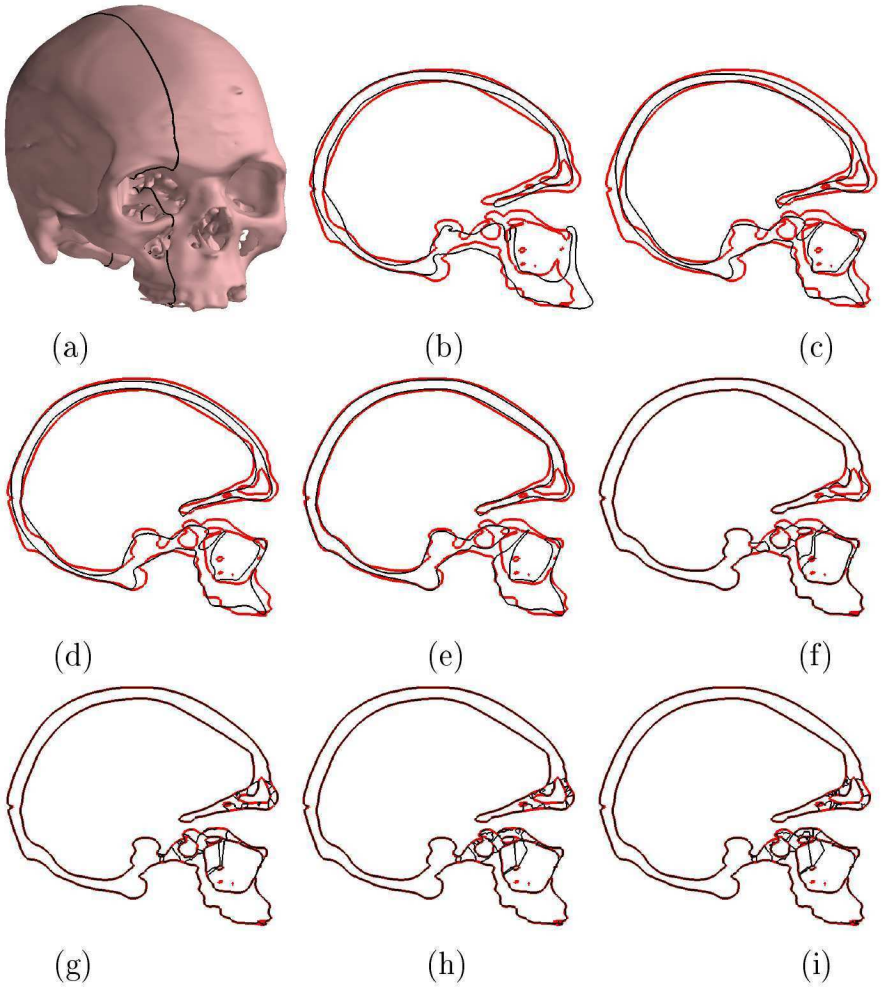

Figure 5.16: Lateral view of elastic registration on the orthognathic skull. (a) The cut plane illustrating the position of the subsequent figures taken for the registration result. (b) The target and deformable geometry after isotropic scale ICP registration. (c) The result of an initial surface feature registration. Elastic surface registration is performed after an initial feature registration resulting in base mesh deformation at iteration (d) 10, (e) 20, (f) 30, (g) 40, (h) 50 and (i) 60. The red line represents the position of the target surface in that plane and the black line the deformable mesh surface.

UNIVERSITEIT VAN PRETORIA
UNIVERSITY OF PRETORIA
YUNIBESITHI YA PRETORIA

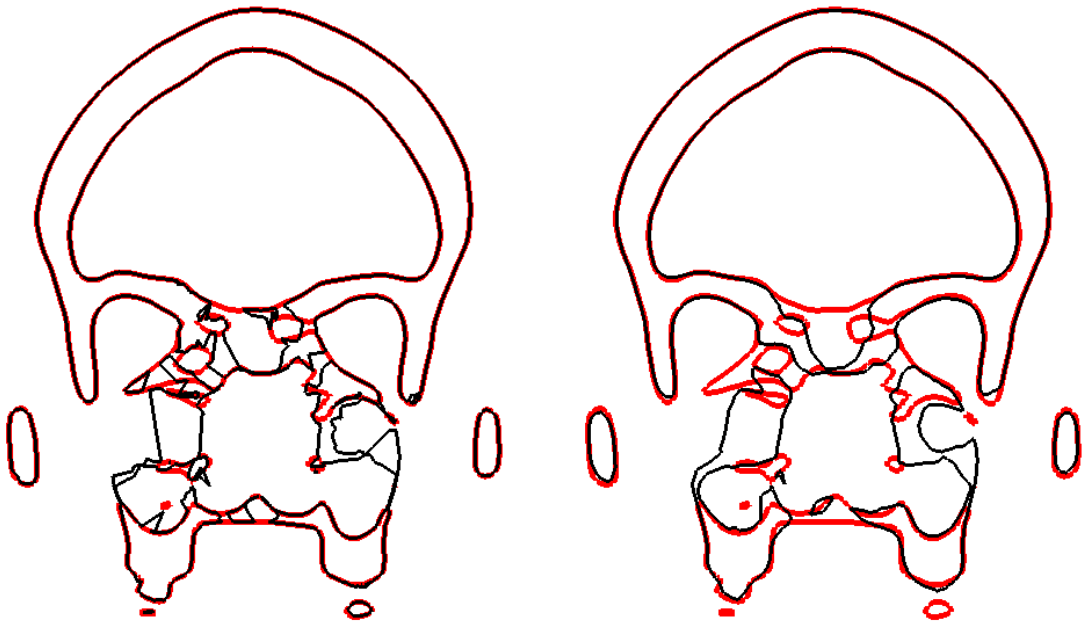

(a) (b)

Figure 5.17: Difference between the original and smoothed registration result at iteration 60. (a) Result of the elastic surface registration at iteration 60. This is the same cut as visible in Figure 5.15 (i). (b) The result showed in (a) after 10 Taubin [61] smoothing iterations. The red line represents the position of the target surface in the cut plane and the black line the deformable mesh surface.

Chapter 6

Proposed Registration Procedure

The proposed registration procedure is explained in this chapter. This registration is seen as if it were done on a new subject from a statistical sample of skull geometries. To illustrate the procedure a generic skull shape is deformed into a representation of the orthognathic skull.

Although a completely automatic registration to such a complex shape would be ideal, a semi-automatic registration tool is described that requires very little user interference, apart from setting up the problem and describing constraints. In future work proposed on a sample of human skull geometries, the registration could be done in conjunction with an anthropologist or medical expert. In this way the correct features to use during registration should be kept and a new subject is registered with only the relevant features in mind.

In this example, the user of this registration tool could be expected to manipulate the target and generic geometries so that the influence of the sinuses for example is minimised or removed. This could be done by manually allocating areas of the geometry as unallowed. During registration, the displacements to fit unallowed parts of the surface is ignored and the generic surface is moved using only the registration with higher confidence. A flow chart of the registration procedure assembled from various methods discussed in this report is visible in Figure 6.1.

The registration is done on a generic tetrahedral mesh, generated from the generic surface using TetGen [9]. The generic representation then consists of the original surface and the volume mesh. The tetrahedral mesh is deformed using the registration of the surface mesh.

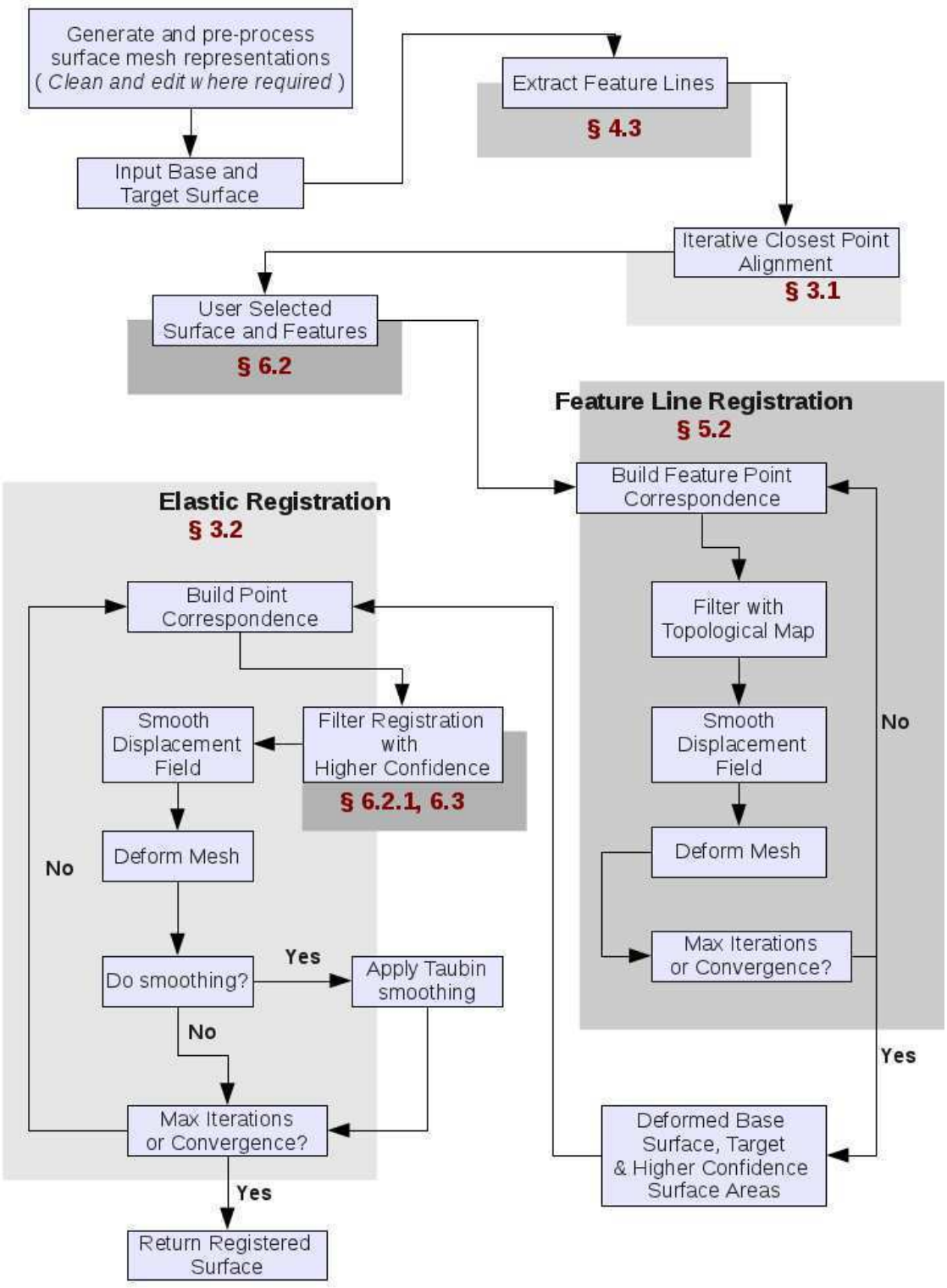

Figure 6.1: Flow diagram illustrating the various components of the registration procedure proposed and implemented.

UNIVERSITEIT VAN PRETORIA
UNIVERSITY OF PRETORIA
YUNIBESITHI YA PRETORIA

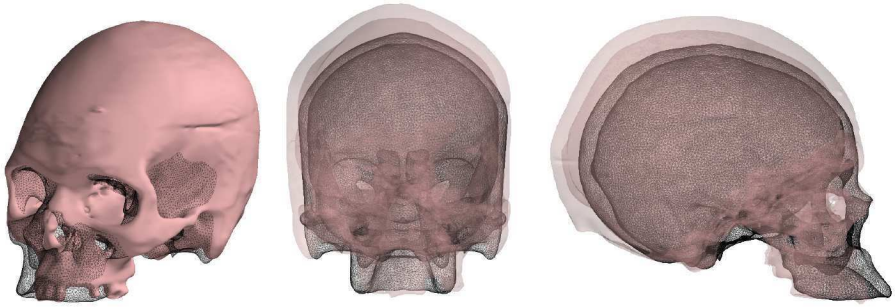

(a) (b) (c)

Figure 6.2: (a) Original position of the orthognathic skull geometry relative to the smoothed base skull. (b) Frontal and (c) lateral view of the orthognathic skull and base skull represented by the black wire-frame mesh.

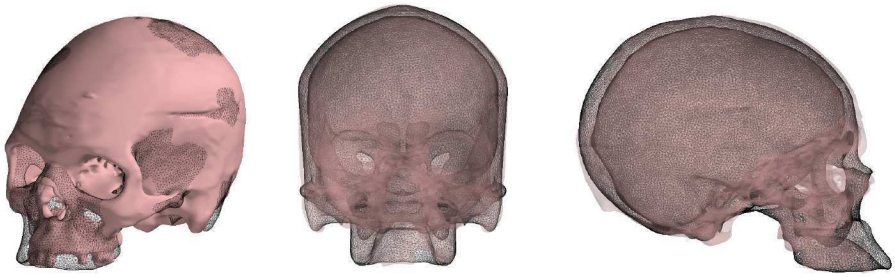

(a) (b) (c)

Figure 6.3: (a) Rigid registration position of the orthognathic skull geometry relative to the smoothed base skull after an isotropic ICP registration. (b) Frontal and (c) lateral view of the orthognathic skull and base skull represented by the black wire-frame mesh.

6.1 Step 1: Rotate, Scale and Translate

Before deforming the generic skull shape into a representation of the orthognathic skull form, a rigid registration is performed. Using the implemented ICP procedure, the orthognathic skull is registered and aligned to the generic shape. The orthognathic skull in it's original position relative to the symmetric base mesh is visible in Figure 6.2. The result after performing an isotropic scale ICP is visible in Figure 6.3.

UNIVERSITEIT VAN PRETORIA
UNIVERSITY OF PRETORIA
YUNIBESITHI YA PRETORIA

6.2 Step 2: Use Lines of Curvature

After a rigid registration to scale and align the target geometry to the generic mesh, a feature line registration is performed. As an example, only user selected features on the generic mesh is kept during the registration. The reason for doing this in the example is the vast difference in internal features between the skull geometries as visible in the facial regions as depicted in Figures 2.6 and 2.7.

The broken and decayed areas in the skull are also extracted as features and could be registered to different areas in other skull geometries. The generic mesh is created from an edited and smoothed version of the prognathic skull surface mesh. In removing areas of the decayed skull, most of the features internal to the facial region on the generic skull form are artificial. Mainly features with greater confidence are therefore selected on the generic skull shape and allowed to register. The surface in this edited area is selected manually. These areas are allowed to register but shouldn't be registered by the target.

The sinuses also have vastly different shapes, as visible in Figure 2.5. These along with other internal features of the facial area are removed from the allowable feature lines and surfaces on the generic skull shape for this example.

The user selected allowable features for registration in this example are displayed on the generic skull shape in Figure 6.4. In the proposed work on a sample of skulls however, the valid feature lines that would be found on all skull geometries would be allowed to register. These would be extracted from a fixed generic mesh and chosen as valid features with the help of a medical professional.

Registration of the allowable feature lines on the generic skull to the orthognathic form is displayed in Figure 6.5. In this figure, the generic features are first displayed in their original position on the top with the location of the deformed lines after registration to the orthognathic form below. For visual clarity, the feature lines extracted from the orthognathic skull is omitted.

User specified feature lines are again displayed in their deformed positions in Figure 6.6, along with the corresponding features on the target geometry. The unregistered features on the target are discarded and are not visible in this figure.

6.2.1 Feature Surfaces

The feature surfaces associated with the unregistered feature lines are extracted and classified as untrusted registration surfaces. This is done because registration

UNIVERSITEIT VAN PRETORIA
UNIVERSITY OF PRETORIA
YUNIBESITHI YA PRETORIA

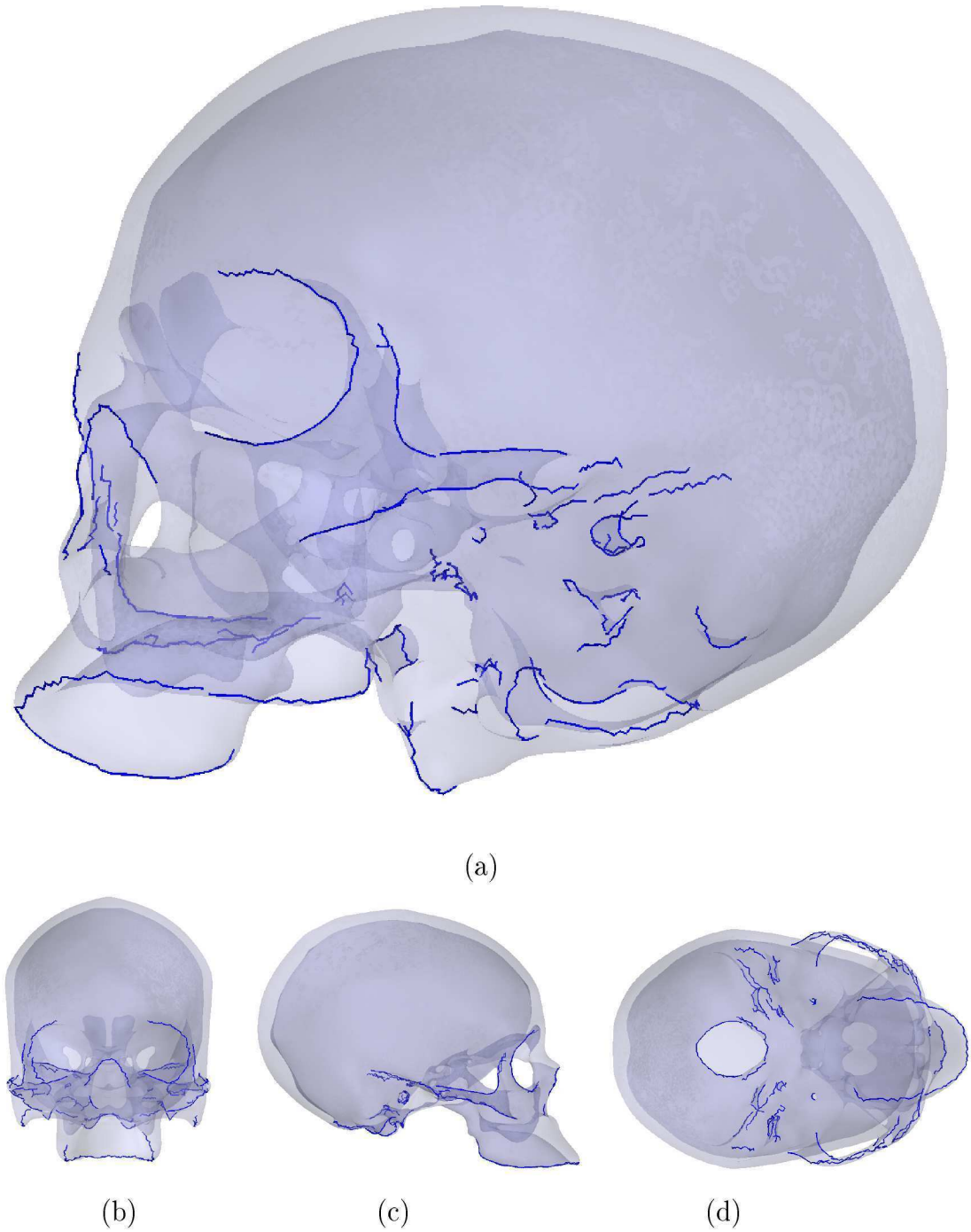

(a)

(b) (c) (d)

Figure 6.4: (a) User selected allowable features on the symmetric base skull geometry. (b) Frontal, (c) lateral and (d) lower view.

UNIVERSITEIT VAN PRETORIA
UNIVERSITY OF PRETORIA
YUNIBESITHI YA PRETORIA

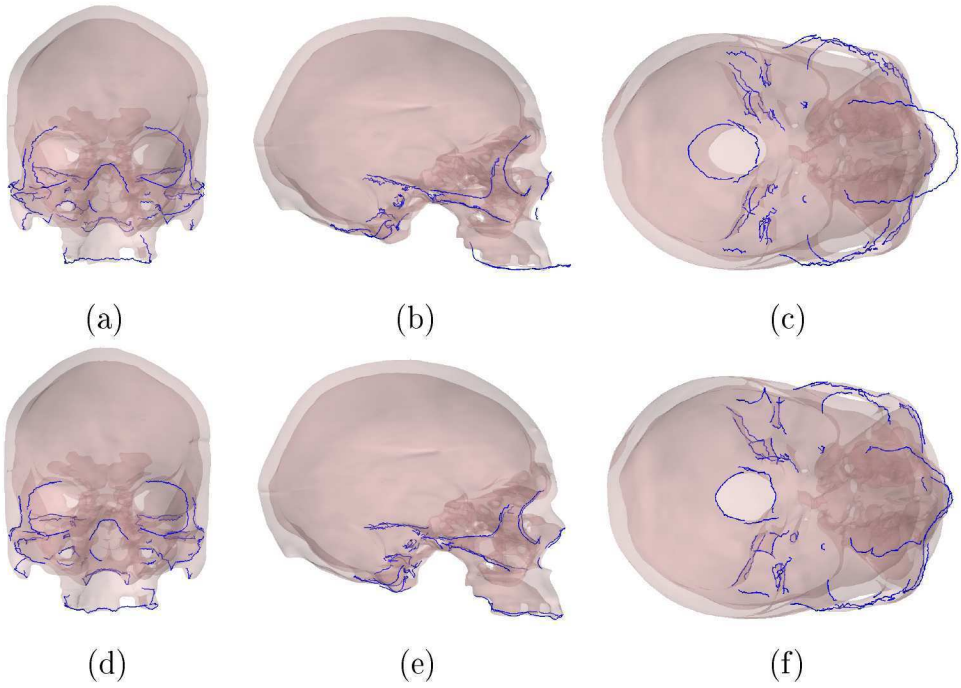

(a) (b) (c)

(d) (e) (f)

Figure 6.5: Registration of allowable base geometry features to the orthognathic skull. (a) Frontal, (b) lateral and (c) lower view of the base geometry features relative to the orthognathic skull. (d) Frontal, (e) lateral and (f) lower view of the base geometry features registered and deformed to the corresponding features on the orthognathic skull.

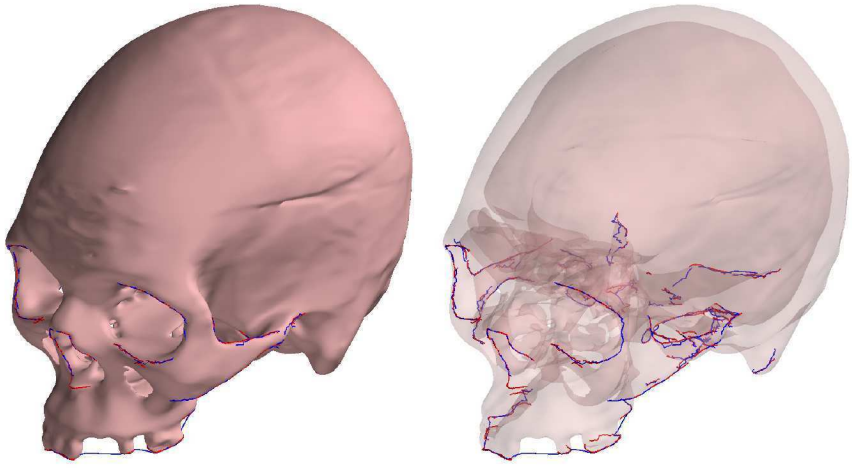

(a) (b)

Figure 6.6: Registration of allowable base geometry features to the orthognathic skull. (a) The registration result on an opaque target skull and (b) semi-transparent target surface. Blue lines indicate the features of the deformable surface with red lines indicating the target features.

UNIVERSITEIT VAN PRETORIA
UNIVERSITY OF PRETORIA
YUNIBESITHI YA PRETORIA

to unmatched features could result in a distorted mesh, as seen in Figures 5.14 through 5.16.

The feature points used in this example are classified using the result of the MLS method. Curvature information obtained on the geometries is used to construct feature lines. Using the magnitudes of the principal curvatures, the feature rich areas are described. All the feature points satisfying the chosen conditions on the generic and target mesh are illustrated in Figures 6.7 and 6.8. The values of 0.2 and 0.18 are arbitrarily chosen on the different skull geometries. This is done so that the same approximate size of the relative feature areas are highlighted. The curvature estimation was done before performing the scaling visible in Figures 6.2 and 6.3, so the difference is highly likely due to the difference in scale between the geometries at the time of curvature information extraction.

Using the user specified features on the base mesh and the registered feature lines on the target, the corresponding allowable feature points are chosen. The allowable feature points are displayed in Figures 6.9 and 6.10.

Allowable feature points are extracted using the following procedure on a given surface mesh:

- A $k-d$ tree representation of all the points in the extracted and thresholded set of feature lines is set up for nearest neighbour search.
- For each point within the set of feature points:
  - The closest point on a feature line is searched using the $k-d$ tree.
  - If the point closest to the feature point is on a user specified or registered line, the current point is added to a list of allowable feature points. If not, the current point is added to a list of low confidence feature points.

The allowable and low confidence feature points for both the base and target mesh are extracted. The list of triangles representing each surface is inspected. A list of low confidence triangles is set up using the allowable and low confidence feature points.

A triangle is marked as a low confidence surface triangle if any one of it's nodes are in the list of low confidence feature points. Registration is then only allowed to the surface triangles and points with higher confidence.

UNIVERSITEIT VAN PRETORIA
UNIVERSITY OF PRETORIA
YUNIBESITHI YA PRETORIA

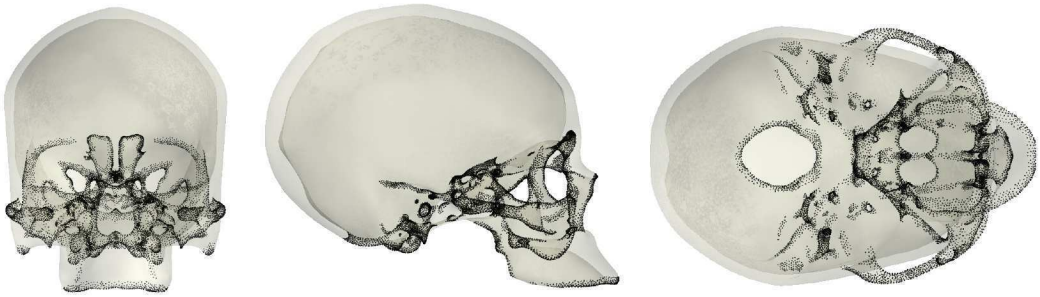

(a) (b) (c)

Figure 6.7: All feature points on the symmetric base skull for $\kappa_{\max} > 0.2$ and $\kappa_{\min} < -0.2$. (a) Frontal, (b) lateral and (c) lower view.

(a) (b) (c)

Figure 6.8: All feature points on the orthognathic target skull for $\kappa_{\max} > 0.18$ and $\kappa_{\min} < -0.18$. (a) Frontal, (b) lateral and (c) lower view.

(a) (b) (c)

Figure 6.9: Feature points on the symmetric base skull for $\kappa_{\max} > 0.2$ and $\kappa_{\min} < -0.2$ corresponding to the user specified allowable feature lines in Figure 6.4. (a) Frontal, (b) lateral and (c) lower view.

UNIVERSITEIT VAN PRETORIA
UNIVERSITY OF PRETORIA
YUNIBESITHI YA PRETORIA

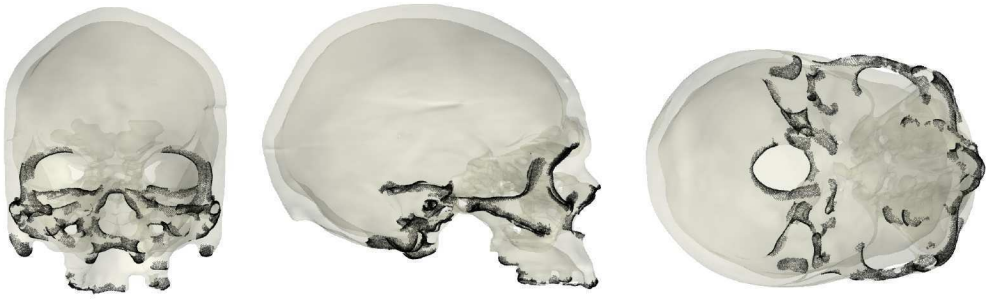

(a) (b) (c)

Figure 6.10: Feature points on the orthognathic target skull for $\kappa_{\max} > 0.18$ and $\kappa_{\min} < -0.18$ corresponding to the user specified allowable feature lines in Figure 6.6. (a) Frontal, (b) lateral and (c) lower view.

6.3 Step 3: Register Allowable Surface

The tetrahedral mesh is deformed using the Gaussian weighting function implemented into the registration procedure. Deformation during feature line registration is still performed in the same way using the registered position of points in the set of feature lines. To make the elastic surface registration more robust to unwanted deformation and the possible inversion of elements, the deformation obtained as a result of the Gaussian function is smoothed again using Taubin smoothing.

Modifications to the original registration procedure is outlined in this subsection. The model shape $\mathcal{M}$ not only consists of triangles but also tetrahedral elements. Key steps to deform the generic shape $\mathcal{M}$ into the target $\mathcal{P}$ with the modified version of the elastic registration procedure are:

- The deformed generic tetrahedral shape after feature line registration is used as the initial condition before elastic surface registration.
- Registered positions are only found for higher confidence points on both the generic and target surfaces. These allowable points can be user specified or obtained after the feature line registration procedure as described in subsection 6.2.1.
- Registration to any part of the surface (either points or surfaces) with a low confidence level is ignored.
- Only the registration of surface points with a higher confidence level is used to deform the tetrahedral mesh. An initial update on tetrahedral mesh

UNIVERSITEIT VAN PRETORIA
UNIVERSITY OF PRETORIA
YUNIBESITHI YA PRETORIA

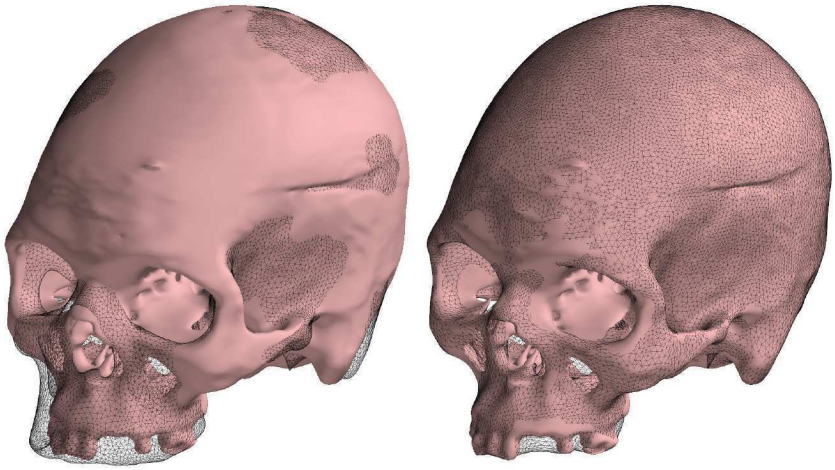

(a) (b)

Figure 6.11: Elastic registration on the orthognathic skull. (a) The rigid registration result to align the orthognathic skull to the deformable mesh with (b) the registration result at iteration 60. This registration result is obtained after an initial allowable feature registration and filtering for allowable surfaces. The compared result of Figure 5.14 employed full feature and subsequent full elastic surface registration.

nodal coordinates are obtained with higher confidence registrations and Equation (3.8).

- Taubin smoothing is applied to the computed deformation field.
- After the deformation field is smoothed, it is applied to the generic tetrahedral mesh. Inverted elements would restrict the use of the mesh post-registration. The reason for smoothing the deformation is to make the deformed mesh more resilient to unwanted distortion. Unfortunately a simple smoothing strategy does not penalise unwanted distortion precisely and element inversion could still occur.

The result of performing an elastic registration on the orthognathic skull with user specified and automatic constraints is visible in Figures 6.11 through 6.13. For this example, an allowable surface for registration on the generic skull is done manually. Also, the internal surface of the facial area is selected manually, and registration to this part of the generic mesh is not allowed.

Higher confidence nodes on the generic surface and orthognathic surface is obtained after feature line registration as described in section 6.2. Registration is then

UNIVERSITEIT VAN PRETORIA
UNIVERSITY OF PRETORIA
YUNIBESITHI YA PRETORIA

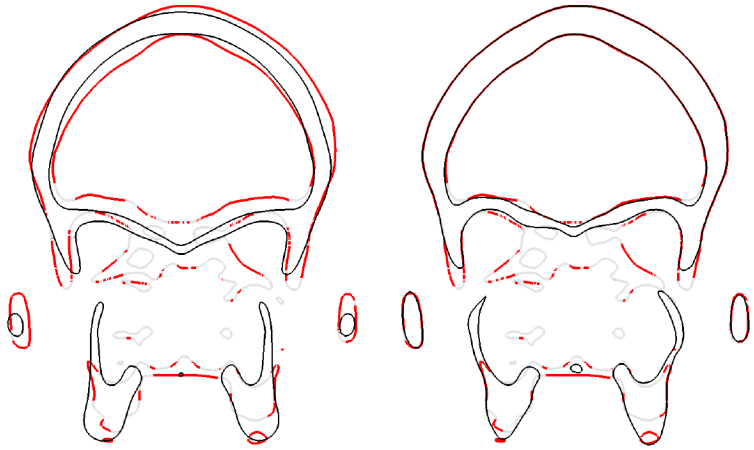

(a) (b)

Figure 6.12: Frontal view of elastic registration on the orthognathic skull for automatically selected allowable features. (a) The target and deformable geometry after isotropic scale ICP registration. After the initial registration of selected features in Figure 6.6, elastic surface registration is performed and smoothed resulting in (b) the smoothed registration result at iteration 60. The gray and red line sections represent the target surface. Grey represents the automatically discarded areas while the red lines represent the allowable and featureless target surface in the same plane as Figure 5.15. The black line represents the deformable mesh surface.

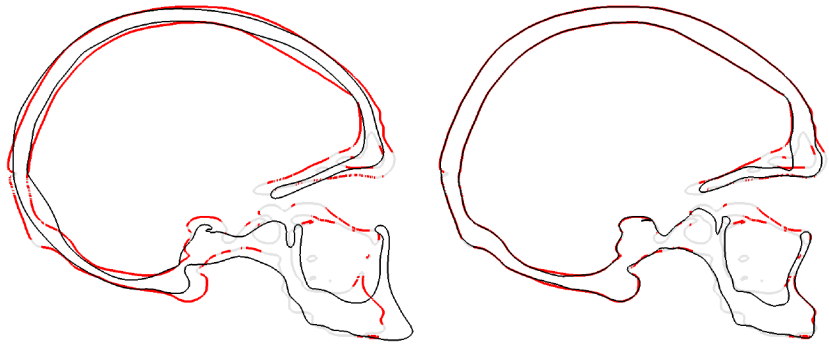

(a) (b)

Figure 6.13: Lateral view of elastic registration on the orthognathic skull for automatically selected allowable features. (a) The target and deformable geometry after isotropic scale ICP registration. After the initial registration of selected features in Figure 6.6, elastic surface registration is performed and smoothed resulting in (b) the registration result at iteration 60. The gray and red line sections represent the target surface. Grey represents the automatically discarded areas while the red lines represent the allowable and featureless target surface in the same plane as Figure 5.16. The black line represents the deformable mesh surface.

UNIVERSITEIT VAN PRETORIA
UNIVERSITY OF PRETORIA
YUNIBESITHI YA PRETORIA

done using the higher confidence surface triangles on the orthognathic skull and the user selected allowable surface triangles on the generic skull.

Comparing the cut planes in Figures 6.12 and 6.13 to those in Figures 5.15, 5.16 and 5.17, there is a possible improvement on the result at iteration 60 if registration is approached in this selective manner. In doing a proper registration, additional user interference may still be required to obtain a better representation of the target skull geometry in this example. Although this is not ideal, at least the amount of user interference in performing an elastic registration on these complex geometries is reduced.

The target geometry in this example is left totally unedited with all the user specified constraints and restrictions applied to only the generic deformable mesh. Compared to the original full elastic registration, this combined procedure implemented translates to far less user input needed in registering a large statistical sample of skull geometries. This is because each new geometry could be used with very little pre-registration editing required. It is however noticed in the cut planes of Figures 6.12 and 6.13 that editing a target geometry before registration could result in an improved representation of that skull.

As a further example of registration with the proposed method using user specified and automatic constraints, both prognathic and orthognathic skull geometries are registered. The target shapes are the original surfaces visible in Figure 6.14 (a) and (d). The procedure for matching feature lines and determining lower confidence registrations is then applied to both models and the generic surface is deformed into the target representations visible in Figure 6.14 (b) and (e).

If the generic model is deformed into a target shape and then the reflected target shape, the average of the two deformed meshes can be used to create a symmetric version of the target. Examples of the approximate symmetric versions of both the orthognathic and prognathic skull geometry are illustrated in Figures 6.14 (c) and (f).

6.4 Step 5: Mesh Quality

Mesh quality can be improved by using the quality improvement toolbox MESQUITE [5]. In this example, a tetrahedral finite element mesh is generated on the average symmetric skull surface. This average symmetric skull surface is determined after first creating symmetric versions of the two geometries as illustrated in Fig-

UNIVERSITEIT VAN PRETORIA
UNIVERSITY OF PRETORIA
YUNIBESITHI YA PRETORIA

Figure 6.14: (a) Orthognathic target skull geometry with (b) the registration result and (c) the symmetric version on the registration result. (d) Prognathic target skull geometry with (e) the registration result and (f) the symmetric version on the registration result.

UNIVERSITEIT VAN PRETORIA
UNIVERSITY OF PRETORIA
YUNIBESITHI YA PRETORIA

ures 6.14 (c) and (f). The tetrahedral mesh was generated using TetGen [9] and had 1′687′795 elements.

The mesh generated on the average skull surface was then deformed by doing an FEA where the target boundary positions is known and so a known displacement is applied to boundary nodes. This is done in the hope that the movement of internal nodes would occur in a reliable manner when deforming the average mesh back into prognathic and orthognathic representations.

Element inversion occurred for applied nodal displacement higher than approximately 40% of the actual displacement required when using simple linear elastic elements in the analysis. This is considered a problem because FEBio solves the large set of equations in a matrix free manner. The problem moves internal nodal coordinates using a linear elastic analysis and hits a wall if displacement updates cause element inversion.

It is decided to do a simple nodal coordinate update based on the displacement information up to the 40% mark. Mesh untangling and quality improvement is planned at the final stage. The displacement of the internal nodes with 40% of the boundary displacement applied is multiplied with a factor of 2.5. This displacement is then applied to the original internal nodal coordinates along with 100% known boundary displacement to create the mesh representing the prognathic and orthognathic skull.

6.4.1 Quality Metric

The quality metric used in this report is one of the tetrahedron shape measures used by Escobar *et al.* in constructing objective functions for mesh untangling and smoothing [29]. This quality metric is obtained by algebraic operation and can therefore be computed efficiently.

The chosen quality metric can be constructed as in the work done by Escobar *et al.* [29]. If $\mathcal{T}$ is a tetrahedral element in the physical space whose vertices are given by $\mathbf{x}_j = \begin{pmatrix} x_j & y_j & z_j \end{pmatrix}$, $j = 0, 1, 2, 3$ and $\mathcal{T}_R$ is the reference tetrahedron with vertices $\mathbf{u}_0 = \begin{pmatrix} 0 & 0 & 0 \end{pmatrix}$, $\mathbf{u}_1 = \begin{pmatrix} 1 & 0 & 0 \end{pmatrix}$, $\mathbf{u}_2 = \begin{pmatrix} 0 & 1 & 0 \end{pmatrix}$ and $\mathbf{u}_3 = \begin{pmatrix} 0 & 0 & 1 \end{pmatrix}$, a translation vector $\mathbf{x}_0$ can be chosen so that the affine map $\mathbf{x} = \mathbf{J}\mathbf{u} + \mathbf{x_0}$ takes $\mathcal{T}_R$ to $\mathcal{T}$. In this affine map, $\mathbf{J}$ represents the Jacobian matrix

UNIVERSITEIT VAN PRETORIA
UNIVERSITY OF PRETORIA
YUNIBESITHI YA PRETORIA

referenced to node $\mathbf{x}_0$ and can be determined from

$$\mathbf{J} = \begin{bmatrix} x_1 - x_0 & x_2 - x_0 & x_3 - x_0 \\ y_1 - y_0 & y_2 - y_0 & y_3 - y_0 \\ z_1 - z_0 & z_2 - z_0 & z_3 - z_0 \end{bmatrix}. \tag{6.1}$$

A tetrahedron $\mathcal{T}_I$ is equilateral with all of its edges length one. The vertices of $\mathcal{T}_I$ are located at $\mathbf{v}_0 = \begin{pmatrix} 0 & 0 & 0 \end{pmatrix}$,$\mathbf{v}_1 = \begin{pmatrix} 1 & 0 & 0 \end{pmatrix}$,$\mathbf{v}_2 = \begin{pmatrix} 1/2 & \sqrt{3}/2 & 0 \end{pmatrix}$ and $\mathbf{v}_3 = \begin{pmatrix} 1/2 & \sqrt{3}/6 & \sqrt{2}/\sqrt{3} \end{pmatrix}$. If $\mathbf{v} = \mathbf{W}\mathbf{u}$ is a linear map that takes $\mathcal{T}_R$ to $\mathcal{T}_I$, the Jacobian matrix is given by

$$W = \begin{bmatrix} 1 & 1/2 & 1/2 \\ 0 & \sqrt{3}/2 & \sqrt{3}/6 \\ 0 & 0 & \sqrt{2}/\sqrt{3} \end{bmatrix}. \tag{6.2}$$

The affine map that now takes $\mathcal{T}_I$ to $\mathcal{T}$ is given by $\mathbf{x} = \mathbf{J}\mathbf{W}^{-1}\mathbf{v} + \mathbf{x_0}$, and its Jacobian matrix is $\mathbf{Q} = \mathbf{J}\mathbf{W}^{-1}$. The matrix norms, determinant or trace of $\mathbf{Q}$ can be used to construct algebraic quality measures of $\mathcal{T}$. The quality metric chosen and reported in Table 6.1 is determined for the m^{th} tetrahedron as [29]:

$$q_m = \frac{3\sigma_m^{2/3}}{|\mathbf{Q}_m|^2}, \tag{6.3}$$

where $\sigma = \det(\mathbf{Q})$ and $|\mathbf{Q}|$ is the Frobenius norm of the Jacobian matrix $\mathbf{Q}$ defined by $|\mathbf{Q}| = \sqrt{\text{tr}\,(\mathbf{Q}^T\mathbf{Q})}$. This quality metric is slightly modified by Escobar *et al.* [29] by introducing the use of the positive and increasing function $h\,(\sigma)$ instead of the original σ. The quality metric is then rewritten as:

$$q_m = \frac{3h\,(\sigma_m)^{2/3}}{|\mathbf{Q}_m|^2}. \tag{6.4}$$

This ensures element quality to be in the range of $(0, 1]$. The reason for doing this is twofold.

- An inverted element has a negative Jacobian and so determining $\det(\mathbf{Q})^{2/3}$ poses a problem. The positive and increasing function $h(\sigma)$ actually allows the calculation of element quality for a negative determinant of the Jacobian matrix.

UNIVERSITEIT VAN PRETORIA
UNIVERSITY OF PRETORIA
YUNIBESITHI YA PRETORIA

- The inverted elements have a quality close to zero so that the inverse of the element quality approaches infinity as elements become more degenerate. The inverse of the modified quality metric is set to a range $[1, \infty)$ using this modification. The inverted metric is used to construct an objective function for simultaneous mesh untangling and smoothing during an optimisation procedure by Escobar *et al.* [29]. In constructing the objective function per element in this manner, inversion or degeneration of tetrahedral elements is penalised heavily.

The positive and increasing function used is defined by [29]

$$h(\sigma) = \frac{1}{2}\left(\sigma + \sqrt{\sigma^2 + 4\delta^2}\right). \tag{6.5}$$

Here δ is chosen and applied when determining the quality of all elements in such a way that

$$\delta \geq \delta_{\min} = \begin{cases} \sqrt{\zeta\left(\zeta - \sigma_{\min}\right)} & \text{if } \sigma_{\min} < \zeta \\ 0 & \text{if } \sigma_{\min} \geq \zeta \end{cases} \tag{6.6}$$

where ζ is taken as approximately machine epsilon ($0 < \zeta \ll 1$) or some user selected minimum. This means that the final element quality for all elements can only be determined after inspecting all elements for inversion. Constructing ζ in this way insures $h(\sigma) \geq \zeta$. The implementation done for this report used python code with $\zeta = 10^{-8}$.

6.4.2 Usable Skull Mesh Generation

The meshes used as an example to again analyse and determine difference in stress field due to cranial shape variation in masticatory induced stress is first generated on the average skull mesh surface. This mesh generated consists of 1′687′795 tetrahedral elements with a minimum element quality of 0.155 and an average quality of 0.797, using the quality metric in Equation (6.4).

The tetrahedral mesh is deformed into the symmetric prognathic and orthognathic skull representations. These representations are obtained by applying the registration procedure discussed in this chapter. To obtain a prognathic and orthognathic representation of the tetrahedral mesh generated on the average surface, the following is done:

UNIVERSITEIT VAN PRETORIA
UNIVERSITY OF PRETORIA
YUNIBESITHI YA PRETORIA

	Original	Prognathic		Orthognathic	
		Initial	Improved	Initial	Improved
$\sigma < 0$	0	10	0	15	4
δ	0	0.0001169	0	0.0003271	0.0002487
min (q)	0.1549	8.48e-6	0.1042	7.48e-6	8.5e-6
max (q)	0.99998	0.99971	0.99966	0.99984	0.99958
average (q)	0.79713	0.78306	0.80434	0.78734	0.80894
$q < 0.5$	81568	90603	33173	87702	30886
$q < 0.15$	0	26	2	21	4

Table 6.1: Mesh Quality compared to original mesh generated from the symmetric skull surface. The tetrahedral mesh representations representing the prognathic and orthognathic skull shapes are then improved using MESQUITE [5] with boundary nodes constrained.

- 40% of the known nodal displacement to either the prognathic or orthognathic representation is applied to the boundary nodes of the tetrahedral mesh. This is used in a linear elastic finite element analysis with $E = 16$ GPa and $\nu = 0.3$, the same material properties used in the initial analysis to represent a linear elastic bone material. The displacement is known as all of the surface mesh representations have one-to-one correspondence and identical topology.

- Nodal displacement is extrapolated to the 100% mark. The updated nodal coordinates after performing an FEA is used and the displacement from the initial undeformed configuration to the deformed configuration is applied to the original tetrahedral mesh using a scale factor of 2.5. Linear elastic elements are used and so linear deformation may be assumed.

- The tetrahedral skull representation is optimised using the coordinates of internal nodes as design variables while the boundary surface nodes are constrained. The MESQUITE Mesh Quality Improvement Toolkit [5] is used in this step.

Original and improved mesh quality are visible in Table 6.1. Not only is the average quality of the mesh improved but the mesh is also untangled with the only inverted elements left after optimisation those on the surface where nodal coordinates are constrained. The four surface elements that remain inverted after quality improvement on the orthognathic skull mesh are shown in Figure 6.15.

These inverted elements are situated on the surface and is far removed from the

UNIVERSITEIT VAN PRETORIA
UNIVERSITY OF PRETORIA
YUNIBESITHI YA PRETORIA

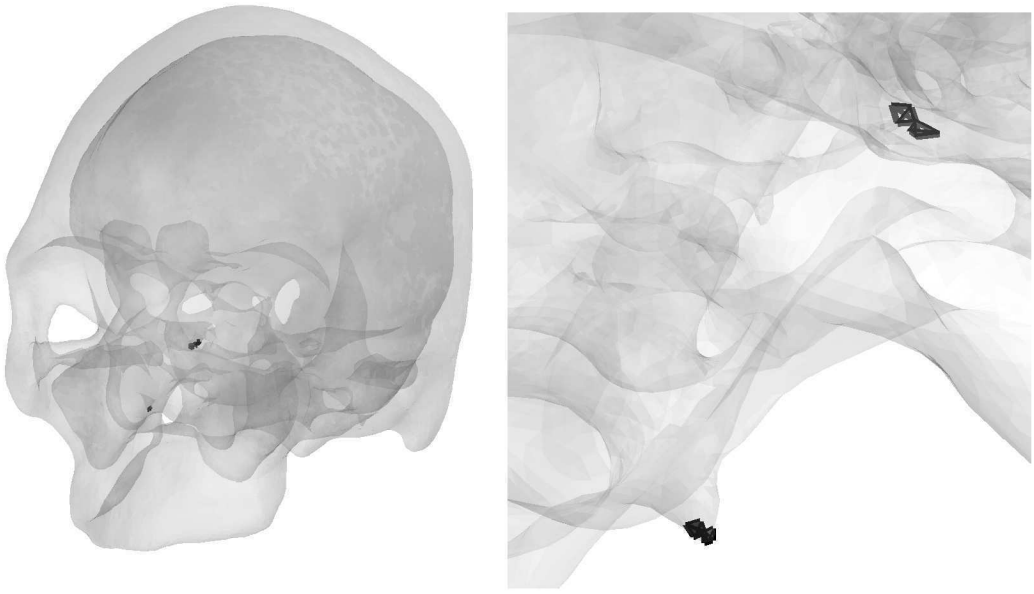

(a) (b)

Figure 6.15: Inverted elements retained after mesh improvement in the orthognathic skull representation. (a) Global position of inverted elements. (b) Detail showing the four inverted surface elements.

(a) (b) (c)

Figure 6.16: Mesh quality evaluated using Equation (6.4). (a) Symmetric prognathic skull representation. (b) Original mesh generated on the average surface using TetGen [9]. (c) Symmetric orthognathic skull representation.

UNIVERSITEIT VAN PRETORIA
UNIVERSITY OF PRETORIA
YUNIBESITHI YA PRETORIA

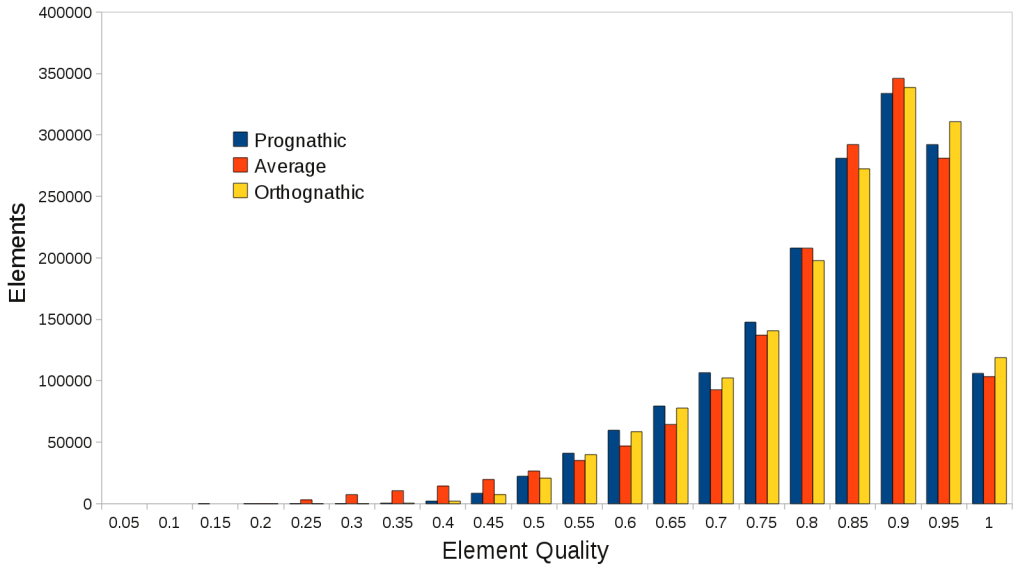

Figure 6.17: Histogram illustrating the element quality of the optimised prognathic and orthognathic mesh representations as well as the element quality of the original mesh generated on the average skull surface.

facial area of interest. It is therefore decided that the result obtained from an FEA would not suffer in their absence. These four elements are removed from all mesh representations so there could still remain an identical mesh topology for all meshes of interest. The final tetrahedral meshes representing the prognathic, orthognathic and average skull geometry are visible in Figure 6.16. All have identical mesh topology with a total of 1′687′791 elements. The histograms visible in Figure 6.17 show the distribution of element quality for all three of the meshes visible in Figure 6.16.

The mesh quality of these tetrahedral mesh skull representations are fairly consistent and would seem to be as a result of mainly the quality of the original mesh generated.

6.5 Analysis on Registered Skull Geometries

The three tetrahedral meshes illustrated in Figure 6.16 are analysed for molar bite force as an example. This is done to illustrate the benefit of having the same mesh topology with only a difference in nodal coordinates to represent all the geometries of interest.

The nodes where boundary conditions are applied in an FEA are the exact

UNIVERSITEIT VAN PRETORIA
UNIVERSITY OF PRETORIA
YUNIBESITHI YA PRETORIA

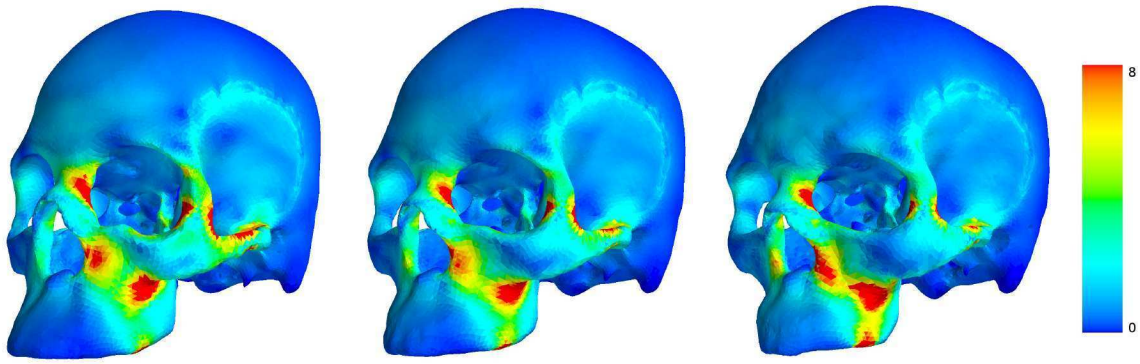

(a) (b) (c)

Figure 6.18: Von Mises stress contours for a molar bite scaled to show a maximum of 8 MPa. (a) Prognathic, (b) Average and (c) Orthognathic skull shape.

same nodes in this case for all three meshes. Boundary conditions are set up as in section A.4 of Appendix A where the initial finite element analysis on the skull shapes is discussed. The direction of the forces for the average case is obtained by interpolating between the known directions in the prognathic and orthognathic case. Material properties are selected as that of the linear elastic material also used in the initial analysis with Young's modulus $E = 16$ GPa and Poisson's ratio $\nu = 0.3$.

The results of the FEA can be manipulated in a few ways if one-to-one mesh correspondence is available for all the geometries analysed. In Figure 6.18, the Von Mises stresses are given in the usual way with all stresses higher than 8 MPa simply shown in red. The maximum Von Mises stress for this analysis is 18.56 MPa for the prognathic skull form, 15.334 MPa on the average and 17.589 MPa for the orthognathic skull form. These stresses fall into the same range and no artificial stress concentrations are present that do not occur in all three skull forms. The relative scale of the skull geometries allow comparison of the stress field without further manipulation or scaling.

In Figure 6.19, the resulting stress in the prognathic and orthognathic form are compared in a way that is possible due to one to one correspondence between all the meshes. Here the Von Mises stresses in the orthognathic skull form is subtracted from the prognathic skull form in an element-wise manner. This is done and illustrated on the mesh representing the average skull in Figure 6.19 (c).

Inter-patient variation in masticatory induced stress field is presented in Figure 6.19. It would appear from this analysis that there is a higher stress in the

UNIVERSITEIT VAN PRETORIA
UNIVERSITY OF PRETORIA
YUNIBESITHI YA PRETORIA

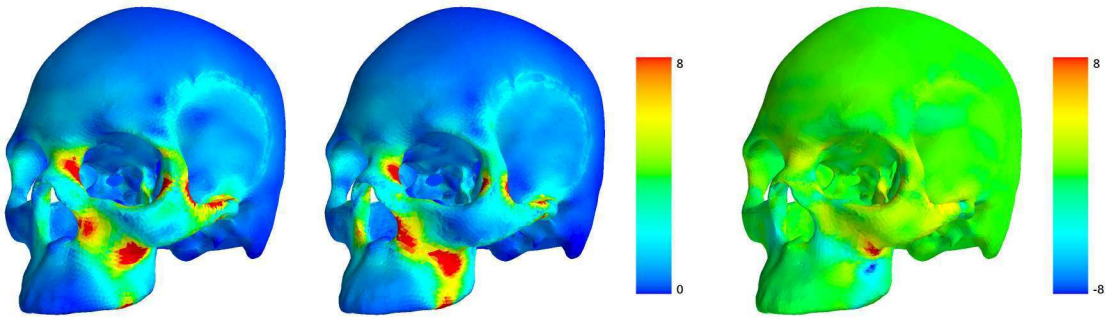

(a) (b) (c)

Figure 6.19: (a) The Von Mises stress in the prognathic skull shape plotted on the mesh representing the average shape. (b) The Von Mises stress in the orthognathic skull shape plotted on the mesh representing the average shape. (c) The difference in Von Mises stress between the prognathic and orthognathic finite element results $\sigma^{\text{vM}}_{\text{prognathic}} - \sigma^{\text{vM}}_{\text{orthognathic}}$ shown for the range $[-8, 8]$ MPa. All of the contours are plotted on the mesh representing the average skull shape. (a)-(b)=(c)

zygomatic arch and bridge of the nose in the prognathic skull form while the orthognathic form has a higher stress concentration in the maxilla or upper mandible. The locality of high variation in stress field is visible. Only the analysis on the masticatory induced stress during a molar bite is used as an example.

Conclusions on the link between prognathism and stress can be drawn from an analysis on more skulls as well as better detailed models. These conclusions should be done with the aid of an expert in the field such as an Anthropologist and is not done in this report.

6.5.1 The effect of non-unique registration on FEA result

The structural analysis (FEA) should ideally be done with a registration tool that produces unique and reliable representations and it is therefore proposed that the current procedure be improved further. It would be undesirable to assign significance to a specific variation in stress or some other quantity due to variation introduced by the elastic registration procedure.

Various meshes representing both the prognathic and orthognathic skull geometries are created in an attempt to quantify the effect of non-unique registration and discretisation on the FEA result. This is done following the same logic used to illustrate the sensitivity of the registration procedure to user selected smoothing parameters. The various meshes obtained for the femur geometry is visible in Fig-

UNIVERSITEIT VAN PRETORIA
UNIVERSITY OF PRETORIA
YUNIBESITHI YA PRETORIA

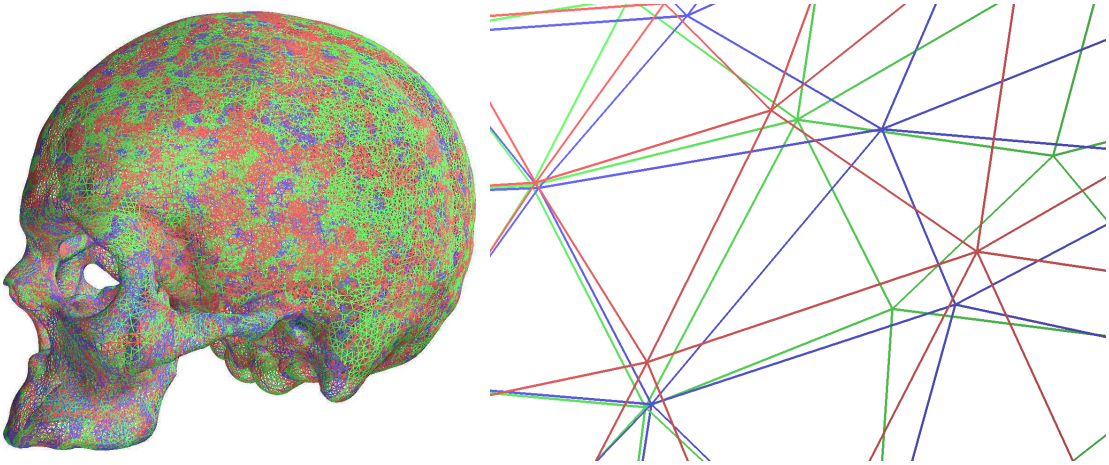

(a) (b)

Figure 6.20: (a) Three different meshes representing the orthognathic skull shape. (b) Detail of the meshes in (a) illustrating a difference in nodal coordinate positions. This is done for both prognathic and orthognathic skull shape. Three meshes representing each shape is used to quantify the influence the uniqueness of a registration result obtained by this method has on the final FEA result.

ure 3.8. An FEA on all the meshes could produce an approximate quantification of the uncertainty in the results displayed in Figure 6.19 (c).

The surface representing the symmetric version of the orthognathic skull in Figure 6.14 (c) is used as the target surface during a registration procedure. Two elastic surface registrations are performed with the generic mesh used in this chapter. The smoothing parameters used in the procedure are chosen as:

- $\gamma = 2$, $\sigma_0 = 10$ and $f = 1.0715$ and
- $\gamma = 2$, $\sigma_0 = 20$ and $f = 1.0715$.

The original surface mesh representing the orthognathic skull shape along with the result obtained from the two registrations are visible in Figure 6.20. Figure 6.20 (a) shows that the three meshes represent the same geometry while the detail of Figure 6.20 (b) shows that there is not a unique representation. The nodal coordinates close to feature registered areas coincide or are closely similar, even when using different smoothing parameters.

The same is done using the prognathic mesh surface as a target in the registration procedure, resulting in three different meshes that represent this shape. The tetrahedral mesh, generated on the average mesh illustrated in Figure 6.16 (b), is

UNIVERSITEIT VAN PRETORIA
UNIVERSITY OF PRETORIA
YUNIBESITHI YA PRETORIA

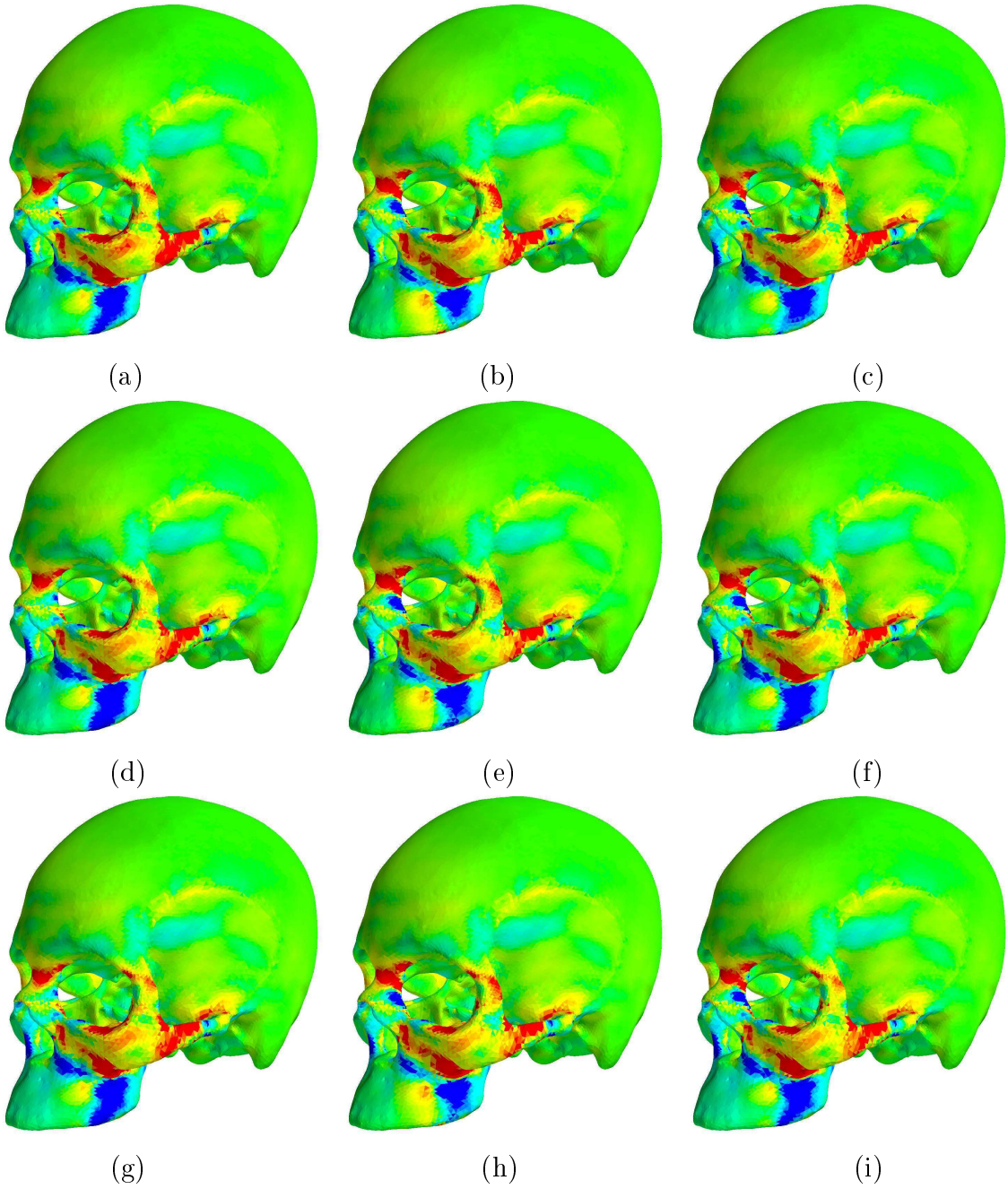

Figure 6.21: The difference in Von Mises stress between the results obtained using different prognathic and orthognathic skull shape mesh representation. Three mesh versions of the prognathic and of the orthognathic skull shape are used. An FEA is done on the molar bite load case using all six meshes. The FEA result on the prognathic meshes is compared to the result on the orthognathic meshes in the same way as Figure 6.19 (c). In each row the same prognathic mesh is compared to a different orthognathic mesh while each column shows the result of the same orthognathic mesh compared to a different prognathic mesh. Contours are given for the range $[-2, 2]$ MPa.

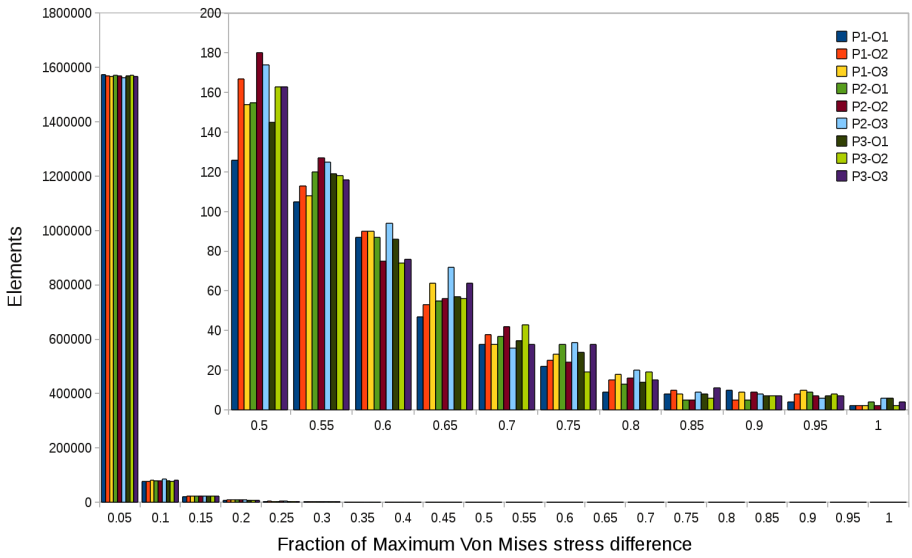

Figure 6.22: Histogram illustrating the distribution of stress variation. The results given in Figure 6.21 is categorised to show the small percentage of elements where a significant variation occur. The absolute value of these results are used and normalised to illustrate them on the same histogram. The majority of elements are seen to fall below 5% of the maximum absolute difference in Von Mises stress.

deformed using the displacement of boundary nodes. This is done as described in section 6.4 and mesh quality improvement is performed to generate usable meshes.

P1 refers to the original prognathic mesh while P2 and P3 refers to the two new prognathic meshes used in this subsection. The three orthognathic meshes are referred to as O1, O2 and O3. The Von Mises stresses of the results on these six meshes are compared in the same way as presented in Figure 6.19. Figure 6.21 shows the difference in Von Mises stress when various combinations of representations are used.

Figure 6.21 (a) is the same results as illustrated in Figure 6.19 (c) but shows contours for $\sigma_{\mathrm{P1}}^{\mathrm{vM}}$-$\sigma_{\mathrm{O1}}^{\mathrm{vM}}$ in the range $[-2, 2]$ MPa. Figures 6.21 (a), (b) and (c) are generated by comparing the same original prognathic mesh result ($\sigma_{\mathrm{P1}}^{\mathrm{vM}}$) with the three different orthognathic mesh results ($\sigma_{\mathrm{O1}}^{\mathrm{vM}}$, $\sigma_{\mathrm{O2}}^{\mathrm{vM}}$ and $\sigma_{\mathrm{O3}}^{\mathrm{vM}}$). The distribution of the absolute difference in Von Mises stress is given in Figure 6.22.

The figures displayed in Figure 6.21 only show contours of the difference in Von Mises stress for the range $[-2, 2]$ MPa with the true range interval for each comparison given in Table 6.2. Slight variation is noted in the difference in Von Mises stress between the prognathic and orthognathic shape when comparing the

	Orthognathic 1	**Orthognathic 2**	**Orthognathic 3**
Prognathic 1	$[-7.978, 12.839]$ MPa	$[-7.171, 12.332]$ MPa	$[-7.584, 12.232]$ MPa
Prognathic 2	$[-8.169, 12.464]$ MPa	$[-7.239, 11.958]$ MPa	$[-7.619, 11.857]$ MPa
Prognathic 3	$[-7.998, 12.367]$ MPa	$[-7.238, 11.860]$ MPa	$[-7.614, 11.760]$ MPa

Table 6.2: Range values for difference in Von Mises Stress. In each case the Von Mises stress result of the analysis of a molar bite on a orthognathic skull representation is subtracted from the same analysis done on a prognathic skull representation per element.

results displayed in Figure 6.21. The greatest deviation is visible for the second column of figures, especially in the bridge of the nose and upper mandible where the bite force is applied. To inspect the variation in the difference in Von Mises stress it is decided to compare the results used to generate Figure 6.21.

In Figure 6.23 the variation in difference in Von Mises stress is inspected. The result obtained when comparing the original prognathic and orthognathic stresses is used as a baseline. Four comparisons are made using the additional two prognathic and two orthognathic meshes along with the original representations. Figure 6.23 (a) is the result used to generate Figure 6.21 (b) $\sigma^{\text{vM}}_{\text{P1}}$-$\sigma^{\text{vM}}_{\text{O2}}$ subtracted from the result used to generate Figure 6.21 (a) $\sigma^{\text{vM}}_{\text{P1}}$-$\sigma^{\text{vM}}_{\text{O1}}$. Contours are displayed for the range $[-0.8, 0.8]$ MPa while the true range for this result is $[-4.93, 5.43]$ MPa. The other three figures also display contours for the range $[-0.8, 0.8]$ and are as follow:

- Figure 6.23 (b) is Figure 6.21 (a) - Figure 6.21 (c). $\left(\sigma^{\text{vM}}_{\text{P1}} - \sigma^{\text{vM}}_{\text{O1}}\right) - \left(\sigma^{\text{vM}}_{\text{P1}} - \sigma^{\text{vM}}_{\text{O3}}\right) = \sigma^{\text{vM}}_{\text{O3}} - \sigma^{\text{vM}}_{\text{O1}}$ has a range of $[-5.20, 5.23]$ MPa.
- Figure 6.23 (c) is Figure 6.21 (a) - Figure 6.21 (d). $\left(\sigma^{\text{vM}}_{\text{P1}} - \sigma^{\text{vM}}_{\text{O1}}\right) - \left(\sigma^{\text{vM}}_{\text{P2}} - \sigma^{\text{vM}}_{\text{O1}}\right) = \sigma^{\text{vM}}_{\text{P1}} - \sigma^{\text{vM}}_{\text{P2}}$ has a range of $[-5.26, 1.99]$ MPa.
- Figure 6.23 (d) is Figure 6.21 (a) - Figure 6.21 (g). $\left(\sigma^{\text{vM}}_{\text{P1}} - \sigma^{\text{vM}}_{\text{O1}}\right) - \left(\sigma^{\text{vM}}_{\text{P3}} - \sigma^{\text{vM}}_{\text{O1}}\right) = \sigma^{\text{vM}}_{\text{P1}} - \sigma^{\text{vM}}_{\text{P3}}$ has a range of $[-2.50, 1.53]$ MPa.

The two additional orthognathic mesh representations have the greatest influence on the variation in difference in Von Mises stress. The average nodal displacement applied to represent each mesh is reported in Table 6.3. Considering the average displacement required from the chosen generic surface mesh to represent this geometry, it makes sense that the registration to the orthognathic surface would be more sensitive to the user specified smoothing parameters. A greater difference

UNIVERSITEIT VAN PRETORIA
UNIVERSITY OF PRETORIA
YUNIBESITHI YA PRETORIA

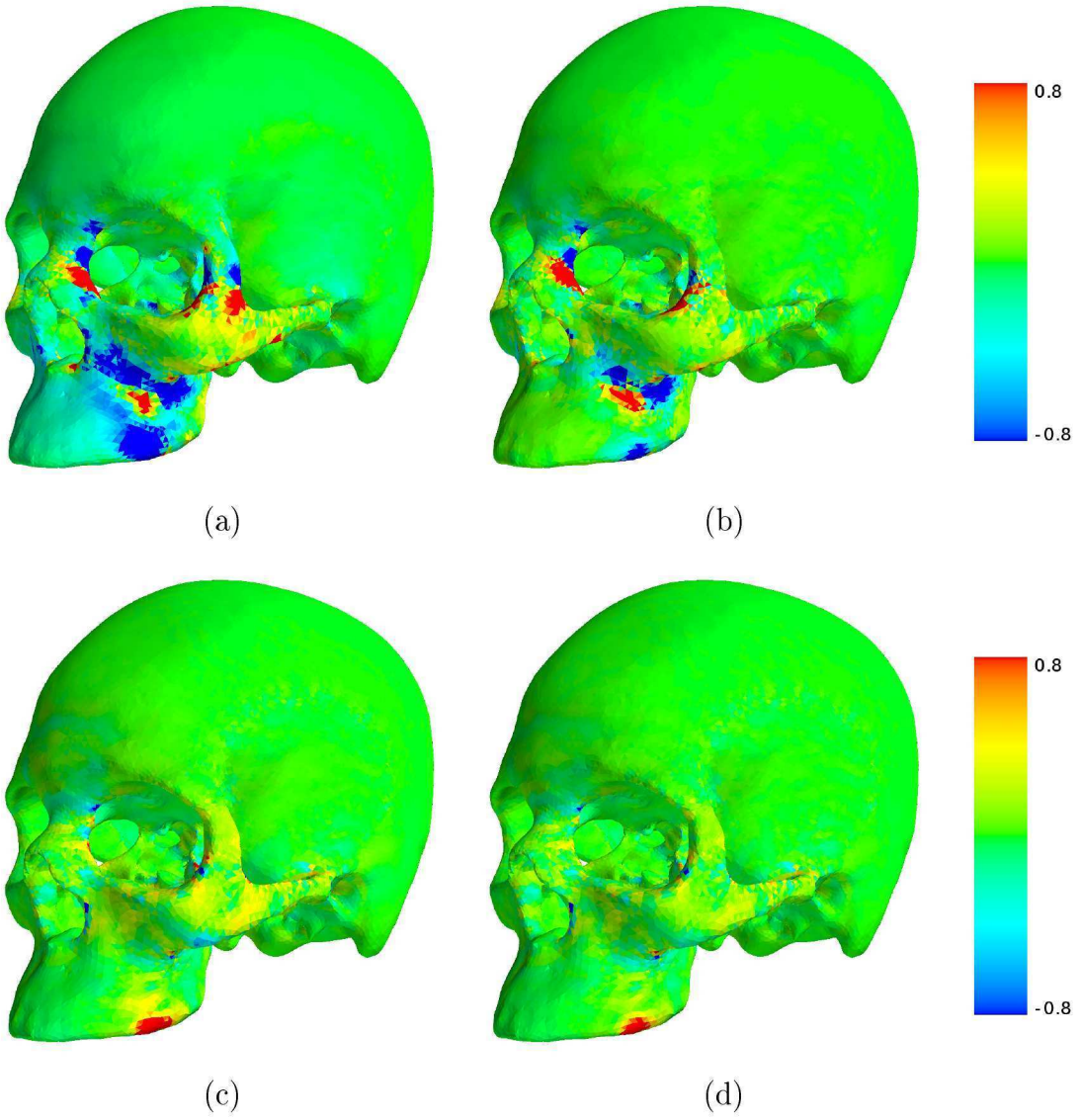

Figure 6.23: The variation of the difference in Von Mises stress using the original results compared to the difference in Von Mises stress when one of the original results is compared with the result on a new mesh representation. (a) Figure 6.21 (a) - Figure 6.21 (b). (b) Figure 6.21 (a) - Figure 6.21 (c). (c) Figure 6.21 (a) - Figure 6.21 (d). (d) Figure 6.21 (a) - Figure 6.21 (g).

UNIVERSITEIT VAN PRETORIA
UNIVERSITY OF PRETORIA
YUNIBESITHI YA PRETORIA

		P1	P2	P3	O1	O2	O3
	Average nodal distances [mm]						
(a)	**surface mesh to base:**	0.583	0.631	0.592	3.557	3.632	3.595
(b)	**tetrahedral mesh to average:**	1.686	1.667	1.671	1.674	1.757	1.720

Table 6.3: Distances from the nodal coordinates on each mesh representation to (a) the position on the generic surface mesh for surface points and (b) the tetrahedral mesh representing the average skull shape.

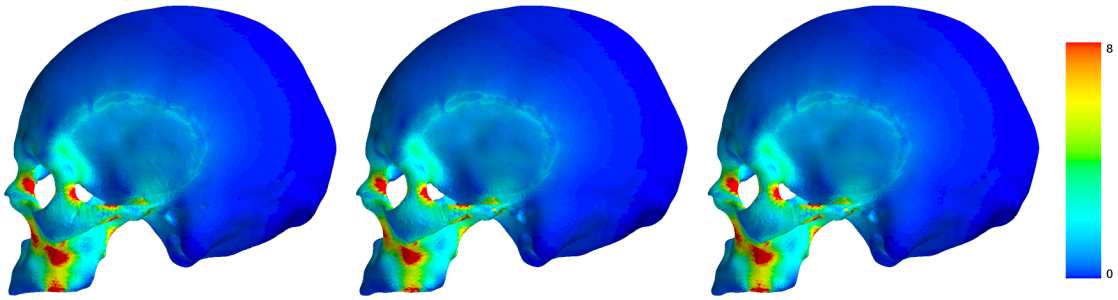

(a) (b) (c)

Figure 6.24: The Von Mises stress result for a molar bite analysis using the same nodes to apply boundary conditions on the three different orthognathic skull shape mesh representations.

in the final nodal coordinates of a mesh representing this shape would be expected due to the greater deformation required.

The Von Mises stress on the three different orthognathic skull representations is visible in Figure 6.24. These results appear to be very similar. The nodes used to apply the boundary condition representing bite force has moved slightly further backward in the second mesh representation of Figure 6.24 (b) when compared to the other two. This would explain the greater variation in the difference in Von Mises stress visible in the upper mandible when this result is compared with the prognathic results.

The elastic registration procedure, uniqueness of the elastic registration result and discretisation of the geometry represented does seem to have an effect on the results of the comparison illustrated in this chapter. If a study on functional morphology or some other comparison on shape and resulting stress field is done using elastic registration or a similar numerical tool, the researcher should use caution when drawing conclusions on the significance of a perceived variation in stress.

Although a slight variation in stress field pattern is visible in Figure 6.21, the

UNIVERSITEIT VAN PRETORIA
UNIVERSITY OF PRETORIA
YUNIBESITHI YA PRETORIA

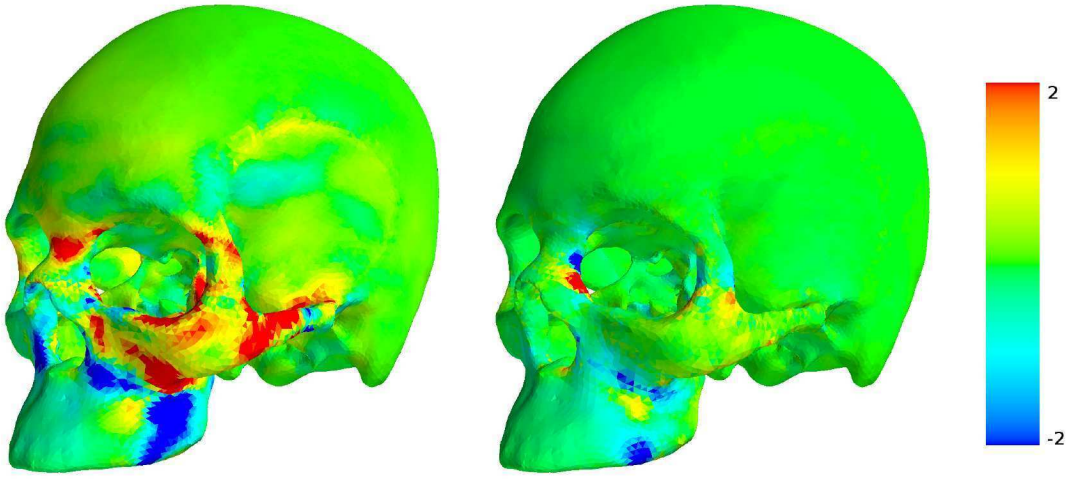

(a) (b)

Figure 6.25: (a) The difference in Von Mises stress for the original prognathic and orthognathic skull analyses also displayed in Figure 6.19 (c). (b) The variation noticed when comparing the Von Mises stress for the original prognathic and second orthognathic skull analyses to the original also displayed in Figure 6.23 (a). Contours are given for the range $[-2, 2]$ MPa.

overall difference in stress field observed here between the two skull forms analysed may likely be attributed to the difference in form and not the uniqueness of the mesh that represents that form. This is communicated in Figure 6.25 where the original comparison is displayed along with the variational result of Figure 6.23 (a) for contours given in the same range of $[-2, 2]$ MPa.

6.5.2 Linearity and constructing an approximate result from principal shape components

The linearity of the problem is illustrated next. The average of the results from an FEA done on the prognathic and orthognathic shape is compared to the FEA done on the average skull mesh. This is done to inspect whether it would be possible to simply construct an approximate representation of the stresses in the average shape from the analyses done on the two ends of the spectrum.

In this example, the average skull is seen as a new skull geometry that requires analysis. The meshes representing the prognathic and orthognathic shapes have already been analysed and it is now desired to check whether it would be possible to approximate the results on the new geometry from the results obtained on the

UNIVERSITEIT VAN PRETORIA
UNIVERSITY OF PRETORIA
YUNIBESITHI YA PRETORIA

meshes representing it's principal shape components.

The results are compared by taking the difference in Von Mises stress. This is because Von Mises stress is rotationally invariant. The difference in stress tensor for instance is not an accurate representation of the actual difference in stress. Stress tensors are recovered from a finite element analysis on different geometries with the same mesh topology. For each different mesh the same element is more than likely to have a different global orientation. A proper interpolation scheme is required or one may compare invariants of the stress tensor such as the eigenvalues (principal stresses).

In Figure 6.26, three different contours are presented on the mesh representing the average skull shape:

- (a) is the Von Mises stress contours for the range $[0, 8]$ MPa resulting from an FEA on the average skull shape with $\max\left(\sigma^{\text{vM}}_{\text{average}}\right) = 15.334$ MPa.
- (b) is the average of the Von Mises stresses for the range $[0, 8]$ MPa resulting from an FEA on the prognathic and orthognathic skull shape with $\max\left(\sigma^{\text{vM}}_{\text{prognathic}} + \sigma^{\text{vM}}_{\text{orthognathic}}\right)/2 = 16.006$ MPa.
- (c) is the difference in Von Mises stress $\sigma^{\text{vM}}_{\text{average}} - \left(\sigma^{\text{vM}}_{\text{prognathic}} + \sigma^{\text{vM}}_{\text{orthognathic}}\right)/2$ for the range $[-0.8, 0.8]$ MPa.

The distribution of the absolute difference in Von Mises stress illustrated in Figure 6.26 (c) is represented in the histogram of Figure 6.27. From this distribution it seems that there is a highly localised area of the skull where significant difference in Von Mises stress is present. The majority of elements vary with less than 5% of the maximum absolute difference in Von Mises stress. This means that the greater majority of elements have an absolute difference in Von Mises stress less than 0.162 MPa with the maximum absolute difference in Von Mises stress 3.247 MPa.

Because the optimisation procedure is required to untangle and improve the quality of the mesh, the coordinates of nodes on the average skull mesh is not the exact same as the average between the prognathic and orthognathic nodal coordinates. The difference between a node on the original average mesh and the location of that node on the average between the prognathic and orthognathic mesh is about 0.181 mm. There are 2402 out of the total of 290569 nodes that differ by more than 0.5 mm and 7 out of those differ by more than 1 mm.

UNIVERSITEIT VAN PRETORIA
UNIVERSITY OF PRETORIA
YUNIBESITHI YA PRETORIA

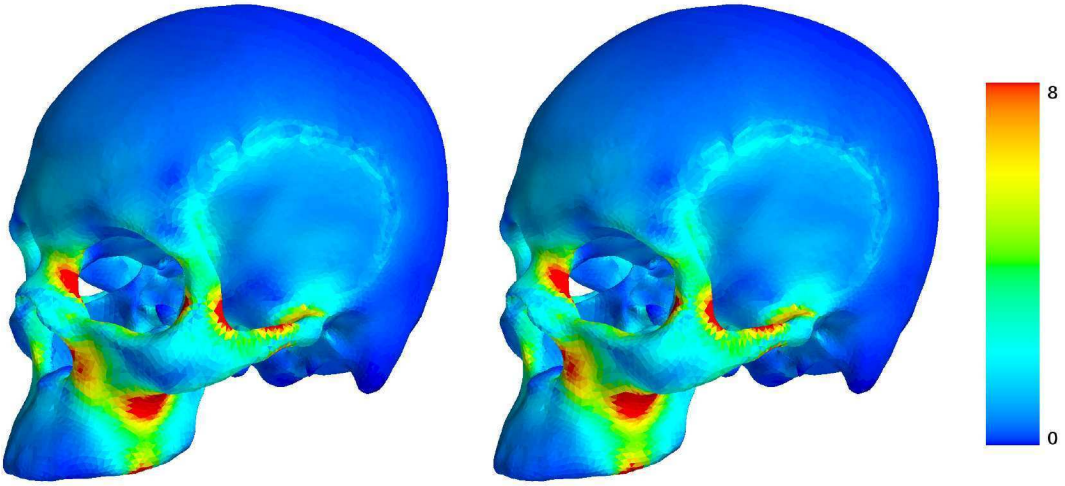

(a) (b)

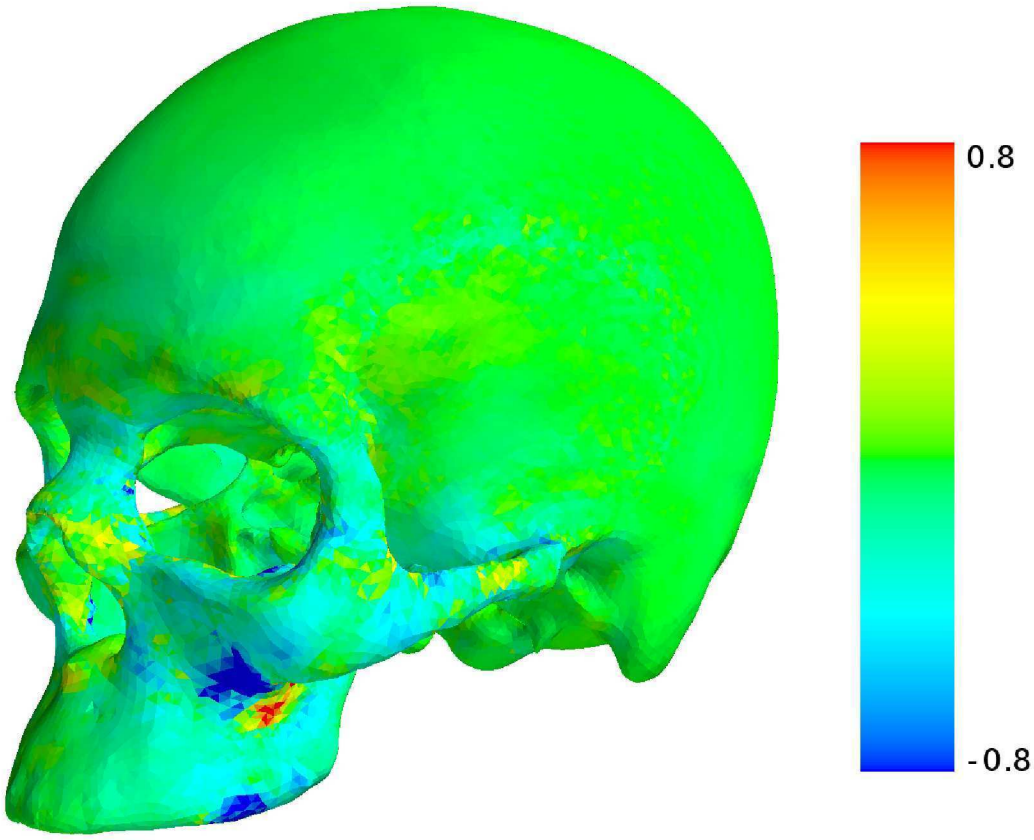

(c)

Figure 6.26: (a) The FEA resulting Von Mises stress on the average skull shape. (b) The average Von Mises result of the prognathic and orthognathic stresses plotted on the average skull mesh. (c) The difference in Von Mises stress $\sigma^{\text{vM}}_{\text{average}} - \left(\sigma^{\text{vM}}_{\text{prognathic}} + \sigma^{\text{vM}}_{\text{orthognathic}}\right)/2$. This falls in the range $[-2.699, 3.247]$ MPa.

UNIVERSITEIT VAN PRETORIA
UNIVERSITY OF PRETORIA
YUNIBESITHI YA PRETORIA

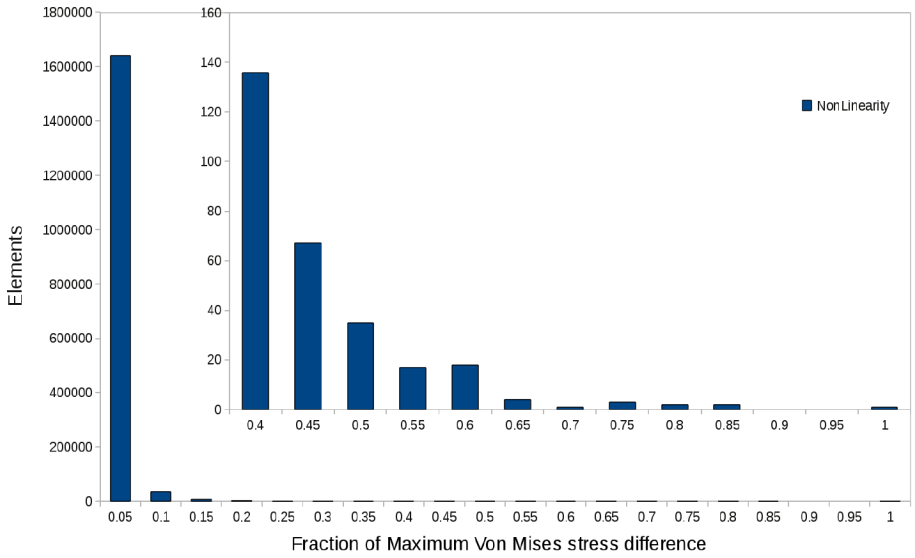

Figure 6.27: Histogram illustrating the distribution of stress variation. The absolute value of the results given in Figure 6.26 (c) is categorised to show the small percentage of elements where a significant variation occur. The majority of elements are seen to fall below 0.162 MPa, which is 5% of the maximum difference in Von Mises stress 3.247 MPa.

As the average mesh used is not exactly the same mesh obtained when taking the average of the prognathic and orthognathic meshes, some of the perceived non-linearity in Figure 6.26 (c) may be due to the non-linearity of the discretisation between these geometries. If one compares the contours that illustrate the sensitivity of discretisation on the compared FEA results visible in Figure 6.23 to this non-linearity of the result in Figure 6.26 (c) for the same range of $[-0.8, 0.8]$ MPa, it seems a very plausible explanation of the perceived non-linearity. Once a fully reliable registration procedure and interpolation scheme is in place, the non-linearity of a specific problem could be quantified or taken into account during comparisons and interpolations between various geometries. A principal component analysis done using a larger statistical sample of geometries may also prove useful in this regard.

If a linear or linearised problem is possible, performing an analysis on a new skull shape wouldn't be necessary. If a new geometry requires analysis, the linear coefficients of the principal modes of variation that approximate this geometry may be obtained. The result on the required geometry may then be approximated using this linear combination of the results on the principal modes.

Chapter 7

Conclusions

7.1 Remarks, Possibilities, Future Work and Applications

The procedure proposed in Chapter 6 adds functionality to the original elastic surface registration procedure implemented from literature. Feature registration gives an improved initial condition to the surface registration procedure. Not allowing the untrusted registration to unmatched feature areas reduces the need for a generic mesh to be exactly deformed into a target representation. This is helpful when topological inconsistencies between the generic and target shape could pose a problem.

Apart from some of the improvements made, the uniqueness of the registration result and it's dependence on user input is cause for concern and should receive due attention. The variation in masticatory induced stress for example due to prognathism can't be quantified without proper measures in place to describe the accuracy with which a target is represented. A difference in topology between the deformable mesh at the end of registration, and the target it should represent, makes it difficult to quantify how well a registration is performed and where further improvement is required.

Various possible improvements on the registration procedure or a similar elastic registration procedure could be addressed in future work. Many of the processes addressed in this report could be improved and only some of the more pressing changes are highlighted in this section. These improvements should give added reliability and robustness to the registration procedure while producing unique,

UNIVERSITEIT VAN PRETORIA
UNIVERSITY OF PRETORIA
YUNIBESITHI YA PRETORIA

usable registration results. Possible areas of improvement and how it could be beneficial include:

- Added reliability should be introduced into the registration process. One possibility is to investigate an improved correspondence between points. It would be beneficial to better determine where points on the deformable mesh should register. Using something like the shape context as described in Appendix C to do registration could be beneficial. These methods compare the context of each point within the greater shape to match up areas on the deformable and target mesh that likely represent the same position with reasonable accuracy.

- The possibility of comparing reduced model shapes or surface segments could also prove beneficial. A few possibilities exist to compare and register shapes with reduced dimensionality:

  - Most designed geometries can be represented as a combination of various primitive shapes such as boxes, spheres and cylinders. If possible, patient specific shapes could be approximated in this manner for initial crude comparison and registration.

  - The automatic segmentation of mesh surfaces using curvature information could give the same benefit. If this is done the overall surface segments can be compared or used in the approximation of base geometries that make up the patient specific geometry.

  - The use of RBFs to construct an implicit surface representation of a discretised surface is used to approximate and extract the overall features of various surfaces by Ohtake *et al.* [45]. Using a combination of mathematically defined smooth functions to represent a shape rather than the discretised surface mesh, it could be possible to compare a generic and target shape on this function level rather than using and comparing the mesh representations. This could be done to various degrees of accuracy by constructing the representation with more implicit surfaces for example if higher accuracy is required. If it is possible to compare the implicit surface representations instead of mesh representations it could be possible to find a unique registration to deform one implicit representation into the other. The spatial deformation field obtained in this manner could then be applied to the mesh.

UNIVERSITEIT VAN PRETORIA
UNIVERSITY OF PRETORIA
YUNIBESITHI YA PRETORIA

- The use of a finite element mesh and improved physics during the registration process is another area that deserves attention. Using a better defined deformation model than the iterative application of a Gaussian weighted smoothed deformation field could produce improved results. The possible use of better registration techniques along with a better deformation model could better capture the physics required from one state to another in the deformation or alternate state of the same soft organ geometry for example. The use of a hyper-elastic [65] material model or allowing something like "work hardening"[1] to counter element inversion could also be investigated. The use of a single mesh to represent all geometries of concern should remain an integral part of the process deliverable. If element inversion is simply not allowed during mesh deformation, there would be no need to untangle the mesh or remove inverted elements.

- The registration and deformation procedure should be attempted using optimisation. If a finite element mesh is deformed to better represent a target surface or the boundary of a target computational domain for example, the optimum registration should be obtained that represents the target with induced strain at a minimum. If this can be achieved, a unique registration result should be guaranteed.

Future applications of the improved registration procedure are numerous. A few attractive applications are listed that could be pursued once a reliable elastic registration procedure is available:

- The registration of a large sample of similar geometries. This should be done with a procedure that always finds the same unique result for a specific target geometry or computational domain. It would be undesired to extract the principal modes of variation in a statistical sample of registered subjects only to have these be a function of the registration procedure or some user input specified. The change in flow field or stress due to a specific mode of variation could be inspected once this is achieved.

- Registration to transient data of the same geometry. If transient data is available for a heart, an artery or some other soft organ geometry, fluid struc-

[1] Work or strain hardening in numerical methods approximate what happens during the cold working of metals. It is the strengthening of a metal by plastic deformation where the strengthening occurs because of dislocation interaction within the crystal structure of the material [27].

UNIVERSITEIT VAN PRETORIA
UNIVERSITY OF PRETORIA
YUNIBESITHI YA PRETORIA

ture interaction or intra-operable deformation could be studied. This should also be done in a least strain manner if at all possible. The intraoperative[2] tracking of deformation is a major deliverable in patient specific modelling and research. For that reason, this application of the registration procedure should prove useful.

- Research into obtaining *in vivo* material properties for use in numerical modelling [41]. Obtaining material properties *in vivo* could be pursued along with the benchmarking and validation of fluid structure interaction (FSI) simulations. As an example, the boundary of an artery could be tracked and described numerically after a reliable registration procedure is performed on transient geometric data. If the boundary conditions and the movement of the computational domain boundary is known it could be possible to extract material properties from some kind of inverse FSI type simulation. The material properties extracted can then be used in further patient specific modelling.

[2] During surgery

Bibliography

[1] Aim@Shape model repository. URL `http://shapes.aim-at-shape.net/`.

[2] Amira 5.0. URL `http://www.amira.com/`.

[3] FEBio finite elements for biomechanics software. URL `http://mrl.sci.utah.edu/software/febio`.

[4] INRIA model repository. URL `http://www-roc.inria.fr/gamma/download/download.php`.

[5] MESQUITE mesh quality improvement toolkit. URL `http://www.cs.sandia.gov/optimization/knupp/Mesquite.html`.

[6] PostView finite element post-processing software. URL `http://mrl.sci.utah.edu/software/postview`.

[7] PreView finite element pre-processing software. URL `http://mrl.sci.utah.edu/software/preview`.

[8] Python. URL `http://docs.python.org/`.

[9] TetGen. URL `http://tetgen.berlios.de/`.

[10] VRMesh Studio. URL `http://www.vrmesh.com/products/studio.asp`.

[11] SciPy: Open source scientific tools for python, 2001. URL `http://www.scipy.org/`.

[12] L. Aiello and C. Dean. *An introduction to human evolutionary anatomy*, Volume 1990. Academic Press, London.

[13] P.J. Besl and H.D. McKay. A method for registration of 3D shapes. *IEEE Transactions on Pattern Analysis and Machine Intelligence*, 14:239–256, 1992.

UNIVERSITEIT VAN PRETORIA
UNIVERSITY OF PRETORIA
YUNIBESITHI YA PRETORIA

[14] A. Bjork. Some biological aspects of prognathism and occlusion of the teeth. *Acta Odontologica Scandinavica*, 9:3–27, 1950.

[15] N.G. Blanksma and T.M.G.J. van Eijden. Electromographic heterogeneity in the human temporalis muscle. *Journal of Dental Research*, 69:1686–1690, 1990.

[16] N.G. Blanksma, T.M.G.J. van Eijden, L.J. van Ruijven, and W.A. Weijs. Electromographic heterogeneity in the human temporalis and masseter muscles during dynamic task guided by visual feedback. *Journal of Dental Research*, 76:542–551, 1997.

[17] A. Boryor, M. Geiger, A. Hohmann, A. Wunderlich, C. Sander, F.M. Sander, and F.G. Sander. Stress distribution and displacement analysis during an intermaxillary disjunction - a three-dimensional fem study of a human skull. *Journal of Biomechanics*, 41:376–382, 2008.

[18] P. Brown and T. Maedea. Post-pleistocene diachromic change in east asian facial skeletons: shape and volume of the orbits. *Anthropological Science*, 112: 29–40, 2004.

[19] R. Bryan, P.S. Mohan, A. Hopkins, F. Galloway, M. Taylor, and P.N. Nair. Statistical modelling of the whole human femur incorporating geometric and material properties. *Mechanical Engineering and Physics*, 32:57–65, 2010.

[20] D.L.A. Camacho, R.H. Hopper, G.M. Lin, and B.S. Myers. An improved method for finite element mesh generation of geometrically complex structures with application to the skullbase. *Journal of Biomechanics*, 30:1067–1070, 1997.

[21] W. Che, J. Paul, and X. Zhang. Lines of curvature and umbilical points for implicit surfaces. *Computer Aided Geometric Design*, 24:395–409, 2007.

[22] H. Chen and B. Bhanu. 3D free-form object recognition in range images using local surface patches. *Pattern Recognition Letters*, 28:1252–1262, 2007.

[23] S.N. Cobb and P. O'Higgins. Homonins do not share a common postnatal facial ontogenetic shape trajectory. *Journal of Experimental Zoology*, 302B:302–321, 2004.

UNIVERSITEIT VAN PRETORIA
UNIVERSITY OF PRETORIA
YUNIBESITHI YA PRETORIA

[24] R.D. Cook, D.S. Malkus, M.E. Plesha, and R.J. Witt. *Concepts and applications of Finite Element Analysis*. John Wiley & Sons, 2002.

[25] N. Curtis, K. Kupczik, P. O'Higgins, M. Moazen, and M. Fagan. Predicting skull loading: Applying multibody dynamics analysis to a macaque skull. *The Anatomical Record*, 291:491–501, 2008.

[26] A. de Boer, M.S. van der Schoot, and H. Bijl. Mesh deformation based on radial basis function interpolation. *Computers and Structures*, 85:784–795, 2007.

[27] E.P. Degarmo, J.T. Black, and R.A. Kohser. *Materials and Processes in Manufacturing*. Wiley, 9th edition, 2003.

[28] S. Du, N. Zheng, S. Ying, and J. Liu. Affine iterative closest point algorithm for point sets registration. *Pattern Recognition Letters*, 31:791–799, 2010.

[29] J.M. Escobar, E. Rodrigues, R. Montenegro, G. Montero, and J.M. Gonzalez-Yuste. Simultaneous untangling and smoothing of tetrahedral meshes. *Computer Methods in Applied Mechanics and Engineering*, 192:2775–2787, 2003.

[30] M.J. Fehrenbach and S.W. Herring. *Illustrated Anatomy of the Head and Neck*. W.B. Saunders Company, Philadelphia, 1996.

[31] A. Frome, D. Huber, R. Kolluri, T. Bulow, and J. Malik. Recognizing objects in range data using regional point descriptors. In *European Conference on Computer Vision*, volume 3, pages 224–237, 2004.

[32] F. Groning, J. Liu, M.J. Fagan, and P. O'Higgins. Validating a voxel based finite element model of a human mandible using digital speckle patter interferometry. *Journal of Biomechanics*, 42:1224–1229, 2009.

[33] K. Hildebrandt, K. Polthier, and M. Wardetzky. Smooth feature lines on surface meshes. *Eurographics Symposium on Geometric Processing*, 2005.

[34] A. Hsieh, C. Ho, and K. Fan. An extention of the bipartite weighted matching problem. *Pattern Recognition Letters*, 16:347–353, 1995.

[35] I. Ichim, M. Sawin, and J.A. Kieser. Mandibular biomechanics and development of the human chin. *Journal of Dental Research*, 85:638–642, 2006.

[36] I.T. Jolliffe. *Principal Component Analysis, Second Edition*. Springer, 2002.

UNIVERSITEIT VAN PRETORIA
UNIVERSITY OF PRETORIA
YUNIBESITHI YA PRETORIA

[37] S. Kim and C. Kim. Finding ridges and valleys in a discrete surface using a modified mls approximation. *Computer Aided Design*, 38:173–180, 2006.

[38] K. Kupczik, C.A. Dobson, M.J. Fagan, R.H. Crompton, C.E. Oxnard, and P. O'Higgins. Assessing mechanical function of the zygomatic region in macaques: validation and sensitivity testing of finite element models. *Journal of Anatomy*, 210:41–53, 2007.

[39] E.N. L'Abbe, M. Loots, and M.J. Meiring. The pretoria bone collection: A modern south african skeletal sample *Documented Collection*, The University of Pretoria, 2005.

[40] M. Meyer, M. Desbrun, P. Shröder, and A.H. Barr. Discrete differential-geometry operators for triangulated 2-manifolds. *Visualisation and Mathematics III*, 35–57, 2003.

[41] K. Miller, K. Chinzei, G. Orssengo, and P. Bednarz. Mechanical properties of brain tissue in-vivo: experiment and computer simulation. *Journal of Biomechanics*, 33:1369–1376, 2000.

[42] P. Mitteroecker and P. Gunz. Advances in geometric morphometrics. *Evolutionary Biology*, 36:235–247, 2009.

[43] P.M. Moore-Jansen, S.D. Ousley, and R.L. Jantz. Data collection procedures for forensics skeletal material: Report of investigations. Technical Report 48, The University of Tennessee: Department of Anthropology, Knoxville, 1994.

[44] M. Moshfeghi, S. Ranganath, and K. Nawyn. Three-dimensional elastic matching of volumes. *IEEE Transactions on Image Processing*, 3:128–138, 1994.

[45] Y. Ohtake, A. Belyaev, and H. Seidel. Ridge-valley lines on meshes via implicit surface fitting. *ACM Transactions on Graphics*, 23:609–612, 2004.

[46] J. Paphangkorakit and J.W. Osborn. Effects of human maximum bite force of biting on a softer or harder object. *Archives of Oral Biology*, 43:833–839, 1998.

[47] J. Peterson and P.C. Dechow. Material properties of the human cranial vault and zygoma. *The Anatomical Record Part A*, 274 A:785–97, 2003.

UNIVERSITEIT VAN PRETORIA
UNIVERSITY OF PRETORIA
YUNIBESITHI YA PRETORIA

[48] G. Pileicikiene and A. Surna. The masticatory system from a biomedical perspective: A review. *Baltic Dental and Maxillofacial Journal*, 6:81–84, 2004.

[49] H. Preuschoft and U. Witzel. Functional shape of the skull in verebrates: Which forces determine skull morphology in lower primates and ancestral synapsids. *The Anatomical Record Part A*, (283A):402–413, 2005.

[50] C. Provatidis, B. Georgiopoulos, A. Kotinas, and J.P. McDonald. On the fem modelling of craniofacial changes during rapid maxillary expansion. *Medical Engineering and Physics*, 29:566–579, 2007.

[51] A. Quarterioni and S. Fausto. *Scientific Computing with MATLAB and Octave*. Springer, 2006.

[52] B.G. Richmond, B.W. Wright, I. Grosse, P.C. Dechow, F.R. Callum, M.A. Spencer, and D.S. Strait. Finite element analysis in functional morphology. *The Anatomical Record Part A*, 283A:259–274, 2005.

[53] J.H. Robertson. More on skeletal analysis and the race concept. *Current Anthropology*, 20:617, 1979.

[54] D.E. Slice. Geometric morphometrics. *Annual Review in Anthropology*, 36: 261–281, 2007.

[55] H.F. Smith, C.E. Terhune, and C.A. Lockwood. Genetic, geographic and environmental correlates of human temporal bone variation. *American Journal of Physical Anthropology*, 134:312–322, 2007.

[56] J.B. Smith and C.W. Snuggs. Dynamic properties of the human head. *Journal of Sound and Vibration*, 48:35–43, 1976.

[57] D.S. Strait, B.G. Richmond, M.A. Spencer, F.R. Callum, P.C. Dechow, and B.A. Wood. Masticatory biometrics and its relevance to early hominid phylogeny: An examination of palatal thickness using finite-element analysis. *Journal of Human Evolution*, 52:585–599, 2007.

[58] D.S. Strait, Q. Wang, P.C. Dechow, F.R. Callum, B.G. Richmond, M.A. Spencer, and B.A. Patel. Modeling elastic properties in finite element analysis: how much precision is needed to produce an accurate model? *The Anatomical Record Part A*, 283A:275–287, 2005.

UNIVERSITEIT VAN PRETORIA
UNIVERSITY OF PRETORIA
YUNIBESITHI YA PRETORIA

[59] G. Subsol, J.P. Thirion, and N. Ayache. A general scheme for automatically building 3D morphometric anatomical atlasses: application to a skull atlas. *Medical Image Analysis*, 2:37–60, 1998.

[60] K. Tanne, J. Miyasaka, Y. Yamagata, R. Sachdeva, and S. Tsutsumi. Three-dimensional model of the human craniofacial skeleton: method and preliminary results using finite element analysis. *Journal of Biomedical Engineering*, 10: 246–252, 1988.

[61] G. Taubin. A signal processing approach to fair surface design. In *Proceedings of the 22nd Annual Conference on Computer Graphics and Interactive Techniques*, pages 351–358, 1995.

[62] J. Vollmer, R. Mencl, and H. Müller. Improved laplacian smoothing of noisy surface meshes. *Eurographics*, 18:131–138, 1999.

[63] S.H.Y. Wei. Craniofacial variations, sex differences and the nature of prognathism in chinese subjects. *Angle Orthodontist*, 39:303–315, 1969.

[64] W.A. Weijs and B. Hillen. Cross-sectional areas and estimated intrinsic strength of the human jaw muscles. *Acta Morphol Neerl-Scand*, 23:267–274, 1985.

[65] J.A. Weiss, B.N. Maker, and S. Govindjee. Finite element implementation of incompressible, transversely isotropic hyperelasticity. *Computer Methods in Applied Mechanics and Engineering*, 135:107–128, 1996.

[66] T.D. White. *Human Osteology*. Academic Press, San Diego, California, 2000.

[67] S. Wroe, K. Moreno, P. Clausen, C. Mchenry, and D. Curnoe. High-resolution three dimensional computer simulation of homonid cranial mechanics. *The Anatomical Record*, 290:1248–1255, 2007.

[68] D. Xiao, D. Zahra, P. Bourgeat, P. Berghofer, O.A. Tamayo, C. Wimberley, M.C. Gregoire, and O. Salvado. An improved 3d shape context based non-rigid registration method and its application to small animal skeletons registration. *Computerized Medical Imaging and Graphics*, 34:321–332, 2010.

[69] J. Xie, P. Heng, and M. Shah. Shape matching and modeling using skeletal context. *Pattern Recognition*, 41:1756–1767, 2008.

UNIVERSITEIT VAN PRETORIA
UNIVERSITY OF PRETORIA
YUNIBESITHI YA PRETORIA

[70] S. Yoshizawa, A. Belyaev, H. Yokota, and H. Seidel. Fast, robust, and faithful methods for detecting crest lines on meshes. *Computer Aided Geometric Design*, 25:545–560, 2008.

[71] Z. Yu, M. J. Holst, and A. McCammon. High-fidelity geometric modeling for biomedical applications. *Finite Elements in Analysis and Design*, 44:715–723, 2008.

Appendix A

Finite Element Analysis on a Prognathic and Orthognathic Skull Geometry

A.1 Introduction

The forces applied through the cycles of mastication are influenced by a variety of factors. The size and strength of masticatory muscles and their attachment to structures within the crania are of importance. The size and form of these cranial structures and the location of healthy teeth and gums also have a major influence.

To simulate mastication and determine the corresponding stress field, a finite element model can be created and analysed from a digital patient's cranial geometry. This includes decisions as to the appropriate material properties, boundary conditions and imposed loads.

The background work to this project aimed at applying the general rules of bone behavior and muscle activity in order to test a hypothesis about a single facial characteristic. This is done in collaboration with a Ph.D. student in Anthropology. The hypothesis of the Ph.D. work states that the location of bone stress in the crania of a prognathic[1] facial form will vary from that in the orthognathic[2] facial form. With this in mind, the hypothesis is tested with the aid of a finite element tool.

[1] One or both jaws projecting forward.
[2] Jaws don't project forward giving a flatter facial profile.

UNIVERSITEIT VAN PRETORIA
UNIVERSITY OF PRETORIA
YUNIBESITHI YA PRETORIA

Chapter 2 in this report covers most of the ideas and background work done to test the hypothesis. This appendix is included to accompany Chapter 2 and serves as additional documentation of the initial FEA. Although much of this appendix is duplicated from Chapter 2, imposed boundary conditions are covered more accurately and additional results are displayed.

A.2 Geometries

The reason for this study is a validation on the the adaption of skull form to minimise internal stress due to mastication. For this reason two skulls were selected for analysis based on gnathic index and sufficient dentition from the University of Pretoria skull collection [39]. A skull with a gnathic index of 106.9 is used to represent a prognathic facial form and a skull with a gnathic index of 91.5 represents the orthognathic facial form.

A.2.1 Model Creation

A Siemens SOMATOM 16 medical computer tomography (CT) scanner was used to create scans of the selected geometries. 629 slices was made of the prognathic skull and 656 of the orthognathic skull with a set scanner thickness of 0.75 mm. Using these scans as image stacks imported into Amira® 5.0 [2], a triangulated surface mesh was extracted. This is done after a thresholding procedure where adjustments are made on the gray scale of voxel density data. Attenuation of the scans highlights bony morphology while eliminating unwanted material picked up by the scanner.

Intersecting and inconsistent triangles as well as the effects of postmortem trauma and decay has to be taken into account. For this reason the extracted surface representations are then edited and smoothed using VRMesh Studio [10]. Taking into account that exact stress values aren't required and this study is mainly on the variation in stress pattern, a four noded tetrahedral finite element mesh is created from the final surface representation using TetGen [9]. This results in a model for the prognathic skull consisting of 113 104 nodes and 401 455 elements while 110 645 nodes and 397 354 elements are used in representing the orthognathic skull in the initial analysis.

UNIVERSITEIT VAN PRETORIA
UNIVERSITY OF PRETORIA
YUNIBESITHI YA PRETORIA

A.3 Material Properties

Significant variation in material properties have been documented for a range of different bones and within different areas of the same bone structure. The anisotropic nature of bone and how to model it is however not the focus of this research. It is assumed that comparing only the stress fields produced by mastication doesn't require the accurate simulation of bone to the extent that exact stress and strain values are recovered from a finite element analysis.

For similar analyses done in literature, isotropic bone material properties have been found capable of producing realistic stress patterns [17, 20, 32, 35, 38, 60]. Considering the highly reduced level of effort this entails the same assumption was made to model the full skull and teeth with a single linear elastic material.

Tetrahedral finite element meshes are imported into PreView [7] to set up the model by defining material properties and boundary conditions. The Young's modulus and Poisson's ratio used was taken from the literature [17, 20, 32, 35, 38, 50, 60] to be 16 GPa and 0.3 .

A.4 Boundary Conditions

FEBio [3], a solver developed specifically for biomechanics finite element applications is used in this study. Although this package allows muscles and tendons to be modelled using an array of element types it was decided that the forces of mastication would be modelled as external forces on the skull. The forces are applied to nodes in the region representing the approximate sites of muscle attachment as described with the help of Figure 2.1.

The average nodal coordinate value of nodes on the occipital condyles (OC) in the region of the foramen magnum is used as the origin of a Cartesian coordinate axis. Here the x-axis is directed from the right to the left, y-axis orientated anterior posterior (front to back) and the z-axis inferior superior (bottom to top) to the skull.

Muscle force values are first approximated for a vertical bite force on the first incisor and first molar. A system of equations is then set up to solve the bite force and reaction forces at the temporomandibular joint (TMJ) for each skull model before all forces are scaled, resulting in an identical force on the teeth. The skulls are scaled to have the same basion to nasion distance (See ba-n in Figure 1.1) and

UNIVERSITEIT VAN PRETORIA
UNIVERSITY OF PRETORIA
YUNIBESITHI YA PRETORIA

		Temporalis	Superficial Masseter	Deep Head Masseter	Medial Pterygoid
(a)	**Working Side**				
	Force [N]	410	230	100	250
(b)	**Balancing Side**				
	% Working	41	47	36	20
	Force [N]	168.1	108.1	36	50

Table A.1: Initial muscle forces. (a) Working side force values used and (b) balancing side as a percentage of working side force derived from [57] with equivalent force value.

	Section	1	2	3	4	5	6	7
(a)	**Activity [%]**	86	70	56	52	44	47	49
(b)	**Nodes**							
	Prognathic L	57	28	25	32	20	9	15
	R	61	39	35	33	20	11	15
	Orthognathic L	62	32	37	28	22	13	17
	R	69	36	36	38	27	13	18
(c)	**Force per node [N]**							
	Prognathic L	3.22	2.62	2.10	1.95	1.65	1.76	1.83
	R	1.15	0.94	0.75	0.70	0.59	0.63	0.66
	Orthognathic L	2.87	2.34	1.87	1.74	1.47	1.57	1.64
	R	1.05	0.85	0.68	0.63	0.54	0.57	0.60

Table A.2: Temporalis muscle section force distribution. (a) Activity of muscle sections approximated from [15] for a vertical bite force. (b) Nodes in each section and (c) weighted resultant force value.

rotated so a line through the equivalent nodal coordinates of the TMJ would be exactly parallel to the x-axis.

A.4.1 Muscle Forces

Muscle action during the cycles of mastication are different for working and balancing sides. For this stress simulation the left side of the skull is arbitrarily chosen as the working side of the dental arcade where bite force is applied. Force values used here is determined from literature with force scaling factors obtained from a study on muscle activity during mastication [57].

The initial muscle forces used to calculate bite force and reaction forces at the TMJs are given in Table A.1. These forces along with balancing muscle forces

UNIVERSITEIT VAN PRETORIA
UNIVERSITY OF PRETORIA
YUNIBESITHI YA PRETORIA

determined on the opposite side are tabulated.

For each skull, the muscle force directions are determined. This is done from the equivalent average nodal coordinate of nodes selected to represent the location of muscle attachment. A unit vector from this muscle origin to a digital landmark representing the approximate area of attachment on the mandible is then determined.

The temporalis muscle is divided into seven segments, numbered and ordered anterior to posterior. Figure 2.2 (a) shows the approximate positions of the segmentation of the fan like temporalis on the prognathic skull form with numbers 1 through 7. Segmenting this muscle enjoys frequent application for similar studies done in literature [52] and is motivated as follows:

- Temporalis muscle activity and thickness varies from anterior to posterior.
- The segments can act in different directions, representing the fan-like muscle with greater accuracy than a single force direction.

The force values for each segment is determined using the number of nodes in each section along with the approximate muscle activity in that section to give each segment a weight. The relative weight of a segment i is determined from

$$\omega_i = \frac{n_i \times EMG_i}{\sum_{j=1}^{N_{\text{seg}}} (n_j \times EMG_j)}, \tag{A.1}$$

where n is the number of nodes and EMG is the approximate electromyographic reading measured in that section of the muscle for an applied vertical bite force. This is approximated from work done by Blanksma and van Eijden [15]. This weight along with the known direction of force of each segment is used to then calculate the force each segment contributes. The contributions result in 410 N on the working side and 168.1 N on the balancing side positions where the temporalis attaches to the mandible. The muscle section activity, number of nodes in each section and forces applied to the nodes in each section of the temporalis muscle is presented in Table A.2.

The work done by Blanksma and van Eijden [15] does not specify whether temporalis section activity is different for prognathic or orthognathic facial form during an applied vertical bite force. It is assumed that their results may be used for both skull forms analysed.

UNIVERSITEIT VAN PRETORIA
UNIVERSITY OF PRETORIA
YUNIBESITHI YA PRETORIA

A.4.2 Reaction Forces

The model is constrained in the region of the foramen magnum at the occipital condyles in all six degrees of freedom to prevent rigid body movement. The masticatory forces applied usually act on the mandible and so are an internal balanced system. A problem exists however in that only six unknowns can be solved for a statically determinate analysis in three dimensions while there are seven unknowns that require solution:

- One unknown for the z-value of the force at the tooth. The friction forces are not taken into account for this analysis so that the bite force is assumed to have a single component. This is also due to constraints on the number of unknowns that can be solved in a three dimensional statically determinate analysis.
- Six unknowns for the x- , y- and z-values for working and balancing side TMJ forces.

A simple free body diagram of the problem in the $y-z$ plane is visible in Figure A.1. Here the vector components in red represent the components of a muscle force. These are displayed as if applied to the average nodal coordinate of nodes chosen to represent the position of that muscle's attachment. The vector components in blue are the unknown balancing force components at the tooth and TMJs. By solving the system of Equations (A.2), the unknown balancing force values are obtained.

The skull is rotated so a line through the equivalent nodal coordinates of the TMJs is exactly parallel to the x-axis. The components of these forces in the x-direction can now be bundled, allowing a solvable system of equations where only 6 unknowns are present. Static force balance equations are used. The skull is assumed a rigid body that does not undergo any deformation during loading. From

$$\begin{aligned} \sum F &= 0 \\ \sum M_{\mathrm{OC}} &= 0 \end{aligned} \tag{A.2}$$

with F the vector of forces and M_{OC} the moments about the occipital condyles, the resulting system of equations is set up. The six equations that are solved can be

UNIVERSITEIT VAN PRETORIA
UNIVERSITY OF PRETORIA
YUNIBESITHI YA PRETORIA

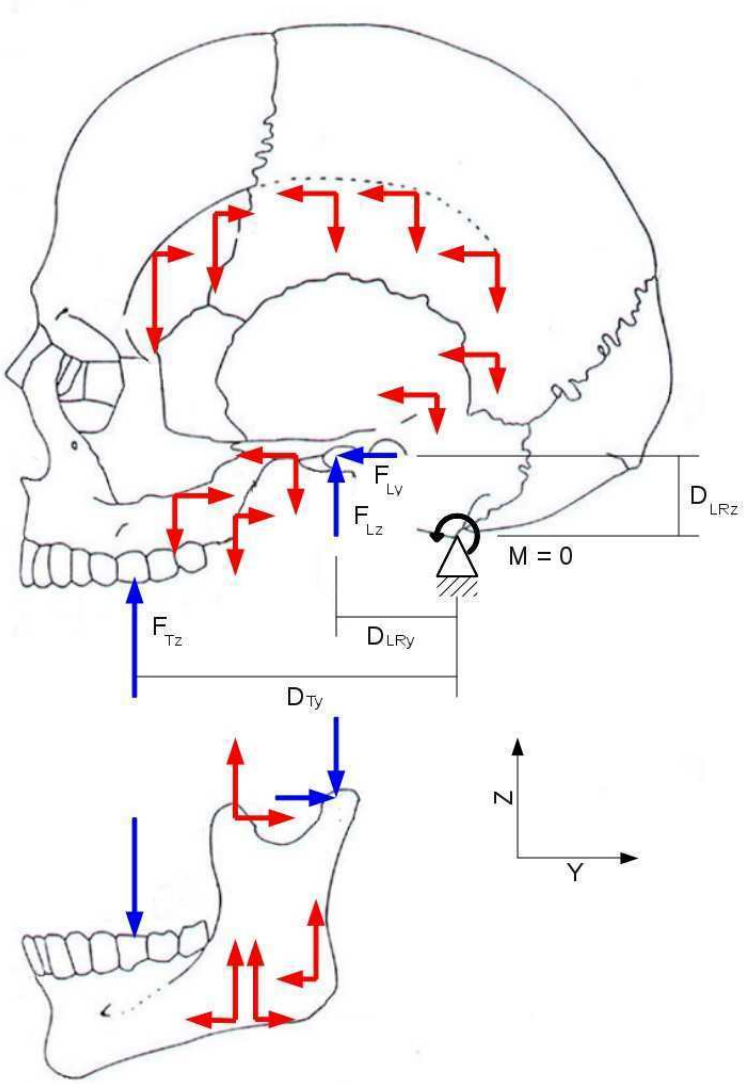

Figure A.1: Free body diagram of the skull in the yz-plane. Muscle force components are visible in their approximate locations (red) as well the reaction forces (blue) for the working side of both the crania and mandible .

UNIVERSITEIT VAN PRETORIA
UNIVERSITY OF PRETORIA
YUNIBESITHI YA PRETORIA

given in the form

$$\begin{Bmatrix} \sum F_x \\ \sum F_y \\ \sum F_z \\ \sum M_{\mathrm{OC}x} \\ \sum M_{\mathrm{OC}y} \\ \sum M_{\mathrm{OC}z} \end{Bmatrix}_{\text{unknown}} = - \begin{Bmatrix} \sum F_x \\ \sum F_y \\ \sum F_z \\ \sum M_{\mathrm{OC}x} \\ \sum M_{\mathrm{OC}y} \\ \sum M_{\mathrm{OC}z} \end{Bmatrix}_{\text{known}} . \tag{A.3}$$

Using a free body diagram as in Figure A.1 along with all of the assumptions made, the system is then set up as

$$\begin{bmatrix} 1 & 0 & 0 & 0 & 0 & 0 \\ 0 & 1 & 1 & 0 & 0 & 0 \\ 0 & 0 & 0 & 1 & 1 & 1 \\ 0 & -D_{Lz} & -D_{Rz} & D_{Ly} & D_{Ry} & D_{Ty} \\ D_{LRz} & 0 & 0 & -D_{Lx} & -D_{Rx} & -D_{Tx} \\ -D_{LRy} & D_{Lx} & D_{Rx} & 0 & 0 & 0 \end{bmatrix} \begin{Bmatrix} F_{LRx} \\ F_{Ly} \\ F_{Ry} \\ F_{Lz} \\ F_{Rz} \\ F_{Tz} \end{Bmatrix}$$
$$= \begin{Bmatrix} -\sum F_{x_i} \\ -\sum F_{y_i} \\ -\sum F_{z_i} \\ \sum F_{y_i} D_{z_i} - \sum F_{z_i} D_{y_i} \\ \sum F_{z_i} D_{x_i} - \sum F_{x_i} D_{z_i} \\ \sum F_{x_i} D_{y_i} - \sum F_{y_i} D_{x_i} \end{Bmatrix} . \tag{A.4}$$

The L and R subscripts indicate left and right side of the TMJs. The T subscript indicates the tooth where bite force is exerted with x, y and z the components of a force. F indicates force while D is the distance in a specific coordinate direction from the occipital condyles average nodal coordinate (OC). The right hand side of the system is calculated as a summation of the muscle force and moment contribution about the OC location due to each muscle i.

The x-values of the force at each TMJ that makes up the bundled F_{LRx} is assumed to divide equally between the two. This gives a seventh equation $F_{Lx} = F_{Rx}$. These components of the force is assumed too small to affect the overall

UNIVERSITEIT VAN PRETORIA
UNIVERSITY OF PRETORIA
YUNIBESITHI YA PRETORIA

results. A simple sensitivity analysis done for various ratio of x-component force proved that the final solution is fairly insensitive to this assumption.

The sensitivity analysis is done to compare the results of a finite element analysis for two scenarios. In the first scenario the force F_{LRx} is divided in such a way that 70% is attributed to the working side and 30% to the balancing side. The other analysis is done with the working side 30% and the balancing side 70%. Results of the FEA is visible in Figure A.2. A slight difference in stress field is visible at values far below the range intended for use to draw conclusions. This gives the impression that results obtained from an FEA on the skull is fairly insensitive to the assumption made on the seventh equation.

With no other constraints applied to the model the bite force on the tooth along with reaction forces at the articular eminances are expected to balance the system. Tables A.3 and A.4 contain all of the forces applicable to the two skull geometries including the reaction forces after solving the set of equations and dividing the bundled F_{LRx} equally between the working and balancing sides.

The forces applied and reaction forces obtained are visible in Figures A.3 - A.6. These figures show boundary conditions for the prognathic and orthognathic skull forms with the red lines indicating the muscle forces applied and the blue lines the reaction forces after solving the system of equations. The force values are scaled with 0.5 for visual clarity. Each muscle's contribution to the reaction forces is also illustrated. After obtaining the resultant forces, the orthognathic skull forces were scaled by 0.9412 for the molar bite and 0.9552 for the incisor bite analysis so the stress patterns for the same applied force at the tooth could be recovered and compared.

A.5 Analysis

Both skulls are treated similarly and several finite element analyses are run for incisal and molar bite using FEBio [3]. Muscle forces with their balancing reaction forces are applied as boundary conditions while the nodal coordinates of the occipital condyles at the foramen magnum are constrained. The use of a linear elastic skull model also allows the analysis of isolated muscle contributions to bite force and reaction forces at the temporomandibular joint.

The analyses run for both prognathic and orthognathic skull form include:

UNIVERSITEIT VAN PRETORIA
UNIVERSITY OF PRETORIA
YUNIBESITHI YA PRETORIA

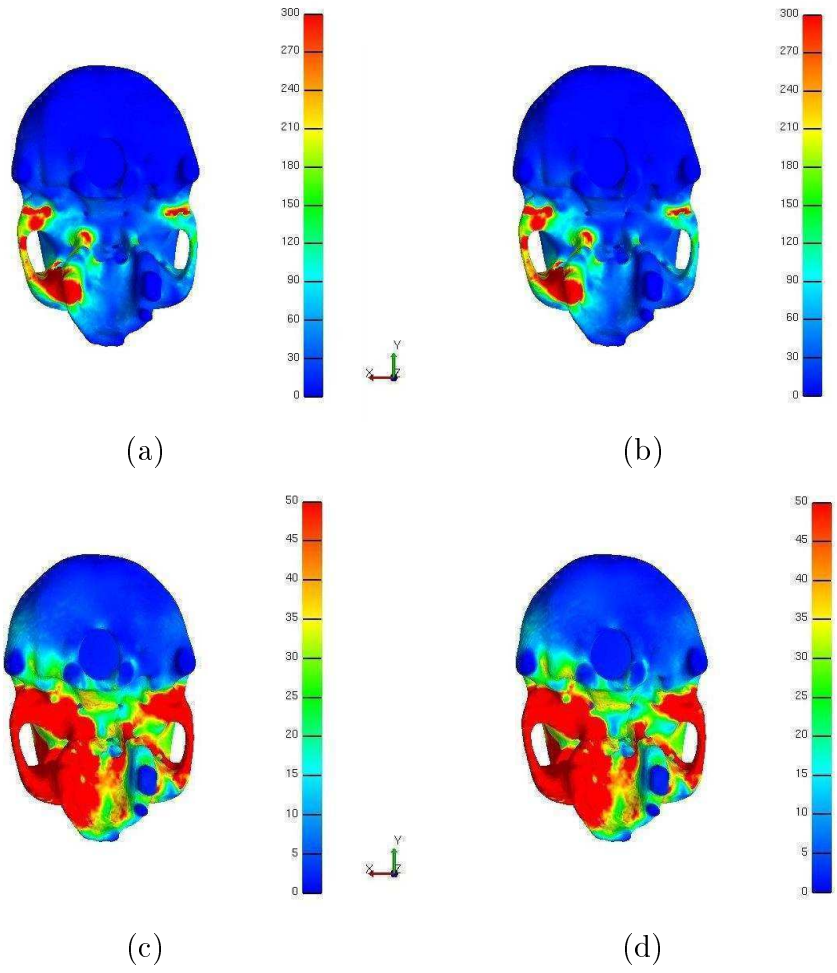

Figure A.2: Results of sensitivity analysis done on the orthognathic skull for a molar bite. This analysis was chosen because F_{LRx} is the largest in comparison to other resultant forces when an incisor bite or prognathic skull shape is considered. Working:balancing ratio of F_{LRx} left 1:$\frac{7}{3}$ and right $\frac{7}{3}$:1 for Von Mises stress set to a maximum of (a), (b) 300 N/cm^2 and (c), (d) 50 N/cm^2. Slight variation in stress field is only visible for stresses far below the range of stresses used in drawing conclusions from FEA results.

	Working Side		Balancing Side	
	Force [N]	**Direction**	**Force [N]**	**Direction**
Temporalis				
Section 1	183.54	{-0.055, 0.14, -0.989}	70.45	{0.039, 0.154, -0.987}
2	73.384	{-0.1, -0.149, -0.984}	36.66	{0.07, -0.144, -0.987}
3	52.42	{-0.138, -0.365, -0.921}	26.32	{0.116, -0.383, -0.916}
4	62.302	{-0.187, -0.582, -0.791}	23.04	{0.15, -0.582, -0.799}
5	32.95	{-0.196, -0.737, -0.647}	11.82	{0.157, -0.743, -0.65}
6	15.84	{-0.21, -0.829, -0.519}	6.94	{0.186, -0.839, -0.512}
7	27.52	{-0.235, -0.849, -0.473}	9.87	{0.241, -0.854, -0.461}
Masseter				
Superficial	230	{-0.09, 0.22, -0.971}	108.1	{0.09, 0.22, -0.971}
Deep Head	100	{-0.37, -0.13, -0.92}	36	{0.37, -0.13, -0.92}
Pterygoid				
Medial:	250	{0.469, 0.399, -0.788}	50	{-0.469, 0.399, -0.788}
	Reaction Forces			
Articular Eminance				
Molar Bite	358.11	{-0.034, -0.044, 0.998}	234.07	{-0.051, -0.08, 0.996}
Incisor Bite	635.65	{-0.019, -0.025, 0.999}	203.13	{-0.059, -0.092, 0.994}
Tooth				
Molar	657.23	{0,0,1}		
Incisor	410.55	{0,0,1}		

Table A.3: Prognathic force values and directions.

	Working Side		Balancing Side	
	Force [N]	**Direction**	**Force [N]**	**Direction**
Temporalis				
Section 1	178.05	{-0.068, 0.22, -0.973}	72.40	{0.094, 0.153, -0.984}
2	74.80	{-0.102, -0.095, -0.99}	30.75	{0.107, -0.123, -0.987}
3	69.19	{-0.121, -0.33, -0.936}	24.60	{0.116, -0.347, -0.931}
4	48.62	{-0.163, -0.551, -0.818}	24.11	{0.134, -0.562, -0.816}
5	32.32	{-0.187, -0.724, -0.664}	14.50	{0.13, -0.725, -0.676}
6	20.40	{-0.231, -0.821, -0.514}	7.46	{0.161, -0.826, -0.54}
7	27.82	{-0.301, -0.803, -0.523}	10.76	{0.234, -0.813, -0.533}
Masseter				
Superficial	230	{-0.07, 0.19, -0.979}	108.1	{0.07, 0.19, -0.979}
Deep Head	100	{-0.16, -0.19, -0.969}	36	{0.16, -0.19, -0.969}
Pterygoid				
Medial:	250	{0.65, 0.12, -0.75}	50	{-0.65, 0.12, -0.75}
	Reaction Forces			
Articular Eminance				
Molar Bite	344.28	{-0.113, 0.06, 0.992}	215.50	{-0.181, 0.116, 0.977}
Incisor Bite	643.28	{-0.061, 0.032, 0.998}	184.54	{-0.211, 0.136, 0.968}
Tooth				
Molar	698.29	{0,0,1}		
Incisor	429.78	{0,0,1}		

Table A.4: Orthognathic force values and directions.

UNIVERSITEIT VAN PRETORIA
UNIVERSITY OF PRETORIA
YUNIBESITHI YA PRETORIA

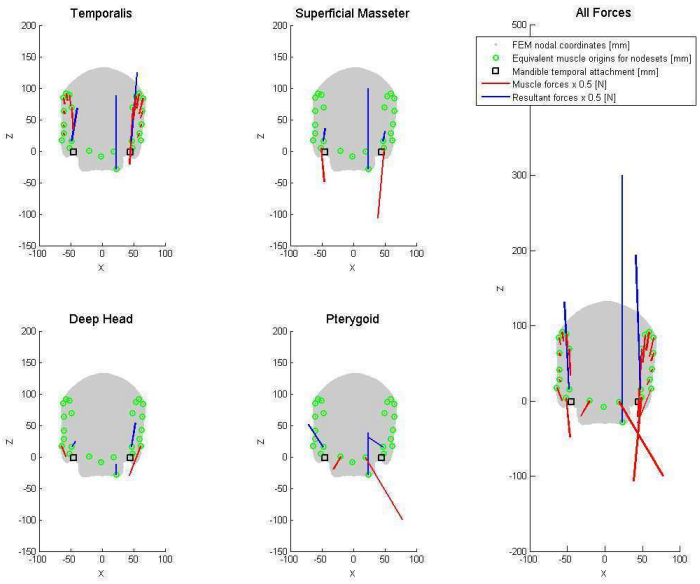

(a)

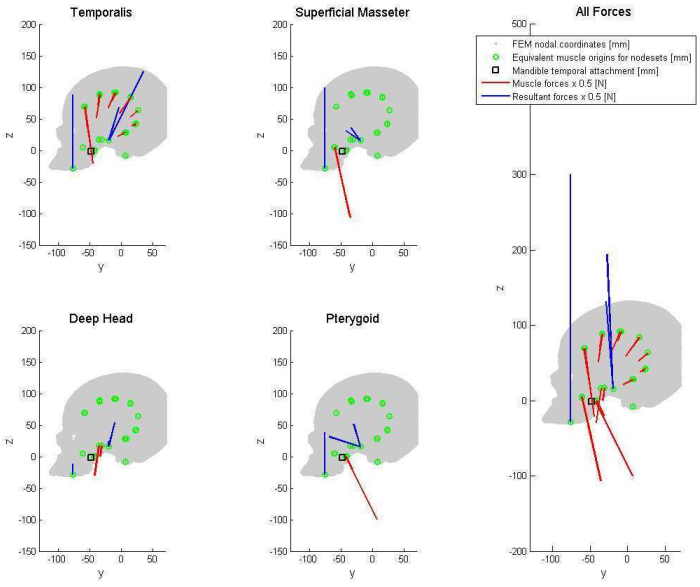

(b)

Figure A.3: Muscle contribution and reaction forces on the prognathic skull for a vertical molar bite.

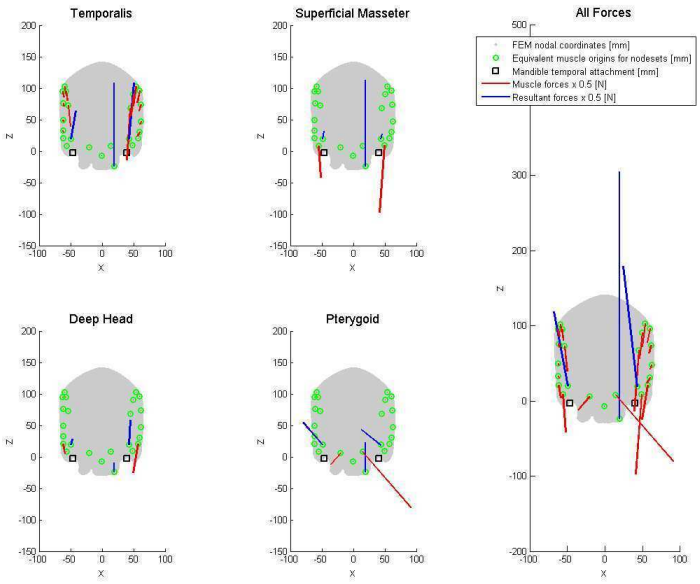

(a)

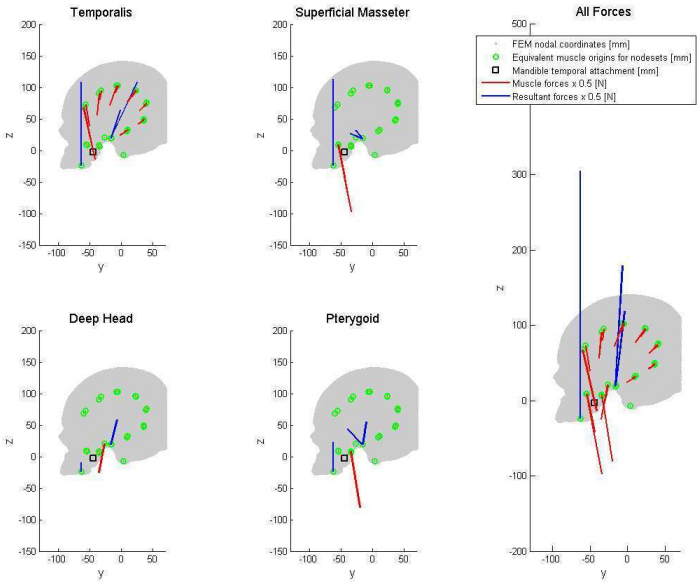

(b)

Figure A.4: Muscle contribution and reaction forces on the orthognathic skull for a vertical molar bite.

UNIVERSITEIT VAN PRETORIA
UNIVERSITY OF PRETORIA
YUNIBESITHI YA PRETORIA

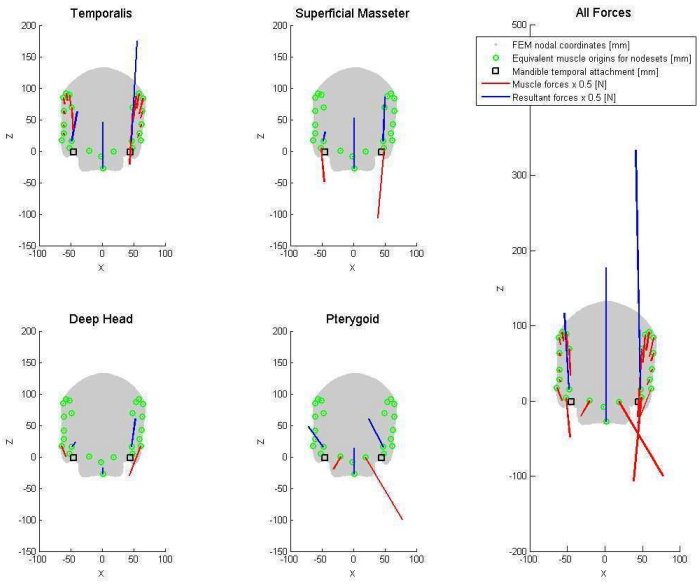

(a)

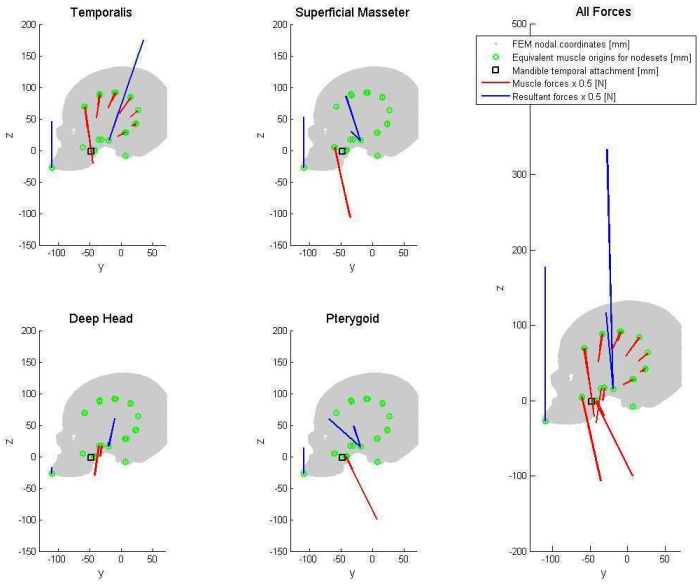

(b)

Figure A.5: Muscle contribution and reaction forces on the prognathic skull for a vertical incisor bite.

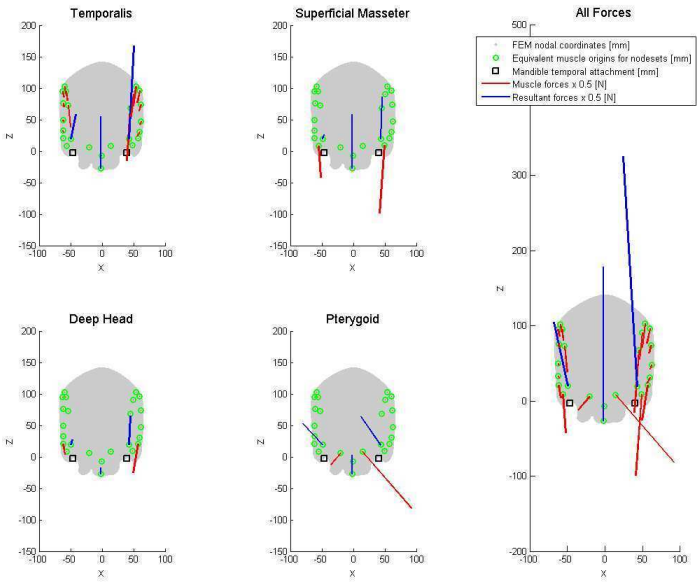

(a)

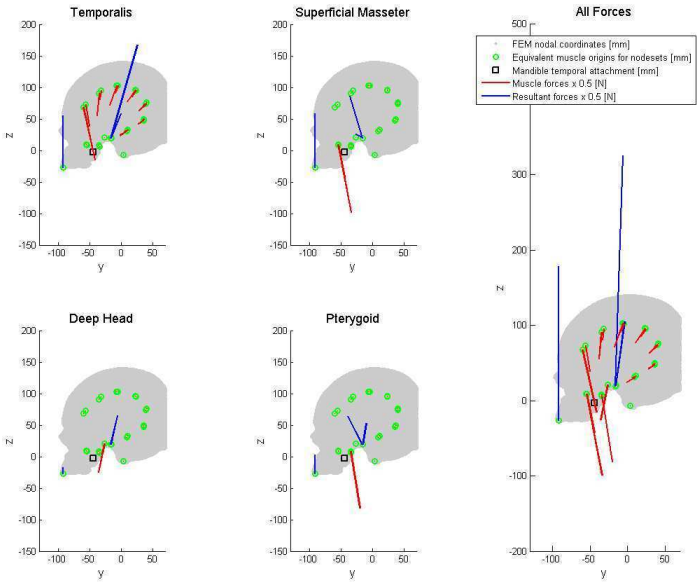

(b)

Figure A.6: Muscle contribution and reaction forces on the orthognathic skull for a vertical incisor bite.

UNIVERSITEIT VAN PRETORIA
UNIVERSITY OF PRETORIA
YUNIBESITHI YA PRETORIA

- The effect of the Temporalis muscle on molar and incisor bite.
- The effect of the Superficial Masseter on molar and incisor bite.
- The effect of the Deep head Masseter on molar and incisor bite.
- The effect of the Medial Pterygoid on molar and incisor bite.
- The effect of all muscle contributions on molar and incisor bite.

This results in a total of 20 analyses done on masticatory induced stress. Post processing and visualisation is done using PostView [6]. Principal stresses, displacements and Von Mises stresses are considered to generate stress state and displacement plots.

Working side stresses are visible in Figures A.7 and A.8 for the full molar and incisor bite simulations. Muscle contribution to the prognathic and orthognathic molar bite Von Mises stress is presented as an example in Figure A.9.

A.6 Results

The displacement results for the full analysis on both skull forms for first molar and first incisor bite are documented in Table A.5. Here the displacements on the prognathic skull are greater than the displacements on the orthognathic form.

The maximum Von Mises stresses for all 20 analyses are given in Table A.6. Comparing these maximums for various muscle contributions, the same analysis for the different geometries occasionally differ by a factor 2. The significance thereof is doubtful as there is no guarantee that the higher stress is not caused by singularities. These singularities could occur due to unsmoothed areas, inadequate element quality and stiffness or greater point loads.

The analysis done for incisal bite on the orthognathic and molar bite on the prognathic skull shape are displayed in Figure A.10. Only the lower view of these analyses is given along with detail to indicate that the maximum Von Mises stresses do indeed occur at singular locations. In Figure A.10 (a) and (c) the stress concentration is due to the discretisation of the shape in such a way that point loads are applied in the region of the TMJ while the stress concentrations in Figure A.10 (b) and (d) seem to occur at holes in the geometry. These holes in the prognathic shape are not present in the orthognathic shape which means that the difference in

UNIVERSITEIT VAN PRETORIA
UNIVERSITY OF PRETORIA
YUNIBESITHI YA PRETORIA

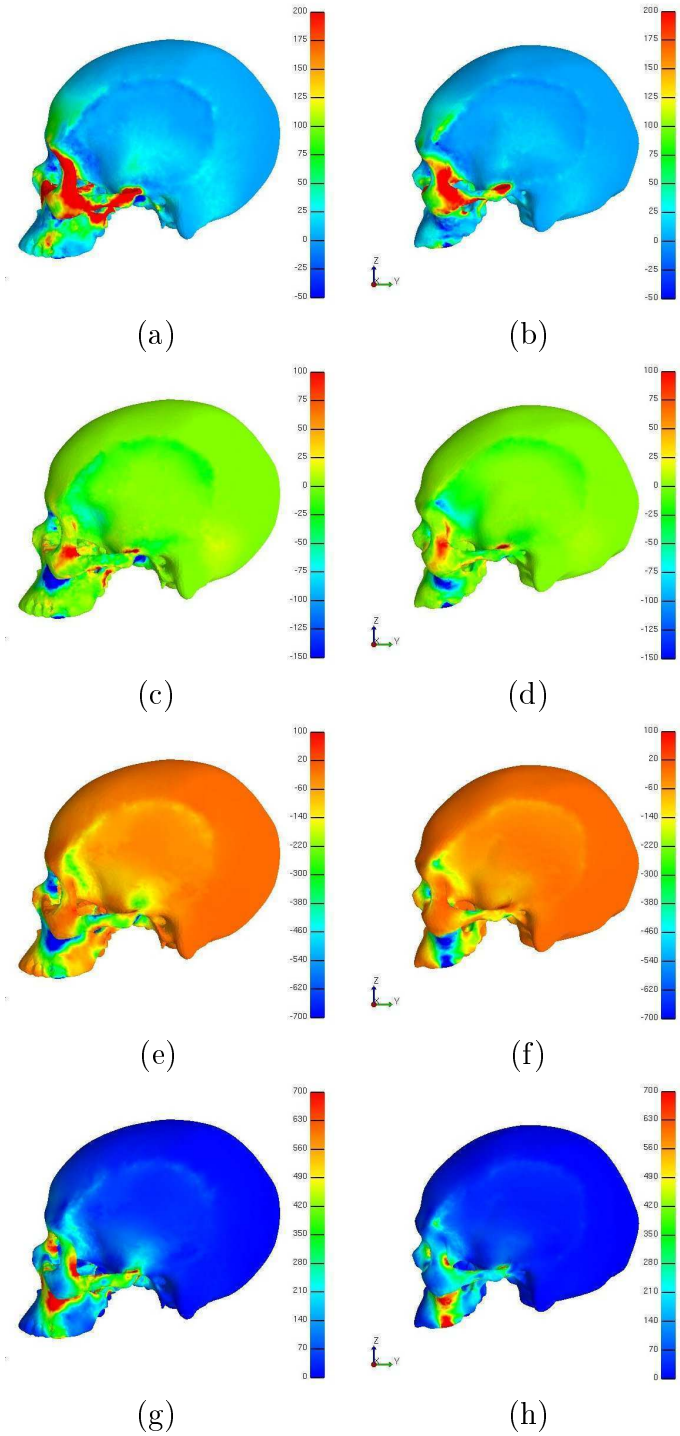

Figure A.7: Lateral view of the working side stresses for a molar bite on full prognathic and orthognathic FEA results in N/cm^2. (a), (b) 1st principal stress (c), (d) 2nd principal stress (e), (f) 3rd principal stress and (g), (h) Von Mises stress.

UNIVERSITEIT VAN PRETORIA
UNIVERSITY OF PRETORIA
YUNIBESITHI YA PRETORIA

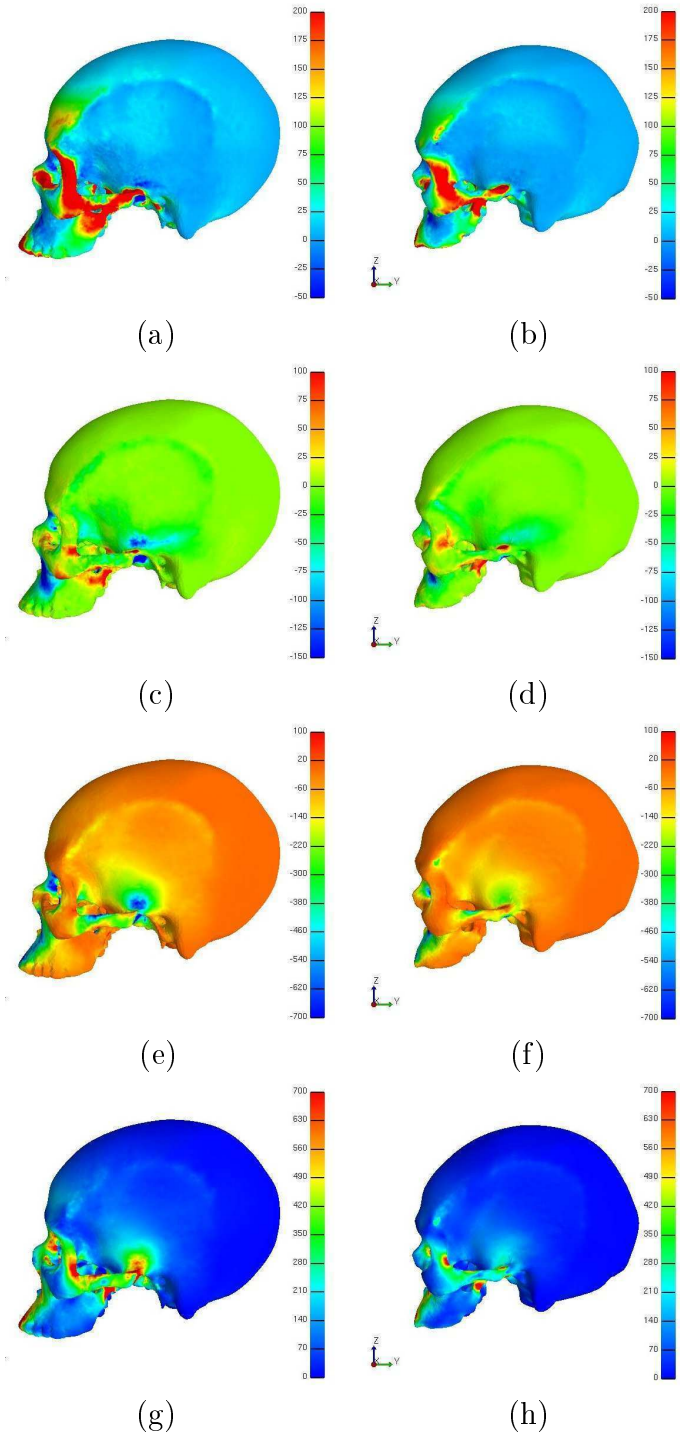

Figure A.8: Lateral view of the working side stresses for incisor bite on full prognathic and orthognathic FEA results in N/cm^2. (a), (b) 1st principal stress (c), (d) 2nd principal stress (e), (f) 3rd principal stress and (g), (h) Von Mises stress.

UNIVERSITEIT VAN PRETORIA
UNIVERSITY OF PRETORIA
YUNIBESITHI YA PRETORIA

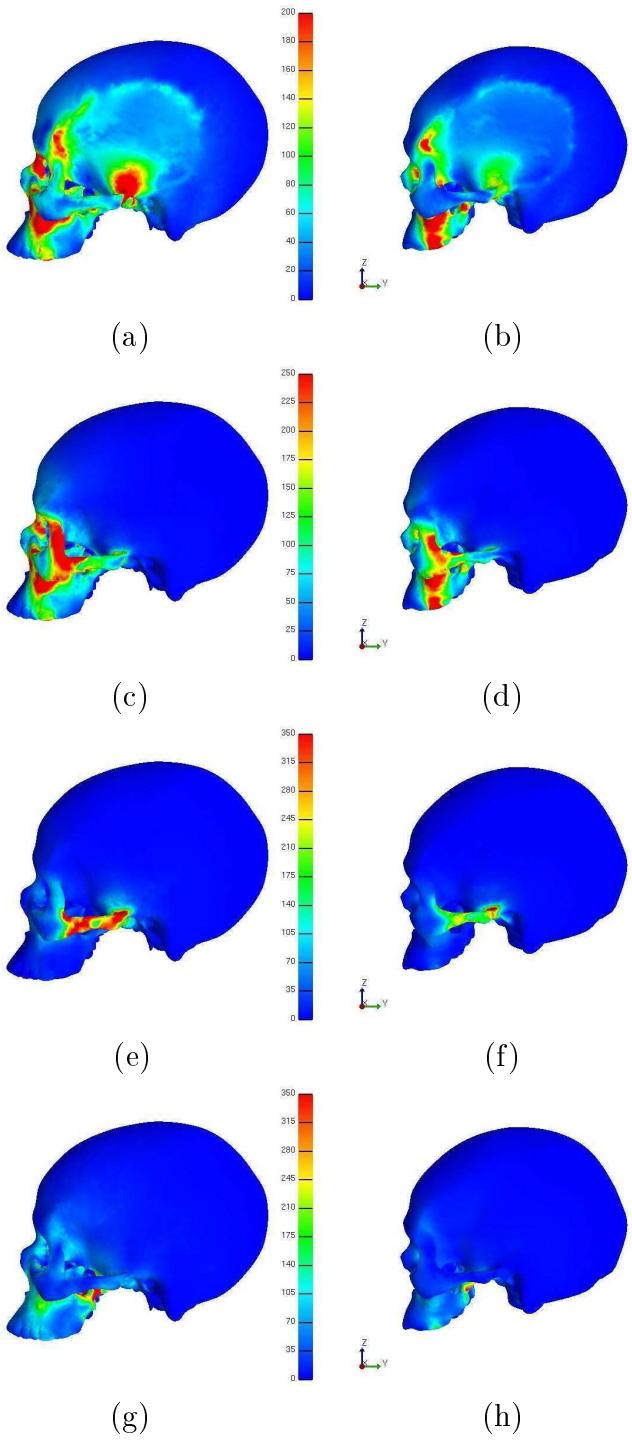

Figure A.9: Lateral view of the working side muscle contribution to Von Mises stress. The molar bite for prognathic and orthognathic FEA results are given in N/cm^2. (a), (b) Temporalis (c), (d) superficial masseter (e), (f) deep head masseter and (g), (h) medial pterygoid contributions.

UNIVERSITEIT VAN PRETORIA
UNIVERSITY OF PRETORIA
YUNIBESITHI YA PRETORIA

	Prognathic		Orthognathic	
	Min [mm]	Max [mm]	Min [mm]	Max [mm]
	Molar Bite			
x	-1.07E-02	2.65E-02	-3.88E-03	1.32E-02
y	-1.80E-02	7.51E-03	-7.34E-03	3.87E-03
z	-3.03E-02	2.63E-02	-1.81E-02	1.56E-02
Total	0	3.99E-02	0	2.08E-02
	Incisor Bite			
x	-8.66E-03	9.82E-03	-5.91E-03	6.45E-03
y	-5.21E-02	1.25E-02	-4.08E-02	6.27E-03
z	-2.00E-02	8.51E-02	-1.59E-02	4.61E-02
Total	0	9.72E-02	0	6.11E-02

Table A.5: Minimum and maximum displacements obtained from finite element analysis for all mastication forces.

	Molar Results [MPa]		**Incisor Results** [MPa]	
	Prognathic	Orthognathic	Prognathic	Orthognathic
Temporalis	7.12	16.45	10.85	24.58
Superficial M	8.35	7.34	11.85	10.16
Deep Head M	7.51	6.77	7.40	7.70
Pterygoid	15.42	8.89	15.10	9.64
All Muscles	14.72	24.65	30.49	45.52

Table A.6: Maximum Von Mises stress obtained from finite element analysis for individual mastication forces and full analysis.

maximum Von Mises stress reported in Table A.6 could also be due to topological inconsistency between the skull geometries.

It is noted from the initial analysis that the skull geometries vary in more ways than just prognathism. These variations seem to play a significant role in the stresses that are reported and further attention should be given to the similarities and differences of the skull forms represented.

When the skull computational domains vary in only their relative degree in prognathism, a conclusion may be drawn on the effect of prognathism on masticatory induced stress.

UNIVERSITEIT VAN PRETORIA
UNIVERSITY OF PRETORIA
YUNIBESITHI YA PRETORIA

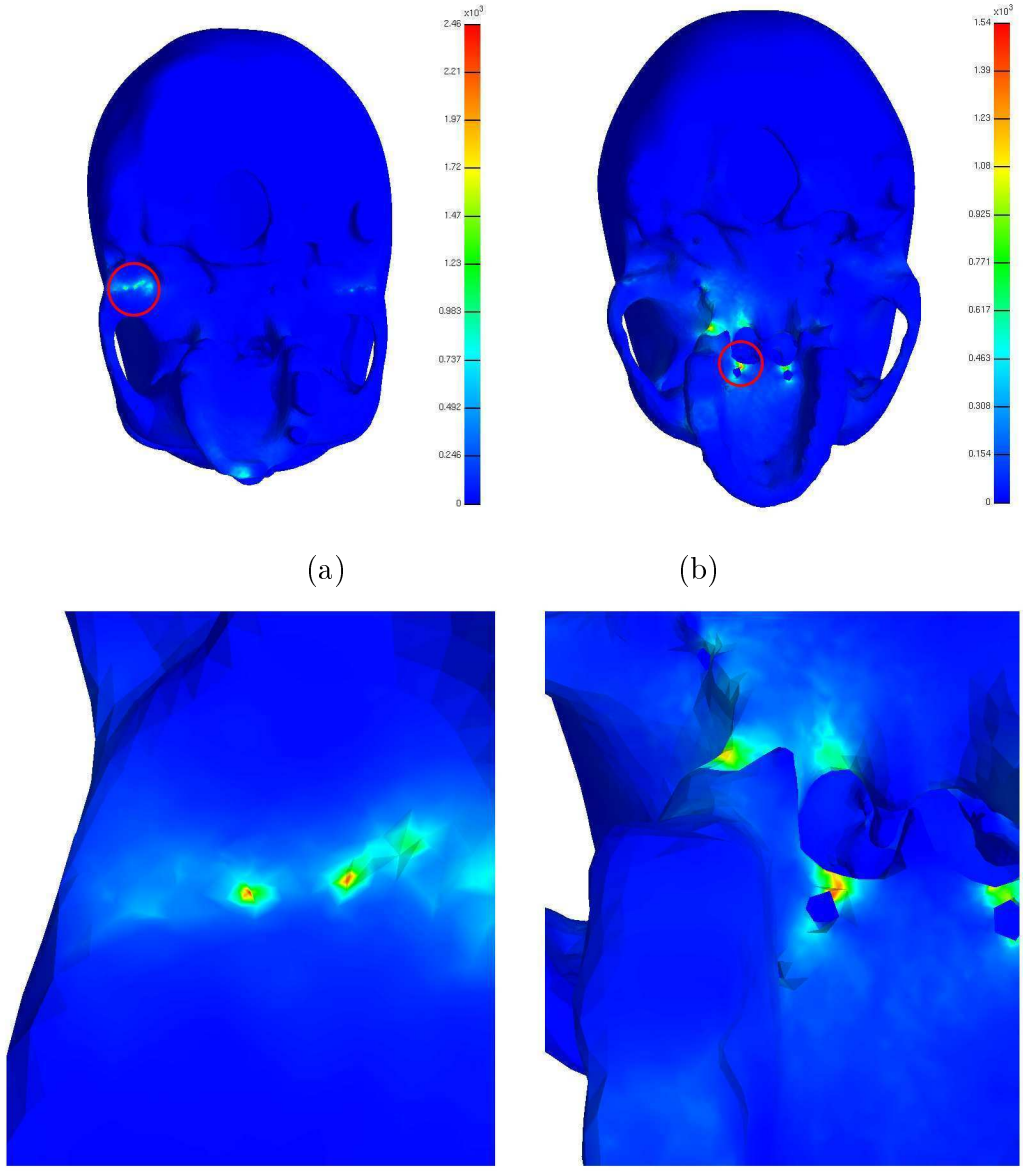

(a) (b)

(c) (d)

Figure A.10: Von Mises stress concentrations. (a) Lower view of the incisal bite analysis on the orthognathic skull geometry with detail in (c). (b) Lower view of the molar bite analysis on the prognathic skull geometry with detail in (d). Stress concentrations in these two analyses are shown with reference to Table A.6. Maximum Von Mises stress occurs at stress concentrations and can not be compared.

Appendix B

Affine Iterative Closest Point Problem

B.1 Reformulating the ICP problem

Reformulating the Iterative Closest Point algorithm mentioned in subsection 3.1.1 is done as in the work by Du *et al.* [28]. First assume that an affine transformation is to be applied to one point set. This is done in such a way that it matches a subset of another point set. The problem is still to find an affine transformation T that best aligns $\mathcal{P}$ to $\mathcal{M}$:

$$\min_{T,j\in\{1,2,\ldots,N_m\}} \left(\sum_{i=1}^{N_p} \|T(\mathbf{p}_i) - \mathbf{m}_j\|_2^2 \right). \tag{B.1}$$

This affine transformation is expressed explicitly as an invertible matrix $\mathbf{A}$ and translation vector $\mathbf{t}$ so that the problem is again expressed as in Equation (3.2). Using Singular Value Decomposition (SVD), the invertible matrix can be decomposed into two orthogonal matrices $\mathbf{U}$ and $\mathbf{V}$, as well as a positive diagonal matrix $\mathbf{S}$ so that $\mathbf{A} = \mathbf{USV}^T$. It is assumed that $\mathbf{R}$ is the orthogonal rotation matrix $\mathbf{V}^T$.

The affine transformation problem is rewritten in such a way that T is represented by the orthogonal reflection and rotation matrices $\mathbf{U}$ and $\mathbf{R}$, with a scale transformation $\mathbf{S}$, and a translation $\mathbf{t}$.

UNIVERSITEIT VAN PRETORIA
UNIVERSITY OF PRETORIA
YUNIBESITHI YA PRETORIA

The problem set up in Equation (B.1) now takes the form

$$\min_{\mathbf{U},\mathbf{S},\mathbf{R},\mathbf{t},j\in\{1,2,\ldots,N_m\}} \left(\sum_{i=1}^{N_p} \|\mathbf{USRp}_i + \mathbf{t} - \mathbf{m}_j\|_2^2\right), \tag{B.2}$$

such that:

$$\mathbf{U}^T\mathbf{U} = \mathbf{I}_m, \quad \det(\mathbf{U}) = 1, \tag{B.3}$$

$$\mathbf{R}^T\mathbf{R} = \mathbf{I}_m, \quad \det(\mathbf{R}) = 1,$$

$$\mathbf{S} = \operatorname{diag}(s_1, s_2, \ldots, s_m), \quad s_j \in [a_j, b_j].$$

where a_j and b_j are the upper and lower bounds of the allowable scale transformation.

This reformulated problem is then iteratively performed in much the same way as the original ICP but with reflection, rotation, scale and translation instead of only rotation and translation.

B.2 Lie group and lie algebra

A set of mappings on a differential manifold is defined as a lie group [28]. A rotation in $\mathbb{R}^m$ can be expressed by a set of $m \times m$ special orthogonal matrices. This matrix is represented as the special orthogonal group

$$SO(m) = \left\{\mathbf{R} \in \mathbb{R}^{m\times m} | \mathbf{R}^T\mathbf{R} = \mathbf{I}_m, \det(\mathbf{R}) = 1\right\}. \tag{B.4}$$

This group then has a linearised form or lie algebra

$$\mathfrak{so}(m) = \left\{\mathbf{R} \in \mathbb{R}^{m\times m} | \mathbf{R} = -\mathbf{R}^T\right\} \tag{B.5}$$

which is an $N_r := m(m-1)/2$ dimensional linear space. The rotation matrix $\mathbf{R}$ can be expressed as

$$\mathbf{R} = \sum_{i=1}^{N_r} x_i \mathbf{E}_i, \tag{B.6}$$

where x_i and $\mathbf{E}_i$ is the first canonical coordinate and basis of $\mathfrak{so}(m)$. The basis in

UNIVERSITEIT VAN PRETORIA
UNIVERSITY OF PRETORIA
YUNIBESITHI YA PRETORIA

two dimensions is denoted by

$$\mathbf{E}_1 = \begin{bmatrix} 0 & 1 \\ -1 & 0 \end{bmatrix} \tag{B.7}$$

and in three dimensions, the basis of $\mathfrak{so}(3)$ is

$$\mathbf{E}_1 = \begin{bmatrix} 0 & 1 & 0 \\ -1 & 0 & 0 \\ 0 & 0 & 0 \end{bmatrix}, \quad \mathbf{E}_2 = \begin{bmatrix} 0 & 0 & 0 \\ 0 & 0 & -1 \\ 0 & 1 & 0 \end{bmatrix}, \quad \mathbf{E}_3 = \begin{bmatrix} 0 & 0 & 1 \\ 0 & 0 & 0 \\ -1 & 0 & 0 \end{bmatrix}. \tag{B.8}$$

A lie group and its lie algebra are related by an exponential mapping. Given an element $\mathbf{B}$ in a certain neighbourhood of $\mathbf{A}$ in $SO(m)$, a unique $\mathbf{Q} \in \mathfrak{so}(m)$ exists such that there is a smooth exponential mapping between them

$$\mathbf{B} = \mathbf{A}e^{\mathbf{Q}}. \tag{B.9}$$

B.3 Performing an Affine ICP transformation

As with the ICP method, the first step to performing a k^{th} affine transformation is setting up a point correspondence. This is done using a $k-d$ tree representation of the model shape $\mathcal{M}$ for nearest neighbour search. The implementation is done in python using `scipy.spatial` [11]. The correspondence is set up with the $(k-1)^{\text{th}}$ transformations as

$$c_k(i) = \underset{j \in \{1,2,\ldots,N_m\}}{\arg\min} \left(\|(\mathbf{U}_{k-1}\mathbf{S}_{k-1}\mathbf{R}_{k-1}\mathbf{p}_i + \mathbf{t}_{k-1}) - \mathbf{m}_j\|_2^2 \right), \quad i = 1, 2, \ldots, N_p. \tag{B.10}$$

The optimisation problem posed in Equation (B.2) is simplified using exponential mappings of lie group and their Taylor approximations at each iteration [28]. This is done assuming the change in transformation is small between consecutive iterations such that $\mathbf{U}_k$ is in the neighbourhood of $\mathbf{U}_{k-1}$ for example, allowing the use of exponential mapping.

After setting up a point correspondence, the translation required for a minimum

UNIVERSITEIT VAN PRETORIA
UNIVERSITY OF PRETORIA
YUNIBESITHI YA PRETORIA

value of the cost function in Equation (B.2) can be calculated as [28]

$$\mathbf{t}_k = \frac{1}{N_p}\sum_{i=1}^{N_p}\mathbf{m}_{c_k(i)} - \frac{1}{N_p}\sum_{i=1}^{N_p}\mathbf{U}_{k-1}\mathbf{S}_{k-1}\mathbf{R}_{k-1}\mathbf{p}_i \tag{B.11}$$

where $\mathbf{m}_{c_k(i)}$ is the closest point on $\mathcal{M}$ for $\mathbf{p}_i$ on $\mathcal{P}$.

Taking this known translation into account, the objective function is rewritten. If

$$\mathbf{p}_{\mathbf{t}i} \triangleq \mathbf{p}_i - \frac{1}{N_p}\sum_{i=1}^{N_p}\mathbf{p}_i, \quad \mathbf{m}_{\mathbf{t}i} \triangleq \mathbf{m}_{c_k(i)} - \frac{1}{N_p}\sum_{i=1}^{N_p}\mathbf{m}_{c_k(i)}, \tag{B.12}$$

the objective function can be rewritten as

$$\min_{\mathbf{U},\mathbf{S},\mathbf{R},\mathbf{t},j\in\{1,2,\ldots,N_m\}} \left(\sum_{i=1}^{N_p}\|\mathbf{USR}\mathbf{p}_{\mathbf{t}i} - \mathbf{m}_{\mathbf{t}i}\|_2^2\right). \tag{B.13}$$

Because each k^{th} transformation matrix is in the neighbourhood of the previous, the lie group and lie algebra allow updating them at each iteration as in Equation (B.9):

$$\begin{aligned}\mathbf{U}_k &= \mathbf{U}_{k-1}e^{\sum_{j=1}^{N_r} u_j\mathbf{E}_j}, \\ \mathbf{R}_k &= \mathbf{R}_{k-1}e^{\sum_{j=1}^{N_r} r_j\mathbf{E}_j},\end{aligned} \tag{B.14}$$

where $N_r := m\,(m-1)\,/2$ for a problem in $\mathbb{R}^m$.

The scale matrix is also updated using a smooth exponential mapping. This smooth mapping may be expressed as

$$\mathbf{S}_k = \mathbf{S}_{k-1}e^{\sum_{j=1}^{N_s} s_j\mathbf{D}_j},$$

where $\mathbf{D}_j$ is the set of the bases of a diagonal matrix with only $D_{jj} = 1$ and $N_s := m$ for a problem in $\mathbb{R}^m$.

If the change in transformation is not large, the Taylor series of the exponential mappings are guaranteed to converge and are rewritten with the higher order terms omitted [28]. This results in the k^{th} iteration constrained optimisation problem

UNIVERSITEIT VAN PRETORIA
UNIVERSITY OF PRETORIA
YUNIBESITHI YA PRETORIA

written in the form

$$\min_{\mathbf{c}} \quad \sum_{i=1}^{N_p} \left\| \mathbf{U}_{k-1} \left(\mathbf{I} + \sum_{j=1}^{N_r} u_j \mathbf{E}_j \right) \mathbf{S}_{k-1} \left(\mathbf{I} + \sum_{j=1}^{N_s} s_j \mathbf{D}_j \right) \times \mathbf{R}_{k-1} \left(\mathbf{I} + \sum_{j=1}^{N_r} r_j \mathbf{E}_j \right) \mathbf{p}_{\mathbf{t}i} - \mathbf{m}_{\mathbf{t}i} \right\|_2^2 \tag{B.15}$$

with $\mathbf{c} \triangleq \{u_1, ..., u_{N_r}, s_1, ..., s_{N_s}, r_1, ..., r_{N_r}\}^T$, consisting of N_r reflection, N_s scale and N_r rotation variables, to be determined. The scale constraints are updated at each iteration using the initial boundaries a_j and b_j and the previous scale matrix:

$$\sum_{j=1}^{N_s} s_j \mathbf{D}_j \in \left[\ln \left(\mathbf{S}_{K-1}^{-1} \text{diag}(a_1, ..., a_{N_s}) \right), \ \ln \left(\mathbf{S}_{K-1}^{-1} \text{diag}(b_1, ..., b_{N_s}) \right) \right]. \tag{B.16}$$

Appendix C

Shape Context Correspondence

Methods have been developed to classify feature points within the context of shape. These shape contexts can then be used to create point correspondences for use in registration.

Given a set of points on a surface, a 3D shape context for each point can provide the approximate corresponding point locations on a target surface with a similar shape. Once a matching is established, the base surface can be warped to represent the target with a smooth deformation model such as a thin plate spline (TPS) radial basis function (RBF).

A limiting factor of using shape context for point matching is the significant amount of mismatched points that may occur between two objects because of global and local dissimilarity and the existence of outliers [68]. This is classically improved by the straightforward removal of a percentage of correspondences with the highest cost. This is done with the assumption that a mismatched point correspondence would have a greater difference between the initial and registered coordinate position than a trusted registration.

The method for setting up point correspondences for shape context non-rigid registration is described in this section and accompanied by figures and results found in literature.

C.1 Shape Context

The shape context of a point is a measure of the distribution of relative positions of neighbouring points [68]. This distribution is defined as a joint histogram where

UNIVERSITEIT VAN PRETORIA
UNIVERSITY OF PRETORIA
YUNIBESITHI YA PRETORIA

each axis represents a parameter in a polar coordinate system. In two dimensions, a 2D log-polar histogram is set up as in the template given in Figure C.1 (a). This can also be extended to 3D using the spherical coordinates of Figure C.1 (b).

To set up a shape context histogram, the user specifies the number of bins to use. The support region is divided into bins by equally spaced boundaries in the azimuth and elevation dimensions with logarithmically spaced boundaries along the radial dimension. Sampling logarithmically makes the descriptor more robust to distortions in shape further from the basis point [31]. With the number of radial bins J, a minimum radius $r_{\min}$ and maximum radius $r_{\max}$ specified, the $J+1$ radius boundaries are calculated as [31]

$$R_j = \mathrm{e}^{\ln(r_{\min})+\frac{j}{J}\ln(r_{\max}/r_{\min})}. \tag{C.1}$$

A shape context histogram is set up with the points within a spherical radius of $r_{\max}$ of the point under consideration. The contribution to the bin count for a point p_i is given by

$$\omega_i = \frac{1}{\rho_i \sqrt[3]{V_i\left(j,k,l\right)}} \tag{C.2}$$

where $V_i\left(j,k,l\right)$ is the volume of the bin at the j^{th} radial, k^{th} elevation and l^{th} azimuth that contains point p_i. ρ_i is the local point density around the bin [31]. Normalising in this way takes the large variation in bin size with radius and elevation into account. The local point density ρ_i is simply estimated as the count of points in a sphere of radius δ around p_i.

The example of matching and registering two elephant outlines using shape context is presented with the aid of Figures C.2 and C.3. After setting up the histograms of feature points A to D in these figures for example, a measure of similarity between two shape context can be computed as a cost between the two histograms. This is done by using the χ^2-distance [22, 68, 69]:

$$C_{mn} = \frac{1}{2}\sum_{i=1}^{N_b}\frac{\left(h_m\left(i\right)-h_n\left(i\right)\right)^2}{h_m\left(i\right)+h_n\left(i\right)} \tag{C.3}$$

with h_m and h_n the shape context histograms of the points m and n having the bins $i = 1, 2, ..., N_b$. In this equation, C_{mn} is the associated cost of matching points m and n where a low cost value by this definition translates into a high similarity between the two points.

UNIVERSITEIT VAN PRETORIA
UNIVERSITY OF PRETORIA
YUNIBESITHI YA PRETORIA

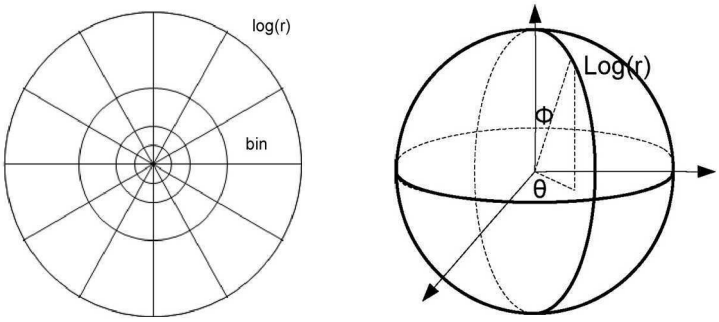

(a) (b)

Figure C.1: a) 2D log-polar histogram bins for 2D shape context. b) 3D spherical coordinates for use in setting up 3D shape context histogram. [68]

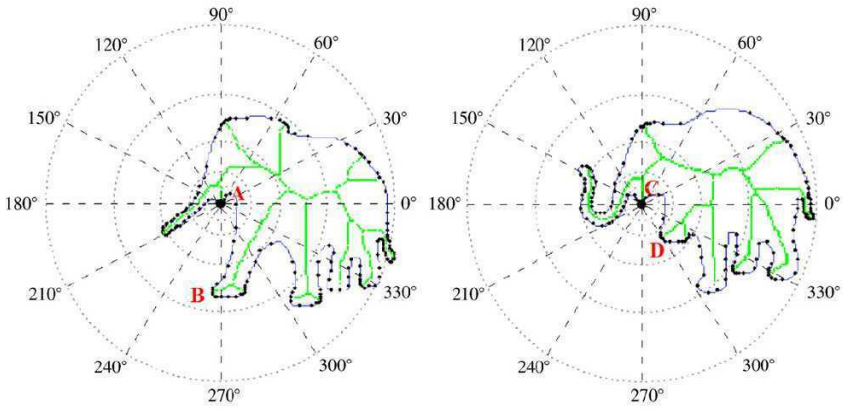

(a) (b)

Figure C.2: Shape context after first creating skeletal lines. This is done here by Xie *et al.* [69] for two different elephant outlines. The images illustrate the image position for setting up a shape context histogram for points A in (a) and C in (b).

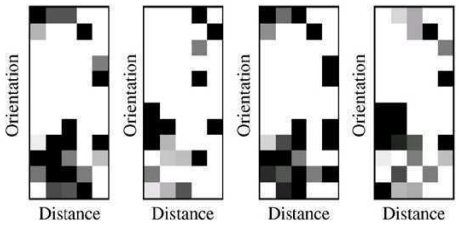

(a) (b) (c) (d)

Figure C.3: Shape context histograms of the four points a) A, b) B, c) C and d) D marked in Figure C.2 [69]. Here the corresponding points are seen to have similar histograms if (a) and (c) are compared for example.

UNIVERSITEIT VAN PRETORIA
UNIVERSITY OF PRETORIA
YUNIBESITHI YA PRETORIA

C.2 Point Matching

In performing registration, the shape context local feature comparison is done on point sets from two similar surfaces.

A cost matrix is set up between the two shapes with the number of rows equal to the number of points of shape one and the number of columns the same as the number of points in shape two for example. Each value in the matrix is the associated cost of similarity between the points represented by the specific row and column as expressed in Equation (C.3).

An ideal set of correspondences are the set of points in shape 1 that best resemble the associated set of points in shape 2. The goal is to find the matched points resulting in lowest total registration cost. This is represented as a bipartite matching problem and can be solved using various techniques [34]. Techniques such as the Hungarian method used in Xiao *et al.* [68] guarantees a number of matched point pairs equal to the number of points in the smaller point set. The spare points from the larger point set without matched points are discarded.

After completing the search, a fixed percentage of correspondences with low cost are traditionally selected as the point sets with high confidence. The matches with highest cost are discarded and the rest used to determine and apply a deformation.

Appendix D

Feature Registration on Dolphin Geometries

The performance of the implemented feature registration procedure is illustrated using two dolphin geometries. The two original geometries is obtained from the INRIA model shape repository [4]. One of the geometries is then refined, manipulated and smoothed to generate the target geometry in the feature registration example. The other geometry is only refined and smoothed.

Crest lines on the two geometries is extracted and thresholded to get rid of less significant lines. The target geometry and it's crest lines are displayed in Figure D.1. In this figure the lines on the generic dolphin shape are displayed in their original position.

A rigid registration is performed on the target geometry allowing isotropic scale with upper and lower constraints arbitrarily set as 0.5 and 1.5. The results of the isotropic scale ICP registration is displayed in Figure D.2. After rigid registration, the feature line registration procedure is implemented to deform the lines on the generic dolphin geometry to better represent that of the target. Resulting registered and deformed lines are visible in Figure D.3. Only the registered lines with a matched point portion of at least 50% is used and displayed.

UNIVERSITEIT VAN PRETORIA
UNIVERSITY OF PRETORIA
YUNIBESITHI YA PRETORIA

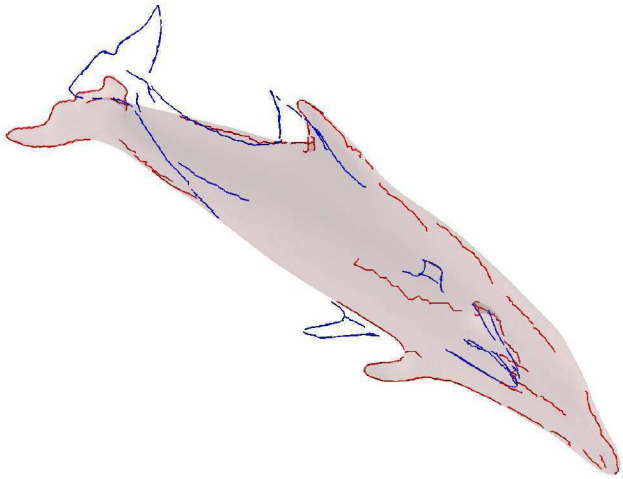

(a)

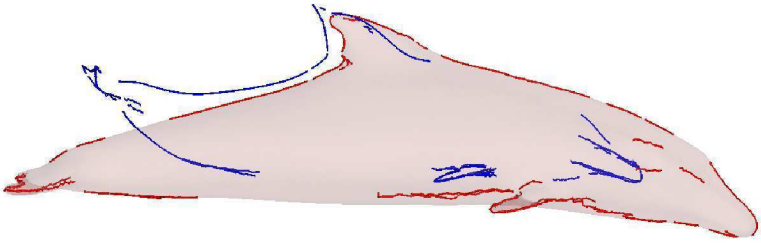

(b)

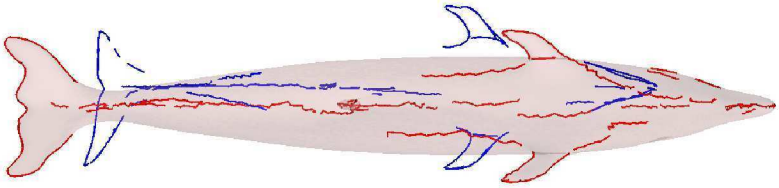

(c)

Figure D.1: Original position of a target and base dolphin geometry. The target geometry is illustrated in its original position with the target features in red and the base geometry features in blue. (a) Isometric, (b) lateral and (c) lower view.

UNIVERSITEIT VAN PRETORIA
UNIVERSITY OF PRETORIA
YUNIBESITHI YA PRETORIA

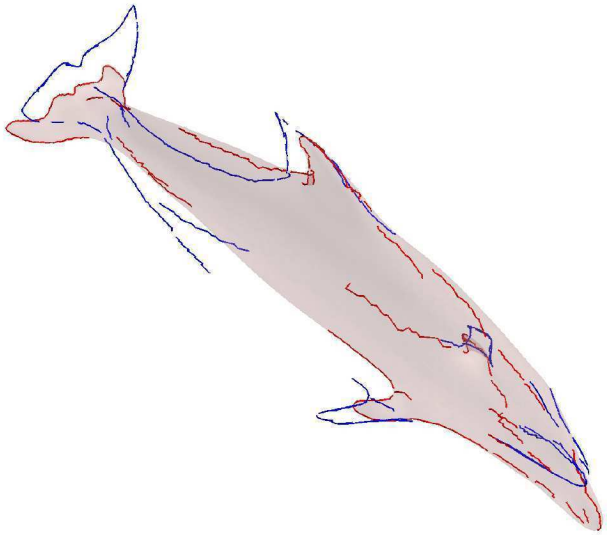

(a)

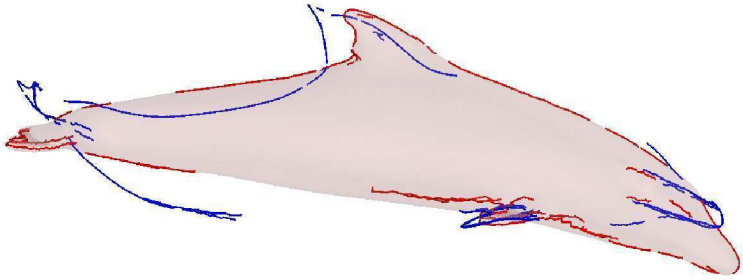

(b)

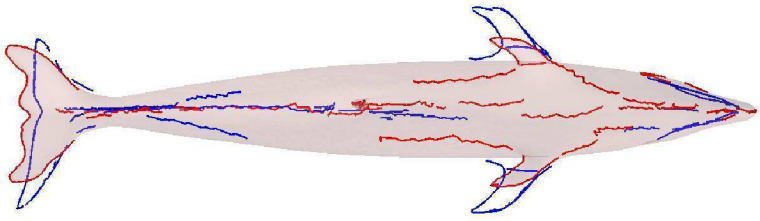

(c)

Figure D.2: Position of a target dolphin geometry relative to the base shape after isotropic scale ICP registration. The target geometry is illustrated in its registered position with the target features in red and the base geometry features in blue. (a) Isometric, (b) lateral and (c) lower view.

UNIVERSITEIT VAN PRETORIA
UNIVERSITY OF PRETORIA
YUNIBESITHI YA PRETORIA

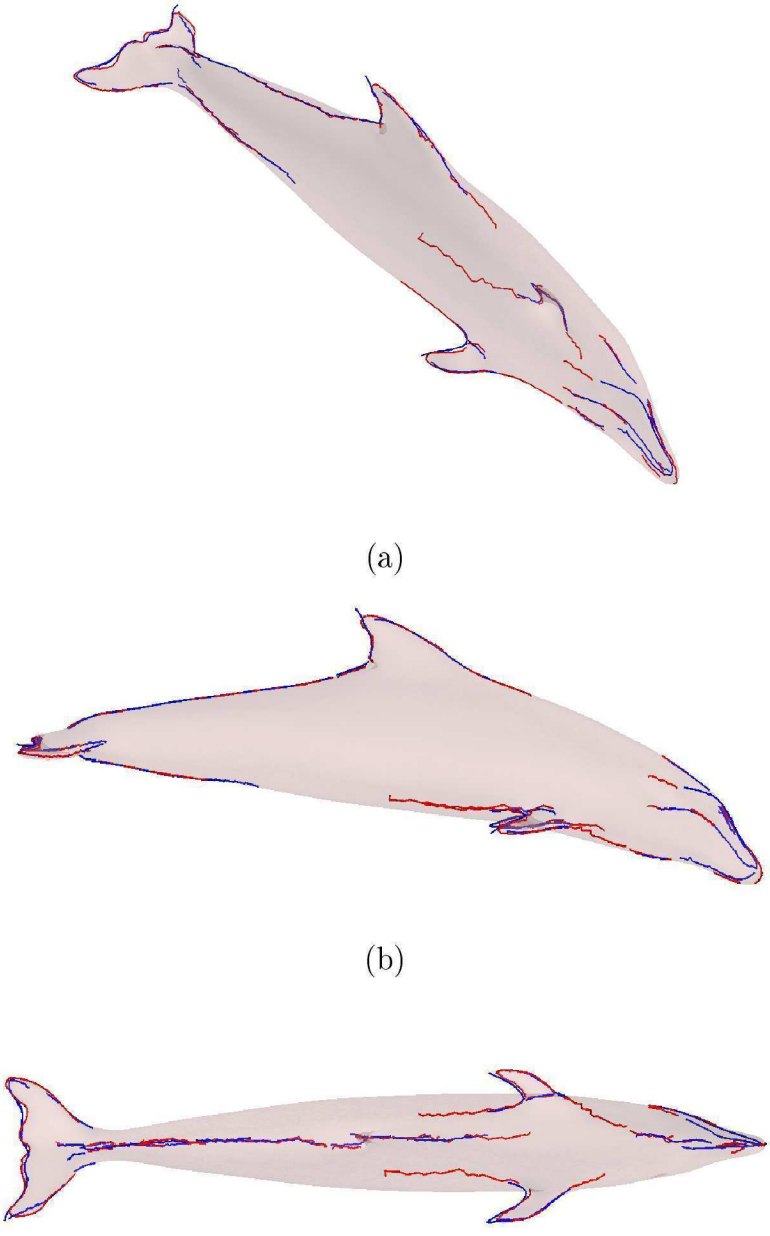

(a)

(b)

(c)

Figure D.3: Feature registration of a base dolphin to the aligned target configuration. The target geometry is illustrated in its aligned position with the target features in red and the deformed base geometry features in blue. Only the registered feature lines on both geometries are shown. (a) Isometric, (b) lateral and (c) lower view.